Stony Brook University

CARDIAC ARRHYTHMOGENESIS IN URBAN AIR POLLUTION: OPTICAL MAPPING IN A TISSUE-ENGINEERED MODEL

A Dissertation Presented

by

Harold H. Bien

to

The Graduate School in

Partial fulfillment of the

Requirements for the

Degree of

Doctor of Philosophy

in

Biomedical Engineering

Stony Brook University

May 2007

Stony Brook University

The Graduate School

Harold H. Bien

We, the dissertation committee for the above candidate for the
Doctor of Philosophy degree,
hereby recommend acceptance of this dissertation.

Emilia Entcheva (Advisor)
Assistant Professor, Department of Biomedical Engineering

Yingtian Pan (Chair)
Associate Professor, Department of Biomedical Engineering

Ira S. Cohen
Leading Professor, Department of Physiology and Biophysics

Richard T. Mathias
Professor, Department of Physiology and Biophysics

Arkady M. Pertsov
Professor, Department of Pharmacology, SUNY Upstate Medical University

This dissertation is accepted by the graduate school

Lawrence Martin
Dean of the Graduate School

ABSTRACT OF THE DISSERTATION

CARDIAC ARRHYTHMOGENESIS IN URBAN AIR POLLUTION: OPTICAL MAPPING IN A TISSUE-ENGINEERED MODEL

by

Harold Bien

Doctor of Philosophy

In

Biomedical Engineering

Stony Brook University

2007

Recent epidemiological evidence has implicated particulate matter air pollution in cardiovascular disease. We hypothesized that inflammatory mediators released from lung macrophages after exposure to particulate matter predisposes the heart to disturbances in rhythm. Using a rational design approach, a fluorescent optical mapping system was devised to image spatiotemporal patterns of excitation in a tissue engineered model of cardiac tissue. Algorithms for automated data analysis and characterization of rhythm stability were developed, implemented, and verified. Baseline evaluation of spatiotemporal instability patterns in normal cardiac tissue was performed for comparison to an in-vitro model of particulate matter air pollution exposure. Exposure to particulate-matter activated alveolar macrophage conditioned media resulted in paradoxical functional changes more consistent with improved growth. These findings might be indicative of a "stress" response to particulate-matter induced pulmonary inflammation, or may be specific to the animal model (neonatal rat) employed. In the pursuit of elucidating the proposed pathway, we have also furthered our understanding of fundamental behaviors of arrhythmias in general and established a model where further testing might ultimately reveal the mechanism for urban air pollution associated cardiovascular morbidity.

TABLE OF CONTENTS

LIST OF SYMBOLS AND ABBREVIATIONS

ν	angular velocity
δR	inter-groove spacing in radial distance
#F	F-number (of a lens)
d	lens diameter
f	focal length
k_d	dissociation (equilibrium) constant
n	index of refraction
r	radial distance, i.e. radius
t	time
w	duration of an event, e.g. CTD or APD
x,y,z	spatial coordinates in Cartesian space with z usually denoting depth
Γ	reference (activation) time
δt	temporal resolution = interval between start of exposures
$\delta x,\delta y$	linear resolution (in-plane)
δz	resolution in depth (along optical axis)
θ	velocity, e.g. CV or CPV
λ	wavelength = $w\times\theta$
3D	three dimensional
AM	alveolar macrophages
AMI	acute myocardial infarction
APD	action potential duration
AQCDPM	Air Quality Criteria Document for Particulate matter
AQI	air quality index
BAL	bronchoalveolar lavage (fluid)
CA	cellulose acetate
CAD	coronary artery disease
CCD	charge-coupled device
CCM	charge-carrier multiplication (see also EMCCD)
CFI	contact fluorescence imaging
CM	cardiomyocytes
CMOS	complementary metal-oxide semiconductor (device)
CNC	computer numeric controlled (milling)
COPD	chronic obstructive pulmonary disease

CPS	calcium propagation slowness = 1/CPV
CPV	calcium propagation velocity
CRI	calcium relaxation interval
CRP	C-Reactive Protein
CS	conduction slowness = 1/CV
CTD	calcium transient duration
CV	conduction velocity
Cx43	connexin-43 (gap junctional protein)
DI	diastolic interval
DMA	direct memory access
DOF	depth of field
DOI	depth of (fluorescence) integration
DR	dynamic range
EC	excitation-contraction (coupling)
ECM	extracellular matrix
EMCCD	electron-multiplying CCD (see also CCM)
EPA	Environmental Protection Agency
F-12k	Kaighn's modification of Ham's F-12 medium
FB	fibroblasts
FC	focal center (of excitation/contraction)
FCS	fetal calf serum
FOV	field of view
FPGA	field programmable gated array
GB	gigabytes, 1024MB or 1,073,741,824 bytes
GL	grayscale level
HDD	hard disk drive
HTC	heart tissue construct
HUMR	high-definition, ultra-wide band macroscopic recorder
I-CCD/CMOS	intensified CCD or CMOS
IL-1β	interleukin-1 beta
KB	kilobytes, 1024 bytes
LCA	light collecting ability
LP	(Columbia) long-playing (format)
LPS	lipopolysaccharide
M199	Medium 199
MB	megabytes, 1024KB or 1,048,576 bytes

MCP	micro(multi-)-channel plate (architecture)
MEMS	micro-electromechanical structures/systems
MTF	modulation transfer function
NA	numerical aperture
NAAQS	National Ambient Air Quality Standards
NNT	number needed to treat
NRVM	neonatal rat ventriculomyocyte
PDA	photodiode array
PDMS	polydimethylsiloxane
PM	particulate matter
PM_{10}	particulate matter, 10μm mean aerodynamic diameter or smaller
$PM_{2.5}$	particulate matter, 2.5μm mean aerodynamic diameter or smaller
PMT	photomultiplier tube
PM_{uf}	ultra-fine particulate matter, less than 0.1μm mean aerodynamic diameter
PS	phase singularity or singularities (of a spiral)
PSF	point spread function
QE	quantum efficiency
RAM	random access memory
RGB	red, green, and blue (channels)
ROFA	residual oil fly ash, i.e. combustion by-products
ROS	reactive oxygen species, e.g. O^{3-}
SCAT	sequential, co-localized, and alternating in time (measurements)
SE	standard error (of measurement)
SEM	scanning electron microscopy
SLA	selective laser ablation
SLS	selective laser sintering
SNR	signal-to-noise ratio
SRM	source reference material
TL	tandem lens
TNF-α	tumor necrosis factor, alpha

LIST OF FIGURES

LIST OF TABLES

PREFACE

Little did he know that with each sip of air the tiny deadly particles filtered through his nasal passages and slowly settled inside his lungs, irritating his immune system's sentinels – the macrophages. Once triggered, the macrophages engulfed the particles and recruited more macrophages to the scene by releasing many inflammatory signaling molecules. The resultant maelstrom of white blood cells pumping out potent toxic agents like bleach and hydrogen peroxide further incensed the situation, killing both friend and foe alike.

Meanwhile, downstream of the lungs, his heart was dutifully pumping his blood throughout his body at a steady 80 beats per minute – oblivious to the fury of activity in the lungs – bathing all cells, especially the heart muscle itself, in oxygen rich nutrient medium. Like the man himself, the heart, too, was unaware of the dangers lurking in the very blood it was drinking and circulating. The inflammatory signals being generated in the lungs were now also traveling around the body in the blood, and the myocardium began to sense something was amiss.

The battle that ensued in the lungs caused the vasculature to become leaky and dilate – the better to permit white blood cells leaving the blood and entering the lung tissue itself. This caused a reduction in blood flow, and the autonomic nervous system responded by requesting an increased heart rate. As in the case with most illnesses, it was the weakest ones that were the most susceptible – and these few cells, not able to keep up with the increased demands, started to take longer to cycle from contracted to relaxed states and propagated the contraction wave ever slower until finally, some beats were becoming blocked and the contraction wave halted at that point.

The incessant activity of the neighboring cells, however, meant that sometimes the tissue behind the conduction block could still become activated, albeit by the backward motion of an expanding contraction wave that had detoured around the block. Suddenly, the contraction waves circled and spiraled around in the heart triggering inappropriately early activation and drowning out the well timed pulses of the pacemaker cells. The contraction and excitation waves broke apart and rejoined in seemingly random patterns resembling a churning, foamy, stormy ocean.

No longer efficiently contracting in a synchronized fashion, the heart failed to deliver the requisite blood supply, and this further aggravated the muscle cells – now beating at over 200 beats per minute and yet starved for nutrients. As the muscle cells began to die, the man pressed his clenched fist against his breastbone – his face now ashen gray and his respirations in fast, shallow, strokes – and collapsed to the floor.

* * *

Were the "tiny deadly particles" some kind of biochemical or nanotechnological warfare weapon, delivered in a typical terrorist-style attack on an unsuspecting public? Possibly – but it could also simply be urban dust or diesel exhaust particles in the air people breathe everyday.

ACKNOWLEDGEMENTS

Thanks for all the help and assistance from the "kids" in the lab. In particular, thanks to Lenny for his work with particulate matter and taking care of the macrophages; to Vikram for scaffold characterization and working out the details of the ELISA; to Rupinder for his sense of independence and bringing us to the GUI age; to Adiba and Sal for manually analyzing the transients; to Shams and Jeremy for tracking the tips of spirals; to Rohit and Mohit for investigating the role Na and Ca play in our model and thus enabling precise pharmacological perturbation; to Melissa, Hui-Jing, Jawaad, and Ravi for their pioneering work on patterning; and to Ujas for his work on temperature dependence of electrophysiology. Without their assistance, much of the following work would not have been possible. I'd also like to acknowledge the tireless efforts of Chiung-Ying for the neonatal rat cultures, and for the wonderful insight from Jia on the spatially discordant alternans– you've only been here for a short time but you sure picked things up fast! Also, despite the few free hours available to an intern, Puja somehow managed to create time for the empirical tests of optical resolution. Last, but not the least, Lihong has helped me get started in the lab as well as spent countless hours pouring over printouts convincing me that a better solution must be sought.

I guess it's only proper to include my parents as well – they have suffered long and hard through all my school years, never complaining, and always encouraging.

All my fellow MSTP classmates – especially those in my "class": sticking together we survived the first two years of medical school: Chris, Raajit, Helen, Margie, and Christi.

To my committee members: Ira, Rick, Pan, and Pertsov – thanks for putting up with my last-minute submissions and sometimes rambling dissertation as well as your ever helpful career advice. I'll try to listen and follow, but if my past life's experience has taught me anything – it's that sometimes, you have to fail and get hurt first before you can really understand the sound input of people wiser than myself.

Finally, I owe an immeasurable amount of gratitude, "luck", knowledge, and skills to my multi-roled friend, mentor, advisor, protector, partner, debater, supervisor, teacher, professor, and reluctant disciplinarian: Emilia. Through these past years I know I've tortured you while you nurtured me. We don't always see eye-to-eye (unless it's science), but it's our differences, I believe, that form the strength and foundation of our special relationship. As always, I look forward to working together with you in the not-too-far-off future as collaborators, co-conspirators, and yes, friends. You gave (and still give) me too much credit and refuse to accept your responsibility in making me who I am today.

1. SPECIFIC AIMS

Abstract

Epidemiological and basic science research has associated particulate matter inhalation with pulmonary inflammation and elevated blood concentrations of inflammatory mediators. These same inflammatory cytokines reportedly influence cardiac arrhythmias in vitro and in vivo. Therefore, we hypothesize that airborne particulate matter might induce dysrhythmias via the actions of inflammatory signaling molecules released from the pulmonary vasculature. Since cytokines are known to interact with a wide variety of tissues including white blood cells, endothelial cells, and even cardiac fibroblasts, a reduced model with more restricted tissue types is required to unveil distinct pathways. Specifically, we are interested in the effects of cytokines released from resident lung alveolar macrophages exposed to particulate matter on cardiac tissue.

Introduction

Particulate matter (PM) exists in the atmosphere around us to varying degrees and extents and may have very different composition, shape, and thus effect(E.P.A. 2004c). Consider the growing evidence of airborne PM exposure's association with cardiovascular morbidity and mortality(Peters 2005) combined with the fact that cardiovascular morbidity and mortality reigned and remain as the leading cause of hospitalization and death(National Center for Health 2004), a significant fraction of which are related to cardiac arrhythmias(Brook, Franklin et al. 2004; Rich, Schwartz et al. 2005). Could the wide-spread exposure to PM contribute to the prevalence and incidence of cardiovascular disease?

Epidemiological and basic science research have established particulate matter inhalation's association with pulmonary inflammation(Bouthillier, Vincent et al. 1998; Ishihara and Kagawa 2003; Roberts, Richards et al. 2003) and elevated blood concentrations of inflammatory mediators(Killingsworth, Shore et al. 1997; van Eeden, Tan et al. 2001; Gong, Sioutas et al. 2003). These same inflammatory cytokines reportedly influence cardiac arrhythmias(Cesari, Penninx, Newman, Kritchevsky, Nicklas, Sutton-Tyrrell, Rubin et al. 2003; Cesari, Penninx, Newman, Kritchevsky, Nicklas, Sutton-Tyrrell, Tracy et al. 2003; London, Baker et al. 2003). Therefore, ***we hypothesize that airborne particulate matter might induce arrhythmias via the actions of inflammatory signaling molecules released from the pulmonary system.*** This project proposes to use a tissue engineering approach coupled with advanced imaging technology to establish a plausible mechanism for how particulate matter air pollution contributes to cardiac arrhythmias, and in doing so also improve current understanding of cardiac instabilities in general.

Aim 1: An *in-vitro* experimental model

Since cytokines are known to interact with a wide variety of tissues including white blood cells, endothelial cells, and even cardiac fibroblasts, a reduced model with more

restricted tissue types is required to unveil distinct pathways. The ability to isolate and culture neonatal rat cardiomyocytes(Rohr, Shoelly et al. 1991) provides an opportunity to study the effects of inflammatory cytokines on pure cardiac tissue without additional tissue types. It is important to note that while the effects of inflammatory cytokines on excitation-contraction (EC) coupling and other cellular-level properties of isolated cardiomyocytes have been well studied(Henriksen and Newby 2003), the arrhythmogenic potential of such changes are less certain, in part because some studies were performed on isolated cardiomyocytes where spatially extended arrhythmias were not possible. Clearly then, at minimum, an interconnected network of cardiac cells (a reduced tissue model) is required to assess arrhythmogenic potential. While an intact heart preparation would yield the most realistic model, the inability to determine activation state of deeper layers with inherently two-dimensional measurement techniques combined with the complex geometry of native heart tissue would render studies unduly complex. To reduce the potential influence of structure on cardiac behavior, a well-defined surface geometry will also be required. In addition, because the identity and concentration of the inflammatory cytokines released from the lung exposed to PM is not yet known, an experimental model is required to duplicate the systemic environment of a heart in an individual exposed to PM. As exposing an intact animal to PM is a complex and expensive endeavor, a simplified *in vitro* model of PM induced pulmonary inflammation is desirable. Although a wide range of cells in the lung can secrete cytokines, the principal source of PM evoked inflammatory cytokines is believed to be alveolar macrophages(Devalia, Bayram et al. 1997). *Therefore, a two-dimensional system with controllable geometry and inter-connected network of cardiac cells will be sought to assess arrhythmogenicity and explore changes brought about by exposure to signaling molecules released by alveolar macrophages activated by particulate matter air pollution.*

***Specific Aim 1a**: Assemble a two-dimensional, networked heart tissue construct with specified geometry.*

Using an established two-dimensional heart tissue construct (HTC) consisting of a monolayer of neonatal rat cardiomyocytes(Rohr, Shoelly et al. 1991) as an inter-connected network of cardiac tissue, we will attempt to culture the cardiomyocytes on a scaffold suitable for optical mapping and engineered surface geometry. The limits of surface topographies attainable with the selected micro-machining methodology will be explored, and we will also perform a baseline characterization of the cardiomyocytes grown on scaffolding with various topographies to determine the role of surface geometry on the morphology and function of such cells.

***Specific Aim 1b**: Design a simulated particulate matter air pollution exposure model consistent with the hypothesis that inflammatory mediators released from the pulmonary system is responsible for the cardiovascular effects.*

An exposure model will be designed such that potential signaling molecules released from activated lung tissue will be used to treat HTCs, and the electrophysiological effects of such treatment will be assessed. Bronchoalveolar lavage (BAL) derived alveolar macrophages (AM) or an AM cell line with traits consistent with native AM cells will be exposed to varying concentrations of PM *in vitro*. Cytokines released by activated AM will be collected after 24 hours in the culture media (AM conditioned media) and used to treat HTCs for an additional 24 hours. Activation of AM with standard irritants such as lipopolysaccharides (LPS) will be used as controls and to determine maximal levels of select inflammatory cytokines released by

AM. HTCs grown in culture medium with PM or LPS without any AM will be used to control for potential influences from trace PM or LPS in the culture media.

Aim 2: Optical mapping of HTCs

To establish the role of PM pollution and cardiac arrhythmias, the arrhythmogenic potential of HTCs treated with cytokines as described above must be quantitatively measured. Arrhythmias can arise from dynamic instabilities (in time) or regions of varying activation states (in space). Knowledge of HTC activity over space and time can discriminate between the two possibilities but require simultaneous multiple measurements across the entire two dimensional HTC surface. Fluorescent indicator dyes provide an instantaneous multi-point tissue-level examination of activation state (via transmembrane potential) and EC coupling (via intra-cellular calcium cycling). Optical recording, via a cinematographic recorder or camera, of the fluorescent intensities of HTCs stained with such indicator dyes will reveal the patterns of propagation and the spatiotemporal evolution of paced activity or arrhythmia – a technique known as optical mapping. A system for optical mapping of HTCs will need to simultaneously sample many spatial points rapidly over a period of time. How many spatial points sampled, i.e. the spatial resolution, and how rapidly they are read, i.e. temporal resolution, determine the quality and quantity of information recorded about HTC activation. Current technology imposes limits on spatial and temporal resolution as well as their product, typically expressed as bandwidth. Optimization of maximum available bandwidth with respect to spatial and temporal resolution requires first determination of the minimum acceptable spatiotemporal resolutions. After the minimum spatial and temporal resolution requirements have been calculated or decided, an actual system will need to be constructed that can meet or exceed the spatiotemporal specifications. Finally, the quantity of data collected from such a system will require automated or at least assisted data analysis to extract meaningful statistical data or trends from the observations. *Thus, a high definition, ultra-wideband macroscopic recorder (HUMR) shall be designed and constructed to image and record the fluorescence intensities of labeled HTCs over time, i.e. optical mapping, and image/signal processing algorithms will be developed to analyze collected data.*

Specific Aim 2a: *Determine spatiotemporal resolution requirements for optical mapping of activation patterns in HTCs.*

Using a simple model of propagation, the minimum spatiotemporal resolution required for optical mapping will be determined. An optimization strategy will then be developed to maximize the utility of available bandwidth, and a rational specification for spatial and temporal resolution of HUMR will be developed to ensure adequate capture of the spatiotemporal evolution of activation patterns in HTCs.

Specific Aim 2b: *Evaluate existing imaging technologies and construct a HUMR with adequate spatiotemporal resolution and optimized bandwidth utilization.*

After establishing a rational HUMR specification, a survey of existing imaging technologies will enable selection of the most appropriate imaging sensor, optical elements, and data transfer mechanism to achieve the required specifications. Real-word testing of individual components as necessary will further validate theoretical performance claims. The selected imaging sensor, optical elements, and data transfer system will then integrated to form a HUMR capable of recording fluorescence signals from labeled HTCs in a field of view no

less than 1cm x 1cm to ensure sufficient area for formation of spatial propagation patterns and visualization of spatiotemporal evolution of HTC instabilities.

Specific Aim 2c: *Design, implement, and verify algorithms for automated waveform analysis.*

The ultra-wide band property of HUMR means an enormous amount of data will be generated quickly precluding manual data analysis. Algorithms will need to be developed and implemented for automated, fast, efficient, and accurate determination of waveform morphology. Prototyping and design of algorithms will be done with MATLAB numerical analysis system, and a final optimized version will be developed using either MATLAB or another more suitable programming platform. Human verification of algorithm accuracy and performance will be conducted in selected abridged datasets by multiple operators.

Specific Aim 2d*: Design, implement, and verify algorithms for visualization and analysis*

Large quantities of dynamic data over space require a method of presenting data in such a manner as to be readily interpretable. Algorithms will be developed that enable appropriate transformations of data into more meaningful visual displays, taking into account the spatiotemporal characteristics of data. Processing over both space and time domains will enable analysis of spatiotemporal patterns. Software will be written that can analyze and display the recorded data.

Aim 3: Mechanism of PM-exposure induced arrhythmias

Armed with the instruments and tools capable of assessing arrhythmogenicity of HTCs exposed to varying concentrations of signaling molecules from PM-exposed lung tissue, we can now set forth a potential pathway linking PM-exposure and cardiac arrhythmias. As stated before, arrhythmias in a spatially extended system can arise from either spatial or temporal considerations, making an "index of arrhythmogenicity" a very difficult yet much sought after ideal. In order to provide a relate observed changes to arrhythmogenic susceptibility, behaviors common to all spatiotemporal instabilities in cardiac tissue will be studied to identify key attributes of arrhythmias in general. Then, changes brought about by treatment with AM conditioned media in these specific parameters will provide a qualitative index of arrhythmogenicity, but because HTCs were exposed to all signaling molecules released by PM-exposed AM in AM conditioned media, the actual agent(s) responsible for the observed changes remain unknown. If the actual causative factor or factors could be identified, then appropriate therapy could be initiated to ameliorate the effects of PM-pollution on heart disease. *Therefore, we will provide a plausible mechanistic explanation of how particulate matter air pollution influences cardiac arrhythmias and attempt to identify the causative factor or factors in AM conditioned media.*

Specific Aim 3a: *Characterize specific attributes common to spatiotemporal instabilities*

Optical mapping of normal (not treated) HTCs paced at high rates to unmask instabilities will be performed to determine common modes of spatiotemporal instability evolution and their association with arrhythmias. By examining the electrophysiological response to varying pacing stimuli, a frequency-response curve or restitution curve can be constructed for various parameters. Using quantitative measures of waveform morphology, we will explore how activation kinetics and properties (as reflected by transient morphology) relate to instabilities, and how spatial dispersion of properties influences the development of arrhythmias.

Specific Aim 3b: *Assess HTCs treated with AM conditioned media and estimate its vector of arrhythmogenic potential.*

Optical mapping of HTCs treated in conditioned media from AM exposed to varying concentrations of PM or a control agent will be conducted to quantitatively assess the arrhythmogenicity of treated HTCs. Transient morphology and other key attributes identified earlier to be indicators of arrhythmogenic potential will be determined to establish a putative link between PM exposure and cardiac arrhythmias.

Specific Aim 3c: *Identify signaling molecule(s) responsible for HTC changes.*

We will assay for the concentrations of well known inflammatory mediators in AM conditioned media, and reconstitute artificial media by adding exogenous cytokines at measured concentrations to normal (not AM conditioned) cell culture media. Optical mapping of HTCs exposed to artificial media will be compared to HTCs exposed to AM conditioned media to determine whether the artificial media can recapitulate the arrhythmogenic susceptibility from AM conditioned media. Finally, identification of the putative causal factor(s) will be made by using blocking antibodies to demonstrate the lack of effect of AM conditioned media on HTC when the causative factor(s) are removed.

Summary

Using a tissue-engineering approach coupled with optical mapping techniques, a potential mechanistic link between PM exposure and cardiac arrhythmias will be established while also developing a pseudo-marker, i.e. vector, of arrhythmogenic susceptibility in HTCs. Such knowledge will inevitably aid in better prevention of cardiac sequelae of people living in industrialized nations or otherwise exposed to particulate matter air pollution, and may advance future anti-arrhythmic therapies by better understanding the pathogenesis of cardiac arrhythmias in general. Furthermore, the tools and techniques developed in this project can be easily adapted for other investigations on factors of cardiac arrhythmogenesis.

2. IDENTIFICATION OF AT-RISK SUB-POPULATIONS THROUGH UNDERSTANDING PARTICULATE MATTER INDUCED CARDIOVASCULAR PATHOGENESIS

Abstract

Despite epidemiological evidence linking particulate matter (PM) air pollution and cardiovascular disease, little is known about the mechanism underlying the role ambient PM plays in inciting cardiac pathology. Considering the large population exposed to PM and the small number of people profoundly impacted by it, identification of vulnerable at-risk groups becomes imperative. An argument is made here that epidemiological methods, typical for such public health issues, is not the right tool in identification of these sub-groups due to the low incidence of PM-induced cardiac disease. Therefore, better understanding of the pathogenesis of PM-induced cardiovascular pathology will lead to better identification of at-risk sub-groups.

Introduction

Particulate matter (PM) air pollution is one of the six regulated pollutants under the Clean Air Act(E.P.A. 2005b). Section 108, Part A, of Title I of the Clean Air Act specifies that the United States Environmental Protection Agency (EPA) is responsible for setting "National Ambient Air Quality Standards" (NAAQS) according to the "latest scientific knowledge" of the pollutant's effects on human health and welfare. Through a public review process, the NAAQS is set for a given pollutant after publication of a criteria document laying out the measurement techniques and standards for compliance(E.P.A. 2004a; E.P.A. 2004b). In the latest revision of the criteria document for PM, "Air Quality Criteria Document for Particulate Matter" (AQCDPM), October 2004, PM was classified based on the mean aerodynamic diameters into 2 broad groups: a "coarse" fraction ($PM_{10-2.5}$) with diameters between 10μm and 2.5μm, and a "fine" fraction ($PM_{2.5}$) with diameters less than 2.5μm. Additional terminology for referring to specific sub-populations or combinations of particles include the "thoracic" particles (PM_{10}) less than or equal to 10μm in mean aerodynamic diameter, i.e. combined $PM_{10-2.5}$ and $PM_{2.5}$ fractions), and "ultra-fine" particles (PM_{uf}) having diameters less than 0.1μm (**Figure 2-1**). In this sense, PM air pollution is somewhat distinct from the rest of the regulated pollutants in that it is classified by size, not chemical composition. In fact, there is not only widespread regional and seasonal differences in PM composition (2004c; Sharma and Pervez 2004; Reff, Turpin et al. 2005; Sheesley, Schauer et al. 2005), but coarse and fine PM populations each have distinct chemical profiles(E.P.A. 2004c) making interpretation of PM levels difficult, and correlation to other indicators of health tenuous. In fact, one study alone using PM_{10} from different zones in Mexico City found surprisingly varied biological *in vitro* effects dependent upon the location of the origin of PM(Alfaro-Moreno, Martinez et al. 2002).

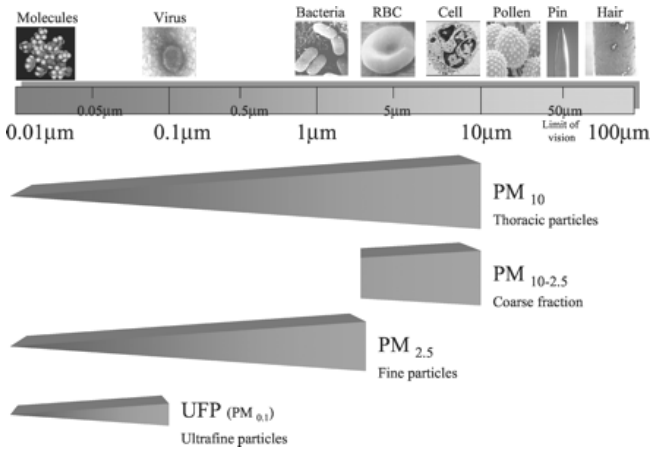

Figure 2-1 Schematic illustration relating relative sizes of particulate matter classifications.
Classification is via mean aerodynamic diameter (size) in microns. Above are several common items for reference(Brook, Franklin et al. 2004).

However, while the AQCDPM sets limits for $PM_{10}$and $PM_{2.5}$[1], it also readily admits that measurement technologies vary and therefore estimates of PM_{10}, $PM_{2.5}$ and especially the PM_{uf} may vary as a result of measuring technology employed. Nevertheless, the standards set forth by the AQCDPM of 2004 used the 99th percentile of monitoring stations(E.P.A. 2004b). It should come as no surprise, then, that as of December 2004 there were only 208 counties out of 3141 counties (6.6%) that were designated by the EPA as "non-attainment sites"(E.P.A. 2005a). The fact that there was more than 1% non-attainment sites probably reflects the inclusion of neighboring areas thought to contribute to PM pollution in the non-attainment designation(E.P.A. 2004c). Despite the small number of non-attainment sites and a clear decline in PM levels across the nation(E.P.A. 2004c), there has been a recent spate of attention on the links between PM and human health – more specifically cardiovascular health(Pope 2004).

Epidemiology

Most of the recent reports focus on the numerous epidemiological studies that have demonstrated a small but significant association between PM levels and cardiovascular morbidity and mortality, reviewed in (Brook, Franklin et al. 2004). Using generalized linear models and sliding time-lag analysis techniques, excess morbidity and mortality has been attributed to increased levels of PM air pollution in both acute and chronic exposure scenarios. Most of the studies have focused on acute spikes in PM concentrations and correlated that with increased hospital admissions, cardiovascular mortality, and all-cause non-traumatic deaths(Pope 2000) and were restricted to outcomes in the local neighborhood. However, two large scale multi-site studies conducted in the United States (NMMAPS) and Europe (APHEA-2) have confirmed a slight yet significant association between $PM_{2.5}$ levels and cardiovascular health(Brook, Franklin et al. 2004).

[1] There was a contentious legal battle between the EPA and the Trucking association regarding the limits for $PM_{2.5}$ set forth in the 1997 AQCDPM. For more details, see the first chapter in the 2004 AQCDPM detailing the legal battles and outcome.

While longer-term studies are few, two rather large multi-site retrospective studies were performed(Pope, Burnett et al. 2002), and both indicated increased risk of all-cause mortality and cardiovascular mortality. More interestingly, they also found an increased risk of mortality to those with lung cancer – a surprising finding given that the longest study covered just 16 years. Most people with a history of tobacco use, i.e. exposed to much more than ambient PM levels combined with numerous other toxic gases and chemicals, are diagnosed with lung cancer after 50 years of age(Veness, Delaney et al. 1999) or 32 smoking years if they started at age 18. Furthermore, that lung cancer has a variety of causes including genetic mutations makes it even more unlikely that PM levels can provoke or accelerate death from an existing pulmonary cancer. Yet the fact remains – there *is* an increased rate of mortality from lung cancer that is linked to increased levels of PM, together with increased rates of all-cause mortality and specifically cardiovascular mortality. If PM is not the proximate cause, then why does the association exist?

Remember that cardiovascular disease and lung cancer remain the leading cause of death for people over 25 years of age in the United States(National Center for Health 2004). If PM were to increase mortality rates in a randomly selected sub-population, one would still expect an increased prevalence of lung cancer and cardiovascular disease mortality in this subgroup. If this were true, then the at-risk population is not necessarily those with pre-existing cardiovascular diseases or pulmonary cancers, but rather a select sub-population who may or may not be over represented in the population of people with cardiovascular and pulmonary diseases. This theory is bolstered by the fact that most studies reviewed report relative risk ratios (or odds ratios) in the vicinity of 1.1 to 1.2(Pope 2000; Peters and Pope 2002; 2004b) – numbers that may be significantly greater than 1, but not by much. In fact, Brook et al. point out that these relative risks are lower than from obesity or tobacco smoking(Brook, Franklin et al. 2004). They are also quick to state, however, that despite the seemingly small relative risks, the large population exposed to ambient PM makes this a public health issue. A review of the declining levels of PM combined with the decline in death rates overall would indicate that PM may contribute to excess deaths. However, medical technology's role in improving one's odds of survival cannot be discounted, and in fact, probably far out-strip any excess mortality arising from PM exposure as the life expectancy has only increased, not declined, since the industrial revolution.

Identifying populations at risk from PM exposure

Given the small number of people at increased risk of death from PM air pollution, the focus should be on identifying those select populations at risk. This strategy is borne out by the Air Quality Index (AQI) published by the EPA(E.P.A. 2003). It is a normalized scale from 0 to 500 categorized by color with advice for specific at-risk populations on days with elevated levels of pollutants. The at-risk population identified by the EPA in the AQI for PM – "people with heart or lung disease, older adults, and children"(E.P.A. 2003) – however, lacks firm scientific support, drawing instead from epidemiological studies demonstrating a significant but weak relationship between the elderly and the young(Brook, Franklin et al. 2004). Hypotheses ranging from pre-existing cardiovascular and pulmonary diseases in the elderly to more active and therefore exposed children have been used as potential mechanisms underlying their susceptibility(Levy, Greco et al. 2002; Liu, Box et al. 2003).

Attempts have been made using epidemiological data to identify at-risk groups, including a study by Bateson et al. that showed an almost two-fold increase in relative risk of increased mortality in diabetics(Bateson and Schwartz 2004). However, in general, due to the low incidence of excess deaths attributable to PM (or conversely, due to the high background mortality caused by existing PM levels), epidemiological methods to identify at-risk groups will require a large sample size dwarfing even that of the multi-site Harvard Six Cities study(Dockery, Pope et al. 1993).

Research into the potential mechanisms underlying PM's toxicity has just begun, especially with regard to cardiovascular disease(Brook, Franklin et al. 2004). Understanding how PM exerts its toxic effects is another potential route towards identifying those most at risk, and in doing so can only further our understanding of physiology and toxicology of PM. The scientific council established for AQCDPM in 1997 established a general research model suggesting how one goes about determining "safe" levels of PM, but another possible approach is to examine PM pollution of the body in direct analogy to standard pollution models used today for air pollution.

General model of PM's effects *in vivo*

A typical air pollutant model would include a source, transport mechanisms and possible chemical or physical reactions, and a receptor that is affected by the presence of the pollutant. In a similar manner, we have a source – the ambient air we breathe, several transport mechanisms ranging from simple mass air flow into the lungs to the complexities of the circulatory system, reactions that can occur during transport such as inflammation and subsequent release of local inflammatory mediators (akin to secondary pollutants), and the target organs (receptors).

Source

Air intake, more specifically oxygen intake, is a requirement for continued aerobic respiration in human physiology. Thus, a potential source of PM from the ambient PM surrounding a person is always present. As detailed extensively in the AQCDPM, the range of PM sizes that can penetrate the innate defenses and present a threat to health are typically in the $PM_{2.5}$ fraction (**Figure 2-2**). Once inside the airways, mass flow from the act of breathing and air exchange help move PM deep within a subject, especially $PM_{2.5}$ which includes the PM_{uf} fraction. Once inside the alveoli, PM can leach off aqueous phase components including toxic metal elements such as zinc and vanadium(Gavett, Madison et al. 1997; Kodavanti, Schladweiler et al. 2002) and other foreign organics including lipopolysaccharide, i.e. endotoxin, a component of the outer wall of bacteria that is highly reactive with white blood cells(Soukup and Becker 2001). Once absorbed, the foreign material readily dissolves into the pulmonary vascular bed where it is then circulated via the mechanical pumping action of the heart throughout the body.

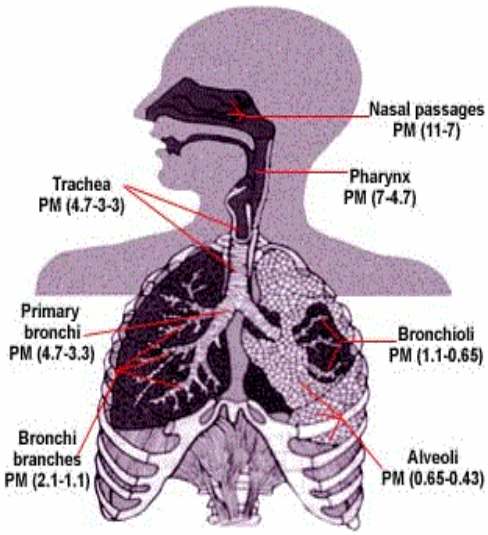

Figure 2-2 Sites of deposition for various fractions of particulate matter in the human respiratory system.
The range of sizes of particulates are denoted in parenthesis after the location in microns(Spengler, Koutrakis et al. 1996).

Transport and reaction

Meanwhile, the foreign matter irritates the local resident population of macrophages, white blood cells designed to "clean up" the lungs by phagocytosis, and the cells lining the alveolar walls, i.e. the epithelial cells(Soukup and Becker 2001; van Eeden, Tan et al. 2001; Bagate, Meiring et al. 2004; Chauhan, Breznan et al. 2004). These cells in turn release inflammatory mediators as a signal to recruit more white blood cells. These inflammatory mediators, typically cytokines of various types, can be considered a secondary pollutant. Not only do the cytokines recruit additional white blood cells, but the arriving white blood cells are then induced to release more inflammatory cytokines such as interleukin-1beta (IL-1β), tumor necrosis factor-alpha (TNF-α), and damaging reactive oxygen species (ROS)(van Eeden, Tan et al. 2001) as part of the natural innate defense mechanism against foreign body invasion. It should come as no surprise that this sequence of events is very similar to that of any type of irritant/pollutant exposure, including ozone and even chemical warfare gas agents such as mustard gas(Iyriboz 2004) and chemical pepper spray, e.g. Mace®(Reilly, Taylor et al. 2003).

The leachables from PM and inflammatory mediators are then circulated from the pulmonary vascular bed to the heart. Due to the high metabolic (and hence oxygen) requirement of the myocardium, the coronary arteries come off the root of the aorta, i.e. where the aorta originates from the left ventricle, giving the heart a "first pass" at the oxygen rich blood. Unfortunately, this "first pass" also means that the myocardium is exposed to the highest concentrations of PM absorbed materials and inflammatory mediators second only to the pulmonary vascular bed. This also means that the blood has not yet passed through the liver, normally considered a "detoxifying" organ.

After the heart, the blood circulates throughout the entire body providing any absorbed substances and inflammatory mediators access to many vital organs including the liver, kidneys, and spleen (an immune organ concerned mostly with filtration of dead red blood cells, but in and of itself also acts as a screening organ and an inspection organ for the immune system to survey the blood for foreign agents). Even the brain, with its vaunted blood-brain barrier, has been shown to be exposed to PM_{uf} circulating in the blood(Oberdorster, Sharp et al. 2004).

Receptors

Lungs

The primary target organ is the lung since it is directly exposed to PM. However, as an organ typically exposed to the outside environment, it has a layer of constantly replenishing epithelial cells much like the skin of a person. This makes it a bit more durable to PM exposure. In terms of reaction to PM, the lung can be divided into three distinct histological sub-types: the alveolar macrophages, epithelial cells, and the endothelial (blood vessel lining) cells. The macrophages, as noted earlier, are responsible for ingesting particulate matter and other foreign body. Animal models have demonstrated that PM can induce macrophages to release potent inflammatory cytokines and even reactive oxygen species (ROS) which are directly damaging to the lungs (similar to ozone's effects), but the degree of activation and the specific mixture of cytokines released may vary depending upon the chemical composition and size of PM(Soukup and Becker 2001; van Eeden, Tan et al. 2001; Chauhan, Breznan et al. 2004; Harkema, Keeler et al. 2004).

The epithelial cells lining the airways are also sensitive to PM. Studies have demonstrated not only prototypical inflammatory changes at the gene transcription level(Koike, Hirano et al. 2004) but also secretion of ROS upon stimulation with residual oil fly ash (ROFA)(Voelkel, Krug et al. 2003). The inflammatory cytokine TNF has also been implicated in pulmonary disease(Lundblad, Thompson-Figueroa et al. 2005). The dying and damaged epithelial cells themselves can trigger additional waves of inflammation as their cellular DNA contents spill out. At the organ and tissue level, local inflammation of the airways, or bronchitis, has been linked with $PM_{2.5}$ exposure in children and is especially worse for those with a history of atopic pulmonary inflammation, i.e. asthma(Pino, Walter et al. 2004). Chronic inflammation can lead to persistent lung parenchyma damage such as chronic bronchitis and emphysema or other chronic obstructive pulmonary diseases (COPD). A good example of an accelerated process would be tobacco smoking which has be positively linked strongly to the progression and development of COPD(Briggs Dd 2004). While it may seem trivial to suggest that since PM has been linked with pulmonary inflammation, one would expect an exacerbation for a patient with pre-existing respiratory disorders, especially a chronic inflammatory condition such as COPD or asthma, this does not really aid in identification of "at-risk" target populations. Most asthma attacks and exacerbations of COPD are not that serious, and they rarely lead to death(Ringbaek, Seersholm et al. 2005). The idea that PM may simple depress the border between the sickest-sick and the recently deceased, an idea termed "harvesting" has been largely discounted by epidemiological and post-hoc studies(Schwartz 2001). Therefore, excess mortality from PM cannot be merely attributed to aggravation of existing pulmonary disease as the postulated mechanisms of action would not be expected to be fatal except in exceptionally large doses(Hunt, Abraham et al. 2003).

Blood vessels

The endothelial cells lining the pulmonary vasculature are similar to other endothelial cells – they are often extremely fragile and sensitive to inflammatory cytokines as well as shear stress. This makes them then sensitive target for PM-induced pulmonary damage, and indeed vascular changes have been noted in association with PM exposure in the laboratory(Nurkiewicz, Porter et al. 2004). Inflammation has been implicated in the development of atherosclerosis, a major factor in the progression of cardiovascular disease(Hansson 2005), and the cytokines released by the activated alveolar macrophages may ultimately encourage atheromatous plaque growth. This effect is not limited to the pulmonary vascular bed – the endothelial cells line all the blood vessels in the body, and in that sense, the blood vessels may have the greatest exposure in terms of surface area, but this hides the fact that the pollutant/toxin is usually diluted quite a bit before it reaches systemic circulation. Numerous inactivators of inflammation and clotting exist in the blood stream to limit such effects to local areas, however the extent to which these extremely potent inflammatory mediators play a role in vascular lesions remain unclear.

Blood

Normally not considered an organ by itself, blood is a complex mixture of cells and fluids that is constantly being circulated around the body and being exposed to the gaseous environment via the pulmonary vascular bed. PM exposure has been demonstrated to change several properties of blood, including its viscosity and C-reactive protein (CRP), an inflammatory marker protein(Donaldson, Stone et al. 2001; Pope, Hansen et al. 2004). Increased viscosity means the heart has to work harder to pump the blood, and the increased CRP levels usually indicate underlying low-level inflammatory process somewhere in the body. The actual effect of CRP is not well understood, but one study has linked CRP to atherosclerosis through its interaction with circulating white blood cells(Devaraj, Du Clos et al. 2005). More importantly, changes in blood coagulation parameters including platelet activity has been found to be linked epidemiologically to PM exposure(Nadziejko, Fang et al. 2002). However, most of these effects have only been studied in humans using epidemiological data. More research using animal models will be required to establish a mechanistic pathway of toxicity from PM.

Heart

Regardless of what mechanism lead to increased blood viscosity, CRP concentrations, and altered coagulation status, the impacts on the heart can be reliability predicted. For instance, increased blood viscosity will require greater energy for blood transport – this is a simple matter of physics. Altered coagulation states may not impact the heart muscle, myocardium, directly *per se* but can significantly impact its function via changes in coronary blood flow. Heart disease, more specifically coronary artery disease, (CAD) remains one of the leading causes of death in the United States(National Center for Health 2004). CAD is characterized by blocked coronary arteries associated with inflammatory changes of the vasculature and increased coagulation state of the blood(Hansson 2005). PM exposure, then, would likely induce acute myocardial infarction (AMI, or heart attack) where the coronary arteries are blocked. While such a link was reported by Peters et al. (Peters, von Klot et al. 2004), two subsequent studies including one by Peters et al. group found no such link(Peters, von Klot et al. 2005; Sullivan, Sheppard et al. 2005). Instead, the current focus of research is

on inflammation's effects on the heart and sympathetic nervous tone as well as potential direct toxicity of the ultra-fine particles. One proposed model is shown in **Figure 2-3**.

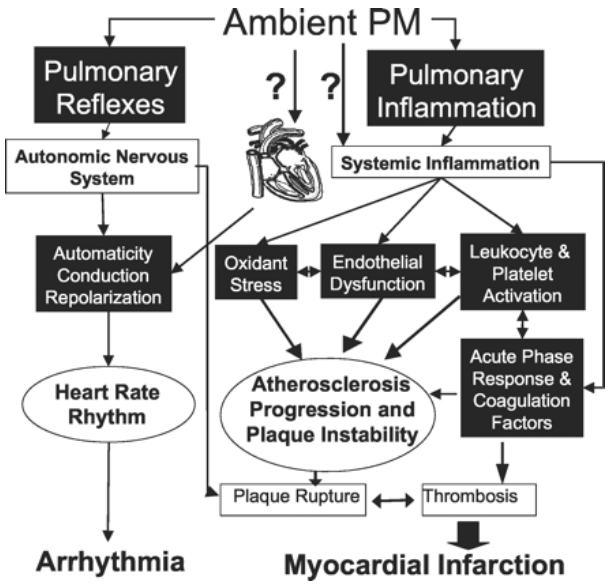

Figure 2-3 Potential pathogenesis of particulate matter (PM) induced cardiovascular disease(Brook, Franklin et al. 2004).

Heavy metals such as zinc and vanadium associated with PM_{uf} has been shown, *in vitro*, to induce arrhythmias(Graff, Cascio et al. 2004). A full-blown inflammatory response in the heart is usually catastrophic, viz. endocarditis and septic shock; however a sub-clinical inflammatory state may still set the heart in a pro-arrhythmic state. The inflammatory cytokines released by the pulmonary system have been shown to adverse affect the stability of the heart's electrical activity. Studies using transgenic mice over-expressing TNF and exogenous administration of IL-1 has demonstrated a clear link between IL-1 and TNF – the prototypical inflammatory mediators, and cardiac arrhythmias both *in vitro* and *in vivo*(Tang, McGowan et al. 2004). Evidence of decreased heart rate variability after PM exposure (Magari, Schwartz et al. 2002; Chen and Hwang 2005) may be explained by increased sympathetic tone or simply increased heart rates. In either case, increased adrenergic stimulation, i.e. increased sympathetic activity, can induce an acute MI. This is often seen, for instance, in the increase of AMI during "catecholamine rush" morning hours when one awakes(Kumagai 2004). Furthermore, chronic levels of inflammatory cytokines such as TNF has been linked to heart failure in a transgenic mouse model(Tang, McGowan et al. 2004) suggesting that chronic PM exposure may play a role in heart failure. The bewildering array of possibilities in alteration of function of the heart as a result of exposure to inflammatory mediators is a reflection of the complex interactions that occur between the immune system, the nervous system, and the cardiac system. Each cell responds in their own slightly different manner when challenged by a specific cytokine, and the effect of multiple input signals, i.e. cytokines and nervous system input, is very hard to predict. For instance, it is known that there exists at least two different types of cellular receptors for the cytokine TNF – one promotes growth and the other cellular suicide (apoptosis). How the

cell decodes a particular TNF concentration signal remains to be solved. Therefore, it becomes critical to understand and map out the pathways of how "secondary pollutants" such as IL-1 and TNF affect the myocardium. Furthermore, the direct cytotoxic potential of ultra-fine particles cannot be ignored.

Other target organs

So far, the target receptors discussed above have been the most intensely studied. However, there are clearly more potential target organs including the liver and the brain that may be affected by PM exposure. One study has actually linked inflammatory cytokine levels with amyloid load – a marker of Alzheimer's disease(Patel, Paris et al. 2005). This surprising result should serve as a warning that systemic inflammation is not to be under-estimated, and that un-expected target organs may be affected by inflammation secondary to PM exposure. The liver is another potential target organ. Typically the "filter" of the body, the liver is tasked with "scrubbing" the blood and removing drugs and other foreign species. The impact of PM exposure on the hepatic system is not well researched(Brook, Franklin et al. 2004), and therefore remains a large unknown in the mechanism of PM toxicity.

Hints of reproductive anomalies have also been detected in epidemiological studies(Brook, Franklin et al. 2004). However, these again have been relatively weak correlates and a mechanism linking PM exposure to birth defects has yet to be proposed. The germline cells, like the brain, are in an immunologically "privileged" area to prevent auto-immunity against the germ cells. This would normally warrant them some protection from possible PM induced damage short of direct exposure, but keep in mind that the brain is also privileged and surrounded by the formidable blood-brain-barrier, which can be breached through the secondary effects of inflammation.

Conclusion

Numerous reviews have already been published including the AQCDPM demonstrating the epidemiological link between particulate matter air pollution and cardiovascular health. However, the majority of reviews have been authored by a select few groups that have been extensively researching the link between PM air pollution and health. It stands to reason therefore that the major consensus on most of these studies is more research is needed before a definite conclusion can be drawn. While this may be true, the sword that is being held over the heads of the public is the possibility that the very air you breathe can kill you (or at least make you die faster). It would be near impossible to ensure everyone breathed pure air without any particulates, and in fact the public drive for "pure air" – like the current craze for "antibacterial soaps" resulting in widespread antibiotic resistance – may very well end up being more harmful than helpful. There is already some evidence that excessively clean environments may be contributing to the increase in asthma and other allergies.

The existing epidemiological evidence only points at a very small increase in risk of death from PM exposure – so small that obesity, hypertension, and other easily preventable factors far outweigh the benefits, if any, of PM reduction. From a public health perspective, money would be better spent on behavior modification that have demonstrated cardiovascular benefits with easily modifiable factors rather than attempting to reduce over-all ambient PM

levels that are already declining and are not excessively high in the majority of the United States.

More research *is* needed, but mostly in elucidating the mechanism(s) of action of PM toxicity. For it is only through a detailed understanding of how PM toxicity works can we begin to identify the groups truly at risk. Epidemiological research can only go so far, and are most useful when a large population suffers from an ailment. When the target population is very small compared to the potential exposed population, a more rational, scientific approach is called for to determine who is really at risk. The identification of this small, select group may prevent increased mortality from PM exposure.

Most of the mechanisms postulated rely on the secondary pollutant, the inflammatory cytokines. It stands to reason, then, that anti-inflammatory drugs may help reduce one's risk of PM toxicity. The small relative risks, however, would indicate that a large number of people would have to undergo chronic anti-inflammatory treatment before you would see an effect on reducing mortality from PM exposure if inflammation is the principle mechanism of toxicity of PM. This concept is encoded in the "number needed to treat" (NNT) statistic – the number of patients that one would have to apply the therapy to in order to see a benefit in *one* patient. Decreasing your potential population, via selective targeting of those at greatest risk, can help reduce NNT, and perhaps chronic anti-inflammatory therapy could be instituted or patients advised to avoid outdoor activities and to keep a strict watch on PM levels.

Chronic anti-inflammatory therapy is not really an option. Inflammation – while painted as the culprit of many negative effects in this report – is our main defense against bacterial and viral infection. It would be awfully ironic, indeed, if by our prejudicial rush to smear the world with antibiotics and chronic anti-inflammatory therapy, we manage to engineer humanity's next greatest public health threat: massive bacterial infections that are resistant to current antibiotics and vulnerable human hosts with compromised immunity.

We can choose either to ignore the PM's effects on human health (as there is little we can do to further reduce excess mortality from PM air pollution other than to prevent acute disasters), or take the opportunity to elucidate the mechanism(s) underlying PM's effects on human health in general, and the cardiovascular system in general. Identification of those truly at risk of death or serious injury from PM exposure should be sought and either prophylactic therapy or education can then be used to prevent excessive deaths attributable to PM air pollution. Due to the low incidence of people who have actually *died* as a result of PM exposure, retrospective epidemiological data will either require an impractical number of samples or never yield a conclusive result. Our best chance at identifying those at risk are to use logical deduction from postulated (and proven) mechanisms of action of PM toxicity, keeping in mind that PM chemical concentrations and sizes may vary widely making it very likely that multiple mechanisms will have to be studied before a population can be positively identified.

3. ACCOUSTIC MICRO-MACHINED SCAFFOLDS FOR ENGINEERED HEART TISSUE CONSTRUCTS

Abstract

Cultured cardiac myocytes provide a unique opportunity to study the behavior of myocardium in isolation from other tissue types, yet lacks some of the morphological traits of native tissue. Perhaps the most glaring difference is the inherent anisotropy found in cardiac tissue but lacking in cultured myocytes grown on standard, flat surfaces. The ability to engineer cell-culture compatible materials with specified topographical geometries will enable both the study of fundamental reaction of cardiomyocytes to structural cues and more closely mimic native tissue. Traditional methods for sculpting surfaces relied on photolithographic techniques where binary masks are employed resulting in sharp edges. Using an established, time-tested technique of acoustic micro-machining, we propose an inexpensive, versatile analog technique of smoothly varying surface features and demonstrate its ability to host myocytes. Using a simple model we predict how sound inputs transform into surface shapes, and showcase the versatility of such a technique in areas as diverse as micro-fluidics and shaped polymer manufacturing.

Introduction

Microfabrication and micropatterning have found wide application in elucidating basic cellular responses in biological systems(Folch and Toner 2000; Walker, Zeringue et al. 2004). The ability to engineer micron-scale structures with multiple heights, i.e. three-dimensional (3D) structures, permits one to study 3D interactions between cells and their extracellular environment, not otherwise attainable in traditional 2D flat culture systems. Stringent 3D control is even more important for microelectromechanical (MEMS) and microfluidic applications where precise geometry is critical. Traditional photolithography produces features of uniform height by virtue of the photomask used in the creation of these structures. Multiple masks can be used to create multi-level surfaces with certain restrictions, and recently several modified photolithographic techniques have been published providing fine discrete steps in feature height(Tien, Nelson et al. 2002; Chen, Hirdes et al. 2003). To circumvent the problem of clean rooms and toxic photoresist materials required for photolithography, there have been attempts to create templates by casting self-assembled structures or optical diffraction gratings(Xia, Tien et al. 1996) but such solutions are limited to simple repeated patterns of small height. Truly programmable 3D surfaces can be obtained using computer-numeric-controlled (CNC) milling techniques, selective laser ablation (SLA), or selective laser sintering (SLS). Although CNC milling is a more flexible method than the technique we describe below, it suffers from its discrete, coarse steps. SLA and SLS both are prohibitively expensive, have a limited repertoire of materials that are compatible with the process, and require complex programming.

All of the techniques discussed so far produce discrete (in the z-dimension) surface features. In this paper, we explore the capabilities of an established method and technology – the vinyl record manufacturing industry - to produce custom-designed inexpensive templates suitable for controlled cell growth and general biological applications. The Columbia Long-Playing (LP) microgroove recording technique was established in 1948, and soon after that became the major music recording technology until the introduction of newer media(Goldmark, Snepvangers et al. 1949; Gravereaux 1985). The LP production process offers micron-scale capabilities, deep feature sizes, and a non-discrete (smooth) variation in depth and width in response to the audio signal, effectively producing analog 3D patterns. We demonstrate the use of the method in obtaining microfluidics structures, manufacturing high-surface area wavy polymer fibers, for assembly of cell networks on scaffolds with 3D topography, and microcontact printing of proteins and cells. We also discuss the advantages and limitations associated with the proposed technique.

Experimental Methods

Acoustic Micromachining

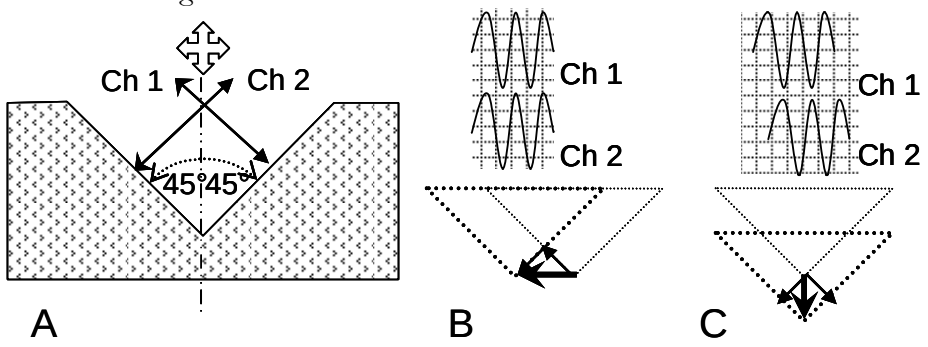

Figure 3-1 The acoustic encoding process
(a). The movement of the cutting head (stylus) along the normals to the walls of the groove is modulated by the encoded signal for the two amplifier channels, Ch 1and Ch 2; **(b).** For a monaural record, both channels are driven by in-phase signals, but due to a (historically-introduced) inversion of one of them, a net lateral motion is reproduced (see resultant vector); **(c).** For a stereo record, both channels are driven by anti-phase signals (shifted by 180°), thus the stylus is moving in the vertical (z-direction).

Topographic encoding of the acoustic signal

An audio signal is transferred into a topographic image by cutting V-grooves at constant angular velocity onto a soft lacquer layer. The movement of the cutting head (typically a sapphire with a 90° finish) is modulated electromagnetically and independently by the signal through a left and a right amplifier, as outlined schematically in **Figure 3-1**. Alternative shapes of the stylus, including sharper angles are available but are considered exotic in the standard production process. For technical and historical reasons, the movement encoded by both channels is along the normal to a side wall and is inverted between the two channels. Therefore, identical (in-phase) signals for the two amplifiers (essentially a monaural record) result in a lateral motion, while pure vertical motion is achieved by inverting one channel, or in the case of regular periodic signals shifting one channel 180° anti-phase to the original signal.

The *depth* of the grooves is adjustable and determines the dynamic range, e.g. volume, of the signal; the *distance* between the grooves is determined by the degree of packing (a tradeoff of dynamic range and capacity of the record), and can be optimized during the recording process using a groove computer or set manually at the start of the cutting procedure. The cutting speed has to be properly adjusted and stylus - heated to achieve clean cuts and avoid the formation of "burrs" of material.

Production of metal templates

For mass production purposes, the lacquer is used as a template and destroyed in the process of creating a nickel-alloy template having a negative image of the lacquer which itself can be used in producing a metal positive impression. Silver nitrate is sprayed onto the surface to create a conductive layer. Then a galvanic electroforming process is applied with the silver layer acting as a cathode, and nickel from the bath being deposited onto the silver layer. The nickel layer, a negative of the lacquer, is removed and becomes a *Master*. From this Master, further copies are produced: a *Mother* (a positive replica of the lacquer) and a *Stamper* (a negative of the lacquer), which is used, as the name implies, to stamp out the actual vinyl LPs.

Custom design and limitations of the process

The metal Mother and Stamper are durable and ideal for further molding of various materials. For a conventional cutting head, the obtained features are trapezoidal grooves with triangular peaks (V-peaks) (from the Mother) and V-grooves (from the analogous Stamper). The depth can be adjusted from approximately 6μm (0.25 mils) up to the thickness of the lacquer (about 150μm). The groove-to-groove spacing is adjustable, with a lower limit about 30μm. Parallel V-grooves with a constant depth can be obtained by recording 'silence', i.e. no frequency modulation; changing the volume/depth while recording, will achieve spatial depth variations.

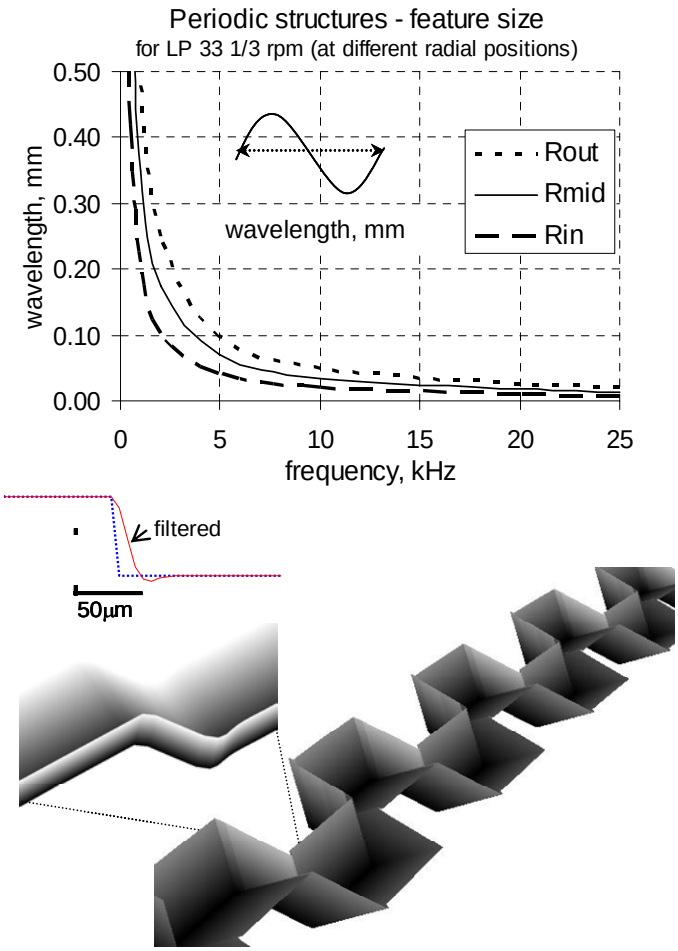

Figure 3-2 Feature size and patterns limitations
(a). Size (wavelength) of periodic features that can be produced if sinusoidal signals of prescribed frequencies (x-axis). The three curves refer to three radial positions on a standard 12" disk – outside radius, mid-radius and inner radius, which result in different wavelengths because of the variable linear (constant angular) stylus speed during manufacture; **(b).** Computer-simulated cut-out groove pattern by a 500Hz square wave after low-pass filtering to account for the stylus size. Inset zooms in on the edge of the pattern; shown is also the original versus the filtered version of the signal.

The frequency response for this process is in the range of 7Hz to 25kHz with a maximum sustained frequency of about 16kHz. During production, a constant angular velocity (variable linear velocity) is maintained (33.3 or 45rpm for the current standards), thus feature size decreases as a function of the radial position during the cutting process. Given the internal (378mm) and external (900mm) circumference of a 12" record, the range of linear velocities obtained for a 33.3rpm LP is from 210 to 500mm/s. **Figure 3-2a** outlines the spatial features obtainable as a function of the modulating frequency. Periodic structures below 100µm can be obtained for frequencies >2kHz; the smallest periodic structures are in the range of 10µm for the maximum attainable modulation frequency. **Figure 3-2b** shows a computer simulated V-groove encoded using a 500Hz square wave monoaural signal (after low-pass filtering with a

Butterworth filter, cut-off frequency15kHz). The equations for tracking the motion of the stylus in Cartesian coordinates (*x, y, z*), where *z* is depth, are given below for arbitrary signals supplied to the two amplifier channels, s_L and s_R.

$$x(t) = \cos(2\pi\nu t)(R_{\max} - \nu t\delta R) + \cos(\frac{\pi}{4})[s_L + s_R]$$
$$y(t) = \sin(2\pi\nu t)(R_{\max} - \nu t\delta R)$$
$$z(t) = z_0 + \sin(\frac{\pi}{4})[s_L - s_R]$$

The following symbols are used here: ν [*rad/sec*] is the angular velocity of the stylus; δR [μm] is the inter-groove spacing – fixed or variable; $R_{\max}$ [μm] is the initial radial distance from the origin; and z_0 [μm] is the initial groove depth.

Polymer molding and surface characterization

Polydimethylsiloxane or PDMS (Sylgard 184 from Dow Corning, Midland, MI) was mixed in the usual ratio 1:10, molded out of the metal templates to introduce 3D topography, and baked for 2h at 60°C (Bien, Yin et al. 2003). Mother templates yielded V-grooves in the PDMS while Stamper templates formed V-peaks. The obtained patterns (cut in $1cm^2$ pieces) were used in microfluidic applications, to grow cells after protein coating, or as protein stamping surfaces. Alternatively, a mixture of cellulose acetate and acetone (0.05g/ml, both from Aldrich, Milwaukee, WI) was poured over the metal templates in a pre-determined amount, which after acetone evaporation resulted in the formation of discrete separable fibers(Entcheva, Bien et al. 2004). In some cases, Congo red (Sigma, St. Louis, MI) dye was used to better visualize molded structures or fluid patterns. Surfaces were imaged directly or in a cross-section using optical microscopy (Nikon TS100) or scanning electron microscopy (SEM).

Cell culture, cell assembly, and cell imaging

Primary cardiomyocyte culture was prepared as described previously (Bien, Yin et al. 2003; Entcheva and Bien 2003). Briefly, the hearts of 3 days old Sprague-Dawley rats were digested enzymatically using trypsin and collagenase at 1mg/ml (Worthington Biochemical, Lakewood, NJ). Cardiomyocytes (CM) were collected after centrifugation and preplating, and seeded on fibronectin-coated (50μg/ml, BD Biosciences, Franklin Lakes, NJ) PDMS surfaces. In this process, cardiac fibroblasts (CF) were separated during the preplating step and cultured on fibronectin-coated surfaces. Cells were kept in a CO_2 incubator in Medium 199 (Invitrogen, Carlsbad, CA) at 37°C.

For cell patterning experiments, 3D PDMS stamps were used for microcontact printing of fibronectin on polystyrene surfaces, and cells were plated after surface treatment with 0.5% w/v Pluronic F-127 (Sigma) to avoid non-specific attachment(Detrait, Lhoest et al. 1999).

For structural characterization, cells were fixed in 3.7% formaldehyde and permeabilized with 0.02% Triton-X 100 (Sigma). Cell cytoskeleton was fluorescently stained with phalloidin–Alexa Fluor 488 (Molecular Probes, Eugene, OR) for F-actin. Nuclei of fixed cells were labeled with TOTO-3 (Molecular Probes, Eugene, OR). Structural fluorescence imaging was performed using an inverted fluorescence microscope with a 40x objective (NA 0.95) or, in some cases, using a confocal laser-scanning microscope BioRad Radiance 2000 with a 60x oil-immersion objective (NA 1.4).

Dynamic fluorescence imaging in live cardiomyocyte networks was performed to track propagation of electrical waves at >60000 locations using a voltage-sensitive dye di-8-ANEPPS (Molecular Probes), an intensified CCD camera (DAGE MTI, Michigan City, IN) and a custom-built optical setup, as described previously (Bien, Yin et al. 2003). Propagation maps were constructed by plotting contours of activation times over the imaged space, where closeness of contours is inversely related to the velocity of propagation.

Results and Discussion

Figure 3-3 Manufactured 3D surfaces imaged by scanning electron microscopy (SEM) **(a).** Encoded silence (no frequency modulation) results in straight grooves. Shown is a polymer (PDMS) mold of V-grooves; **(b).** In-phase (monoaural) signals to the two amplifiers result in lateral stylus modulation and wavy (in x-y) grooves. Shown are a V-grooved (left) and V-peaked (right) replica of the surfaces produced by 10kHz sinusoidal signals; **(c).** Anti-phase (stereo) signals to the two amplifiers result in vertical stylus motion and height modulation. Shown are V-peak (left) and V-grooved (right) replica of the surfaces produced by 5kHz and10kHz sinusoidal signals. Scale bar is 100μm.

Manufacture of 3D structures by acoustic micromachining

Audio signals representing silence, 5kHz and 10kHz monaural or stereo modulation were used for this proof-of-principle study. The signals were encoded (cut) into a lacquer template using variable volume, effectively resulting in surfaces between 6 and 50μm deep. The packing/spacing between grooves was varied from 60 to 500μm, with most of the structures being 120μm apart. The metal (Ni) surfaces of the templates were durable, easy to clean and did not introduce any adverse effects through the polymer molds on the proteins and cells used in this study. **Figure 3-3** shows SEM images of PDMS surfaces obtained by molding. Encoded silence (no frequency modulation) results in nearly straight grooves; in-phase (monoaural) signals result in a lateral stylus modulation and wavy (in x-y) grooves; while anti-phase (stereo) signals to the two amplifiers result in a vertical stylus motion and smooth

height modulation. For the analyzed samples, the amplitude of sinusoidal undulations was within 5μm. The radius of curvature introduced by the sinusoidal stylus motion varied between 8.6μm and 50.3μm, determined by the frequency of the signal and the radial position on the template. Such geometrical modulations of the surface (depth or width) can invoke a response within a single cardiomyocyte or cardiac fibroblast having typical length between 60 and 120μm, and width between 20 and 60μm. **Table 3-1** summarizes parameters related to the standard record cutting process (data from personal communication).

Table 3-1 Summary of record cutting limitations using standard equipment

Parameter	***Min***	***Typ***	***Max***
Unmodulated depth, z_0 (μm)	0	35	150
Unmodulated width, $w = 2z_0$ (μm)	0	70	300
Wall Angle (degrees)	-	90	-
Lateral deviation (μm)	$-\frac{1}{2}\delta R$	-	$\frac{1}{2}\delta R$
Vertical deviation (μm)	$-z_0$	-	$150-z_0$
Inter-groove distance, δR (μm)	w	150	-
Instantaneous Freq. Response	7Hz	-	25kHz

It has to be noted that the nature of the cutting process limits the complexity of the patterns that can be obtained (no small closed-loop or sharp-edge structures can be fabricated). This is in contrast to photolithography where 2D spatial patterns of extremely high complexity can be produced.

Figure 3-4 demonstrates several possible applications of the micromachined structures. To obtain confined microfluidic channels, we sealed (by heating) a PDMS of a stereo signal with V-grooves to a clean cover glass surface. Congo red dye was used to color the fluid; a droplet was deposited asymmetrically on one side (upper left corner in this case, **Figure 3-4a**) and the capillary action-induced flow in the variable height grooves was imaged. The smooth (non-discrete) variations in the diameter of the channels can be used to mimic biologically relevant problems in vitro, such as aneurisms, plaque formation, associated local turbulence, to mention a few. Microfluidics can also be used for 2D molecule and cell patterning (Tien, Nelson et al. 2002), as illustrated in Figure 3-4**b**, using a red-colored fluid pattern. **Figure 3-4c** shows the production of wavy cellulose acetate fibers with high surface-to-volume ratio, which can be then post-processed into biodegradable structures for cell and tissue growth(Entcheva, Bien et al. 2004).

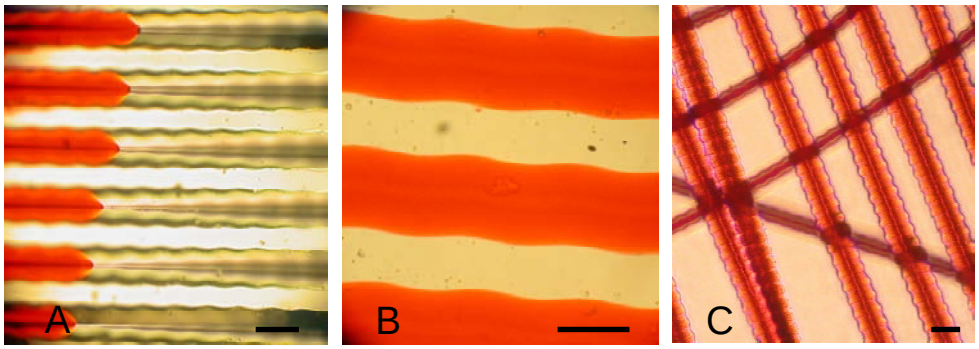

Figure 3-4 Applications of manufactured surfaces
(a). Microfluidic application is shown, where a PDMS V-peaked mold of a 5kHz stereo signal was attached to a glass surface and red-colored fluid was fed from the left upper corner, moving by capillary action in the grooves; **(b).** Microfluidic surface patterning (red traces) using PDMS V-peaked replica of a monoaural 5kHz signal; **(c).** Polymer wavy fibers (cellulose acetate with mixed red dye) having high surface-to-volume ratio were produced by molding out of a nickel V-grooved template (10kHz stereo). Scale bar is 50μm.

Cell assembly and control by manufactured surfaces

The utility of the micromachining technique for cell growth was explored by using two primary cell types: cardiac fibroblasts and cardiomyocytes onto fibronectin-coated PDMS surfaces. **Figure 3-5a&b** illustrates some results obtained with CF on 3D surfaces. As shown in previous studies(Curtis and Wilkinson 1998), cell guidance and alignment was easily achieved by both V-groove and V-peak scaffolds. Interestingly, CF were more likely to stretch and form transverse bridges between the peaks (**Figure 3-5b**) despite the greater distance relative to crossing the V-grooves. Two simple examples are shown how PDMS stamps prepared from the metal templates can be used for microcontact printing of extracellular matrix proteins (fibronectin, in this case) and patterning of fibroblasts and myocytes (**Figure 3-5c&d**).

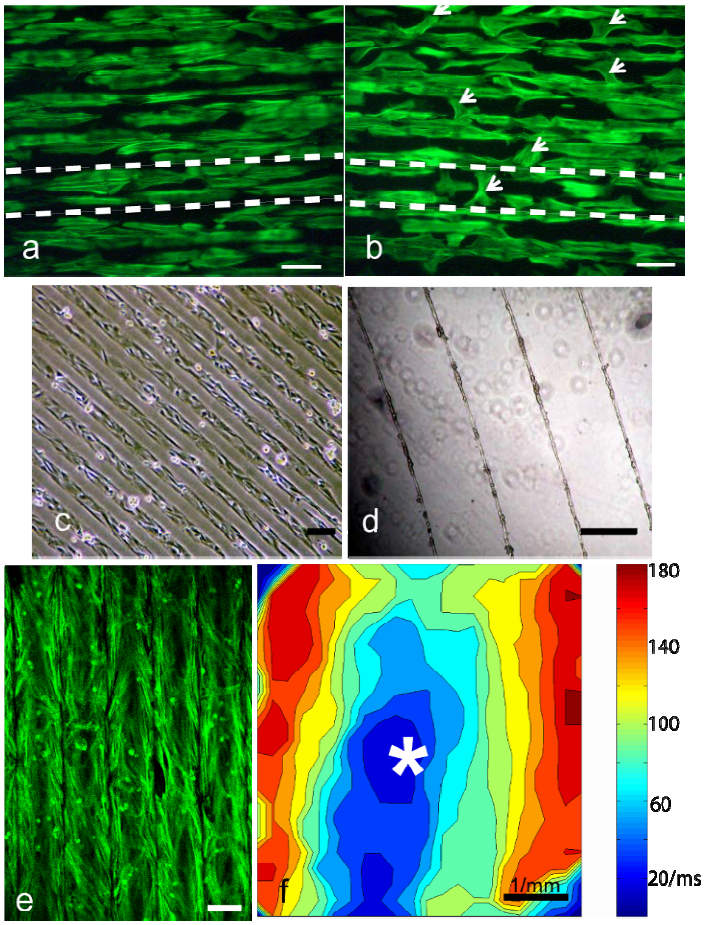

Figure 3-5 Patterned cell growth and functional assessment.
Cell growth and patterning (a) & (b) Fibroblasts grown on V-grooved and on V-peaked PDMS surface, respectively. Arrows indicate where cells bridged between the peaks; dotted lines indicate the bottom of the grooves or the top of the peaks, respectively; **(c).** Patterning of fibroblasts after microcontact printing of fibronectin using V-grooves; **(d).** Patterning cardiomyocytes in thin lines with V-peaks; **(e).** Oriented (anisotropic) growth of cardiomyocytes on V-peaks; **(f).** Fluorescently measured anisotropic propagation of electrical waves in the cardiomyocyte network, triggered from a point (*). Color represents time of activation (in [ms]), blue being the earliest. F-actin cytoskeleton was labeled in green in (a), (b) and (e). Scale bar is 100μm.

Cardiomyocytes grown directly onto V-peak scaffolds maintained a characteristic angle with respect to the direction of the peaks(Bien, Yin et al. 2003), **Figure 3-5e**. Functional connectivity between these cells and anisotropy in the wave propagation was confirmed using fast fluorescence imaging at multiple locations in live cardiomyocyte networks (**Figure 3-5f**). Point stimulation elicits an elliptical rather than circular pattern of propagation, dictated by the assembly of the cells. This is a characteristic natural behavior for the heart tissue.

Biological applications of acoustic micromachining

The applications outlined in **Figure 3-4** and **Figure 3-5** present only several of the numerous possibilities for these 3D surfaces. Biological applications calling for controlled cellular environments or molecule manipulation platforms include: structure-function cellular studies by the use of patterning; integration of cells with microelectromechanical devices for BioMEMS design; microfluidics solutions for molecule and cell manipulation and patterning. The need for relatively simple 3D (vs. highly complex 2D) structures is apparent in several specific biological applications: (1) Enforcement of prescribed cell morphology and assembly to mimic anisotropic tissue properties, by micropatterning or "topographic guidance"; (2) Fluid flow studies and effects of flow on cells, where the structure (diameter/depth) of the channels is spatially variable; (3) Studies of the effects of curvature and/or spatial frequencies on cell organization, effects of 3D microenvironment on cell attachment and function, where deep surface features are needed; and (4) Compartmentalization platforms for cells and molecules to study local autocrine/paracrine effects, effects of pharmacological agents etc.

Summary

Soft lithography (Whitesides, Ostuni et al. 2001), combining photolithography with polymer molding, has facilitated in an unprecedented manner the development of biological applications requiring spatial control of molecules and cells. The advantages of the technique lie with its simplicity and accessibility for the regular researcher. In the same venue, we report in this paper the utility of an even simpler non-photolithographic method, acoustic micromachining, for microscale design of surfaces and 3D structures. A simple encoding of desired topographical features into an audio signal is used, and a template is generated via an established production process and equipment. We showed how acoustic micromachining can produce features ranging from several microns to hundreds of microns suitable for various biological applications.

The major limitation of acoustic micromachining is decreased flexibility in microstructure design. Groove geometry is determined by the shape of the cutting head, fixing the width-depth correlation. The rotating platform imposes yet another restriction on possible topologies in acoustic micro-machining as most cutting lathes are designed to spiral towards or away from the center of the disk at a fixed rate precluding the design of arbitrary networks of grooves. However, many microstructure applications require relatively simple features, where acoustic micromachining can successfully complement the more sophisticated photolithography (for 2D) and other general 3D methods. Geometry-encoding "music" can help effectively address current biological questions in a simple and inexpensive way.

4. TENSION DEVELOPMENT AND NUCLEAR ECCENTRICITY IN TOPOGRAPHICALLY CONTROLLED CARDIAC SYNCYTIUM

Abstract

Using acoustic micro-machining, we explored the effect of growing cultured neonatal rat ventriculomyocytes (NRVM) on micro-grooved versus flat topographies. Deep (50μm) grooves in elastic scaffolds were manufactured from PDMS via acoustic micro-machining, and NRVM were grown to confluency. Engineered heart tissue constructs on the topographically modified (T) scaffolds showed higher order of intra- and intercellular organization (fiber-like structures) compared to those grown on flat surfaces (F) of different materials, and developed self-organized persisting electrical and mechanical activity. These structural and functional changes were accompanied by a statistically significant ($p<0.001$) increase in nuclear eccentricity (mean±S.E.: 0.79±0.01, n=137 in T vs. 0.64±0.01, n=863 in F), and a preferential nuclear orientation forming a shallow angle to the axis of the grooves. The nuclear orientation correlated well with the actin fiber arrangement in the T-samples as well as with the direction of maximum displacement. Topography-induced nuclear deformation, a sign of tension development, implies further functional changes in transcription and cell signaling. In conclusion, we demonstrate topographic control of electro-mechanics independent of the underlying scaffolding material in engineered heart tissue without external mechanical or electrical stimulation. These findings suggest a possibility to use controlled microenvironments in the design of biological autonomous force generators with reconstituted excitable tissue.

Introduction

Engineering functional cardiac tissue *in vitro* is an ambitious and actively pursued endeavor(Zimmermann, Schneiderbanger et al. 2002),(Fink, Ergun et al. 2000). Along with the obvious clinical benefit of the eventual final product (tissue repair for the human heart), a few potential *in vitro* applications seem of no lesser importance and interest. One of them is the use of successfully engineered cardiac tissue for drug development – target screening and validation of potential pharmacological compounds(Nave, Becker et al. 2002). Another interesting application of engineered excitable and contractile tissue (such as cardiac muscle) stems from its potential(Kakugo, Sugimoto et al. 2002) to be used as a biological machine for performing useful work with high efficiency. Achieving the desired functionality through minimum external intervention, relying on the self-organizing properties of biological matter, is a laudable, yet insufficiently explored approach.

Previous research has demonstrated the feasibility of perturbing cell function and survival by controlling the cellular microenvironment(Chen, Mrksich et al. 1997). In the context of cardiac tissue, cell patterning and guidance have been applied by manipulating the extracellular matrix (ECM) proteins: micropatterns of desired shape and size(Rohr, Shoelly et al. 1991) or oriented gels(Simpson, Terracio et al. 1994) invoked reciprocal structural and functional cellular responses. Most of these studies dealt with two-dimensional preparations.

Topographic control within a true three-dimensional setting is expected to promote higher order of organization. Several groups(Clark, Connolly et al. 1990), including one(Deutsch, Motlagh et al. 2000) dealing with primary cardiac cells at low density, have pointed out the ability of the cells to make use of topographic features for out-of-plane support. Our goal in this study was to engineer cardiac syncytium on microfabricated, topographically complex scaffolds. We anticipated that the three-dimensional landscape, combined with such a well-connected network of excitable contractile cells would bring about unique system behavior, including the promotion of organized electrical and mechanical activity. We characterized several aspects of topography-induced structural and functional changes, focusing on nuclear deformation as a consequence of the increased level of organization and enhanced inherent mechanical activity, and with important implications for re-programming the cells.

Methods

Scaffolds and Topography

Several different scaffold materials were used in this study. As flat rigid surfaces for cell growth we used glass and polyvinylchloride (both from VWR), polydimethylsiloxane (PDMS) and cellulose-acetate (CA) surfaces. PDMS scaffolds (Sylgard 184 from Dow Corning, Midland, MI) were prepared in the usual ratio of 1:10 of curing agent to elastomer and baked for 2 hours at 60°C. CA membranes were prepared from cellulose acetate, triethyl citrate and acetone (all from Aldrich) and let form thin membranes over 4-5 hours. To investigate the effects of topography on cellular growth and function, PDMS scaffolds were constructed by molding from pre-manufactured micro-grooved masters. The resultant scaffold surface had regularly spaced features of uniform height with trapezoidal grooves and triangular ridges. The features, explored here, are significantly larger than those examined in previous studies(Deutsch, Motlagh et al. 2000). Cross sections of scaffolds were imaged under conventional microscopy to confirm topographical features (**Figure 4-1A**).

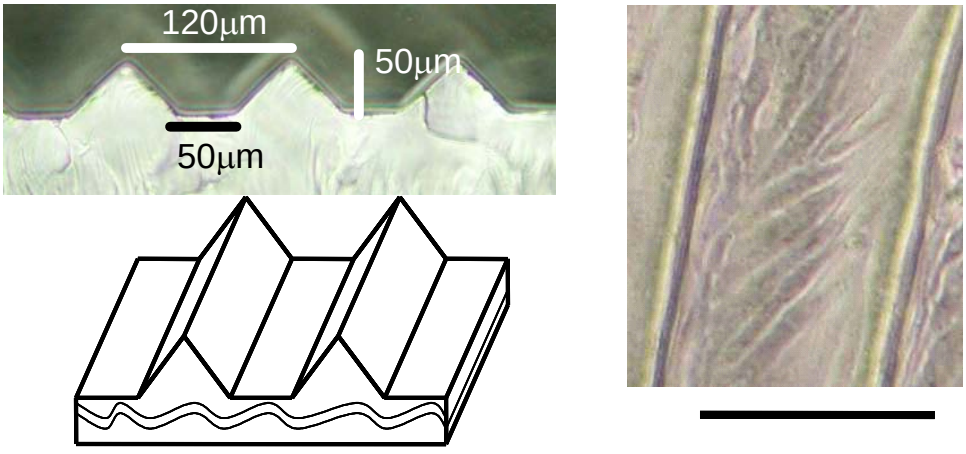

Figure 4-1 Geometry of topographically complex scaffolds constructed by molding from micro-grooved masters, and cardiac cell network grown on the scaffolds.

Cardiac Syncytium

Cardiomyocytes were cultured from neonatal rat hearts as described elsewhere(Entcheva, Lu et al. 2000). Briefly, cardiomyocytes were isolated from the ventricles of 3-day old rats by enzymatic digestion with trypsin and collagenase. Cells were plated at high density (0.9×10^6 cells per ml) onto fibronectin-coated scaffolds to allow the reconstitution of cell-to-cell contacts and the establishment of a functional syncytium. Electrical cell-to-cell connections were confirmed by gap junctional (Connexin 43) staining (Bien, Yin et al. 2002) and assessment of multicellular behavior. The engineered cell constructs (**Figure 4-1B**) were maintained at 37°C with 5% CO_2 in medium 199 supplemented with 2% fetal bovine serum.

Electromechanical Measurements

Electromechanical measurements were performed at day 3-6 after culturing, under perfusion with oxygenated Tyrode's solution at 32-35°C. Intracellular calcium levels were determined using a ratiometric fluorescence measurement technique, as described previously(Bien, Yin et al. 2002). Cells were stained with 10μM of the calcium-sensitive dye Fura-2 (Molecular Probes) at room temperature for 20 min, and unincorporated stain was washed out for another 20 min. Samples were then imaged using an inverted fluorescence microscope (Nikon 20x Fluor objective, NA 0.75) with excitation at 365nm and 380nm, and the fluorescence intensity determined through a 510nm band-pass filter using a photo-multiplier detector (IonOptix, MA). Cell length was tracked simultaneously at long wavelengths using fast (250Hz) imaging with a CCD camera and software video-trackers of cell edges along the axis of deformation. Movies of multicellular deformation were recorded using a Nikon Coolpix 950 camera attached to eyepiece of the microscope.

Fluorescent Labeling and Confocal Microscopy

At day 7 of culture cardiomyocytes were fixed in 3.7% formaldehyde and permeabilized with 0.02% Triton-X 100. Cells were co-stained with phalloidin–Alexa 488 (Molecular Probes) for F-actin and with TOTO-3 (Molecular Probes) for nuclei. Samples were then mounted on a glass slide with VectaShield (Vector Laboratories, Burlingame, CA) and imaged with a confocal scanning laser microscope BioRad Radiance 2000 with a 60x objective (N.A. 1.4), excited simultaneously at 488nm for actin and 637nm for TOTO-3. Emission at 535nm was mapped to the green channel and 680nm to the blue channel in a 24-bit RGB format containing 1024x1024 pixels representing 195μm x 195μm area. Only the blue channel, reflecting TOTO-3 staining, was used for nuclear analysis as an intensity scale.

Automated analysis of Nuclear Morphology

We developed and applied an automated technique for nuclear morphology analysis using the confocal images. After thresholding a grayscale nuclear image using Otsu's method(Otsu 1979), median spatial filtering was applied to clean nuclear edges, and the whole image was segmented into connected regions. Based on criteria including region size, "solidity" and degree of concavity, individual nuclei were discriminated from noise. Ellipsoidal shape was automatically fitted around each identified nucleus, and the parameters (size, eccentricity, orientation) of this (ellipsoidal) envelope were further used in the analysis. The algorithm was implemented using the Image Processing Toolbox in Matlab (MathWorks), and validated by comparison to manually selected and characterized nuclei.

Results

In this study we engineered cardiac tissue-like constructs on different materials, specifically seeking to quantify the effects of topography on the cell construct structure and function. All materials used were biocompatible and optically clear, allowing easy cell visualization and functional microscopy studies. Unlike previous attempts at cell alignment through patterning(Rohr, Shoelly et al. 1991) or orientation(Simpson, Terracio et al. 1994) of the extracellular matrix (ECM), here we employed true 3D structures (deep wide microgrooves), and assessed self-organized syncytial behavior.

Cardiomyocytes grown on topographically complex scaffolds exhibited a highly organized pattern of growth and attachment (**Figure 4-1B**) compared to flat scaffolds. Structural changes were obvious in the actin arrangement – cells in the grooves formed *in vivo* -like fiber structures, making use of the out-of-plane lateral support and extending in the spaces between the triangular peaks, and orienting themselves at a shallow angle with respect to the long axis of the grooves (**Figure 4-2A**), whereas cardiomyocytes grown on flat surfaces spread out in all directions, with low order of cytoskeletal organization (**Figure 4-2B**). Additional structural changes included a larger size for the cells on the topographically complex surfaces, and a more pronounced sarcomere pattern along the actin fibers.

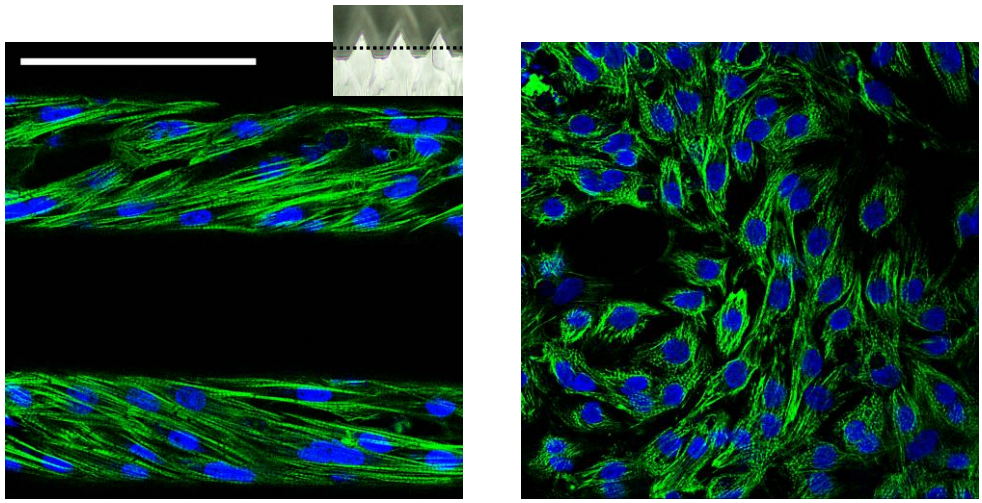

Figure 4-2 Engineered cell constructs on topographically complex scaffolds exhibit *highly organized cytoskeleton* with efficient use of topographical features for attachment.
Confocal image of cardiomyocytes grown on microgrooved PDMS (A) and flat PDMS (B) scaffolds. Intracellular structures have been labeled with phalloidin-Alexa 488 (green) and TOTO-3, a nuclear stain (blue). Note the higher order of organization of the contractile fibers in (A), running from side to side in the grooves. Scale bar is 100μm. Inset shows schematically the position of a confocal slice with respect to the scaffold structure (exaggerated vertical dimension).

The cytoskeletal re-arrangement and changes in cytoarchitecture in response to topography were accompanied by functional changes. Constructs on topographically modified scaffolds developed self-organized synchronous contractions after day 3 in culture. The

persistence and the magnitude of these contractions were much more pronounced than similar activity observed sporadically on any of the flat surfaces. Cell-driven deformation of the underlying scaffold was observed (movies available). The frequency range of the observed spontaneous activity was 0.8-2.5Hz at 32-37°C. Representative recordings are shown in **Figure 4-3**, where the frequency of the inherent activity is about 1Hz. The cell strain was recorded and evaluated along the axis of maximum displacement, which was close to the axis of actin fiber orientation, depicted in **Figure 4-2**.

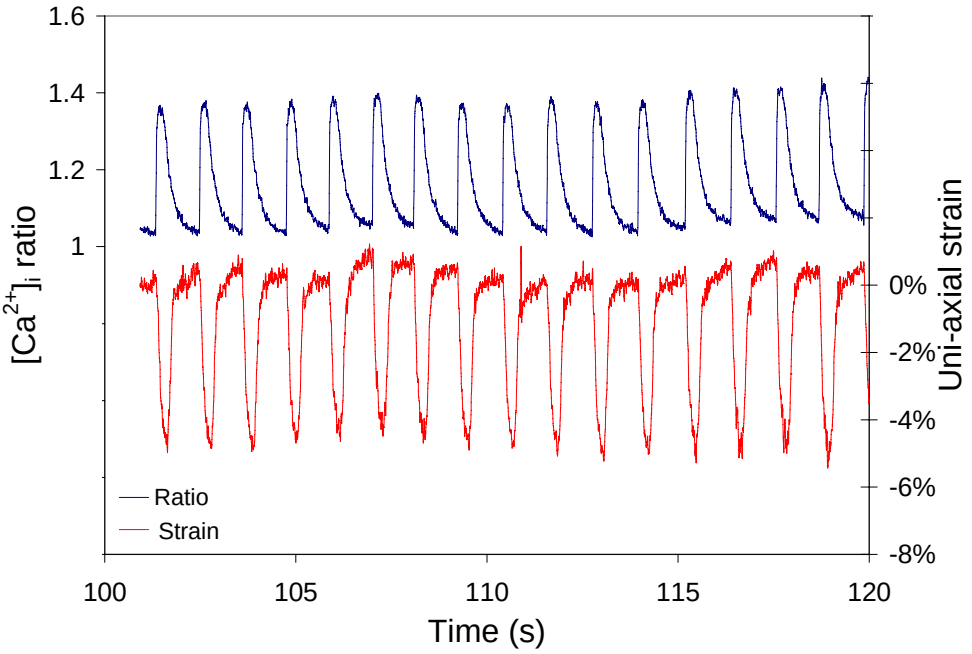

Figure 4-3 Engineered cell constructs on topographically complex scaffolds exhibit *self-organized persistent electrical and mechanical activity* without external load / stimulation.
Intracellular calcium, $[Ca^{2+}]_i$, was assessed using a ratiometric fluorescence measurement with a calcium-responsive dye Fura-2, excited at 365nm and 380nm. Higher ratios correlate with higher intracellular calcium concentrations. Cell length was measured using fast computer-aided videomicroscopy. Uniaxial strain was computed as the difference between the initial (diastolic) length and current length, divided by the diastolic length.

Visually, the nuclei of cells grown on topographically complex scaffolds appeared more elongated (**Figure 4-1B**). This was definitively demonstrated by using custom developed automated software to determine nuclear morphology in the engineered constructs. Summary of the data is presented in **Figure 4-4**. The mean nuclear eccentricity of cardiomycytes grown in a syncytium on a flat surface was found to be very close to 0.64±0.01 (mean±S.E.), n=847, regardless of scaffold material. Statistically significant increase in nuclear eccentricity to 0.79±0.01, n=137, was observed in the cells on topographically modified PDMS surfaces. These nuclei were longer and narrower than the control ones (major axis 13.5±0.25 (T) vs. 12.7±0.12 (F) and minor axis 7.6±0.13 (T) vs. 9.3±0.08 (F)). Given the large width of the grooves employed with respect to cell dimensions, it is unlikely that nuclear deformation

occurred as a result of geometry confinement, or simple orientation along the grooves (see next paragraph).

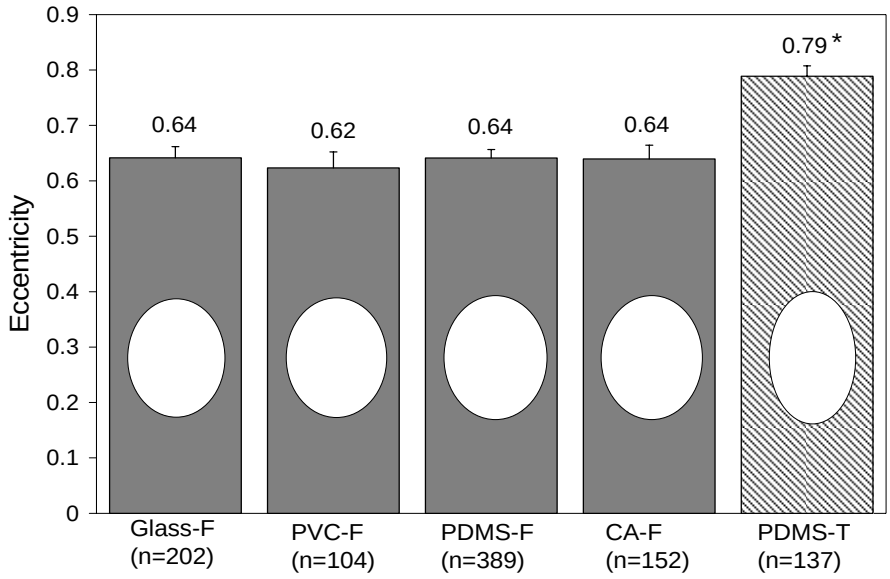

Figure 4-4 Engineered cell constructs on topographically complex scaffolds exhibit *greater nuclear eccentricity* ($p<0.001$).
Eccentricity of 0 indicates a perfect circle, eccentricity of 1 – a line. The examined scaffold materials include flat (F) PDMS, PVC, CA and glass, and topographically modified (T) PDMS. Error bars indicate 95% confidence intervals, and the ellipses are a graphical representation of the mean nuclear geometry scaled proportionally to the mean major and minor axis lengths.

Nuclear morphological changes were accompanied by development of a preferential orientation (**Figure 4-5**). While orientation of cell nuclei on flat substrates (regardless of material) did not deviate significantly from the random distribution, cell nuclei on topographically modified surfaces had a preferential orientation, $p<0.001$, chi-square results presented in **Table 4-1**. The range of orientation angles, followed by the oriented nuclei, was –20/+20 degrees with respect to the groove direction, with a drop at 0 degrees. This was consistent with the preferential direction of actin fiber orientation and the direction of developed maximum contractions.

Same sets of data were used for calculations of nuclear eccentricity and nuclear orientation. Data were collected from 25 scaffolds for flat (different materials) and 7 scaffolds for topographically modified PDMS.

	Glass-F	PVC-F	PDMS-F	CA-F	PDMS-T
Number of nuclei	202	104	389	152	137
χ^2	34	44	36	41	144
Degrees of freedom	35	33	35	35	28
p	0.52	0.10	0.43	0.22	<0.001

Table 4-1 Chi-square test for deviation of nuclear orientation on different surfaces (examined in Figure 4) from the uniform (non-biased) distribution.
Only topographically complex scaffolds promoted ($p<0.001$) preferential orientation of the nuclei within –20/+20 degrees from the axis of the surface grooves (see also Figure 4-5).

Discussion and Conclusions

This study demonstrates topographic control of cardiac electromechanics, as assessed by structural changes on the single cell and on the network (tissue) level, as well as functional changes in engineered cardiac syncytium on deeply microgrooved scaffolds.

We report three pieces of evidence for topography effects on engineered cardiac constructs. First, cytoskeletal rearrangement and alignment of actin stress fibers of cells grown on topographically complex T-constructs compared to F-constructs was observed. More mature looking (sarcomered) cytoskeleton was characteristic for the T-constructs. Cell (actin fibers) and nuclear orientation come as no surprise in response to guiding topography (Clark, Connolly et al. 1990). The interesting finding here is the deviation from the axis of the grooves and the formation of twisted fiber-like structures, mimicking real heart tissue.

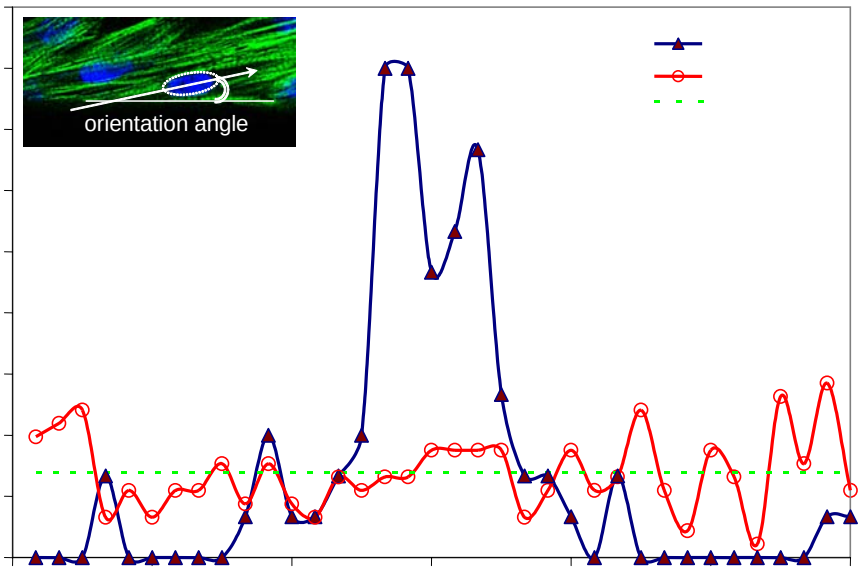

Figure 4-5 Engineered cell constructs on topographically complex scaffolds exhibit preferential nuclear orientation ($p<0.001$), consistent with the orientation of the contractile fibers (Fig. 2) and the direction of maximum strain (Fig. 3).
The inset illustrates the definition of the orientation angle: between the major axis of a fitted ellipse around a nucleus and the horizontal axis of the confocal image (before angle calculations, coordinate transformation was applied to align topographical features with the x-axis). Dashed line indicates expected relative frequency for random orientation (uniform distribution). Frequency data were binned in 5-degree increments. Cell nuclei on topographically modified scaffolds deviated significantly from the uniform distribution (see also Table 1).

The second, functional, result of scaffold topography, deals with the promotion of synchronous persistent electrical and mechanical activity. The induction of topographically driven functional changes, observed here, is in concert with our previous results(Bien, Yin et al. 2002), where a statistically significant increase in the magnitude of intracellular calcium transients was found for cells on topographically modified vs. flat surfaces. Calcium is the triggering signal for contraction in cardiac myocytes; hence our overall results support the idea of topography effects on excitability and contractility.

Finally, we quantify nuclear morphology and orientation. In contrast to a tightly maintained nuclear shape in cell networks on flat substrates, the cells in T-constructs exhibited higher nuclear eccentricity. Furthermore, the nuclei of these cells followed the preferential alignment of the stress fibers. Previous studies have clearly demonstrated nuclear deformation as a result of external mechanical stretch(Maniotis, Chen et al. 1997; Arnoczky, Lavagnino et al. 2002). We believe that the changes in nuclear morphology, reported here, result from combined structural and functional effects. The latter are associated with tension developed within the highly active T-constructs.

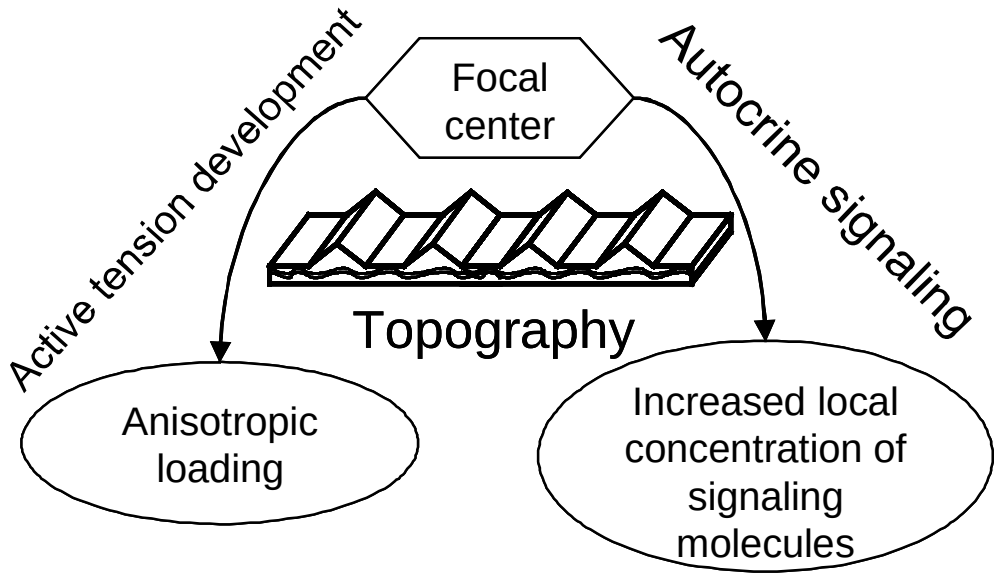

Figure 4-6 Proposed pathways (mechanical and biochemical) for topography-induced enhancement and synchronization of electro-mechanical activity in cardiac cell constructs on the microgrooved scaffolds.

The exact mechanism of these topography-mediated phenomena is unknown; below we propose a framework of possible pathways for the evolution and facilitated synchronization of electro-mechanical activity in the T-constructs. As shown in **Figure 4-6**, a focal center (FC) of spontaneous contractile activity is a necessary starting point. Pacemaking sites do occur in the cultured neonatal rat ventricular preparation, and we have observed them on flat as well as on microgrooved surfaces. The process of propagation and synchronization of this spontaneously occurring activity requires a high degree of connectivity (i.e. a syncytial structure).

Furthermore, we propose at least two plausible topography-related spatial mechanisms of synchronization and reinforcement of this activity. First, through a "mechanical" pathway the FC activity resembles external tensile forces on neighboring cells, attached to the three-dimensional structures. Alternatively, the reaction forces from cellular attachment sites of contracting cells also mimic external tension. Even though a similar interaction of forces does exist in the F-constructs of well-connected cells, the key difference (uniquely brought about by topography) is the anisotropic nature of the applied loads (due to a preferential orientation) and the periodic three-dimensional supports, which further facilitate the intrinsic force development. This periodic load can activate initially quiescent cells through mechano-sensitive channels or other mechanotransduction mechanisms (i.e. elevated intracellular Ca^{2+} levels). A second, "biochemical" pathway is believed to exist through autocrine signaling, i.e. the release of growth factors, hormones etc. by the active FC cells and their effect on initially quiescent neighboring cells. There is extensive evidence in support of this scenario following mechanical activity in cardiomyocyte networks (Ruwhof, van Wamel et al. 2000; van Wamel, Ruwhof et al. 2001). The topography contribution in this regard, for our particular configuration, could be the provision of a somewhat confined space (deep grooves) to reinforce these microenvironment effects.

The development of synchronous mechanical activity and the anisotropic nature of the intrinsic stretch lead to increased nuclear eccentricity by previously established mechanotransduction pathways(Maniotis, Chen et al. 1997). Nuclear deformation then can affect the overall cell function through gene expression and transcriptional mechanisms (Thomas, Collier et al. 2002)by leading to further structural and mechanical changes.

In conclusion, we demonstrate in this study that scaffold topography can induce unique functional changes in a well-connected network of cardiomyocytes. This finding, together with further elucidation of the mechanisms involved, could serve as a guiding point in tissue engineering efforts and the design of autonomous mechanical structures out of excitable cells.

Acknowledgements

We would like to thank Lihong Yin and David Colflesh for help with the cell culture and the confocal imaging, respectively.

5. CARDIAC CELL NETWORKS ON ELASTIC MICROGROOVED SCAFFOLDS

Abstract

Previously, we have shown morphological changes in HTCs grown on micro-grooved surfaces as well as enhanced tension development. Here, we further examine the phenotypical characteristics of HTCs on micro-grooved topographies compared to flat surfaces focusing on intra-cellular calcium and voltage dynamics, gap junctional coupling, and anisotropic propagation. As an extension of our previous observation of preferred nuclear orientation for micro-grooved (G) samples versus control flat (F) samples, we found cardiomyocytes aligned in a bipennate or multipennate fashion in G consistent with greater systolic calcium and stronger developed strain. In addition, we found both higher density and larger size distribution of Connexin-43 positive gap junctions. Synchronized, spontaneous contractions were more often observed in G samples along with a slow, diastolic rise of calcium levels. Finally, optical mapping revealed anisotropic propagation akin to native heart tissue with faster velocities within grooves than across grooves. HTCs grown on microgrooved elastic scaffolds provide a useful test-bed for research on cardiac cell interactions and effects of pharmacological or other biological agents on tissue-like structures.

Introduction

Major initiatives are underway to create implantable engineered heart constructs for repair of damaged myocardium (Akins 2002), but integration of such engineered patches of heart muscle with the injured heart will require deeper understanding of the interactions between cardiomyocytes in networks of cells. Furthermore, while many engineered cardiac constructs lack preferential cell orientation, the actual *in-vivo* heart tissue is structurally and functionally anisotropic (Streeter, Berne et al. 1979). Therefore, we sought to construct a model engineered cardiac construct having anisotropic properties and consisting of inter-connected cardiac cells with syncytial tissue-like behavior. We report basic structural, electrophysiological and mechanical characterization of multicellular tissue-like engineered constructs developed using elastic matrices with 3-D surface microtopography. To properly assess functionality of the constructs in the tissue setting, we employed spatial optical fluorescence techniques enabling measurements at the micro- and macro-scale.

Methods

Cell culture and scaffolding

Neonatal cardiomyocytes were isolated and cultured as previously described (Entcheva, Lu et al. 2000). Briefly, ventricles of 3 day old rats were digested with trypsin (Invitrogen, Carlsbad, CA) and collagenase (Worthington, Lakewood, NJ) before plating at 4.7×10^5 cells/cm^2 on fibronectin-coated scaffolds and kept at 37°C in a CO_2 incubator in medium M199 supplemented with 2% fetal bovine serum (Invitrogen). Cells were grown either on elastic microgrooved scaffolds (G) or control flat surfaces (F). Microgrooved scaffolds were prepared using acoustic micromachining (Entcheva and Bien 2003). In short, we molded

polydimethylsiloxane (PDMS from Dow Corning, Midland MI) from a master template, prepared using phonograph record technology; control flat surfaces were made by pouring PDMS on a smooth surface. The surface topography was chosen to consist of deep (50μm) trapezoidal grooves, separated by triangular ridges about 120μm apart to provide quasi 3-D microenvironment with cell-compatible feature dimensions. PDMS was selected as a scaffold material because of its biocompatibility, elasticity, optical clarity and lack of autofluorescence.

Immunocytochemistry

To examine structural differences between F and G scaffolds, at day 7 of culture the cell constructs were fixed in 3.7% formaldehyde and stained for F-actin using phalloidin conjugated to Alexa-488 (Molecular Probes, Eugene, OR) or for connexin-43 (Cx43) using rabbit anti-mouse Cx43 (Chemicon, Temecula, CA) and goat anti-rabbit antibodies conjugated to Alexa-488 (Molecular Probes). Immunofluorescence images were collected using a scanning laser confocal microscope, BioRad Radiance 2000, with a 60x oil-immersion objective (N.A. 1.4) having vertical resolutions of 0.5-1μm. Quantification of gap junction size and density from optical confocal slices was done by *granulometry* using the Image Processing Toolbox in Matlab (Mathworks, Natick, MA). Morphological operations were used to find objects close in size to a chosen structural element (test pattern). Dividing the number of pixels found by the area of the structural element then estimates the number of clusters having the same area as the structural element without individually enumerating each cluster.

Electromechanical Characterization

Microscopic electrophysiological and mechanical comparison of F and G scaffolds were performed by a dual-sensor fluorescence setup (using an inverted microscope), schematically shown in **Figure 5-1** (Ionoptix, Milton, MA). The system permits simultaneous fluorescence measurements of electrical activity in epi-illumination mode and bright-field imaging of mechanical motion in trans-illumination. The area of measurements was aperture-limited to only a few cells. Intracellular calcium was measured using the calcium-sensitive dye Fura-2 (Molecular Probes) and a dual-excitation ratiometric fluorescence technique to avoid problems with dye loading and to enable quantification. Cell length (for strain calculations) was recorded simultaneously via trans-illumination by computer-assisted software tracking of cell edges or other naturally occurring high contrast features. Calcium-related fluorescence data were acquired at 1kHz with a photomultiplier tube (PMT), while cell length changes were sampled at 0.24kHz with a charge-coupled device (CCD) camera. Experiments lasting 20-60 minutes were typically conducted in pairs (F and G scaffolds), stained simultaneously with 5μM Fura-2 AM and perfused throughout with warm (30-32°C) Tyrode's solution. Electric field stimulation was applied through built-in Pt electrodes in the side walls of the perfusion chamber.

Experimental data were filtered and analyzed to extract quantitative information, i.e., to determine systolic calcium levels (change in Fura-2 ratio from resting to peak values) and cell length (defined as the distance between two cell borders). Cell strain was then computed as the percent change from resting (diastolic) length and peak (systolic) strain extracted. When cell borders were indistinct, high contrast features (typically intra-cellular inclusion bodies or cellular debris on myocyte surfaces) were used to track motion instead. Statistical analysis was performed using Student's t-test.

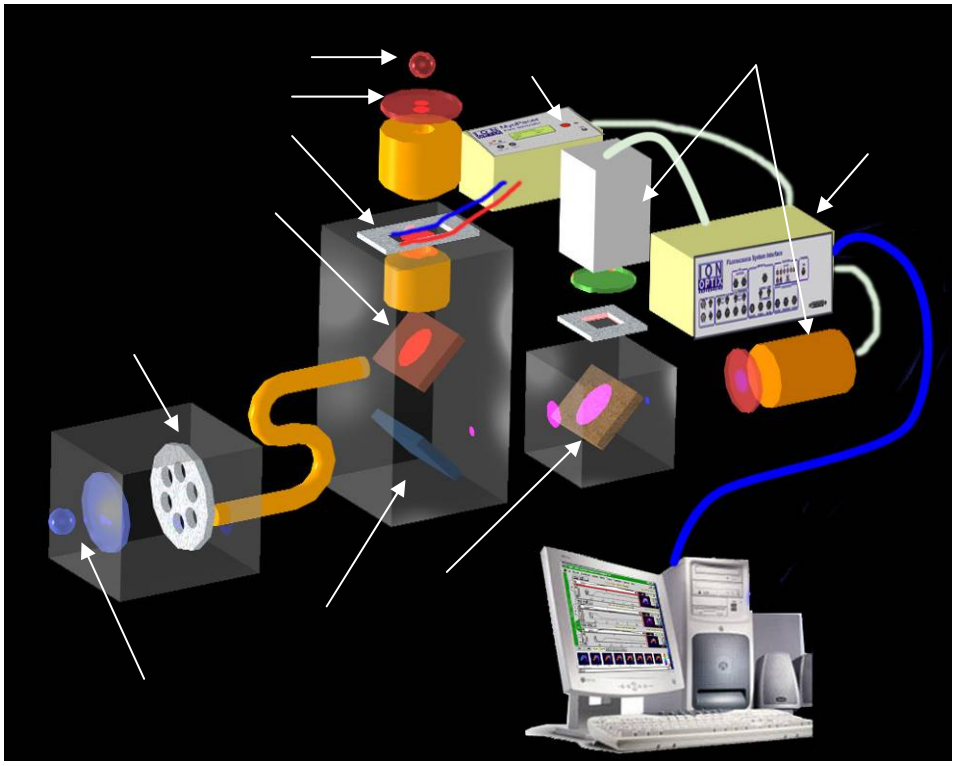

Figure 5-1 Schematic diagram of a microscopic system for simultaneous dynamic fluorescence measurements and mechanical analysis.
Epi-illumination light is supplied by a xenon arc-lamp and is filtered through one of several possible excitation filters (Ex) on a filter wheel before reflecting off the first dichroic mirror (D1, long-pass 400nm) and illuminating the specimen (S). Simultaneously, an incandescent lamp trans-illuminates the sample through a 665nm filter (T). This transmitted light passes through the sample, D1, and a second dichroic mirror D2 (586nm long pass) and enters the CCD camera for mechanical motion analysis. Fluorescence emitted from the specimen also passes through D1 but reflects off D2 and is collected by a photo-multiplier tube (PMT) with an emission filter at 510nm. Internal plain mirrors re-direct light through the optical pathways of the microscope and are represented schematically by M. The detectors and the filter wheel are computer-controlled through the Fluorescence System Interface (FSI).

Optical mapping of electrical propagation

A macroscopic CCD system with high numerical aperture was employed to image spatial patterns of electrical propagation in the cardiac constructs (field of view approximately 8mm in diameter). Cells were stained with a transmembrane potentiometric fluorescent dye, di-8 ANEPPS (Molecular Probes), at 30-50μM for 5 minutes and epi-illuminated at 535nm collecting fluorescence at 610nm. To increase the apparent temporal resolution of the system, cells were chilled to room temperature (21-23°C). An intensified CCD camera (CCD-72S with Genesys II intensifier, MTI Dage, Michigan City, IN) was used to acquire images with 320x240 pixels resolution at 60 frames per second (fps).

Specialized automated analysis software (using the Image Processing Toolkit in Matlab) was developed to handle the large amount of data. The intensity image sequences were cropped and normalized on a pixel-by-pixel basis to saturate the upper and lower 10th

percentile over the entire recording time. After baseline correction, each image was binned up to 10x10 pixel sub-regions and spatially (Gaussian) filtered. Activation times were determined by locating the minimum of a Savitzky-Golay filtered first derivative, and isochronal maps were constructed.

Results

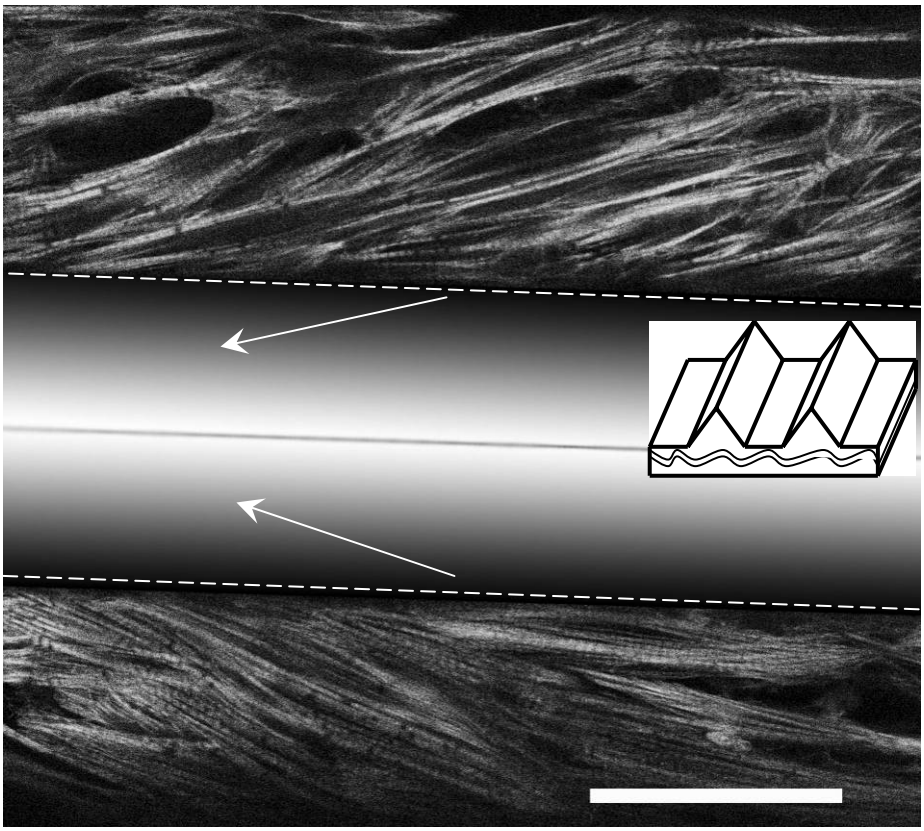

Figure 5-2 Bipennate structure of cardiomyocytes grown on G scaffolds.
A thin optical (confocal) section from a G scaffold with cardiomyocytes stained for F-actin is shown with a schematic representation of the ridge structure separating the grooves in the middle (boundaries marked by dashed-lines). Note the alignment of cytoskeleton at a shallow angle (schematically represented by arrows) to the grooves and the convergence of actin fibers on adjacent grooves mimicking bipennate structures found in skeletal muscle such as rectus femoralis. Inset: A schematic diagram of microgrooved scaffold geometry. Scale bar is 50μm.

The first striking structural difference observed between F and G scaffolds was the peculiar alignment of cells on G scaffolds under phase-contrast microscopy. Cardiomyocytes were seen bridging the grooves under a shallow angle in a pattern reminiscent of bipennate skeletal muscle (fibers converging in a feather-like structure). Confocal imaging confirmed F-actin alignment in a similar arrangement (**Figure 5-2**); consistent with nuclear elongation and alignment we have previously reported in cardiomyocytes grown on G scaffolds (Entcheva and Bien 2003). At higher magnification, well-developed sarcomeres were visible in both F and G scaffolds (**Figure 5-3A**). However, actin cytoskeleton on F scaffolds appeared less mature and more disorganized – never having a bipennate or multipennate structure.

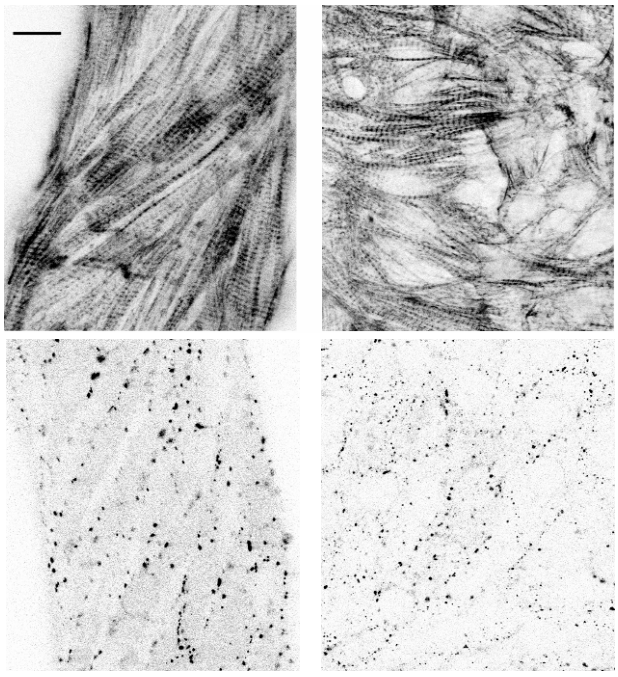

Figure 5-3 Cardiomyocytes grown on microgrooved scaffolds (G, left) exhibit profound structural differences compared to flat scaffolds (F, right).
A) Confocal images of F-actin demonstrate highly organized cytoskeleton with well-defined sarcomere structures oriented at a shallow angle relative to the grooves running vertically in (G) scaffolds. B) Higher density, larger Cx43 clusters are seen in G scaffolds (left) in a typical confocal image of Cx43 compared to F scaffolds (right). Scale bar is 10μm.

In addition to cytoskeletal changes, augmentation of gap junctional proteins (connexin-43) within the grooves was observed (**Figure 5-3B**). Estimation of Cx43 cluster size by granulometry (**Figure 5-4**) revealed both an increase in Cx43 density (as demonstrated by increased numbers of Cx43 clusters in each size category) as well as a shift in the relative distribution of cluster sizes favoring larger clusters (as seen by the increased percentage of Cx43 clusters at larger sizes relative to total number of clusters). Together, these data imply that the greater numbers of larger Cx43 clusters was not simply a reflection of increased Cx43 density (in which case the percentage of large Cx43 clusters would have remained the same).

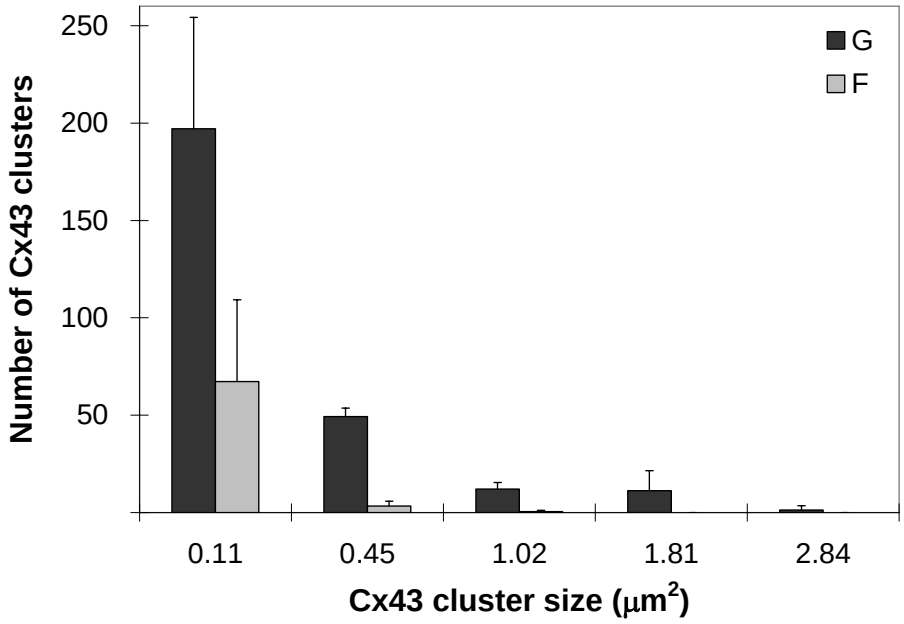

Figure 5-4 Quantitative granulometry reveals both increased gap junctional size (no flat scaffolds had gap junctions greater than 1.02μm²) and increased numbers of gap junctions.
Granulometry involves a combination of morphological operations with increasing element sizes to separate objects of specific sizes. Dividing the number of pixels found in this method by the area of the element size approximates the number of objects having dimensions similar to the shaping element used in the morphological operations. Data shown are mean±SD, n=5 G and n=7 F images were analyzed.

Electromechanical testing was then performed to see if these structural changes resulted in any functional differences. Microscopic recordings demonstrated significantly increased peak systolic intra-cellular calcium levels (p<0.05, **Figure 5-5A**). Consistent with this finding is the observation of increased cellular strain (p<0.05, **Figure 5-5B**) since intra-cellular calcium concentration is linked to the mechanical performance of the cardiomyocytes. Additionally, spontaneous and persistent synchronized contractions were often observed on G scaffolds as early as day 3 after plating. Such pacemaking activity can also be seen in the characteristic slow "depolarization" in some calcium transients observed (**Figure 5-5C**). In contrast, F scaffolds rarely exhibited such organized and persistent pacemaking behavior and spontaneous contractions.

One of the intents of creating these engineered cardiac constructs was to induce structural and functional anisotropy. A low magnification, large area imaging was performed to assess action potential propagation across microgrooves. Such macroscopic optical mapping revealed highly anisotropic conduction velocities with near instantaneous propagation within the grooves (>10cm/s) but delayed conduction across the grooves (<2cm/s,**Figure 5-6**) at the lowered temperatures used during imaging of the samples.

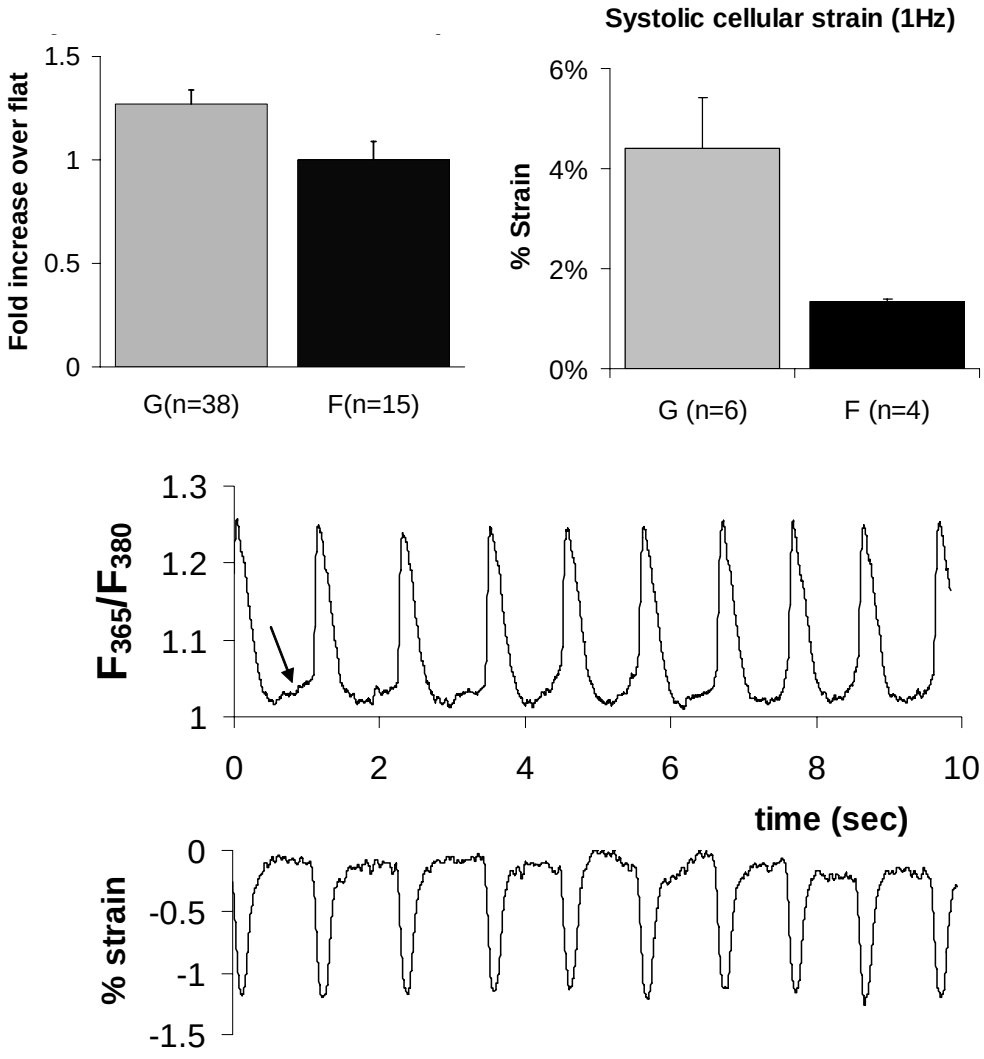

Figure 5-5 Optical recordings of functional changes (calcium and strain) in microgrooved samples vs. control.

A) Cells grown on microgrooved surfaces (G) have significantly increased systolic calcium levels compared to cells on flat (F) surfaces when field-stimulated at 1Hz. B) Increased uni-axial strain of cells on G versus F scaffolds. C) Example traces of intracellular calcium ratios (top) and mechanical strain (bottom) in spontaneously contracting cells on a G scaffold. Peak (systolic) intracellular calcium concentration is proportional to the ratio of fluorescence at 365nm (F_{365}) and 380nm (F_{380}), while mechanical strain is defined as percent change from diastolic (resting) length. Note the slow depolarization characteristic of pacemaking cells (arrow). Data shown are mean±SEM (*n* is number of examined scaffolds); stars indicate significance at $p<0.05$.

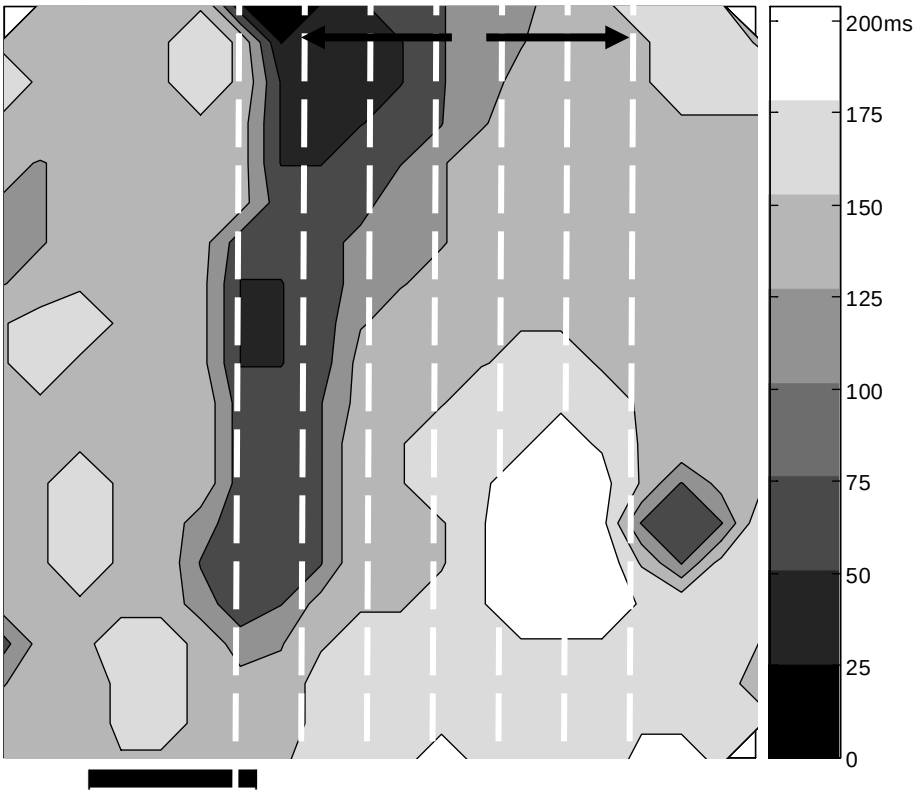

Figure 5-6 Cells on grooved surfaces exhibit anisotropic propagation.
The activation map shows spontaneous propagation within grooves faster than across grooves. Plotted are times of activation of each location relative to the earliest activation (in this case, at the top center of the image). The action potentials spread laterally to both sides (indicated by the arrows on top) as well as from top to bottom. Orientation of the microgrooves is schematically depicted as dashed white vertical lines (not drawn to scale). Contours indicate isochronal activation times in milliseconds, as shown on the right. Scale bar represents 1mm.

Discussion and Conclusions

Anisotropy is an essential feature of cardiac tissue. Previous attempts to mimic it *in vitro* have employed 2D micropatterning (Rohr, Shoelly et al. 1991; Bursac, Parker et al. 2002), extracellular matrix manipulations (Simpson, Terracio et al. 1994; Fast, Darrow et al. 1996) or surface microabrasions (Bursac, Parker et al. 2002). In contrast, our approach involved the introduction of a 3-D microenvironment and resulted in some interesting structural characteristics (bipennate arrangement). Functionally, the engineered constructs exhibited extreme levels of anisotropy, which could be well controlled in our system by the spatial features in the master template. The chosen approach to engineer a model cardiac tissue also brought about significant functional changes (in calcium and strain levels), possibly attributable to 3-D effects in cell attachment and subsequently altered mechanical environment.

Thus developed engineered tissue bears essential features of the real heart and combined with the optical mapping tools, reported in this paper, could serve as a platform for

mechanistic studies in cardiac electromechanics, drug testing, computer model validation and investigation of cell-scaffold responses for tissue engineering and tissue regeneration purposes.

6. AN IN-VITRO PARTICULATE MATTER EXPOSURE MODEL

Abstract

We hypothesized that particulate matter dust particles will incite low-level pulmonary inflammation, and the associated release of inflammatory mediators from the lungs will lead to a pro-arrhythmic state. To test this hypothesis in a controlled fashion, we have devised an *in-vitro* exposure model combining alveolar macrophages and cultured nenonatal rat cardiomyocytes. Alveolar macrophages (AM) were cultured in the presence of particulate matter dust and the conditioned culture medium was assayed at several time points for the secreted amount of two selected inflammatory cytokines: tumor necrosis factor alpha (TNF-α) and interleukin 1 beta (IL-1β). We found that levels of TNF-α peaked at 12 hours and persisted for another 24 hours with TNF-α secretion much greater than IL-1β. Interestingly, stimulation of AM with lipopolysaccharide (LPS) resulted in similar levels of cytokine release but a more robust IL-1β response and reduced TNF-α levels. Use of cardiomyocyte culture medium with 2% serum supplementation as opposed to normal AM culture medium with 15% serum resulted in dramatically worse cytokine secretion. Cardiomyocytes tolerated being cultured in AM culture medium for one day without any noticeable functional changes. As an *in vitro* particulate matter exposure model, we will culture AM in the presence of particulate matter dust for 24 hours in AM culture medium and then transfer the conditioned media to cardiomyocytes for an additional 24 hours.

Introduction

The typical inflammatory response involves a variety of tissue types, most associated with the immune system(Cesari, Penninx, Newman, Kritchevsky, Nicklas, Sutton-Tyrrell, Tracy et al. 2003). To better study the effects of inflammatory mediators on cardiac tissue itself, a reduced model without other contaminating cell types is required. The engineered heart tissue construct model described and characterized earlier provides an ideal test-bed for examining the response of cardiac myocytes to factors released from the lung after particulate matter dust exposure. However, an *in vivo* exposure model would require complicated and expensive equipment as well as elaborate animal protocols(Laskin, Morio et al. 2003). An *in vitro* delivery system would provide for a more consistent and controllable dose as well as eliminate the need for special inhalational delivery devices. To fully reproduce the effects of an *in vivo* exposure, one would require an artificial lung. Since we are examining the effects of mediators released from the lung after exposure to particulate matter, we decided to focus on alveolar macrophages (AM) first. While endothelial cells and lung epithelial cells can contribute to an inflammatory reaction secondary to particulate matter exposure, AM is thought to be the primary cell type responsible for induction and maintenance of pulmonary inflammation(Becker, Soukup et al. 2003). *In-vitro* testing has revealed greater sensitivity of AM than epithelial cells to soluble metals from PM(Riley, Boesewetter et al. 2005). Dust particles from the World Trade Center collapse were also found to induce a stronger cytokine release from AM than from epithelial cells (Type II pneumocytes)(Payne, Kemp et al. 2004).

Interleukin-1beta (IL-1β) and tumor necrosis factor-alpha (TNF-α) released from AM exposed to PM can induce lung epithelial cells to secrete more IL-1β and TNF-α among other inflammatory markers, but these effects can be abrogated with blocking anti-IL-1β and anti-TNF-α antibodies(Ishii, Fujii et al. 2004). Thus the first step in PM exposure is presumably AM activation followed by induction of lung epithelial tissue to secrete more inflammatory mediators.

AM can be collected from bronchoalveolar lavage (BAL) fluid – a procedure which is fairly invasive but not necessarily terminal(Laskin, Morio et al. 2003). However, for simplicity and better consistency, a cell line was sought that recapitulated the key functional characteristics of AM. Specifically, we required a cell line that was responsive to PM exposure and released inflammatory mediators such as TNF-α and IL-1β as reported for human AM(Ishii, Fujii et al. 2004). Through a literature search, we were able to identify a rat AM cell line, NR8383, from American Type Culture Collection (ATCC) that releases TNF-α and IL-1β, prototypical inflammatory mediators, upon challenge with lipopolysaccharide (LPS)(Helmke, German et al. 1989) at levels as low as 10ng/mL. LPS is a component of the outer membrane of gram-negative bacteria and a potent stimulator of professional phagocytes such as monocytes and macrophages. Although the role of lipopolysaccharide (LPS) or bacterial endotoxin in PM induced pulmonary inflammation is still under research(Nave, Becker et al. 2002; Hetland, Cassee et al. 2005; Alexis, Lay et al. 2006), LPS has been commonly used as a non-specific but potent activator of macrophages. NR8383 has also been previously demonstrated to react to dissolved metals from PM (Riley, Boesewetter et al. 2005) and release cytokines in a dose-dependent matter upon exposure to residual fly ash (a potential source of PM)(Diabate, Mulhopt et al. 2002).

We thus set out to create and characterize an *in-vitro* model of PM exposure using NR8383 to assess the impact of released cytokines on HTCs. We confirmed the release of TNF-α and IL-1β from NR8383 exposed to PM or LPS after 12 to 24 hours, and AM cultured in HTC culture medium (supplemented with 2% serum versus the regular AM culture medium with 15% serum) suffered a dramatic reduction in cytokine secretion. Fortunately, HTCs cultured in AM culture medium for 24 hours appeared not to have great functional aberrations. We also found evidence for a differential response of AM to LPS compared to PM stimulation; however the extremely low levels of IL-1β assayed across all groups precludes a definitive judgment. In summary, we have designed and validated an *in-vitro* model of PM-exposure's effects on HTCs using an alveolar macrophage cell line, NR8383, and can reliability reproduce a cytokine cocktail generated by macrophages activated by urban air dust particles.

Methods

Alveolar macrophages

Alveolar macrophage cell line NR8383 was obtained from ATCC as a confluent flask and maintained as per ATCC's instructions. Since NR8383 grows as both an adherent and floating population, the cells in suspension were collected, spun down, and resuspended to achieve ATCC's recommended concentration of 1-4x10^5 cells/mL. If the resuspended volume was less than 10mL, it was re-introduced into the originating flask; otherwise a new flask would be populated with the resuspended cells. When enough flasks had been produced, the floating cell population was simply discarded. Flasks were passaged for no more than 8 weeks.

LPS and PM

Lipopolysaccharide (LPS) was obtained from Sigma and reconstituted in endotoxin-free water to a concentration of 1mg/mL before storage at -80°C. Further dilutions to the working concentration of 10ng/mL were performed using AM culture medium (F12k supplemented with 15% fetal calf serum, FCS) on the day of the experiment.

Particulate matter (PM) dust reference particles were obtained from the National Institute of Standards and Technology (NIST) Source Reference Material (SRM 1649a). SRM 1649a was chosen because it has been previously extensively characterized as to its composition. SRM 1649a was diluted to 100mg/mL (1000x) in endotoxin-free water before final dilution to 0.1mg/mL in AM culture medium (F-12k with 15% FCS). Previous studies on human AM have found them to be sensitive to 100μg/mL of PM_{10} after 24 hours(Ishii, Fujii et al. 2004). To avoid microbial contamination, the SRM was also treated with germicidal UV for 3 hours in a laminar flow hood prior to use. Due to the highly turbid mixture with many undissolved particulates, the SRM was mixed well prior to use, but the precise amount of large particulate matter was difficult to control.

Degradation rates

To assess the stability of secreted TNF-α and IL-1β peptides, AM were activated by LPS for 12 hours and then supernatant collected and incubated for an additional 24 hours at 37°C. Samples were collected and analyzed later via ELISA for concentrations of soluble TNF-α and IL-1β. Further experiments treated AM for 24 hours with LPS or PM and then incubated for another 24 hours at 37°C.

Quantifying TNF-a and IL-1β levels

The floating population of an AM flask was centrifuged and transferred to a 50mL conical tissue culture tube at $3x10^5$ cells/10mL initially, and then $3x10^6$ cells/10mL thereafter. LPS, PM, or vehicle (endotoxin-free distilled water) was added as appropriate to individual tubes and cultured for 3 to 24 hours. Secreted TNF-α and IL-1β levels were measured from supernatants using ELISA kits for rat TNF-α and rat IL-1β, respectively (Biosource), per manufacturer's instructions. At each time point, samples were collected and centrifuged to remove particulates and cells prior to freezing at -80°C until ready for analysis.

Statistical tests for concentrations of IL-1β and TNF-α were conducted using two-way ANOVA between groups and culture medium with MATLAB (Mathworks). Post-hoc comparisons were performed with Tukey-Kramer correction. Significance was set at $p \leq 0.05$.

Results and discussion

LPS stimulation induces TNF-a release that peaks at 12 hours and persists to 25 hours

LPS at 10ng/mL was found to induce a potent TNF-α release from NR8383 after as little at 3 hours and plateaued around 12hours (Figure 6-1). Sham and control groups (untouched AM) were all below detection limits except for the initial time-point for sham. Since at this time the only source of TNF-α would be from the culture medium itself, and as the other groups did not show any trace of TNF-α, the non-zero reading from the ELISA was probably an artifact. The relatively low levels of TNF-α were near the limits of detection for

the ELISA, and thus we decided to increase the number of AM plated per tube by a factor of ten.

AM remained viable and had no visible morphological changes after activation by LPS or PM

After 24 hours culture in the presence of LPS or PM, the AM did not appear to change morphologically (Figure 6-2). Trypan blue exclusion staining revealed no loss of viability at these levels of LPS and PM (data not shown). A very slight decrease in cell density for the LPS group was noted visually but could not be quantified for verification due to the mixed growth pattern of AM (both in suspension and as an adherent population). However, previous reports have noticed a reduction in proliferation of NR8383 by LPS exposure (Helmke, German et al. 1989).

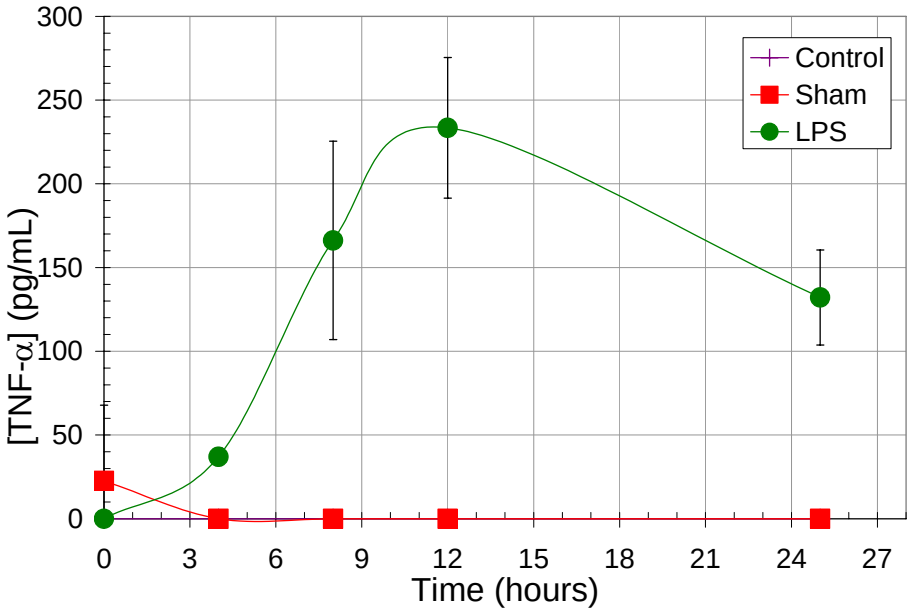

Figure 6-1 TNF-α release peaks at 12 hours and persists until 25 hours.
AM were cultured in 10ng/mL of LPS, sham vehicle, or not modified (control) for 25 hours. Samples of culture media were taken at approximately 0, 3, 9, 12, and 25 hours and frozen at -80°C for ELISA testing. Shown are means levels±SE of TNF-α detected in the culture medium after the indicated time interval. Control samples were all below detection limits. The initial reading of TNF-α at time 0 for sham was near the limit of detection and therefore not reliable.

AM were found to cluster around large particulates from SRM also giving a false appearance of decreased density, but this may be due to the highly heterogeneous distribution of cells(Figure 6-2). As before, quantification was precluded both by the existence of the suspension population of cells and by the limited number of AMs available. Each conical tube required the equivalent of a confluent T175 flask of AM cells, and thus most cells were used for conditioning media for treating HTCs.

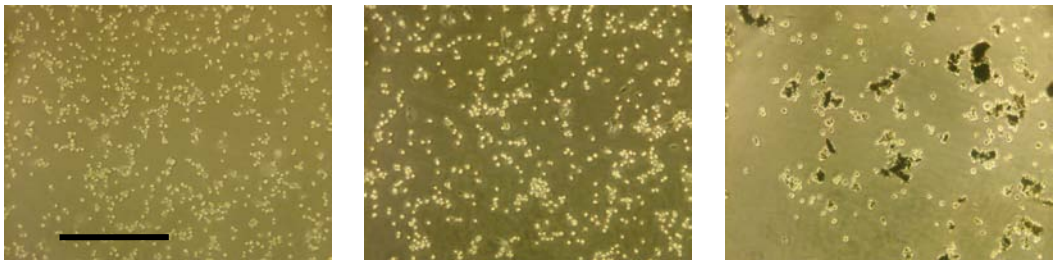

Figure 6-2 Photomicrographs of AM after exposure to vehicle (sham), LPS, or PM.
A. Phase contrast image of NR8383 after 24 hours exposure to vehicle (Sham). B. Phase contrast image of NR8383 after 24 hours exposure to 10ng/mL LPS. C. Phase contrast image of NR8383 after 24 hours exposure to 100μg/mL SRM 1649a. The dark clumps are particulate matter from SRM 1649a. The appearance of lower cell density is probably an artifact from clustering of AM. Scale bar is 400μm and is identical for all photographs.

PM activation results in a differential cytokine release profile from LPS

Since the culture media differed for AM cells (F-12k supplemented with 15% serum) while HTCs required M199 medium with 2% serum, we would have to either culture AM in M199 with 2% serum for 24 hours or culture HTCs in F-12k for 24 hours. By examining the cytokine release profile for LPS and PM activated AM in both M199 and F-12k media, we discovered that serum deprivation (M199 at 2%) resulted in a significant reduction in TNF-α for PM-activated AM (Figure 6-3). Note that due to lack of cells we were unable to test LPS-stimulated AM cultured in M199 thus we cannot say whether IL-1β was similarly affected.

We also found that PM activation yields a slightly different cytokine profile than LPS activated AM when cultured in F-12k. Specifically, LPS activation resulted in relatively low levels of TNF-α while still exhibiting a robust IL-1β release. On the other hand, PM activation induced a very potent TNF-α release but no detectable IL-1β.

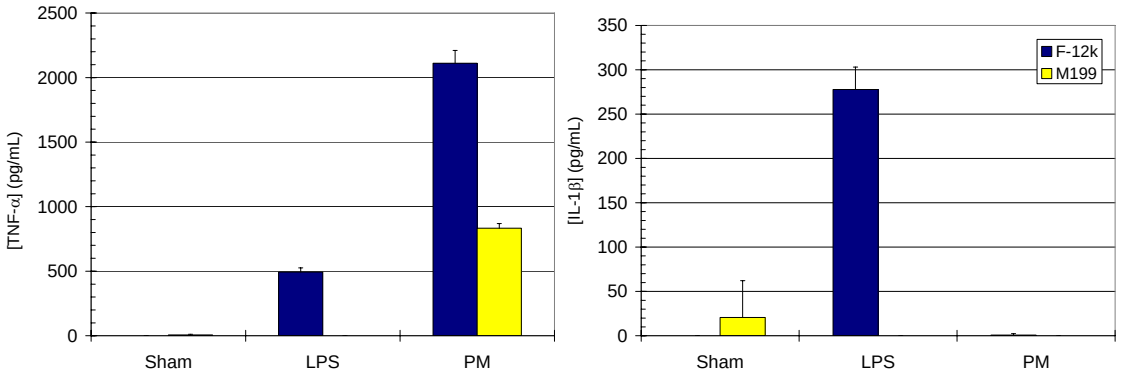

Figure 6-3 AM secreted greater levels of TNF-α and IL-1β in their native F-12k medium
AM were cultured for 24 hours in the presence of 10ng/mL LPS or 100μg/mL of SRM 1649a in either AM culture medium (F-12k with 15% FCS) or HTC culture medium (M199 with 2% serum). LPS in M199 was not tested. Shown are mean±SE for each group.

We then tested the viability of HTCs after 24 to 48 hours in culture with F-12k supplemented with 15% serum. While detailed testing was not conducted, HTCs cultured for 24 to 48 hours in F-12k remained viable as assessed by Trypan blue exclusion and were functional in that they responded to electrical stimulation and visibly contracted. Thus, the decision was made to culture HTCs for 24 hours in conditioned F-12k media to promote the release of cytokines from AM.

TNF-a and IL-1β degrade rapidly over time in M199 but not F-12k

Both TNF-α and IL-1β concentrations fell below detection limits from 24pg/mL and 110pg/mL, respectively, 24 hours after incubation in M199 media with 2% serum (data not shown). However, additional testing in F-12k media with 15% serum demonstrated no appreciable loss in TNF-α concentration over an additional 24 hours after collection from LPS activated AM (2315±247pg/mL at initial collection and 2611±848pg/mL after 24 hours). The slight increase in TNF-α concentration is not significant and most likely represents the non-linearity of the ELISA curve near the upper limit of the assay (at 2000pg/mL). Unfortunately, IL-1β levels were too low to establish a similar effect.

Since M199 differs from F-12k only slightly in terms of their composition, the greatest difference is the amount of serum supplementation. Soluble TNF-α exists as a homotrimer and loses bioactivity at low concentrations where it dissociates into monomers(Corti, Fassina et al. 1992). Serum albumin may help stabilize TNF-α or at the very least enhance its recovery (per manufacturer's ELISA instructions) thus possibly explaining why M199 with only 2% serum had a greater "loss" of TNF-α over time.

Cardiac fibroblasts do not release TNF-a or IL-1β in response to conditioned media

Recent evidence has implicated a role of cardiac fibroblasts and other non-cardiac, non-infiltrating (inflammatory) cells in cardiac inflammation(Gurantz, Cowling et al. 2005; Uemura, Adachi-Akahane et al. 2005). To test whether cardiac fibroblasts were a potential source of additional cytokines, primary cardiac fibroblasts (FB) isolated from neonatal rat cardiomyocytes harvests as described previously (Bien, Yin et al.) were grown on elastic scaffolds akin to those used for HTCs at a lower cell density of $2x10^5$ cells/cm^2. FB samples were exposed to sham, LPS, or PM-activated AM conditioned media for 24 hours and assayed for concentrations of soluble TNF-α and IL-1β. No differences were found in TNF-α levels between empty wells and wells containing FB scaffolds.

	No FB (empty)	*$2x10^4$ FB/cm^2*
Sham	<4[2] pg/mL	<4 pg/mL
LPS	2315±247 pg/mL	2376±191 pg/mL

Table 6-1 Cardiac fibroblasts do not secrete TNF-α in response to conditioned media. Primary cardiac fibroblasts were cultured for 24 hours in conditioned media from AM activated by either LPS or sham. Shown are concentrations of soluble TNF-α in pg/mL, means±SE.

[2] The minimum detectable limit of TNF-α as quoted by the manufacturer is <4pg/mL.

Limitations and future studies

While cardiac fibroblasts may not provide a strong source of cytokines in this model, the original inciting pulmonary inflammation may generate cytokines from sources other than the alveolar macrophages. It has already been demonstrated *in vitro* that culturing lung epithelial cells in media conditioned by PM-activated AM results in greater release of TNF-α and IL-1β(Ishii, Fujii et al. 2004). That this is mediated through secreted factors is further bolstered by the same author's study one year later reporting synergism in reaction to PM when co-cultured even in the presence of blocking anti-bodies to ICAM-1(Kido, Hasebe et al. 2005). Furthermore, co-cultures of macrophage and epithelial cell lines also indicate greater sensitivity to PM(Wottrich, Diabate et al. 2004). The combination of lung epithelial cells with activated AM may well result in even higher concentrations of secreted inflammatory mediators. Future work may involve co-cultures with lung epithelial cell lines to re-create a more realistic pulmonary inflammation milieu.

Conclusion

We have established an *in-vitro* model for testing the effects of PM exposure on cardiac tissue. By leveraging the ease and repeatability of a well characterized AM cell line, NR8383, we were able to demonstrate that PM induces a robust cytokine response from NR8383 that differed slightly from LPS activation. Furthermore, we have optimized several key characteristics of the model by examining the kinetics of cytokine secretion and the influence of culture media employed. Using this model one can assess the impact of PM-activated AM's cytokines on HTCs and dissect the pathophysiological pathway of urban air pollution associated cardiovascular disease.

7. SPATIOTEMPORAL CONSIDERATIONS IN OPTICAL MAPPING

Abstract

Quantifying arrhythmogenesis in HTCs requires collecting data from multiple spatial locations at rapid rates in order to reconstruct the spatiotemporal progression of events. Optical mapping enables one to probe various cellular states at high spatial and temporal resolution. However, technological barriers limit the highest achievable spatiotemporal resolution. In this chapter, we examine the relationship between spatial and temporal resolution for imaging propagating phenomena in order to derive minimum specifications for accurate capture. Fluorescent indicator dye selection, use, and calibration are also discussed. We describe certain difficulties inherent and unique to optical mapping of thin, monolayer cultures such as our HTCs. Finally, we review existing technologies and their limitations addressing our needs or restricting our desires for high speed, high sensitivity optical mapping. In discussing the ideal detector, we forecast the need for a dynamically variable, non-uniform spatiotemporal sampling image acquisition device for maximizing the utility of available bandwidth not unlike the design of human eyesight.

I. Introduction

Excitation waves are complex spatiotemporal phenomena encoding essential functional information for healthy and diseased excitable tissue, including the heart. The visualization of these waves in live tissue was facilitated by the introduction of fast fluorescent probes for changes in transmembrane voltage and intracellular calcium concentration, and by the development of appropriate optical techniques to image their response (Salama and Morad 1976; Grinvald, Salzberg et al. 1977; Ross, Salzberg et al. 1977; Morad and Salama 1979; Tsien 1983; Grynkiewicz, Poenie et al. 1985; Gross, Loew et al. 1986; Ehrenberg, Farkas et al. 1987). Since then, *optical mapping* (multisite fluorescence measurements with high temporal and spatial resolution) has made possible the direct experimental testing of theoretical concepts about cardiac arrhythmias, cardioversion and electrical excitation in the heart. Optical mapping in culture-grown monolayers or patterns of myocytes allows the study of cellular processes in their natural context, avoiding some of the deficiencies associated with the two extremes: isolated cells or whole heart measurements. It permits the true dissection of propagation phenomena and direct links to computational models of the same by controlled local or global alterations of structural and functional properties – a feature not readily available in whole heart or tissue preparations. Thus, cultured cardiomyocyte networks form a natural bridge between single cell and whole heart studies in cardiac electrophysiology.

Optical *microscopic mapping in cardiomyocyte cultures* was pioneered by Rohr, Fast and Kleber at the University of Bern, employing patterned cell growth(Rohr, Shoelly et al. 1991) and custom-developed imaging system using a fluorescence microscope, photodiodes and optical fibers(Rohr and Salzberg 1994; Rohr and Kucera 1998). In a series of elegant optical mapping studies, this group and their collaborators addressed questions of load mismatch in structurally

complex cell network architectures (Fast and Kleber 1993; Fast and Kleber 1995a; Fast and Kleber 1995b; Rohr, Kucera et al. 1997), cell-level polarization patterns in response to external electrical fields in cardioversion and defibrillation(Gillis, Fast et al. 1996; Fast, Rohr et al. 1998; Fast and Ideker 2000; Gillis, Fast et al. 2000; Tung and Kleber 2000; Fast, Cheek et al. 2004), micro-reentrant phenomena in slow propagation conditions (Rohr and Kucera 1997; Kucera, Kleber et al. 1998), etc.

Understanding cell network behavior at the *macroscopic scale* and the study of phenomena underlying dangerous cardiac arrhythmias required the extension of this imaging approach to accommodate a larger field of view (FOV). Signature reentrant waves, believed to be at the core of cardiac arrhythmias, are macroscopic spatiotemporal phenomena, taking place over a spatial scale that is linked to the wavelength for propagation ($\lambda_w = \theta * w$, where θ is the wave's conduction velocity, and w signifies the duration of the events of interest – action potentials or calcium transients). For typical values of θ and w, the spatial scale of interest is in the centimeter range, thus requiring a matching FOV in that range. Due to technical difficulties and limitations of optical imaging at low magnification in low light levels, the transition from micro- to macroscale mapping in monolayer cell cultures is not trivial, i.e. is not as simple as changing an objective.

The first attempts at *macroscale mapping of cardiac electromechanics in cultured cells* (voltage or calcium waves) originated in three laboratories. G. Bub, A. Shrier and L. Glass at McGill University (Bub, Glass et al. 1998; Bub, Shrier et al. 2002; Bub, Tateno et al. 2003) used a charge-coupled device (CCD) -based system to track the dynamics of spontaneous and induced spiral waves as a function of cell density and age in cultured embryonic chick cells. L. Tung lab at Johns Hopkins University (Entcheva, Lu et al. 2000; Iravanian, Nabutovsky et al. 2003; Entcheva, Kostov et al. 2004) developed a contact fluorescence imaging (CFI) approach combining photodiodes and fiber optics to study anatomical and functional reentry in neonatal rat cultures. N. Sarvazyan lab at Texas Tech University(Arutunyan, Webster et al. 2001; Arutunyan, Swift et al. 2002) used a confocal system to assess calcium dynamics in reperfusion injury in cultured cell networks with a geometrically defined ischemic zone. In these first attempts at macroscopic mapping in cardiac cell monolayers, the overall spatiotemporal resolution was insufficient - typically the focus was on one of the aspects - either good temporal or good spatial resolution.

Mechanistic understanding of the spatiotemporal phenomena underlying cardiac arrhythmias calls for both – micro- and macroscale imaging, preferably done simultaneously and using appropriate acquisition rates. The requirement for combined macro/micro examination is of particular importance for phenomena occurring at fine spatial scales or in a heterogeneous setting. Examples include the activity at the core of a macroscopic spiral wave, cell-level phenomena during macroscopic wave meandering and wavebreaks in fibrillation-like conditions, coupling and propagation between discrete structures of cell populations (stem cells and myocytes, for example). The most interesting and clinically relevant excitation phenomena (such as associated with polymorphic ventricular tachycardia and fibrillation) are by definition unpredictable in space-time, therefore it is close to impossible to *a priori* localize the zone of interest (for detailed micro-mapping) within the macro-image. A brute-force approach can be used alternatively – a single *detector with ultra-high spatiotemporal resolution* to

conduct micro-level (subcellular) imaging within a macroscale FOV. To date, no such tools have been described; and, indeed, current *macroscopic* optical mapping has never approached the spatial resolution common for computer models of propagation.

Specific questions concerning optical imaging of spatiotemporal phenomena at the macroscale (>1cm^2) in cell culture preparations have not been addressed in the numerous optical mapping reviews and technical papers published in the field over the last 30 years (Cohen, Salzberg et al. 1978; Morad and Salama 1979; Salama and Loew 1988; Salzberg 1989; Rohr and Salzberg 1994; Baxter, Davidenko et al. 1997; Bullen, Saggau et al. 1997; Rohr and Kucera 1998; Wu, Lam et al. 1998; Bullen and Saggau 1999; Wu, Cohen et al. 1999; Tominaga, Tominaga et al. 2000; Grinvald, Shoham et al. 2001; Sakai and Kamino 2001; Tominaga, Tominaga et al. 2001; Efimov, Nikolski et al. 2004; Grinvald and Hildesheim 2004). With very few exceptions (Rohr and Salzberg 1994; Rohr and Kucera 1998; Bullen and Saggau 1999), most of the above papers have dealt with tissue-level measurements of electrical activity in cardiac and brain preparations, not with cell monolayers.

We have come to the realization that there are unique challenges for macroscopic (low magnification) optical mapping in cultured cell monolayers, and this paper aims at providing the missing perspective. More specifically, this review outlines a theoretical framework where the choice of imaging detector is made based on a "shortest distance" from an "ideal" optical mapping system. In this context, we critically review the newest detector technology with ultra-high spatiotemporal resolution (>5 megapixels per second) and present the first macro-mapping and micro-mapping data at such high resolution. We discuss new technical issues (detector-computer interface), arising only in conjunction with the very high information throughput in this new class of photodetectors.

The structure of the review is as follows: 1) challenges of low magnification fluorescence imaging and suitable optical arrangements for cell monolayers; 2) issues concerning the use and calibration of fluorescent labels; 3) illumination solutions for cell culture imaging; 4) review of state-of-the-art photodetectors with ultra-high spatiotemporal resolution and appropriate sensitivity for cell culture mapping; 5) new technical challenges of very high data throughput, and review of the capabilities of current computer technology to meet them; 6) theoretical analysis for rational design of a "minimal" and an "ideal" imaging systems, and evaluation of the available detector technology in terms of "closeness" to the ideal target.

II. Challenges of low magnification (macroscopic) optical measurements

1. Why is it difficult to map fluorescence at low magnification?

Intuitively, low magnification is expected to provide larger pixel area to collect light from and to improve optical signals. However, this notion is not quite correct – fluorescence imaging at low magnification is adversely affected by the quality of the optics available. In addition, by increasing the number of pixels as the field of view grows to maintain the spatial resolution within acceptable limits, the imaged area per pixel is not substantially larger.

Current high-power microscope lenses (objectives), which have evolved to aid scientific discovery, feature impressive light-collecting ability, usually quantified by their numerical aperture (NA). NA indicates the ability of a lens to effectively collect diffracted rays of light,

and provide high resolution power. $NA = n\sin(\alpha/2)$, where n is the index of refraction of the medium, and α is the maximum solid angle of acceptance of light at the optical axis.

Eq. 7-1) $$LCA = \frac{1-\sqrt{1-(NA)^2}}{2}$$

Macro-scale mapping of electrical propagation is needed to visualize spatiotemporal patterns occurring over a large area ($1cm^2$ or more). At the same time, the imaging area of the current photodetector technology has practical size limitations – the chip size is close to or even smaller than the desired FOV. This requires operation at low magnification. Commercially available objectives in this range (<2x) have very poor light-gathering ability (very low NA). Typically below 10x, it is rare for an objective lens to have NA>0.3 (compare this to NA=1.4 for a good 60x objective).

There are a couple of factors preventing the achievement of high NA in low magnification objectives:

Medium of operation – high NA lenses achieve NA>1 by operating in media different from air (n=1), such as water (n=1.33) or oil (n=1.55). Macroscopic imaging cannot benefit from these higher index of refraction media because of practical reasons – large separation between the sample and the objective (i.e. large working distance).

Working distance – most of the low magnification lenses cover a large FOV and therefore operate at large working distances (WD). The latter means large focal lengths (*f*), which translate into low NA, since for simple lenses the NA is inversely proportional to the focal length ($NA \propto f^{-1}$).

Lens size - A way to compensate for the compromised NA is to increase the lens diameter (*d*), because ($NA \propto d$). However, in a standard microscope setting, there are limits to this diameter increase. For macroscopic lenses outside the microscope, a large diameter is possible, yet it is technically challenging to achieve a high surface curvature needed for a high angle of acceptance in these big lenses.

As a result, high NA lenses for macroscopic imaging are rare. Lenses with suitable characteristics can be found in photography – the so called "fast" lenses, featuring very low F-number (note that $NA=0.5n/\#F$) and used in very low light levels. The lowest #F (highest NA) in a commercially produced compound lens is 0.7 (made by Zeiss 50mm f/0.7, not currently available). Such a lens would have NA=0.71, if operated at infinity. There are currently available large diameter fast lenses made by Canon (50mm f/0.95), Navitar (DO-5095 50mm f/0.95), Leica (Noctilux 50mm f/1), Nikon (Nikkor 35mm f/1.4, Nikkor 105mm f/2) etc., which cover focal distances from 35mm to 105mm, and #F from 0.9 to 2.0 (corresponding $NA=0.55$ *to* 0.25).

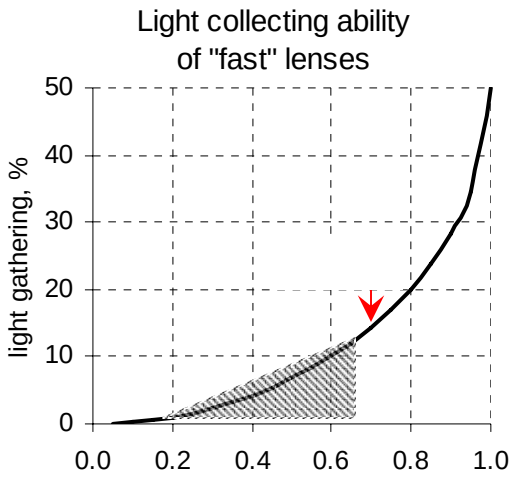

Figure 7-1 Light collecting ability of low magnification imaging lenses is a nonlinear function of their NA (#F).
Light gathering ability is theoretically calculated as percent collected light from the total light from a radially emitting point source, as a function of the numerical aperture (NA) or the #F of a lens. The shaded region shows the range for the currently manufactured "fast" lenses.

Figure 7-1 presents the theoretically determined light-collecting ability (LCA) of lenses in the *NA* range (0.05 – 1), operating in air. Calculations according to Eq. 7-1, based on pure geometrical considerations) are presented as a % collected light (volume fraction) from the total emitted light by an ideal light-radiating point source (the total luminous flux is represented by the volume of a sphere) using standard formulae (Zwillinger 1996). Note that the currently available "fast" lenses cover only the low LCA range. For example, the fastest lens ever made offers 9 times better light-gathering ability than a reasonably fast lens with #F of 2.

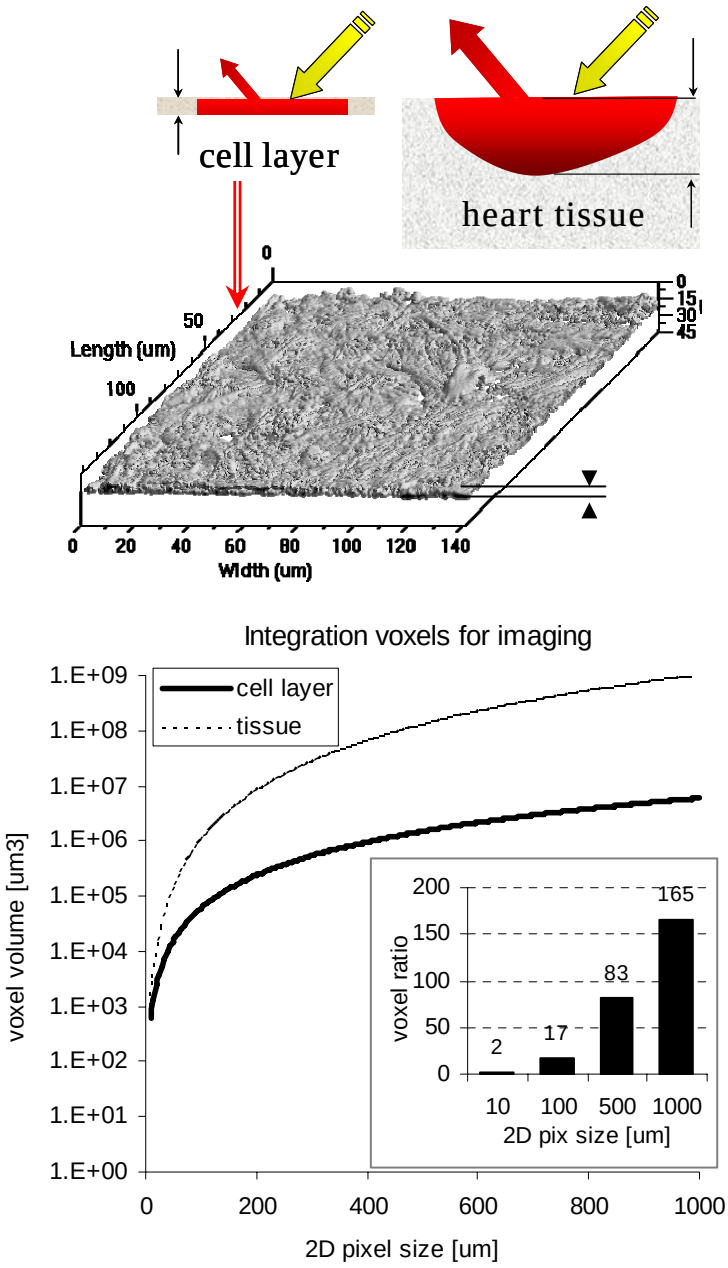

Figure 7-2 Fluorescence signals are volume-integrated, resulting in differences when imaging cardiac tissue vs. cell monolayers.
A. Schematic representation of the integration depth issue when imaging thin cell layers vs. cardiac tissue. On the bottom – an actual 3D reconstruction of a cultured cardiomyocyte layer. The image is based on multiple confocal images of the cytoskeleton (F-actin), total thickness 6µm. B. The graph presents the voxel volume [µm³] for a range of square pixels (10 to 1000µm); a cell height of 6µm is used for the cell monolayer. The inset shows selected ratios of voxel volumes between the two preparations, after the data have been corrected with the empirical exponential functions by Baxter et al. The voxels seen in tissue become 165 times larger than seen in monolayers for 1mm pixels.

In addition to poor light collecting ability, low NA lenses lead to deterioration in spatial resolution, δx, of the signal as per the Rayleigh criterion, Eq. 7-2, (Murphy 2001). For example, for emitted light with wavelength λ=0.6μm, and a lens having low NA=0.1, the limit of resolution (7.3μm according to Eq. 7-2 is considerably worse than the wavelength-determined limit.

Eq. 7-2) $$\delta x = \frac{1.22\lambda}{NA}$$

2. Why do cultured cell systems present more challenges than whole heart measurements?

Fluorescence signals are depth-integrated, thus the challenges of macro-scale mapping increase in inverse proportion to the thickness of the imaged preparation. Upon illumination of the sample, excitation of the fluorescent dye molecules takes place over a certain tissue volume (depth of 0.3-1.3mm below the surface(Knisley 1995; Girouard, Laurita et al. 1996; Baxter, Mironov et al. 2001)). Depending on the local tissue structure, absorption properties and scattering, emitted light is also collected from a volume, rather than a surface plane. In contrast, in cultured cardiomyocyte networks, the thickness of the whole sample is only 5-10μm, as assessed by confocal imaging and 3D volume reconstruction of the cytoskeleton (F-actin was labeled) in our lab, **Figure 7-2A,** or as measured by atomic force microscopy (Domke, Parak et al. 1999). This is at least an order of magnitude thinner than the low limit for the depth of field (DOF) of relevant lenses (Inoue and Spring 1997), thus the monolayer height becomes the limiting factor for the amount of collected light in this type of imaging, regardless of the employed optics. **Figure 7-2B** presents the sample volume (or imaging voxel) difference between tissue and a cell layer, as a function of the spatial resolution (2D pixel size) during imaging. The graph does not take into account the impact of the optics quality via DOF, i.e. the values for tissue measurements might be overestimated for cases where high NA lenses are used, which may somewhat restrict the effective depth of integration. The inset shows selected volume ratios, after a correction function has been applied for the depth contribution of different layers, as derived empirically by Baxter et al. (Baxter, Mironov et al. 2001). This difference alone can contribute to 2-to-165 times larger signals in tissue vs. monolayers, as the spatial resolution varies from 10 μm to 1mm per pixel. The implication is that a corresponding >100 times change in photodetector sensitivity or an overall improvement of all system components might be needed in order to adapt them from tissue-level imaging to mapping in cell monolayers at the same magnification.

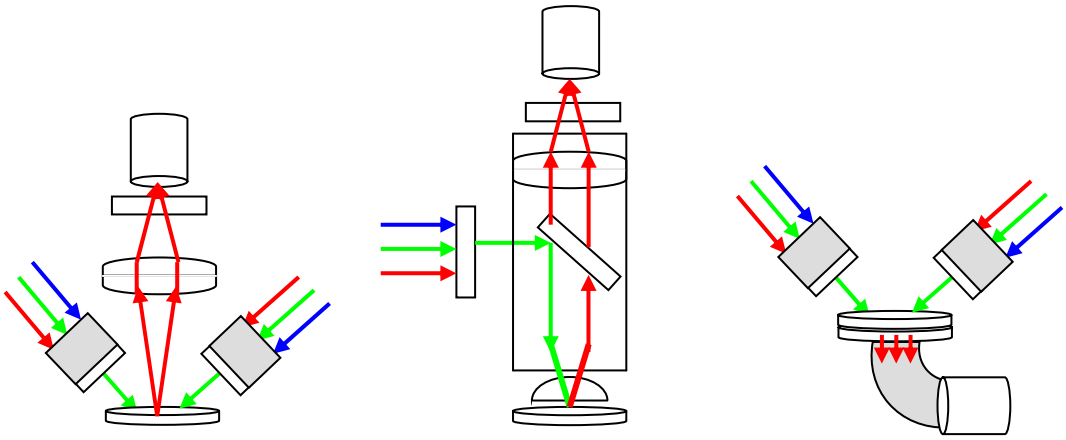

Figure 7-3 Solutions for low magnification imaging in cell monolayers.
A. Single high NA lens; **B.** Tandem-lens assembly; **C.** Contact fluorescence imaging (CFI) setup. The following components are depicted: S – sample; PD – photodetector; LS – light source; Em & Ex – emission and excitation filters; D – dichroic mirror; L – lens; L1, L2 – objective and imaging lenses for TL assembly; FO – fiber optics.

3. Viable optical arrangements for mapping in cultured cell systems

There are three possible solutions to obtain useful signals at low magnification optical mapping in thin cell preparations. These include: 1) the use of high NA large diameter single lenses; 2) Tandem-lens (TL) assembly optics; and 3) lens-less transfer of the image to the photodetector using versions of Contact Fluorescence Imaging (CFI), **Figure 7-3**.

Using a single "fast" lens in front of the detector is a simple solution. However, high NA low magnification lenses typically have a pronounced vignetting effect (loss of light away from the optical axis), and introduce spherical aberrations when operated at small distances. Furthermore, "fast" lenses perform at their maximum NA (corresponding to the indicated #F) when focused at infinity. At finite working distances to the sample (usually a couple of centimeters), the effective NA is lower.

The tandem-lens (TL) configuration (Ratzlaff and Grinvald 1991) combines two "fast" lenses, focused at infinity and facing each other, to guarantee high NA performance at practical working distances to the sample, and to facilitate epifluorescence measurements using identical optical pathways for the excitation light and for the emitted light. The sample is placed at the back focal plane of the smaller lens (L1); the camera is at the back focal plane of the larger diameter lens (L2). The ratio of the focal lengths (f_{L2}/f_{L1}) determines the magnification of the system. The effective light-collecting ability of the TL system is affected by the distance between the lenses to some extent, since the infinity focus does not result in perfectly parallel rays of light from L1 to L2. The actual working distance (L1 back surface to the sample) for a true TL configuration is limited by the particular standard lens chosen. The flange back focal length (distance from the L1 mounting thread to the sample) is 12.5mm for CS-mount lenses, 17.5mm for C-mount lenses and 46.5mm for standard F-mount (35mm

SLR) lenses. Hence, SLR lenses are preferred in a TL assembly. A disadvantage of the TL approach is the increase in the number of glass-air interfaces. This is undesirable because of the decrease in contrast these interfaces might cause due to reflections. Sophisticated compound lenses usually have >6 elements, and any small reflection (0.1-4%) at each of the more than 12 interfaces per lens can contribute to loss in light transmission and image contrast.

Finally, because of the difficulties in finding/designing high NA optics in the low magnification range, it is logical to attempt to directly project the image on the surface of the detector, minimizing separation and avoiding optical relay lenses. It is not practical, however, to have the surface of the photodetector chip in physical contact with the experimental sample, even through a glass coverslip, because of the obvious risk of damage. A practical alternative is offered by an optical fiber coupler - optical fibers arranged in a tight bundle of desired geometry, placed between the experimental sample and the photodetectors. There are standard optical fibers with a reasonably good NA=0.5 (corresponding to #F of 1). We demonstrated this idea by a custom-designed contact fluorescence imaging system (CFI)(Entcheva, Lu et al. 2000; Entcheva, Kostov et al. 2004), where each fiber was linked to an individual photodiode. Such CFI system has the following features: 1) provides a fixed 1x magnification; 2) takes advantage of the planar nature of a cultured cell monolayer; it has no equivalent of a focal plane; 3) solves some of the vignetting and spherical aberration problems and glass-air interface issues characteristic for lens-based approaches, because the light transfer is uniform across the FOV and fully determined by the individual optical fiber properties. Among the limitations of the CFI optical solution are the restriction to only transillumination type of excitation light delivery and the inability for easy change of spatial resolution / magnification.

III. Use and calibration of fluorescent probes for excitation

Two classes of fast-response fluorescent indicators have been developed in the last 30 years suitable for dynamic measurements of cardiac electromechanics - voltage-sensitive (or potentiometric) dyes and calcium-sensitive dyes. For action potentials measurements, the styryl dyes (di-4-ANEPPS, di-8-ANEPPS and RH-237), excitable by visible light, are most widely used for optical mapping in myocyte cultures (Windisch, Muller et al. 1985; Loew, Cohen et al. 1992; Rohr and Salzberg 1994). The fluorescence response of di-8-ANEPPS has been shown to change linearly with transmembrane potential in simultaneous optical and patch-clamp recordings (Bullen and Saggau 1999). Because of the "all-or-nothing" nature of the action potential (constant amplitude), calibration and conversion into millivolts is rarely conducted. Instead, the relative change in fluorescence ($\Delta F/F$) is typically reported. A drawback of the currently used potentiometric dyes is their poor signal-to-noise ratio – for macroscopic measurements in cultured cells, the fluorescence change is typically <5%. There is a clear need for voltage-sensitive dyes with improved response, and such efforts are underway (Efimov, Nikolski et al. 2004).

Along with action potentials, cycling in intracellular calcium is of great interest for better understanding of arrhythmogenesis. Calcium transients are not perceived merely as events unidirectionally controlled by the action potentials. Processes associated with cardiac calcium handling (triggered or spontaneous calcium release, and calcium uptake) can affect the time course and stability of the membrane potential (Chudin, Goldhaber et al. 1999; Eisner, Choi et

al. 2000; Guatimosim, Dilly et al. 2002). Optical measurements of intracellular calcium are facilitated in cell monolayers compared to tissue-level mapping because of the lack of extensive motion artifacts and no need for mechanical immobilization.

Fluorescent indicators for intracellular calcium (Takahashi, Camacho et al. 1999) offer a substantially better signal-to-noise ratio (up to a 1000-fold change in fluorescence upon Ca^{2+} presence) than the currently available voltage-sensitive dyes. They have evolved to cover a spectrum of excitation wavelengths (UV and visible light) and a range of calcium affinity (different k_d constants). For example, the UV-excitable indicator Fura-2AM can be used to distinguish very low levels (<50nM) because of its high Ca^{2+} affinity. This makes it the probe of choice for measuring subtle alterations in diastolic calcium. At the other end of the spectrum are the very low-affinity probes (k_d >1μM) , such as Fluo-4FF, Fluo-5N and Rhod-FF, which can be used if a large dynamic range of calcium concentrations is expected. These indicators are likely to operate in their linear range when physiological systolic calcium levels are encountered, thus they introduce minimum distortion and/or artificial prolongation of the transients due to saturation, the tradeoff being a mediocre SNR (Fast, Cheek et al. 2004).

Common problems in the interpretation of optical measurements of intracellular calcium for most Ca^{2+} indicators are dye loading (compartmentalization and uptake by mitochondria and sarcoplasmic reticulum, incomplete hydrolysis etc.) and *in vivo* calibration. The ratiometric calcium dyes (Fura-2 and Indo-1) exhibit different emission and/or excitation spectra for the free and Ca^{2+}-bound form. This feature allows ratiometric measurements, i.e. forming a ratio after fluorescence is measured at two different wavelengths – excitation ratio for Fura-2 and emission ratio for Indo-1. Such measurements are less sensitive to variations due to dye loading, illumination and other artifacts, and make possible the conversion into Ca^{2+} concentration. A method for two-point Fura-2 calibration was proposed by Grynkiewicz et al.(Grynkiewicz, Poenie et al. 1985) using values at zero and maximum calcium. Zero Ca^{2+} can be achieved after cell treatment with a calcium scavenger (such as EGTA), while saturating intracellular Ca^{2+} concentrations can be reached by a membrane-compromising agent (such as ionomycin), equilibrating intra- and extracellular Ca^{2+} concentrations. Typically, determining the fluorescence at maximum Ca^{2+} is problematic(Yin, Bien et al. 2004). Various calibration approaches have been attempted, including metabolic inhibition to minimize the active processes counteracting ion equilibration (Frampton, Orchard et al. 1991) and BDM treatment to prevent hypercontracture (Cheung, Tillotson et al. 1989), but with variable success.

A distinct difference between optical mapping in intact hearts and cell culture preparations is the method of dye labeling. In whole hearts typically the dyes are delivered via coronary system perfusion, whereas in monolayers the cells are bathed in dye solution with usually higher concentration than used in tissue preparations. As a result, the dye has a higher chance of getting trapped in the extracellular matrix, which may contribute to increased or uneven background fluorescence. Additionally, for intracellular probes, dye entrapment in various organelles seems to be more pronounced for cell monolayers. These differences in dye delivery may partially contribute to higher sensitivity to phototoxic damage (via release of reactive oxygen species) in cell monolayers vs. tissue. In the latter, healthier cells from the sub-surface layers have been suggested to play a protective role serving as a potential anti-oxidant source (Salama and Loew 1988).

The intimate understanding of normal and pathological processes in cardiac electromechanics ultimately requires simultaneous mapping of voltage and calcium. Previous dual dye measurements have used separation of the two signals by excitation, by emission or both. Dye pairs, successfully used in simultaneous measurements of action potentials and intracellular calcium include: di-2-ANEPEQ and Calcium green (Bullen and Saggau 1998); di-4-ANEPPS and Indo-1 (Laurita and Singal 2001); di-4-ANEPPS and Fluo-4 (Johnson, Smith et al. 1999); RH-237 and Rhod-2 (Choi and Salama 2000); RH-237 and Fluo-3/4 (Fast and Ideker 2000; Kong, Walcott et al. 2003). In some of these experiments, the dye spectra and their overlap were of primary interest, thus measurements were not co-localized in space and/or time (Johnson, Smith et al. 1999; Kong, Walcott et al. 2003). Our lab has had success with dual imaging in cultured myocyte layers with no crosstalk using di-8-ANEPPS and Fura-2, where measurements require a broad excitation and optical separation of emission.

IV. Illumination solutions for the cultured cell setting

Due to the transparent flat nature of the cultured cell preparation, two modes of illumination are possible. In *transillumination*, the detector and the light source are at opposite sides of the sample, while in *epi-illumination* mode the delivery of light and the collection of light are on the same side of the sample. Transillumination is a simple solution, typical for work with cultured cells (in fact, is the only solution compatible with CFI), and does not require beam splitters. It can be accomplished by one or more light guides brought to the sample at some angle (avoiding direct coupling into the detector). Problems associated with transillumination are: achieving consistent positioning from experiment to experiment, uniform sample illumination and effective filtering of the delivered light by the emission filter, since interference emission filters perform best when the rays are perpendicular to their surface. Uneven illumination combined with the small response of the voltage-sensitive dyes can result in a substantially reduced dynamic range and can obscure the signals of interest.

Epi-illumination allows the delivery of excitation light through an identical optical path as the collection of the emitted light. This mode of illumination is best served by the TL assembly, where a dichroic mirror (beam splitter) between the two lenses selectively reflects lower wavelengths (in the excitation light range) towards the sample and passes higher wavelengths (in the emitted light range) from the sample to the detector. In epi-illumination, the characteristics of the objective lens (its NA) factor in twice in the quality of the acquired image – via the efficiency of light delivery and the efficiency of light collection.

The intensity of the excitation light has to be optimized carefully. As low as 6mW/cm^2 (achievable by a couple of ultra-bright light-emitting diodes) has been shown to be sufficient for macroscopic fluorescence imaging(Entcheva, Kostov et al. 2004). Increasing excitation light intensity will increase the intensity of the emitted light, and hence will improve the signal-to-noise ratio. However, there is an upper limit - cell monolayers are particularly sensitive to dye photobleaching and phototoxicity, inducible by long exposures to a particularly intense excitation light.

From the traditional light sources, xenon (Xe) arc lamps and quartz-tungsten halogen (QTH) lamps are most often used in conjunction with cell culture imaging. They offer a continuous spectrum over the excitation range suitable for the current voltage-sensitive dyes

and some of the calcium-sensitive dyes (400-700nm) (Lackowicz 1999). The QTH lamps cannot provide UV illumination required for a class of Ca^{2+} sensitive dyes, and have a limited output below 450nm. Semiconductor-generated illumination (ultra-bright LEDs and laser diodes) has only recently become a viable alternative(Entcheva, Kostov et al. 2004), offering a wide range of wavelengths, including those of interest for fluorescence measurements in living cells. LED illumination is a more cost-effective, energy efficient, portable and flexible solution. Computer (TTL-level) control is possible for easy on/off switching and also for high-frequency light modulation. This feature can provide the means for synchronized (lock-in) detection and/or for fast wavelength switching, thus allowing excitation ratio imaging or dual label imaging. High intensity LED illumination appropriate for fluorescence measurements in cultured cells is currently offered by a number of companies – from simple lower current LEDs by Nichia to higher current higher intensity LED lamps by Lumileds.

V. State-of-the-art detector technology

The most important component of an optical mapping system is the detector. There are currently a limited number of suitable detectors in use or of potential interest for fast multisite optical measurements in cardiac preparations. These include: photodiode arrays (PDA), charge-coupled device (CCD) cameras and complementary metal-oxide semiconductor (CMOS) cameras. Since cell cultured systems have special requirements for increased sensitivity (as compared to tissue measurements), two derivative versions of cameras with increased sensitivity are also of interest: 1) on-chip electron multiplication CCDs (or EMCCDs); and 2) intensified camera systems (I-CCD/CMOS). EMCCDs rival in sensitivity the older technological solution, where a camera (CCD or CMOS) is coupled to an intensifier.

Choosing a detector system is a multiparameter optimization problem. We have mapped the five categories of detectors mentioned above onto a three-parameter space, including temporal resolution, spatial resolution and sensitivity (**Figure 7-4**). This qualitative diagram reflects the trends in the current day detectors; it is only to be used as a crude detector selection guide. *Spatial resolution* is the number of pixels in a detector. *Temporal resolution* is defined as frames per second (fps), thus for practical purposes detectors with high spatial resolution appear much slower regardless of their per-pixel rate. Sensitivity is used here in a utility sense – the ability of a detector to produce useful signal at each pixel under optimal illumination conditions. The obvious pitfalls of such definition are that many important factors are not taken into account to equalize the performance metrics – mainly, pixels are not normalized by area.

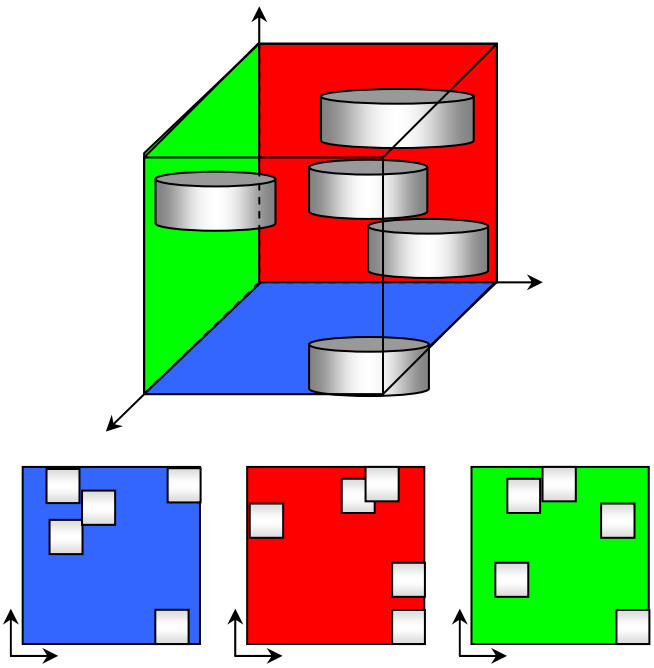

Figure 7-4 Current photodetector technology mapped onto a 3D parameter space of temporal resolution (T), spatial resolution (S) and sensitivity (Sen).
Represented are 1) PDA, 2) CCD, 3) CMOS, 4) EMCCD, and 5) I-CCD/CMOS detectors. See text for details.

In more strict technical terms, the *sensitivity* of a detector is directly affected by three classes of noise: *dark current noise* (Δn_D), *shot noise* (Δn_S) and *readout noise* (Δn_R) (Wu, Lam et al. 1998; Tominaga, Tominaga et al. 2000):

Eq. 7-3) $$noise = \sqrt{\Delta n_D{}^2 + \Delta n_S{}^2 + \Delta n_R{}^2}$$

The *limit of detection* of a system (and the lower bound of its effective *dynamic range, DR*) is determined by the intersection of the floor noise – a combination of Δn_D and Δn_R - and the shot noise (a function of the signal intensity). For imaging in cell monolayers with barely detectable fluorescence signals, special attention should be paid to reduce the floor noise. The readout noise starts contributing significantly when the per-pixel rate (clock rate) of the detector becomes too high (exceeds 5MHz, for example), which is the case for most ultra-high resolution detectors. At the same time, the higher the clock/acquisition rates, the smaller the dark current noise (due to thermal and other factors), hence multi-pixel cameras have lower Δn_D than PDAs. The shot noise reflects random variations in the signal itself due to the quantum nature of light, and scales up with the square root of the signal intensity. For example, 10 times higher intensity of the signal will result in about 3 times better signal-to-noise ratio (SNR) during imaging ($10/\sqrt{10}$). The dynamic range of the detector is particularly important for measurements with voltage-sensitive dyes which have relatively high background fluorescence but a very small dynamic change in fluorescence. The upper bound of the

effective DR of a detector is determined by the pixel *well depth/capacity* (maximum per-pixel charge before saturation). For practical reasons, large well depth (resulting in a higher effective DR) is synonymous with a large light-gathering area, i.e. large pixels. The bit resolution of the photodetector (8 to 16 bits, typically) is informative in terms of theoretical DR, only if the floor noise of the system is known and a fixed bin size is considered. For all practical purposes, the effective DR (as discussed above) is more instructive for the performance of the detector. Another important parameter to consider is the *quantum efficiency, QE,* of the detector, indicating what portion of the photons reaching the detector surface is converted into a measurable signal. For very low light levels (such as in cell monolayers), high acquisition rates and small pixels, it is not uncommon that <10 photons hit a pixel per frame. For a QE of 50%, this will result in SNR of only about 1.3 (Andor).

For measurements in cell culture, photodiode arrays (PDA) are most widely used, including a commercially available 16x16 PDA from Hamamatsu and custom-made PDAs with up to 500 detectors from WuTech(Wu, Cohen et al. 1999). Flexible spatial arrangements can be obtained by custom-developed systems where tightly packed optical fibers are coupled to individual photodiodes (similar to the WuTech solution)(Rohr and Kucera 1998; Entcheva, Lu et al. 2000; Iravanian, Nabutovsky et al. 2003). Currently, PDAs dominate optical mapping in cell culture because they produce signals with good SNR, and provide good temporal resolution. In addition, the PDAs can be operated in AC-coupled regime and background "bias" can be subtracted to stretch the changes in fluorescence across the full dynamic range. This feature is particularly important for voltage-sensitive dyes with high resting level fluorescence and little dynamic changes. PDA's high sensitivity is largely a result of the big pixels - they integrate fluorescence over areas of about 1 mm^2 or more in CFI regime(Entcheva, Lu et al. 2000), while for a comparable magnification camera systems rarely exceed pixel size of 10^{-2} mm^2 without binning (spatial averaging of pixels). The limited spatial resolution is the main disadvantage of the PDA systems, since it becomes impractical and cost-ineffective to expand such arrays beyond 500 photodiodes.

CCD systems, which dominate whole heart optical mapping (Baxter, Davidenko et al. 1997; Lin, Abbas et al. 1997; Gray, Pertsov et al. 1998; Witkowski, Leon, Penkoske, Clark et al. 1998) are currently not widely used for cell culture imaging. The main benefit of CCD camera imaging is the higher spatial resolution. Yet, in the extremely low light level conditions typical for cell monolayers, current day CCDs fail to produce useful signals on a single pixel level at high rates, despite their lower dark current noise. The much smaller pixel size (compared to PDAs) is the major difference. Spatial binning can improve the image, but resolution is lost. In addition, the increased number of pixels per frame (from a typical 256 pix for a PDA to >10000 pix for a CCD) comes with a cost – reduced temporal resolution or increased readout noise. On the market, there are currently very few CCDs which attempt to combine high spatial and high temporal resolution, yet yield useful image. The manufacturers typically optimize one or the other. Successful examples of use of CCD detectors for imaging cell culture typically involve the better performing calcium-sensitive dyes (Bub, Glass et al. 1998). Yet the acquisition rates in these measurements have been sub-optimal. Our own experience includes signals from the RedShirt 80x80 camera, SciMedia MiCAM, pco1600 and Dalsa 128. The tests were not performed at the same light conditions and optics, and the cameras vary in resolution, thus is not straightforward to rank their performance.

CMOS imagers have been usually omitted or briefly mentioned in most reviews on optical mapping in excitable tissue. However, they seem to meet the demands for combined high spatial and temporal resolution. The speedup is achieved by higher level of parallelism compared to CCDs – the serial readout in the CCDs is substituted with individually addressable pixels and per-pixel electronics in the CMOS. The trade-off is a significantly lower sensitivity compared to CCDs. This drawback can be overcome by using a very large well depth (pixels as big as 25x25μm). Technological innovations in the geometry of the CMOS photo elements also include reduction in electrical surface leakage, which reduces the dark current noise. We have tested several of these new CMOS cameras – the Silicon Imaging 1024F (1024x1024 pix), SciMedia Ultima 100x100 pixels, and pco1200 (1280x1024 pix). At high illumination levels and optimized optics, all three cameras have a potential as photodetectors in cell culture. The CMOS cameras are, in general, inexpensive or less expensive than CCDs. However, the specialized large pixel CMOS cameras, with added memory and processing capabilities, are currently forming a sub-category and are selling for a rather high price. While the CCD technology might be approaching its performance limits, especially in the temporal domain, CMOS technology is on the rise and expected to improve further by maximizing the fraction of the light-collecting area on the chip using back-illumination or other methods. Because of technological compatibility with traditional electronics, CMOS sensors can also incorporate image processing as part of the sensor, which is expected to make them more competitive than CCDs in optical mapping.

Ways to improve the performance of the cameras include back-illumination, cooling and addition of intensifiers. Back-illumination is used to improve the QE of the cameras. It involves thinning (etching away) the crystalline silicon substrate along the path traveled by the emitted photons towards the sensing elements, which reduces the loss of photons due to absorption, hence increases QE. Cooling reduces the thermal noise – a major contributor to the dark current noise. When the detectors are operated at high clock rates (low exposure times), improvements in SNR by cooling are not substantial. Image intensifiers improve sensitivity but are generally perceived as noise-introducing and possibly resolution-limiting components in the optical system. They require special handling because of their proneness to damage by direct light. Yet, they are widely used (and needed) for extremely low light level conditions, such as single molecule detection studies. The weak fluorescent signals from a single layer of cells fall into the category of very low light conditions. An intensified CCD system (2 stage intensifier) has been used before in optical mapping of the whole heart (Witkowski, Leon, Penkoske, Clark et al. 1998). We have used a Generation II single-stage intensified MTI-DAGE camera at 60fps with a spatial resolution 320x240pix to image voltage and calcium signals in cultured cells(Bien, Yin et al. 2003; Entcheva, Bien et al. 2004) and Generation III intensified pco1200 CMOS camera at 200fps.

In image intensifiers, first a photocathode converts image photons into e^-, then 1 to 3 multi-channel plates (MCP) guide the e^- multiplication in small channels under high voltage, after which the resultant e^- cloud is steered across a small spatial gap towards a phosphorous screen, which converts the multiplied e^- back into photons (see Chapter 8th in (Inoue and Spring 1997) and (Molecular) for additional information). A fiber optic guide (1:1 or tapered as needed) accomplishes the final transfer of the image at the phosphor screen onto the camera chip. The temporal resolution of an intensifier is limited by the life time of the particular

phosphor used – the common P43 has a life time of about 1ms, while P46, 47 have a sub-microsecond life time. The spatial resolution is mostly limited by the size of the electron cloud per channel, reaching the phosphor screen; current Gen III intensifiers offer at least 64 line-pairs per mm (analogous to 15.6μm effective pixels at 1x magnification). The QE in intensified systems refers to the percentage of the entry photons that are transformed into electrons reaching the MCP; it is as high as 50% for Gen III intensifiers without a protective MCP films. When combined with a fast CCD or CMOS, intensified system can provide enough sensitivity for imaging in cell culture.

A more modern concept for increasing sensitivity is used in the cameras with on-chip electron multiplication, known as EMCCDs (Denvir and Conroy; Robbins and Hadwen 2003) or charge-carrier multiplication (CCM) cameras(Hynecek 2001; Hynecek and Nishiwaki 2003). These are all-solid-state devices, unlike the intensifiers described above; they utilize the process of impact ionization (an avalanche process) before the acquired values are converted into voltage. A fully chip-incorporated "gain register" provides electron multiplication in a serial process involving the application of high electric fields. The major EMCCD benefits include: 1) lower readout noise at higher speeds (which is a common problem for fast CCDs); 2) lower multiplicative noise (involved in the amplification of the original signal plus the shot noise); 3) improved QE compared to intensifiers; 4) minimized image artifacts and distortion (as sometimes seen in intensified systems). A drawback is the decrease in the dynamic range at high gains. Some new EMCCDs, among which Andor Ixon 512 and Roper 512 back illuminated cameras, show promise as high resolution cameras for cell monolayers. However, the EMCCDs currently are rarely driven at >10MHz per pixel, which limits the combined increase in spatial and temporal resolution; chips with higher clock speeds are under development. The EMCCDs face even higher limitations (than CCDs) in terms of achievable per-pixel rates (and hence - improvement in temporal resolution), because switching of higher electric fields is needed at high gains. Nevertheless, in the long run these photodetectors show the highest promise for fast imaging at very low light levels, encountered in mapping of voltage and calcium waves in cultured cells.

VI. High data throughput challenges

With the need to image at a higher spatial resolution while maintaining useful speeds and field of view, the data throughput increases to colossal proportions, not encountered in previous systems for whole heart imaging. This requires special technical solutions at the camera-computer interface. To illustrate the disparate scales of data throughput, in **Table 7-1** we compare the data streams for several typical optical mapping systems, based on commercially available detectors. The data throughput (in Mbytes/sec or MB/s) is calculated as the product of temporal and spatial resolution, scaled by the dynamic range (1 or 2 Bytes per pixel). The observed values span over more than three orders of magnitude in desired bandwidth: 0.6 to 1310 MBs.

A common solution to the high data flow problem is the addition of on board memory for immediate data storage and data transfer to disk afterwards. This memory can be incorporated directly in the camera head (CamRAM) or can be added to the specialized camera-computer interface boards, known as frame grabbers. For example, 4GB on board memory for the pco CMOS camera (used ingenuously by special data packing), allows the

recording of 78sec of data at 200fps for VGA-equivalent region of interest. Such a solution is not practical for continuous recordings >5 min in duration due to prohibitive RAM size required. Alternatively, data can be streamed directly to the RAM of the computer via Direct Memory Access (DMA), where the process will be limited by the expandability of the computer RAM. For 32bit processor systems the limit is 4GB. But 64bit memory-addressing schemes and ultimately 64bit processor systems will be able to offer RAM capacity well in excess of the 4GB limit, and might become the solution of choice for direct data streaming in the future.

	System description	Data throughput	Bit resolution	Temporal resolution	Spatial resolution (pixel size)
1	Hamamatsu 16x16 PDA at 1kHz	0.6 MB/s	>8bit	1000 fps	16x16 pix (950μm/pix)
2	Hamamatsu 16x16 PDA at 10kHz	6 MB/s	>8bit	10000 fps	16x16 pix (950μm/pix)
3	WuTech 500 PDA at 5kHz	5 MB/s	>8bit	5000 fps	500 pix (*)
4	Andor/Roper EmCCD 512 at 30fps	3.9 MB/s	>8bit	30 fps	512x512 pix (16μm/pix)
5	Andor EmCCD 128 at 400fps	13 MB/s	>8bit	400 fps	128x128 pix (24μm/pix)
6	Dalsa CCD 128, 8bit, at 1000fps	16.4 MB/s	8bit	1000 fps	128x128 pix (16μm/pix)
7	RedShirt CCD 256 at 100fps	13 MB/s	>8bit	100 fps	256x256 pix (26μm/pix)
8	RedShirt CCD 80 at 2000fps	25.6 MB/s	>8bit	2000 fps	80x80 pix (24μm/pix)
9	Cooke CCD 1600x1200 at 33fps	126 MB/s	>8bit	33 fps	1600x1200 pix (7.4μm/pix)
10	SciMedia CMOS Ultima 100x100 at 1000fps	20 MB/s	>8bit	1000 fps	100x100 pix (100μm/pix)
11	SciMedia CMOS Ultima 100x100 at 10000fps	200 MB/s	>8bit	10000 fps	100x100 pix (100μm/pix)
12	pco CMOS 1280x1024 at 200 fps, VGA region of interest (ROI)	123 MB/s	>8bit	200 fps	640x480 pix (12μm/pix)

	System description	Data throughput	Bit resolution	Temporal resolution	Spatial resolution (pixel size)
13	pco CMOS 1280x1024 at 500fps	1310 MB/s	>8bit	500pfs	1280x1024 pix (12μm/pix)
14	**"Ideal" Detector** at δt=10μm, δx=5ms (200fps), FOV=2cm (based on wavelength = 0.1s*20cm/s)	**1.6 GB/s**	>8bit	200pfs	2000x2000 pix (10μm/pix)

(*) pixel size depends on the fiber size used in CFI, typically is >500μm/pix.

Table 7-1 Comparison of data throughput produced by some optical mapping systems in use

Can a sustained recording speed of >150MB/s (required by the ultra-high resolution cameras) be achieved with the current computer technology? A diagram of the relevant camera-computer interface components is given in **Figure 7-5**, where the data transfer bottlenecks are circled in red. These include: 1) the camera-computer interface capacity, 2) the internal computer bus bandwidth, and 3) the writing speed to the hard drives.

Detector-Computer Interface	Sustained Speed (MBs)
USB2	40-50
IEEE1394b (Firewire)	50-60
1Gbit Ethernet	128
CameraLink	>200-500
10Gbit Ethernet	1280

Table 7-2 Camera-computer interfaces for fast data transfer

The data transfer from the camera to a computer is done via a standard or specialized *camera-computer interface*. Frame grabbers represent such specialized interface boards. **Table 7-2** lists fast standard interfaces and the sustained rates of data transfer that they can support. While Firewire and USB2, which are routinely included in most current computers, can meet the needs of lower resolution cameras, only the newer CameraLink (from the specialized interfaces) can support real time data transfer for the ultra-high resolution cameras (National). CameraLink is a data transfer protocol using a general purpose interface known as Low Voltage Differential Signaling (LVDS) (PULNix America). Several companies, including National Instruments and Coreco Imaging offer CameraLink frame grabbers. At the high end

of data throughput (see **Table 7-1**), even this high speed standard fails. Future developments using 10Gbit Ethernet interface have the potential to virtually lift the restrictions in bandwidth at the camera-computer interface.

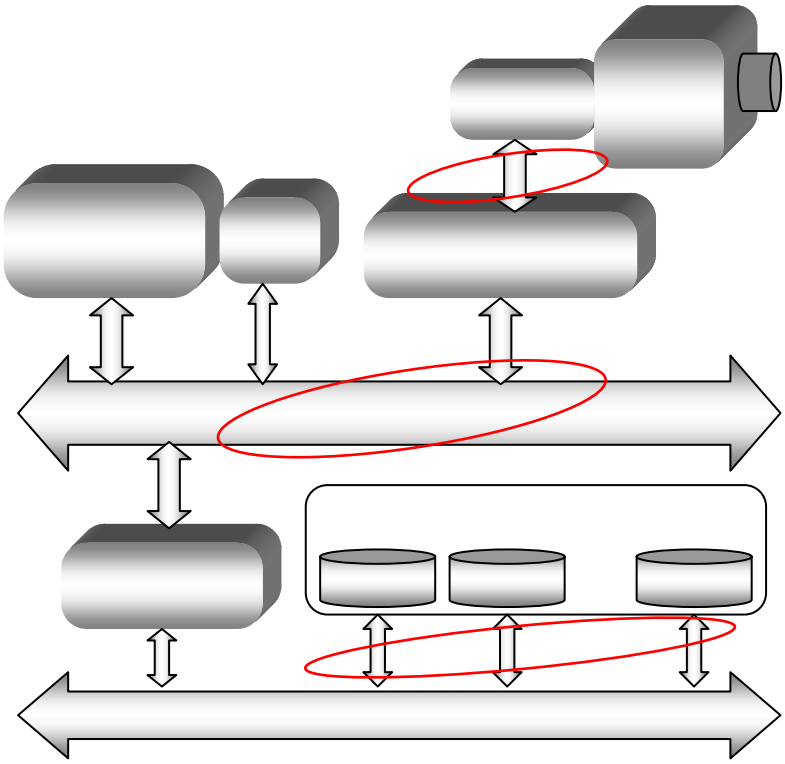

Figure 7-5 Camera-computer interface.
Bottlenecks in data transfer and data storage are circled in red.

The second bottleneck (**Figure 7-5**) is the maximum data transfer rate supported by the internal *communication bus* in the computer. Most frame grabbers use the Peripheral Component Interconnect bus (known as the PCI bus). Several versions of the PCI bus are in use today, offering different speeds (**Table 7-3**) (Group; Wilen, Schade et al. 2002). The current standard, 32bit PCI (sustained rates <100 MB/s), is incapable to meet the demands of ultra-high resolution cameras. Only higher-end desktop computers today offer 64bit versions of the PCI bus. The new standard, PCI-Express, was introduced in 2002, and desktop computers incorporating this very high bandwidth bus just start to appear on the market (end of 2004).

A bottleneck in **Figure 7-5**, which is most difficult to overcome in order to transfer data in real time for ultra-high resolution cameras, is the speed of *writing to a storage device* (hard drive disk, HDD). Common standardized protocols for data transfer to hard drives include ATA, SATA, SCSI, and Fiber Channel (FC) (Corporation; Intel). ATA combines several parallel bus protocols for communication with HDDs, and offers a capacity of up to 100 MB/s sustained rate. It was recently replaced with a serial, faster and easier to configure version, SATA, which features up to 150 MB/s data transfer rates. Configuring a system with ATA or SATA devices

is relatively inexpensive, but the available HDDs compatible with this protocol can only reach sustained writing speed of about 50 MB/s. This is insufficient to use them in real time systems with ultra-high resolution cameras (see **Table 7-1**). A more robust option is the SCSI (Small Computer System Interface) parallel protocol. The current standard Ultra 320 SCSI bus can sustain up to 320 MBs. The SCSI HDDs are more intelligent devices (require less processor intervention) and operate at 10000rpm or 15000 rpm, which translates into 60-70 MBs sustained writing rates per drive (speeds not achievable in SATA drives). Additional attraction of the SCSI solution for storage is extensibility. Up to 15 SCSI drives can be connected to a single-channel SCSI controller, supporting RAID (Redundant Array of Inexpensive Drives) (Patterson, Gibson et al.; Katz, Gibson et al. 1989). In particular, RAID-0 regime allows for very high data transfer (limited by the SCSI bus speed – 320 MB/s) by "stripping" the data to multiple SCSI HDDs in parallel operation (no redundancy). FC drives can also be used in a similar RAID-0 configuration. Such parallel HDD operation seems to provide the best solution for handling the high data throughput in real time (**Figure 7-5**). The tradeoff for the better speeds obtained in RAID-0 regime is the reduced safety in data storage and increased risk for failure as the number of parallel drives increases. Therefore, this solution has to be used only for real time data streaming but not for permanent storage.

Parallel Bus Types (PCI)	Burst Speed (MBs)	Sustained Speed (MBs)
32bits PCI	133	<100
64bits 66MHz PCI	530	>200
64bits 133MHz PCI-X	>1000	>300
64bits PCI-Express (PCI-E)	300-15000	250-4000

Table 7-3 Computer parallel bus speeds

VII. Theoretical considerations for an ideal optical mapping system

Having discussed the capabilities of current imaging technology, in this section we pose the question – how close are we to what can be defined as a "minimal" and as an "ideal" optical mapping system? The theoretical considerations below provide the basis for answering this question.

Minimum requirements

The constraints in choosing the parameters for an optical mapping system are set by the phenomenon/object characteristics, *O*. Important characteristics of the phenomenon/object under observation to be considered for imaging include: 1) the minimum duration of an event of interest (w), which sets the limits for temporal sampling; 2) the minimum radius of wavefront curvature before failure of propagation, setting the limits for the spatial resolution in

2D and 3D; and 3) the conduction velocity (θ), known to be a function of the radius of curvature of the wavefront (Fast and Kleber 1997). The object-determined constraints are:

Eq. 7-4) $$O = \{w_{\min}, r_{\min}, \theta(r)\}$$

The optical system parameters to be optimized are reduced to an essential subset *S*, including: 1) temporal resolution (δt), spatial resolution (δx), and number of pixels (N) to secure a desired FOV. It is assumed that for isotropic tissue, δx and *n* will be applicable for both spatial axes: *x* and *y*.

Eq. 7-5) $$S = \{\delta t, \delta x, N\}$$

The parameters in *S* are linked via the mapped field of view (FOV) as follows:

Eq. 7-6) $$FOV = N \times \delta x$$

Eq. 7-7) $$FOV \geq k \times \delta t \times \theta \text{ , } k \geq 2$$

Eq. 7-7 links space and time, and expresses the requirement to have at least two isochrones (lines connecting points with the same time of activation) within a chosen FOV. Combining equations Eq. 7-5 and Eq. 7-6, one can derive the following relationship, linking the three original parameters of the system, *S*, so that they form a constant-θ 3D surface:

Eq. 7-8) $$\frac{N \times \delta x}{\delta t} \geq k \times \theta$$

Furthermore, considering the most demanding case for temporal sampling, which occurs for the shortest observable event of interest, w_{min}, and the most demanding case for spatial sampling, which occurs for the critical wavelength curvature, r_{min}, we obtain:

Eq. 7-9) $$k \times \delta t \leq w_{\min}$$

Eq. 7-10) $$k \times \delta x \leq r_{\min}$$

From Eq. 7-7, Eq. 7-8, and Eq. 7-9, a 3D hyperbolic surface is obtained that encompasses the parameter space for an optical system capable of capturing propagation in a cardiac preparation with known typical and minimum characteristics. The parameters of an optical mapping system have to fall on the upper side of the plotted minimum parameter surface, satisfying the Nyquist sampling criterion in space and time:

Eq. 7-11) $$N \times \delta x \geq k \times \delta t \times \theta_{typ} \geq w_{\min} \times \theta_{typ} \text{ , } k=2$$

Examples of such hyperbolic constant-θ 3D surface, satisfying Eq. 7-11), are shown in **Figure 7-6** for variable conduction velocities, assuming w_{min} of 20ms. It is seen, that most of the current detectors in use do meet these minimal criteria (are on the upper side of the 3D surfaces). The spatiotemporal characteristics of the sample under observation can vary, i.e. the duration of the events of interest can vary according to the restitution (frequency-dependent) properties of the tissue. The conduction velocity can also exhibit restitution-dependent variations, as well as changes due to the wavefront curvature (Fast and Kleber 1997). The choice of specific parameters for optical mapping has to take into account the worst case scenario for these sample characteristics.

Spatiotemporal resolution for an ideal mapping system

Registering the existence of a propagating wave (using the minimum requirements above) is a much less restrictive condition than requiring the full capture of spatiotemporal events of cardiac propagation in their complexity. This new, more restrictive, set of requirements is discussed below.

The *physical limits* for optical mapping are determined by the properties of the fluorescent dyes available. For the voltage-sensitive dyes, these limits are: $\delta x_{phys}>0.5\mu m$ (optical limits of resolution) and $\delta t_{phys}>5\mu s$ *(f<200 kHz),* due to the dye response time limitations (Grinvald and Hildesheim 2004). Note that imperfect optics can make these limitations more stringent.

Temporal resolution, δt

By physiological constraints, cardiac electrical events are not instantaneous in time. Cardiac activation includes a very fast upstroke but always followed by some refractory period, during which a new event is not possible. If the goal of optical mapping is to elucidate spatiotemporal phenomena, but not necessarily preserve the exact morphology of the activation events, then it is sufficient to consider the highest possible frequency of events. For mammals, this frequency varies between 0.5 and 12Hz in normal rhythm(Noujaim, Lucca et al. 2004). Ventricular fibrillation (VF) admittedly represents the high frequency limit for activation. Previous reports for VF frequency fall mostly in the 8-20Hz range (Gray, Pertsov et al. 1998; Witkowski, Leon, Penkoske, Giles et al. 1998; Berenfeld, Mandapati et al. 2000; Zaitsev, Berenfeld et al. 2000; Choi, Nho et al. 2002; Wu, Lin et al. 2002), but for small mammals (mice) frequencies up to 50Hz can be reached. Considering conservatively, the highest frequency of events to be twice that high limit – i.e. 100Hz ($\delta t=10ms$), we need a minimum sampling frequency (maximum time step, δt) of *200Hz* ($\delta t_{max}=5ms$). For the proposed temporal resolution (200Hz), when a minimum FOV of 1cm and a maximum θ of 30cm/s for a cultured cell system are considered, at least six isochrones in the FOV would be guaranteed. It has to be understood, that this temporal resolution assures that no event would be missed, but it does not guarantee reconstruction of the exact temporal profile of the events.

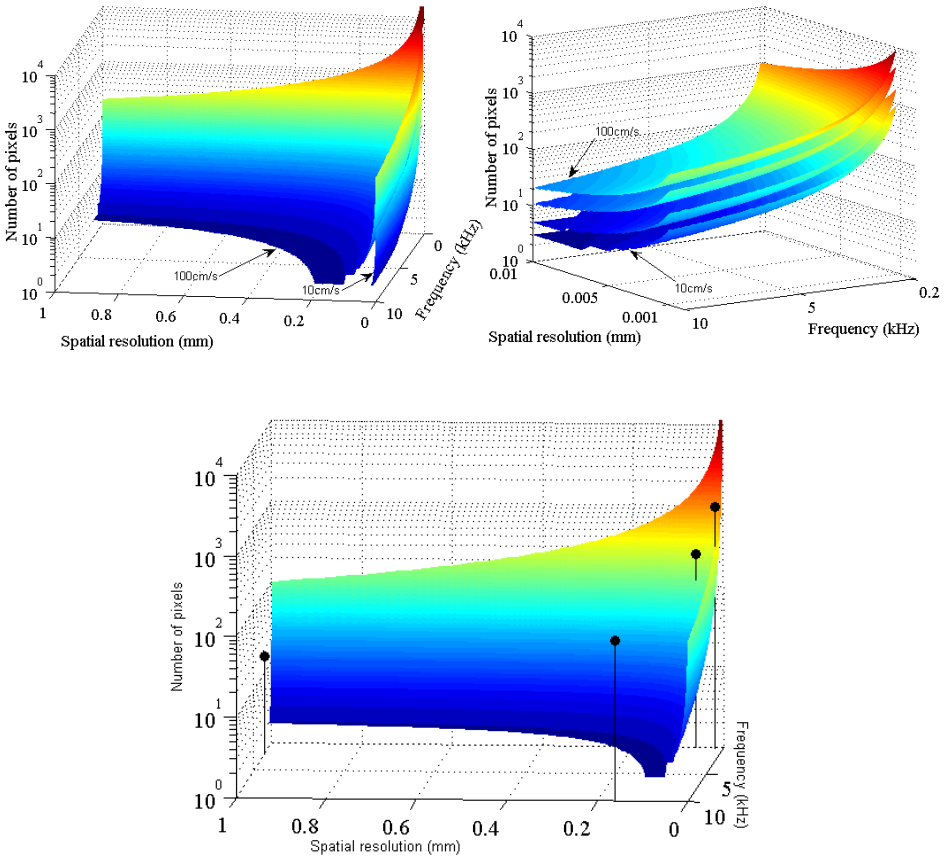

Figure 7-6 Minimum 3D surface for an optical mapping system.
The three axes include: spatial resolution, temporal resolution (frequency) and total number of pixels. **A.** View at the minimum requirements surface for imaging samples with conduction velocity of 10cm/s and 100cm/s; **B.** A closer view at the constant-θ 3D surfaces in the range of relevant spatial and temporal resolution; **C.** The minimum requirement 3D surface for θ=50cm/s plotted along four current detectors (black dots). The selected detectors are: 1) 16x16 PDA at 1kHz; 2) 512x512 CCD at 0.1 kHz; 3) 1200x1024 CMOS at 0.2kHz; and 4) 100x100 CMOS at 10kHz, – all satisfied the minimum requirements (appear on the upper side of the surface).

Spatial resolution, δx

While the temporal limits of electrical events of interest (action potentials and calcium transients) are well studied and understood, the spatial limits relevant to propagation are much harder to define. What is the smallest space in which discrete events affecting propagation can take place? This question goes at the heart of the philosophical debate about continuous vs. discrete nature of cardiac propagation.

On the one hand, cells in the heart are very well coupled (Jongsma and Wilders 2000), and for practical purposes, heart tissue is viewed as a syncytium. In this representation, the lower limit for the spatial scale of events of interest should be functionally linked to the

wavelength, most likely through a critical geometrical parameter for propagation – the *radius of critical curvature* before propagation failure. Knowledge of this sample characteristic is informative in setting the lowest spatial resolution for the mapping system. Winfree examined the scale of events (Winfree 1997; Winfree 1998), viewing the heart as a classical reaction-diffusion system. His analysis of the radius of critical curvature yielded a number in the range of 300μm for a system satisfying the continuum requirement, i.e. having a diffusion coefficient $D>1mm^2/s$ (Winfree 1998)). This critical curvature of the wavefront has been probed experimentally in studies dealing with point stimulation, propagation through an isthmus or spiral wave propagation (Cabo, Pertsov et al. 1994; Knisley and Hill 1995), well summarized in a review by Fast and Kleber (Fast and Kleber 1997). These experimental results showed that the radius of the critical curvature can be as low as 100μm, but the exact number is still not known.

On the other hand, the discrete nature of cardiac propagation events has been exemplified in theoretical (Spach and Heidlage 1995; Spach, Heidlage et al. 1998; Spach, Heidlage et al. 2000) and experimental studies. Discrete propagation is more relevant to pathological conditions, which are of interest in these optical mapping studies. Imaging at progressively smaller spatial scales reveals that complex spatial patterns can occur at the microscale (Kucera, Kleber et al. 1998; Rohr, Kucera et al. 1998; Sharifov, Ideker et al. 2004), or even subcellularly (Cheng, Lederer et al. 1996; Ishida, Genka et al. 1999; Kurebayashi, Yamashita et al. 2004) when calcium concentration is concerned. Slowly propagating calcium waves (conduction velocities 40-100μm/s (Lipp and Niggli 1993; Ishida, Genka et al. 1999)) can have 3-4 orders of magnitude smaller wavelengths than macroscopic events of interest and can indeed be confined within a single cell. Because of the tight link between calcium and transmembrane voltage, such microscopic events might turn out to be of critical importance to understanding arrhythmias. Maintaining macroscopic FOV, and taking into account subcellular events, sets very high requirements for the spatial resolution of an ideal optical mapping system. Even if only two points (Nyquist) are sampled within a cell (along its shorter side), this demands spatial resolution of δx_{max}=10μm over an area >1cm (i.e. >1000 pixels along each dimension). Choosing subcellular spatial resolution might not be appropriate for tissue-level imaging, because of the resolution limit set by extensive light scattering. However, in cell monolayers, non-specific light contribution from scattering is considerably less, allowing us to explore cardiac wave dynamics with finer spatial resolution.

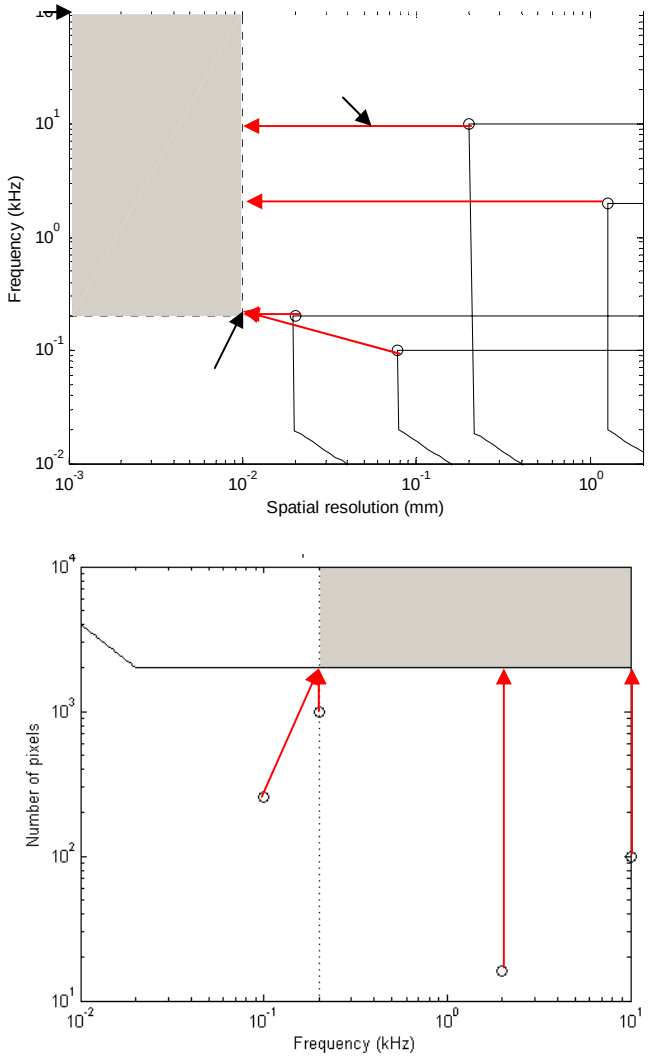

Figure 7-7 Parameter space for an "ideal" optical mapping system (the gray box).
A. The spatial and temporal resolution of a system to image a FOV=2cm were considered here; the distance Δs for the four selected detectors from Figure 6 is shown; **B.** An alternative plane is shown (FOV and temporal resolution), under fixed 10μm spatial resolution; the same four detectors are placed in this plane.

Overall, in the choice of an "ideal" optical mapping system, the available resources (Eq. 7-12) rather than system parameters, become a limiting factor. Requirements for fine spatial resolution are particularly demanding since they factor twice in the bandwidth required for two-dimensional imaging. The resources, *R*, involve factors external to the optical system, such as the information storage capacity, *IC [Bytes],* and the bandwidth, *B [Bytes/sec]*. These are closely linked to parameters of the optical system – number of pixels, *N*, and maximum recordable time-frames, *L*. The theoretical dynamic range (bit resolution of the detector), *DR*, is a scaling factor. IC and B impose real limits for ultra-high resolution detectors, which

operate at the maximum performance of current day computer technology, as discussed in section VI.

Eq. 7-12)
$$R = \{IC, B\} \quad \begin{cases} IC = DR \times N^2 \times L \\ B = \dfrac{DR \times N^2}{\delta t} \end{cases}$$

Current technology vs. the ideal mapping system

The parameter space of an ideal optical mapping system forms a polygon bounded by physical and rationally derived limits: $\{(\delta x_{phys}, \delta t_{phys}), (\delta x_{\max}, \delta t_{phys}), (\partial x_{phys}, \delta t_{\max}), (\delta x_{\max}, \delta t_{\max})\}$, **Figure 7-7.** Having set specific requirements for the temporal and spatial resolution of the ideal mapping system, we can assess the potential of current technology to meet these requirements. To quantify how close is a current detector to the parameter space of an ideal optical mapping system, we use a measure equivalent to the Euclidian distance in space. However, we do the calculations in 3D space-time, including two space dimensions and a time dimension, scaled for spatiotemporal events by the conduction velocity, as follows:

Eq. 7-13)
$$\begin{cases} \Delta s = 0 & , \quad (\delta x \le \delta x_{\max}) \wedge (\delta t \le \delta t_{\max}) \\ \Delta s = \sqrt{2} \times (\delta x - \delta x_{\max}) & , \quad (\delta x > \delta x_{\max}) \wedge (\delta t \le \delta t_{\max}) \\ \Delta s = \theta \times (\delta t - \delta t_{\max}) & , \quad (\delta x \le \delta x_{\max}) \wedge (\delta t > \delta t_{\max}) \\ \Delta s = \sqrt{\theta^2 \times (\delta t - \delta t_{\max})^2 + 2 \times (\delta x - \delta x_{\max})^2} & , \quad (\delta x > \delta x_{\max}) \wedge (\delta t > \delta t_{\max}) \end{cases}$$

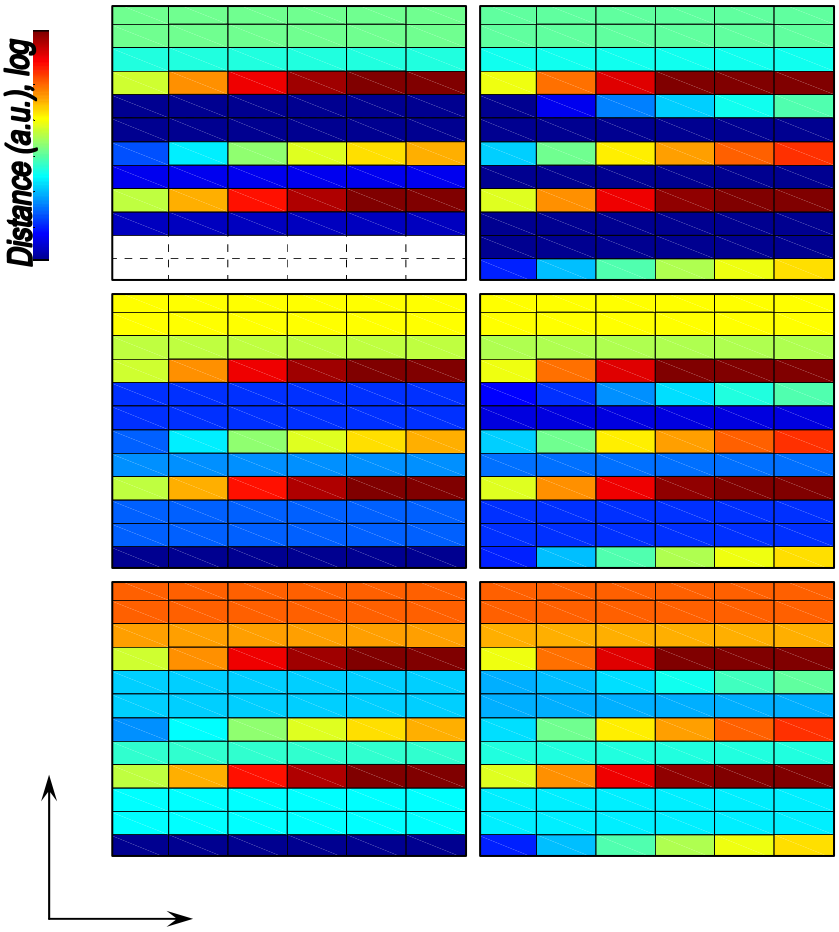

Figure 7-8 Distance of current detectors from the "ideal" mapping system in the parameter space.
The color represents distance from the "ideal" system as calculated by Eq. 7-13 ($\log_{10}$ scale was used; white is zero distance). Each of the six images is a 12x6 matrix, where rows correspond to detectors 1-11 and 13 from Table 7-1, and columns represent 6 conduction velocities in the range 5-50cm/s. Top, middle and bottom image rows correspond to FOV of 1cm, 2cm and 4cm, respectively. The left image column presents the distance of the selected detectors to an "ideal" system having temporal resolution of 200Hz and spatial resolution of 10□m; the right image column presents the distance of the selected detectors to a system with temporal resolution of 1kHz and spatial resolution of 50μm.

Figure 7-8 presents some results for the shortest distance (Δs) from current detectors (**Table 7-1**) to the parameter space of two "ideal" systems – one with the already justified minimum requirements (200Hz, 10μm, left column) and another one with relaxed spatial resolution requirements but increased temporal resolution requirements (1kHz, 50μm, right column). The distance is measured according to Eq. 7-13, and presented in logarithmic format by color (white corresponds to Δs=0). Six maps are shown, each is 12x6, where rows represent 12 detectors from **Table 7-1**, and columns represent six cases of maximum expected

conduction velocity in the sample $\theta = \{5,10,20,30,40,50\,^{cm}/_{s}\}$. As the size of the desired FOV to be mapped increases from 1 to 2 and 4cm (top, middle and bottom), all detectors get further away from the ideal polygon, because of deterioration of their spatial resolution. At the same time, the effect of increasing expected conduction velocity in the sample, affects most negatively the slow detectors (some CCD cameras), while PDAs are not affected by θ increase.

We present two examples of ultra-high resolution imaging with an intensified camera system (pco CMOS 1280x1024), entry 12 in **Table 7-1**. After background subtraction and stretching the values at each pixel to the full dynamic range, color maps of propagation were generated from the original images by converting intensity into phase values using the Hilbert transform (Bray and Wikswo 2002); wavefront was tracked by a black line. No spatial or temporal filtering was applied. First, **Figure 7-9** presents macroscopic imaging in a single layer of cells at 200fps and at 20μm/pix within a FOV>2x2cm. We demonstrate that for both, calcium-sensitive dye Fluo-4 and even voltage-sensitive dye di-8-ANEPPS, single pixel data (at 20μm) are useful. At room temperature experiments, the speed of 200fps is more than adequate to reveal details in cardiac propagation. Rigorous tests are needed to show whether this excessive spatial resolution (within a macro FOV) compared to any previous imaging study reveals essential information not attainable in other mapping attempts. We believe that this mode of imaging brings together the two disparate scales of events (micro and macro, from subcellular to tissue level) in a way that is beneficial and indispensable for validating theoretically proposed arrhythmia mechanisms and guiding therapeutic strategies by uncovering previously not considered aspects.

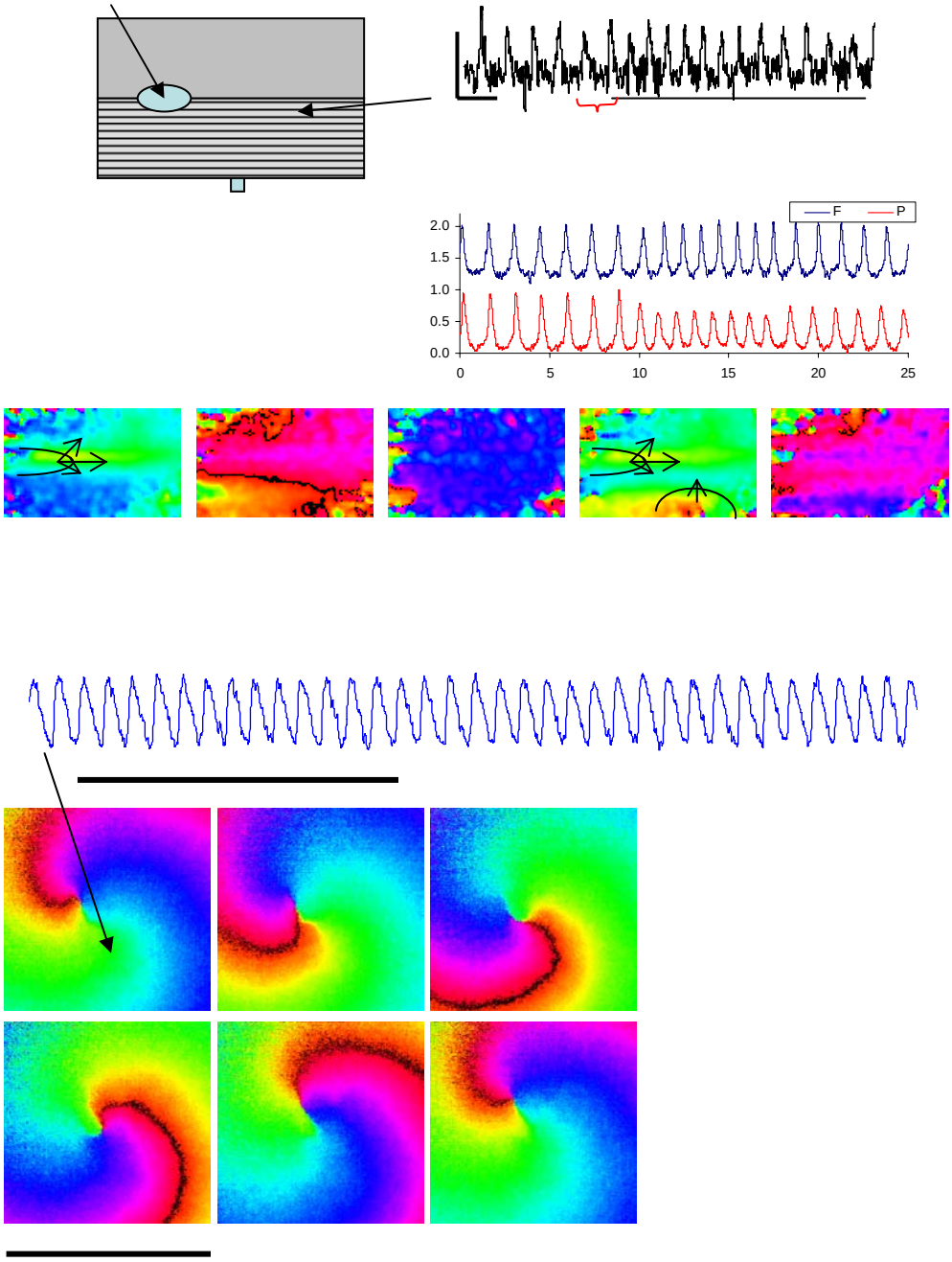

Figure 7-9 Optical mapping with ultra-high spatiotemporal resolution in cell networks. **A**. Transmembrane voltages (di-8-ANEPPS) were imaged (200fps, 20□m/pix) in a cell preparation grown on an elastic scaffold with a flat upper surface and a microgrooved lower surface. Shown are temporal traces from a single pixel, and from 100□m regions from the flat and peak portion. The phase color maps show the spontaneous activity from the border region (*), which was captured by point pacing from the lower border. **B**. Spiral wave, rotating at 2.7Hz, was imaged with Fluo-4 (200fps, 20□m/pix) in a cell monolayer. Raw (unfiltered) single pixel recording is shown from the periphery of the spiral (*), alongside equally spaced (0.075s apart) spatial phase maps.

Finally, **Figure 7-10**, imaged by the same detector, but at 20x microscale in a single murine myocyte stained with Fluo-4, was done at 100fps and 0.58μm/pix (at the optical limit of resolution). The peri-nuclear region of the cell was found to be rich of spiral waves accompanied by phase singularities (PS), confirming some previous observations (Ishida, Genka et al. 1999). The example proves an important point that complexity of spatial patterns in cardiac propagation phenomena is preserved over a large range of spatial scales. For example, the core radius of a supported spiral wave at the macro- and micro-scale can change from 1000μm down to 5μm or less. This more than two orders of magnitude change in the spatial patterns emphasizes the importance and challenge to provide appropriate spatial resolution. Of course, the relevance of these microscale phenomena for arrhythmia genesis and maintenance remains to be confirmed.

VIII. Concluding remarks

The need for optical mapping at the micro- and macroscale simultaneously arises from the spatiotemporal complexity of excitation waves in the heart combined with our lack of full understanding and/or agreement which scale can safely be ignored when analyzing arrhythmias. The brute-force imaging approach solves this problem by imposing uniform requirements for ultra-high spatiotemporal resolution over a large FOV and a long recording period. The technical challenges associated with such solution and the expected performance of current day imaging technology was analyzed here; examples of optical recordings at ultra-high spatiotemporal resolution in cultured cells were also presented. The unprecedented data throughput challenges the current computer technology in terms of data acquisition and data storage. In addition, imaging at such ultra-high spatiotemporal resolution calls for development of specialized real-time data compression schemes and requires new ways to access, display and analyze the data, possibly exceeding the capabilities of current day 32-bit computer systems, including memory and file size limits. These software issues were not discussed in detail in this review, but are expected to become a central point in future imaging developments in this area.

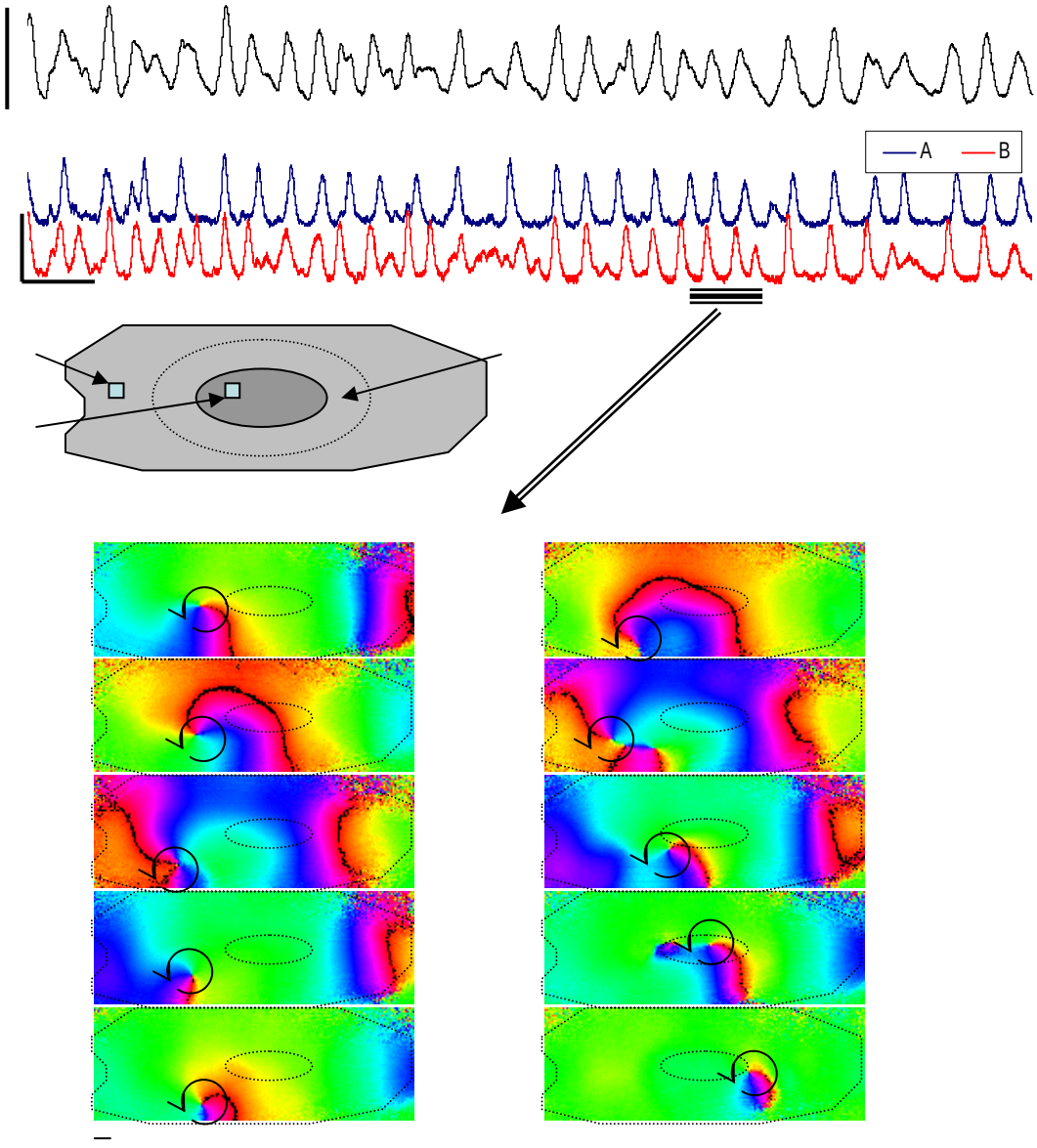

Figure 7-10 Optical mapping with ultra-high spatiotemporal resolution in a single myocytes.
Spontaneous intracellular calcium waves were mapped in a single mouse ventricular myocyte at 100fps and 0.58□m/pix. The mean fluorescence signal (Fluo-4) is shown (overall frequency 0.2Hz), alongside selected single pixel raw data from the region inside and outside the nucleus. No spatial or temporal filtering was applied. Phase maps corresponding to selected 4.5 sec of the recorded temporal sequence are presented. Most phase singularities (PS) were observed in the peri-nuclear region. A meandering spiral wave is shown in the maps; it gets displaced and subsequently eliminated by two target patterns (*), appearing at frames t=3s, and t=4s.

If alternatively to the brute-force approach, two separate imaging systems were used to follow a "zoomed in" and "zoomed out" version of the excitation events, there still remains the need for dynamic positioning/focusing of the micro-mapping unit within the macroscopic

FOV. A more intelligent design would require dynamic reconfiguring of the detector properties and non-uniform sampling to reduce the burden of excessive data generation and handling from regions outside of the zone(s) of interest. Theoretically, individual pixel addressability and control in the CMOS cameras, combined with the ultra-high inherent spatiotemporal resolution of these sensors may allow the implementation of this idea.

Optical imaging of excitation waves rides on cutting-edge technological innovations in the areas of imaging devices and electronics, optics, illumination, and computers; therefore it is hard to predict the future system of choice. We presented here a theoretical framework for rational design of an imaging system based on the "shortest distance" to an "ideal" optical mapping system for a particular application. We offered a critical review of how is this choice influenced by the specific conditions and challenges encountered in imaging of cultured cell networks. The analysis is not limited to cardiac applications only, but is applicable to the dynamic imaging of any excitable cell system.

8. DETERMINANTS OF EFFECTIVE SPATIAL RESOLUTION IN OPTICAL MAPPING

Abstract

Optical mapping of excitation dynamically tracks excitation waves traveling through cardiac or brain tissue by the use of fluorescent dyes. There are several characteristics that set optical mapping apart from other imaging modalities: dynamically changing signals requiring short exposure times, dim fluorescence demanding sensitive sensors, and wide fields of view (low magnification) resulting in poor optical performance. These conditions necessitate the use of optics with good light gathering ability, i.e. lenses having high numerical aperture. Previous optical mapping studies often used sensor resolution to estimate the minimum spatial feature resolvable, assuming perfect optics and infinite contrast. We examine here the influence of finite contrast and real optics on the *effective* spatial resolution in optical mapping under broad-field illumination for both lateral (in-plane) resolution and axial (depth) resolution of collected fluorescence signals.

I. Introduction

Optical mapping of excitable tissue using fluorescent dyes has made it possible to directly test scientific predictions regarding cardiac arrhythmias (Efimov, Nikolski et al. 2004) and neural activity for visual processing (Polimeni, Granquist-Fraser et al. 2005). Capitalizing on the key benefit of optical mapping, namely measurements at high spatial resolution, requires systems with suitably high pixel counts over a wide field of view (low magnification). Such conditions set apart optical mapping from other more traditional imaging modalities due to the unique combination of low light fluorescence signals, rapidly changing images and optics used in sub-optimal conditions (Entcheva and Bien 2005b). Unlike photography or cinematography where inadequate resolution is readily discerned, no indications are available when optical mapping fails to accurately represent the underlying specimen. Understanding the spatial limit of optical mapping is critical in the proper interpretation of data – overestimation gives the false impression of homogeneity when there really is none; underestimation may cause one to aggressively filter out fine spatial features. Recent reports of low spatial frequency in optical mapping of heart tissue (Mironov, Vetter et al.) and controversy surrounding the true spatial limits in neural optical mapping (Polimeni, Granquist-Fraser et al.) naturally lead to the question: what is the "true" spatial resolution of an optical mapping system?

The ability to resolve fine spatial detail is often represented as the diffraction limit for microscopy or the effective pixel size (physical size of each sensor pixel scaled by optical magnification) for macroscopic imaging. However, these measures reflect only the upper bound of spatial resolution as they assume ideal conditions of infinite contrast and perfect optics. For the more realistic case of finite contrast, actual spatial resolution can also be limited by inability to distinguish the difference in intensity between the object and its background, i.e. poor contrast (Smith 1990). As physical pixel sizes shrink in modern detectors (Entcheva and

Bien), the weakly contrasting images of optical mapping due to dim fluorescence aggravated by short exposure times might limit spatial resolving ability rather than pixel size.

Contrast-limited imaging has several important implications for spatial resolution. First, optical components such as lenses can degrade contrast and thus impact resolution. Second, the minimum detectable contrast depends upon the sensor's ability to represent varying intensities as unique digital grayscale levels – a factor not often considered in determination of spatial resolution. Third, the actual resolving ability of an imaging system is a function of the contrast of the object being imaged – for optical mapping, this means constantly changing resolution. In the extreme case where the intensity differences over the entire field of view (FOV) are degraded below the intensity resolution (dynamic range) of the sensor by the imaging optics, resolving ability becomes nil and resolution indeterminate.

When imaging relatively thick specimens, e.g. whole heart or three-dimensional tissue slabs, consideration must also be given to how three-dimensional objects' fluorescence projects onto planar imaging sensors. Experimental studies and simulations (Baxter, Mironov et al. 2001; Ding, Splinter et al. 2001; Bray and Wikswo 2003; Ramshesh and Knisley 2003; Bernus, Wellner et al. 2005; Bishop, Rodriguez et al. 2006) on the depth of fluorescence collected by a planar imaging system have focused primarily on photon scattering and absorption properties of the tissue assuming ideal sensors with full-scale dynamic range responses (infinite contrast). Unlike planar resolution, axial (depth) resolution is almost always limited by contrast unless special care is taken to block out-of-focus light, e.g. confocal imaging. Thus, optics along with light-tissue interactions is expected to substantially affect axial resolution.

We report here a relatively simple method for empirically estimating the effective spatial resolution of a contrast-limited optical mapping system with broad-field illumination. We show how even high performance ("fast") lenses can degrade contrast and hence resolution, and explore the benefits of tandem-lens constructs. Using simple geometric models and empirical tests, we also examine the effect of various optical mapping parameters on axial resolution.

II. Background and Model Details

Spatial Resolution and Contrast

Spatial *resolution* in imaging is defined as the system's ability to reproduce object detail. The highest resolvable spatial frequency in the imaging plane will depend on the pixel size of the detector and the Nyquist criterion (requiring at least two times higher sampling than the signal), while the spatial resolution in the object plane will be inversely scaled by the magnification used. However, resolution as a single number implies infinite contrast; changes in image *contrast* can affect image resolution. ***Contrast Transfer Function (CTF)*** and ***Modulation Transfer Function (MTF)*** have been adopted for quantifying the quality of an imaging system or system component (e.g. lens or sensor) in terms of contrast loss over a range of spatial frequencies (Smith 1990). CTF and MTF differ in the target used to form an image – the response to a black/white binary pattern with sharp transitions is described by the former, while the later is quantified by response to spatial frequencies with sinusoidal modulation of intensity. Both of these characteristics can be calculated theoretically as the amplitude of the Fourier transform of a line spread function for known optical component

characteristics or can be obtained empirically using special test patterns with varying spatial frequency. MTF and CTF are linked through the harmonics of the spatial frequency (ν) via Eq. 8-1 (Coltman 1954). For relatively high spatial frequencies, the relationship can be further simplified to Eq. 8-2.

Eq. 8-1) $$\%\,\mathrm{MTF} = \frac{\pi}{4}\left[CTF(\nu) + \frac{CTF(3\nu)}{3} + \frac{CTF(5\nu)}{5} + \ldots\right]$$

Eq. 8-2) $$\%\,\mathrm{MTF} = 0.785 \times \mathrm{CTF}(\nu)$$

For an idealized, simple (thin) lens, the resolution is limited by diffraction effects and can be quantified through a monochromatic diffraction-limited modulation transfer function (MDMTF). For a monochromatic source, the MDMTF can be computed for a lens with numerical aperture NA and wavelength λ (Smith 1990):

Eq. 8-3) $$MDMTF(\nu) = \frac{2}{\pi}(\phi - \cos\phi \sin\phi)$$
$$\phi = \cos^{-1}\left(\tfrac{\lambda\nu}{2NA}\right)$$

Empirically obtained MTF and CTF curves can be used to predict the spatial frequency at which the imaging system loses sufficient contrast and reaches the practical limit of spatial resolution. The limiting contrast is a function of the amplitude of the original signal ($S_{p\text{-}p}$) and any noise (σ) present in the system. When the degraded signal amplitude falls below the noise level, the spatial feature can no longer be resolved as distinct from the background noise:

Eq. 8-4) $$MTF(\nu) \times S_{p-p} \geq \sigma$$

In the limiting case of a noise-free system, the minimum acceptable contrast will be defined by the bit resolution of the imaging sensor such that the effective contrast, $MTF(\nu) \times S_{p-p}$, must resolve to at least 1 grayscale level (GL). The highest spatial frequency resolvable by a system, ν_{max}, is found for MTF equal to the inverse of the signal-to-noise ratio (SNR) or of the $S_{p\text{-}p}$ in the case of no noise, Eq. 8-5, and forms the basis of what we term *effective* spatial resolution $\delta x_{\min} = \frac{1}{\nu_{\max}}$.

Eq. 8-5) $$MTF(\nu_{\max}) = \begin{cases} \left\lceil \frac{\sigma}{S_{p-p}} \right\rceil = \left\lceil \frac{1}{\mathrm{SNR}} \right\rceil, \text{if } \sigma \geq 1 \\ \left\lceil \frac{1}{S_{p-p}} \right\rceil \text{otherwise} \end{cases}$$

Axial spatial resolution (ASR) versus lateral spatial resolution (LSR)

Optical mapping of three-dimensional tissue is affected by the extent (depth) of tissue from which fluorescence is collected, often termed "depth of field". There are various estimates of "depth of field", defined as the axial distance away from the focus plane that maintains "sharpness" in the image within acceptable limits. This distance can be theoretically calculated as the sum of two components: a diffraction-limited term based on NA, wavelength (λ), and index of refraction (*n*); and a geometric (ray tracing) optics limitation based on sampling (pixel) size (*e*) and magnification (*M*) (Inoue and Spring 1997):

Eq. 8-6)
$$DOF = \frac{\lambda \cdot n}{NA^2} + \frac{n}{M \times NA} e$$

To avoid confusion with the traditional definition of "depth of field", for macroscopic fluorescence imaging we use *depth of integration (DOI)* to quantify the depth at which a point source's intensity will decrease to a specified fraction. The depth contributing to the signal at a pixel is thus the *DOI* that corresponds to a loss of intensity below detectable limits.

A model of intensity profile over depth for a given lens can be obtained by examining how wide a point source spreads as it moves away from the focal plane, i.e. circle of confusion. If a point is substituted instead by a circular source with finite diameter, *q*, each point of the circle will project as a blur spot with diameter *c* when observed out of focus (**Figure 8-1B,** see Appendix). Thus, the resultant image is a larger circle of confusion with diameter $-Mq+c$ in which the original size is scaled by the magnification *M* (note that $M<0$ for real, inverted images). If we further assume that the circular source emits an intensity of I_0 while in focus, then the average intensity of each point source in this circle (while in focus), $\widehat{I}$, is equal to I_0 divided by the area of the source in the image plane:

Eq. 8-7)
$$\widehat{I} = \frac{I_0}{\pi\left(\frac{-Mq}{2}\right)^2}$$

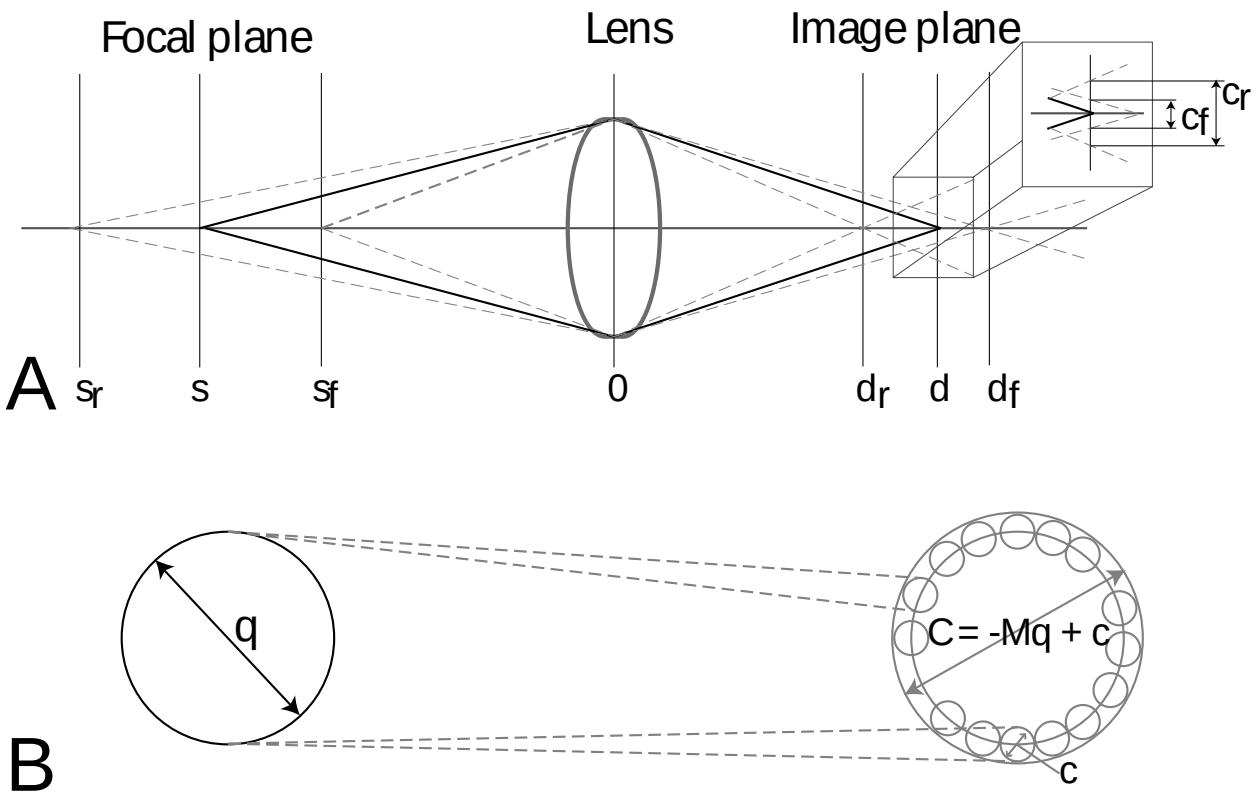

Figure 8-1. Schematic illustration of the "circle of confusion" concept
A) Point sources away from the focal plane project as conical sections, i.e. circles, in the imaging plane. The lens is located at position 0 and the focal plane is at position s in front of the lens with the corresponding image plane at position d behind the lens. Point sources behind the focal plane at s_f would project to a point at d_f and similarly point sources in front of the focal plane (s_f) would project onto d_f. The inset shows the resulting line of length c_f or c_r at the in-focus imaging plane, d. Rotation about the central axis would then yield a filled-circle of diameters c_f and c_r. **B)** A finite circle of diameter q will appear as a larger circle with diameter C=-Mq+c when positioned away from the focal plane.

For images away from the focal plane, the average intensity density (I) will be lower since it's distributed over a larger projected area:

Eq. 8-8)
$$I = \frac{I_0}{\pi\left(\frac{-Mq + c}{2}\right)^2}$$

Intensity away from the focal plane can then be normalized by the intensity at the focal plane, $\widehat{I}$, After substituting the expression derived in the Appendix (Eq. 8-27) for the circle of confusion c, a relative intensity profile is obtained as a function of depth and three lens parameters: aperture a, magnification M, and focal length f:

Eq. 8-9)
$$\frac{I}{\hat{I}} = \frac{\dfrac{I_0}{\pi\left(\dfrac{-Mq+c}{2}\right)^2}}{\dfrac{I_0}{\pi\left(\dfrac{-Mq}{2}\right)^2}} = \frac{(-Mq)^2}{(-Mq+c)^2} = \frac{q^2}{\left(-q + aM\left|\frac{z}{Mf-f+zM}\right|\right)^2}$$

Eq. 8-9 can be solved for z, the distance from the focal plane, to calculate the depth of integration. For example, for an 80% drop in intensity, DOI_{80} can be determined from the two solutions ($z_{80,near}$ and $z_{80,far}$) where h is 0.2 for DOI_{80} and 0.1 for DOI_{90}, etc.:

Eq. 8-10)
$$z_{80,near} = \frac{fq(\sqrt{h}-1)(M-1)}{M\left((a-q)\sqrt{h}+q\right)}; \quad z_{80,far} = \frac{fq(\sqrt{h}-1)(M-1)}{M\left(q-(a+q)\sqrt{h}\right)};$$

Eq. 8-11)
$$DOI_{80} = (z_{80,far} - z_{80,near}) = \frac{2afq\sqrt{h}(\sqrt{h}-1)(M-1)}{a^2hM - (\sqrt{h}-1)^2 Mq^2}$$

Even though optical mapping is done with planar sensors lacking the ability to resolve point sources at varying depths, it is often desirable to know the limits of the depth of volume from which fluorescence is collected, and this can be considered a surrogate for depth resolution. We will employ the term "axial spatial resolution" (ASR), as opposed to lateral spatial resolution (LSR) in the focal plane, to mean the limits to which a point source can be moved away from the focal plane and remain detectable (above background noise). By this definition, ASR is the limiting DOI for which the intensity falls below the noise floor (or the sensor's intensity resolution for a digital, noise-free system), Eq. 8-12.

Eq. 8-12)
$$ASR = DOI_k$$
$$k = \frac{\sigma}{S_{p-p}} \times 100\% = \frac{1}{SNR} \times 100\%$$

So far we have considered the intensity profile in a vacuum. Fluorescence imaging of thick, 3-D specimens will inevitably incur a loss of signal both from attenuation of excitation and emission light as well as photon scattering (Hyatt, Mironov et al. 2003; Bishop, Rodriguez et al. 2006). The collected fluorescence can be expressed as a function of tissue depth, z:

Eq. 8-13)
$$E_{em} = E_{ex} QE_{dye} e^{-\frac{z}{\delta_{em}}}$$
$$E_{em} = \underbrace{I_o e^{-\frac{z}{\delta_{ex}}}}_{E_{ex}} \underbrace{QY_{dye}(1-10^{-[dye]\varepsilon})}_{QE_{dye}} e^{-\frac{z}{\delta_{em}}}$$

where δ_{ex} and δ_{em} are the effective penetration depth for excitation light and the z-dimension emission range, respectively; QE_{dye} is the quantum efficiency of the fluorescent dye (photons emitted per photons absorbed); QY_{dye} is the quantum yield of the fluorescent dye, *[dye]* is the local concentration of the fluorescent dye, and ε is the extinction coefficient of the fluorescent dye.

When the properties of the fluorescent dye are not readily available, the effective depth of the contributing region to the measured intensities can be estimated using simplified mono- and bi-exponential models. This depth has been empirically and theoretically estimated to range from 0.25 to 1.5mm (Girouard, Laurita et al. 1996; Baxter, Mironov et al. 2001). A simple expression for the excitation and emission profiles in depth has been proposed by Baxter et al. which can be used to assess overall fluorescence intensity, *I(z)* (Baxter, Mironov et al. 2001). We have slightly modified it here by normalizing with respect to intensity at the surface, *I(z=0)*, Eq. 8-14, as opposed to integration over the entire tissue depth.

Eq. 8-14)

$$E_{ex} = C_1 e^{-\frac{k_1 z}{\delta_{ex}}} - C_2 e^{-\frac{k_2 z}{\delta_{ex}}}$$

$$E_{em} = C_3 e^{-\frac{k_3 z}{\delta_{em}}}$$

$$I(z) = \frac{E_{ex}(z) E_{em}(z)}{E_{ex}(0) E_{em}(0)}$$

III. Experimental Methods

Sensor and lenses tested

All images were taken with Cooke pco.1200hs CMOS camera (Cooke Corp, Romulus, MI) having 1280x1024 (1.3MP) 12μm square pixels digitized at 10 bits per pixel with exposure times set to 45, 100, or 130ms as indicated. Two fixed-focus 50mm focal length lenses at approximately 0.5x magnification were used for lateral spatial resolution (LSR) testing: a Rodenstock TV-Heligon f/0.75 and a Navitar Platinum f/1.0. To assess the LSR of a tandem lens design (Ratzlaff and Grinvald 1991), a Nikkor 105mm f/2.0 and a Nikkor 55mm f/2.8 were focused at infinity, apertures fully open, and set facing each other to achieve

approximately 0.52x magnification. Formation of a target image for LSR measurement was achieved through the use of a Nikkor 35mm f/1.4 photographic lens focused to infinity and aperture full open. Axial spatial resolution (ASR) was examined with a Navitar 25mm f/0.95 at about 1/10x magnification, maximum aperture, and focus set to infinity.

Estimation of lens performance in macromode

Optical mapping systems often require low to medium magnification forcing the lens to be focused closer than the hyperfocal distance when the object can no longer be accurately considered to be located at infinity. Under these conditions, the published F/# for lenses over-estimate the light gathering efficiency. A correction factor ("bellow's correction") can be used to estimate the loss of light via an increase in the effective F/#, F_{eff}:

Eq. 8-15)
$$F_{eff} = F(1+\frac{|M|}{p})$$

In Eq. 8-15, the magnification M is used to judge departure from infinity focus where M approaches zero; p represents the entrance-to-exit pupil size ratio which is 1 for symmetric lenses. For magnifications $M > 1$, the increase in effective F/# is considerable (two times change at 1x magnification according to this simplified expression). We used a lens pre-design software from Linos Photonics (Milton, MA) to assess the deterioration in F/# due to macromode operation by specifying the fundamental lens parameters: focal length, infinity F/#, and magnification (Linos Photonics Gmb 2006). In a tandem lens design, the effective F/# depends on which of the two lenses functions as the aperture stop and on the magnification, M (ratio of the two focal lengths f_1 and f_2). Assuming simple lenses, the ability to have smaller (better) F/# in a tandem lens design comes from the effective focal length, f_{eff}, being shorter than that of the either individual lens, Eq. 8-16.

$$\frac{1}{f_{eff}} = \frac{1}{f_1} + \frac{1}{f_2}; \qquad a_1 = \frac{f_1}{F_1} \text{ and } a_2 = \frac{f_2}{F_2}; \quad M = \frac{f_2}{f_1}$$

Eq. 8-16)
$$F_{eff} = \frac{f_{eff}}{\min(a1, a2)} = \begin{cases} F_1\left(\frac{1}{\frac{1}{M}+1}\right) \text{ if } a_1 \le a_2 \\ F_2\left(\frac{1}{M+1}\right) \text{ if } a_1 \ge a_2 \end{cases}$$

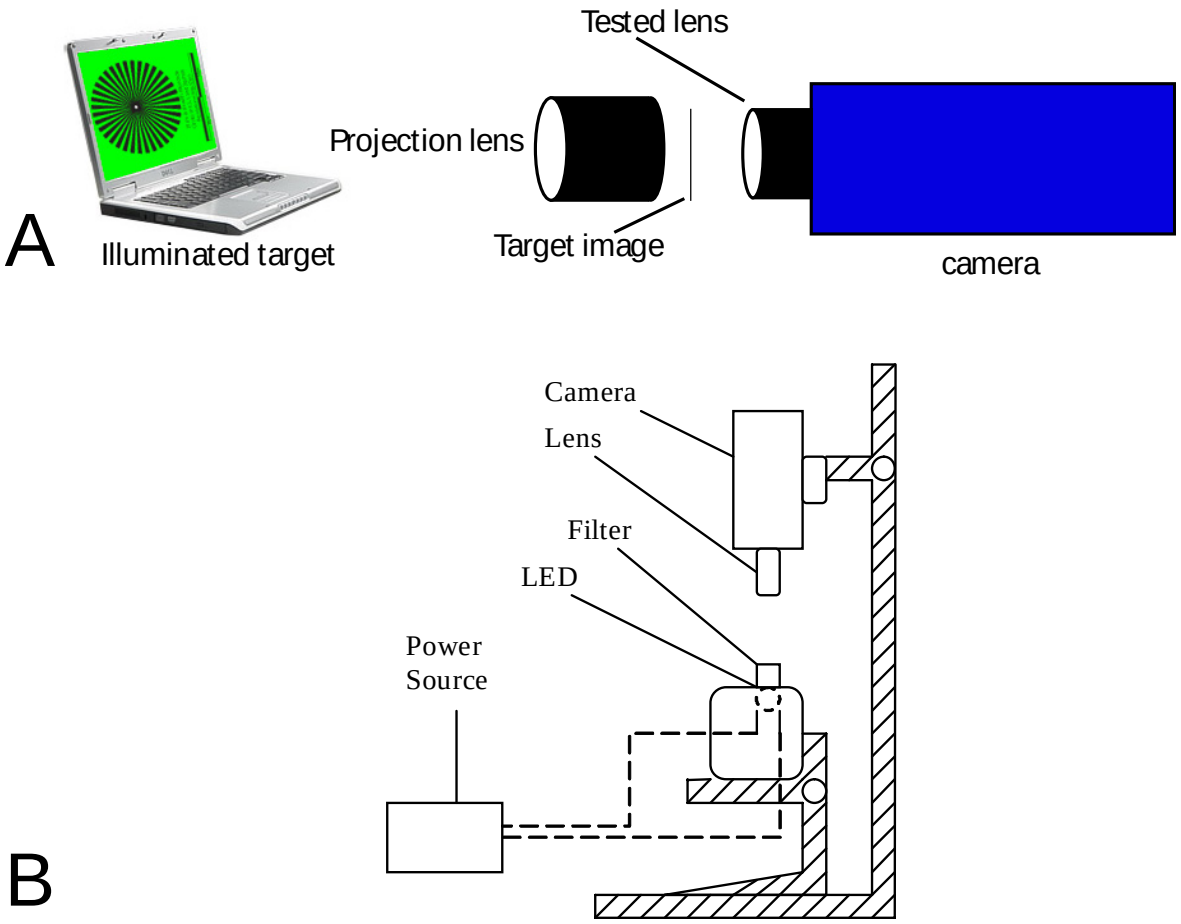

Figure 8-2 Schematic testing arrangements for CTF and DOF/DOI measurements. **A)** Lens testing setup for obtaining CTF curves. A laptop back-lit LCD screen displaying pure green was used to illuminate a Siemens star pattern, which was further reduced 100x with a projection lens before being imaged at 0.5x magnification with the lens under test. **B)** Lens testing setup for estimating depth of field (DOF) and depth of integration (DOI). A blue LED was mounted on a Z-stage for fine (<1mm) adjustments while the camera was mounted to an adjustable rack for coarse (>1cm) adjustments.

Contrast Transfer Function (CTF) measurements

A 21cm diameter resolution target pattern (Siemens star, 36 lp/circumference) was printed on a transparency film (CG5000, 3M) using a Lexmark T632 laser printer at 1200dpi. The transparency was uniformly back illuminated by a 15.4" WUXGA LCD screen displaying pure green at maximum backlight intensity. 1:75 reduction of the target image was achieved through the use of a Nikkor 35mm f/1.4 as a projection lens to obtain a 2.8mm diameter image at near hyperfocal distance (**Figure 8-2A**). To more closely replicate optical mapping conditions and to ensure monochromatic responses, a 535nm bandpass interference emission filter (Chroma) was placed in front of the camera. Using custom software in MATLAB (Mathworks), multiple circumferential intensity curves were extracted from captured images at

different radii corresponding to different resolutions of the Siemens star. Median intensity was determined for each resolution and used as a threshold to classify "high/bright" and "low/dark" intensities. The ratio of the difference between the mean high (I_{max}) and low (I_{min}) intensity values to the sum of the two was used to construct relative CTF curves, i.e. percent contrast (%C) as a function of spatial frequency, ν:

Eq. 8-17)
$$\%\,C = \frac{I_{max}(\nu) - I_{min}(\nu)}{I_{max}(\nu) + I_{min}(\nu)} \times 100$$

Transmission Efficiency

Transmission efficiency of the lenses was assessed by using the clear center of the Siemens star testing pattern (5.7mm in diameter in the real image and 58μm in the projected image). Percent transmission was calculated as a fraction of the intensity of the target image at different exposure times. Assuming constant target intensity over time, line fits were made to each data point across exposures with the *y*-intercept clamped to 0 to estimate the amount of light passing through the lens expressed as grayscale levels per millisecond (GL/ms).

Intensity profile over depth

Axial resolution for the Navitar 25mm f/0.95 lens was probed with a 480nm light emitting diode (LED) (Nichia, Japan) under a 1.3 neutral density filter simulating a quasi-monochromatic point source (**Figure 8-2B**). From the focal plane (determined as the position generating the brightest and sharpest image), images were acquired at various distances and the average light intensity from the central 3x3 pixel region was calculated to yield an intensity profile over depth.

IV. Results

Macromode imaging leads to NA deterioration

Theoretical predictions of the loss of light due to macromode imaging are summarized in **Table 8-1** for the lenses tested. Considering that image brightness is inversely proportional to the square of the F/#, the percent of light collected by a lens in macromode versus infinity-focus can be expressed as the ratio of the infinity F/# squared to the effective F/# squared. Even for large aperture lenses such as the Navitar 50mm f/1, operating at 1x magnification results in a quarter of light intensity. In comparison, for tandem lens setups in which both lenses are focused at infinity, the effective F/# will be lower than the F/# of each individual lens with higher magnifications yielding better performance when the imaging (second) lens is the limiting aperture, Eq. 8-16. The calculations in **Table 8-1** assumed symmetric lenses with pupil magnification ratio p=1. For most lenses, this is the best estimate given the lack of detailed design specifications, but asymmetric lenses with p>1 are possible.

Lens	Focal length	Magnification	F/# (infinity)	Effective F/#	NA	% Intensity
Rodenstock	50	0.5x	0.75	1.13	**0.406**	**44%**

Navitar	25	0.5x	0.95	1.43	**0.331**	**44%**
Navitar	50	0.1x	1	1.1	**0.414**	**83%**
Navitar	50	0.5x	1	1.5	**0.316**	**44%**
Navitar	50	1x	1	2	**0.242**	**25%**
Navitar	50	2x	1	3	**0.164**	**11%**
Navitar	50	4x	1	5	**0.100**	**4%**

Table 8-1 Change in effective F-number and collected light during macromode operation (expressed as fraction of the light seen at the hyper-focal distance) at various magnifications for a subset of high-NA lenses.

Numerical aperture alone does not predict lens resolution

Theoretically, the ability of a lens to preserve contrast at high spatial frequencies is directly proportional to its numerical aperture, quantified by the monochromatic diffraction-limited modulation transfer function (MDMTF), Eq. 8-3. However, our results **(Figure 8-3** and **Figure 8-4A**) indicate that the Navitar 50mm f/1.0 lens (effective NA=0.316) slightly outperforms the Rodenstock 50mm f/0.75 (effective NA=0.406) in the contrast transfer function test. Most surprising is the visibly superior contrast of the tandem lens system with an effective NA of just 0.176 despite the worst predicted MDMTF due to poor NA and multiplication of two MDMTF curves (one for each lens in the tandem lens pair).

Also noticeable in **Figure 8-3** is the brighter image in both 50mm lenses compared to the tandem lens. Because the definition of percent contrast penalizes brighter images by assuming perfectly dark backgrounds per Eq. 8-17, we plotted the raw grayscale values of bright (I_{max}) and dark (I_{min}) regions across spatial frequencies in **Figure 8-4B** to see if the improved contrast of the tandem lens remained. In this view, the difference between bright and dark grayscales is very similar for the tandem and Navitar lenses indicating comparable performance. Surprisingly, the lens with the highest NA (Rodenstock) had the worst contrast – percent-wise and as a raw difference.

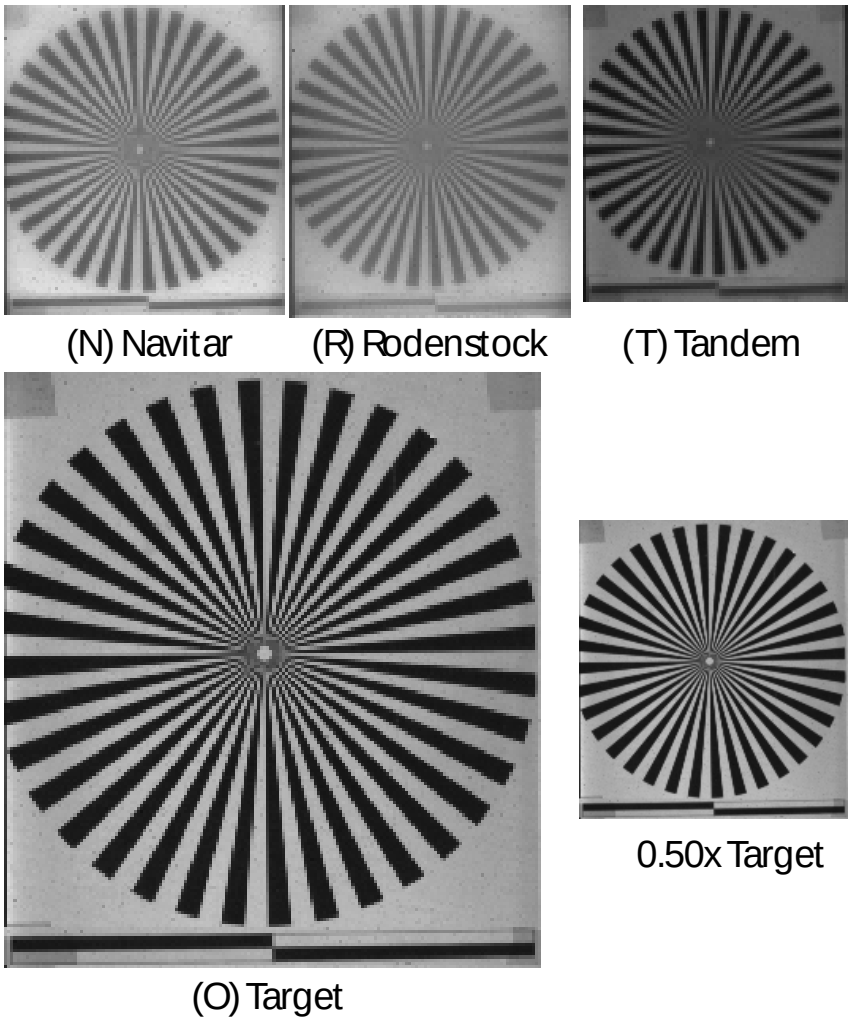

Figure 8-3 Images of the Siemens star pattern containing 36 black/white pairs around its circumference used for CTF estimation.
Bottom scale bar is 10cm per dark segment on the real target; both segments were used for determining magnification. The central portion of the Siemens star is clear and was used for estimation of transmission efficiency. All images shown are at 100ms exposure time. O) Target image generated by projection lens shown to scale. To the right is the same image reduced by 50% for comparison to tested lens images. The scale bar is 993µm. N) Target image viewed through Navitar 50mm f/1.0 fixed focus lens at 0.52x demagnification. Scale bar segment is thus 516µm. R) Target image viewed through Rodenstock TV-Heligon 50mm f/0.75 lens at 0.52x demagnification. Scale bar segment is 513µm. T) Target image viewed through tandem lens assembly composed of Nikkor 105mm f/2.0 and Nikkor 55mm f/2.8, both focused at infinity, achieving 0.48x demagnification. Scale bar segment is 479µm.

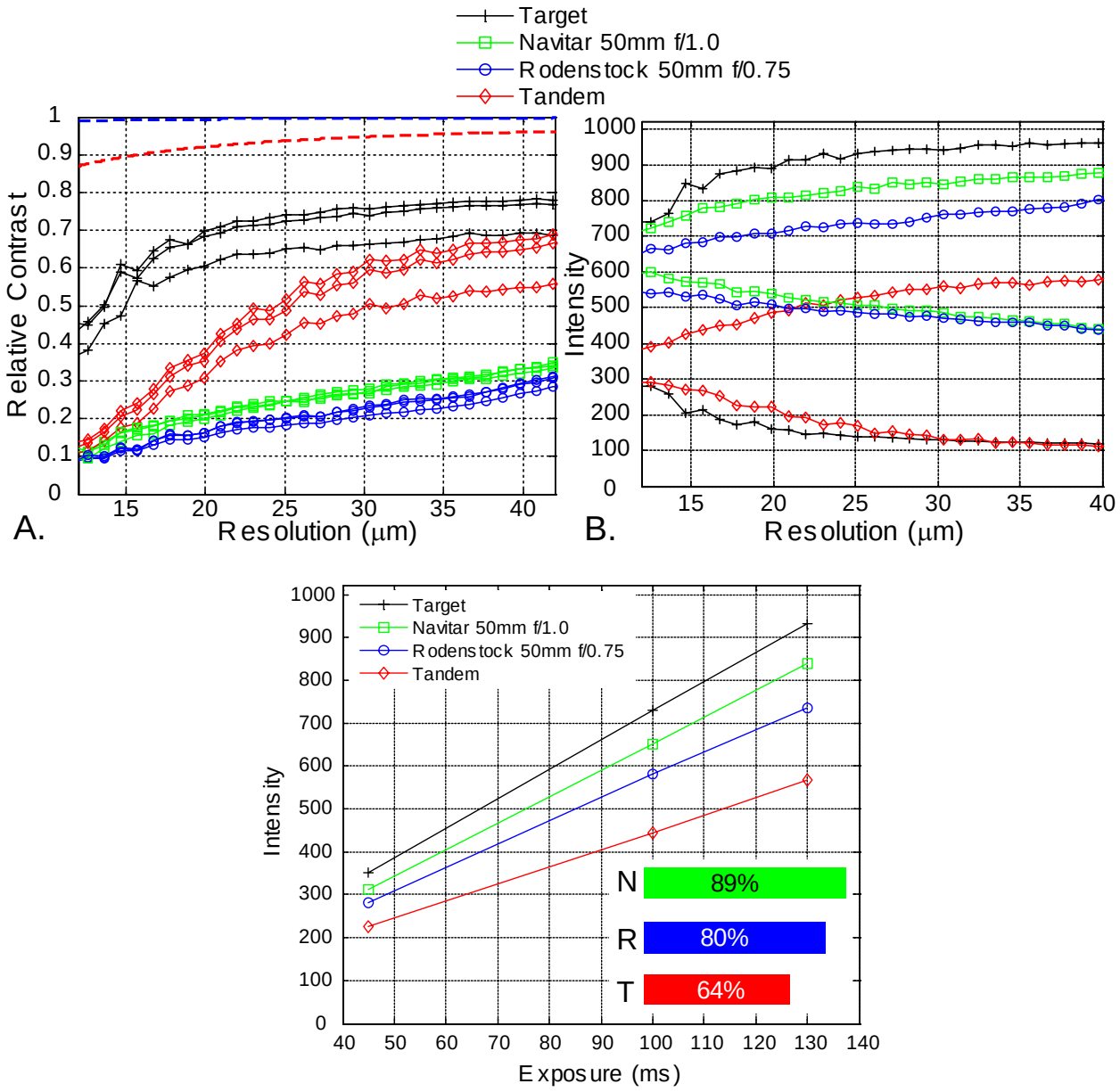

Figure 8-4 Relative and absolute contrast of tested lenses.
A) Relative CTF curves for the tested lenses. For each lens, three exposure curves are shown: 130ms, 100ms, and 45ms. In all cases relative contrast decreased as exposure time decreased. Plotted is the percent contrast (see text for definition) at a given spatial resolution. Most lenses tested were relatively insensitive to exposure times with the exception of the tandem lens. Dashed lines indicate theoretical MDMTF curves for a 50mm f/0.75 lens and for the tandem lens assembly. B) Maximum and minimum intensities recorded for bright (high) and dark (low) areas show the relationship between overall brightness and contrast (normalized difference between high and low values). Maximum reportable intensity is 2^{10} or 1024; exposure time was 130ms. C) Transmission efficiency of selected lenses over different exposure times. Lines were fitted to grayscale intensity as a function of exposure time and slopes extracted in units of grayscale levels per millisecond (GL/ms). Each lens' slope was significantly different from the others (T: 3.4GL/ms, R: 5.1GL/ms, N: 5.5GL/ms, $p<0.05$). Insert: percent transmission with respect to the original target is shown for the three lens configurations at 100ms exposure.

When exposure time was varied from 130ms to 45ms, the CTF of the two 50mm lenses did not change much, whereas the tandem lens suffered significant degradation of percent contrast at shorter exposure times (**Figure 8-4A**). Examination of the raw difference in intensity (**Figure 8-4B**) explains why the tandem lens' contrast is limited by available light (dim image). As exposure time shortens, I_{min} and I_{max} curves for both the Navitar and Rodenstock decline but maintain their separation (absolute contrast) while the tandem lens assembly experiences compression of I_{max} - I_{min} difference due to the inability of I_{min} to fall below the noise floor.

The dim image generated by the tandem lens might be attributed to its poor NA, but the Navitar lens still produces brighter images than the Rodenstock despite slightly worse NA. We quantified this loss of light by evaluating the percent of light transmitted through the clear, central portion of the resolution target. As expected, the tandem lens resulted in only 64% of the original target intensity compared to 89% for the Navitar and 80% for the Rodenstock (**Figure 8-4C**).

Contrast performance depends upon available light or exposure timing

The linear relationship between exposure time and intensity for each lens seen in **Figure 8-4C** demonstrates the camera's linear response and permits one to extrapolate performance at faster exposure times more typical for optical mapping. The slope of each lens' intensity level as a function of exposure time (in units of grayscale levels per millisecond, GL/ms) predicts the loss of grayscale values for a given increase in imaging rate. As noted earlier, contrast will remain the same so long as both I_{min} and I_{max} are permitted to decline. When the predicted grayscale levels dip below zero, reduction of contrast will occur since the camera cannot report negative grayscale values. For example, going from 130ms to 5ms (a reduction of 125ms) will result in a loss of 3.4GL/ms×125ms or 425GL for the tandem lens, which exceeds the minimum black grayscale level of 100 and therefore would be reported as simply 0. The brightest region would be reduced from 600GL to 175GL resulting in maximum intensity differences of just 175GL. Meanwhile, the Navitar lens would lose 688GL reducing contrast from 500GL to 212GL, and achieving better contrast at 5ms (212GL vs. 175GL) than the tandem lens which previously excelled at 130ms (500GL vs. 600GL, respectively).

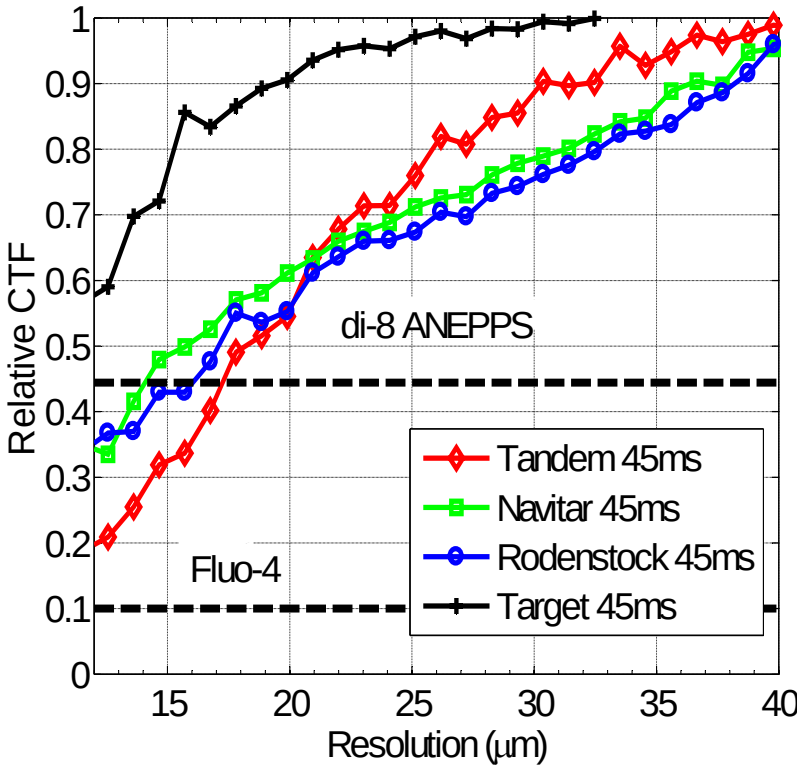

Figure 8-5 Deterioration of effective spatial resolution for different contrast conditions in the object.
Background adjusted CTF is shown against spatial resolution in the image plane for each tested lens at 45ms exposure (different exposures had no effect, data not shown). Broken horizontal lines indicate minimum acceptable contrast for Fluo-4 and di-8 ANEPPS fluorescent signals with SNR of 10 and 2.25, respectively. The absolute limit of spatial resolution is 12µm – the size of the sensor pixel.

A comparison between various lenses can best be performed using background-adjusted CTF, **Figure 5**. By subtracting the minimum black level from all signals yielding a mathematically perfect black background, CTF will always be 1 at very low spatial frequencies and gradually deteriorate as spatial frequencies increase. The CTF of the three lenses are now rather similar with the tandem lens starting at better CTF values until around 21µm resolution where it rapidly falls below that of the Navitar and Rodenstock (these values should be divided by magnification to obtain the spatial resolution in the object plane). As expected from **Figure 8-3B**, the Navitar remained slightly better in contrast (it had greater absolute contrast) than the higher-NA Rodenstock lens throughout the tested range.

Lateral spatial resolution (LSR) in optical mapping depends on dye quality and SNR

Typical optical mapping recordings in our lab from monolayer cardiomyocyte cultures stained with Fluo-4, an intracellular calcium indicator dye, result in approximately 100GL difference with the Navitar 50mm f/1.0 lens at 0.5x magnification and a 10bit sensor. The minimum detectable contrast is thus 1% (1GL) in noise-free conditions, but at our typical signal-to-noise ratio (SNR) of 10, the minimum acceptable CTF is 10% to avoid falling below the noise floor, Eq. 8-5. From **Figure 5**, it is clear that the Navitar lens' CTF does not fall

below 10% at spatial frequencies up to the sensor resolution of 12μm. Therefore, our LSR for Fluo-4 imaging is 24μm (since we operate at 0.5x magnification) in discriminating the wavefront where signal amplitude is greatest. One can also determine the minimum SNR required before the lens will impose a limitation on LSR using Eq. 8-5. For both the Navitar and Rodenstock, the CTF at sensor resolution is approximately 0.35 yielding a minimum required SNR of 2.8 whereas the tandem lens requires at least SNR of 5 to fully utilize the sensor-provided resolution.

For imaging transmembrane voltage, we typically use fast-response potentiometric dyes such as di-8-ANEPPS. The poor response of these styryl dyes often yields SNR around 2.25 with peak-to-peak signal amplitudes of just 18GL in our system. Under these conditions, the minimum acceptable CTF is 44.4% from Eq. 8-5 as depicted in **Figure 5**. Such a high requirement results in optically limited LSR of 28μm, 32μm, and 34μm for the Navitar, Rodenstock, and tandem lens, respectively (at 0.5x magnification) compared to the sensor LSR of 24μm.

Axial spatial resolution (ASR) in optical mapping

For imaging thick specimens, the effective "depth" seen by a pixel is determined by how fast light intensity falls off as the light source moves away from the focal plane. Due to space constraints, a shorter focal length lens, a Navitar 25mm f/0.95, was used instead of the pair of 50mm lenses tested above. Shown in **Figure 8-6** is the measured intensity profile for the 25mm lens operated at 1/10x together with the predicted model from Eq. 8-9. Parameters *a, M* and *f* were known based on the lens specification, while the diameter of the source LED, *q*, was measured as 2.88mm when focused. Note the excellent agreement between the theoretical curve and the experimental data.

As with LSR, the axial spatial resolution (ASR) is limited by the loss of intensity at distances away from the focal plane to the point where it falls below the noise floor; for perfectly noise-free systems the ASR becomes limited primarily by the intensity resolution (1GL) and sensitivity of the sensor as specified by Eq. 8-12. Using the same examples as above, for intracellular calcium imaging with Fluo-4, SNR of 10, and a 50mm f/1.0 lens, the ASR will be the combined distance away from the focal plane where the intensity falls to just 10% of its original value, DOI_{90} or 1.3mm. The ASR for di-8-ANEPPS with SNR of 2.25 will be just 304μm where intensity will have fallen to 44% (DOI_{56}) of the in-focus peak-to-peak signal amplitude. For comparison, in a noise-free, saturated (infinite contrast) system the ASR would be 18.4mm before the signal drops below the 10-bit intensity resolution of the sensor ($DOI_{99.9}$).

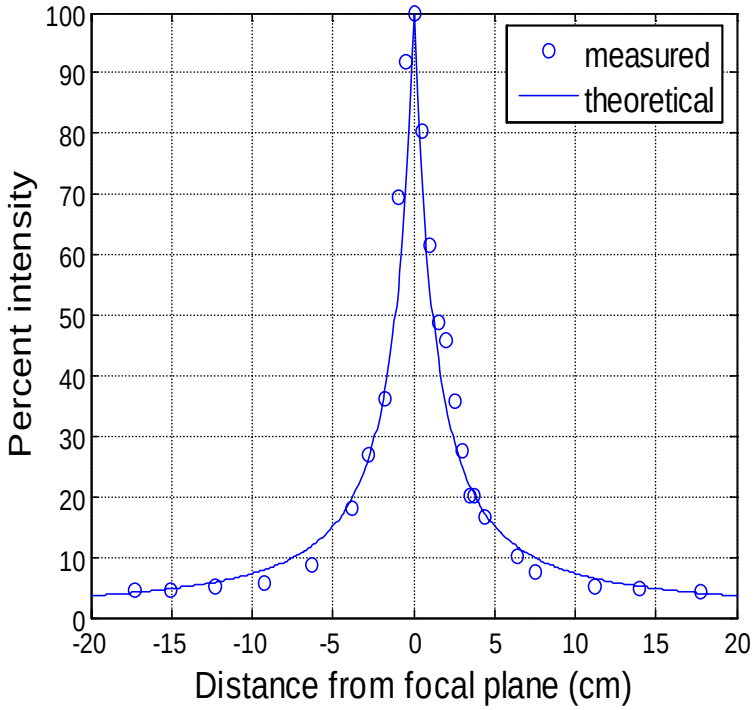

Figure 8-6 Experimental and theoretical estimation of DOI
Plotted are relative intensities as a function of distance from the focal plane; negative distances mean further away from the lens. Also shown is the theoretical curve of how intensity falls considering the size of the circle of confusion. A 25mm f/0.95 lens was used at 1/10x magnification; the spot (LED) size at the focal plane was 2.88mm. Note the excellent match of the empirical results with the theoretical predictions.

Depth of field (DOF) does not correlate well with ASR

The theoretical DOF for an ideal point source using the effective NA of the 25mm lens, magnification of 0.1x and pixel size of 12μm can be calculated as 33μm using Eq. 8-6. Yet, the empirically obtained DOF for a finite sized LED was 5mm, estimated by occurrence of visible blurring. At this distance from the focal plane, the intensity dropped by only approximately 30% (**Figure 6**) and thus light sources as far as 5mm away would still be seen by the imaging sensor. Under ideal, noise-free saturating conditions the ASR for non-scattering, non-absorbing medium would be 6.5cm or about an order of magnitude greater than the visually estimated DOF.

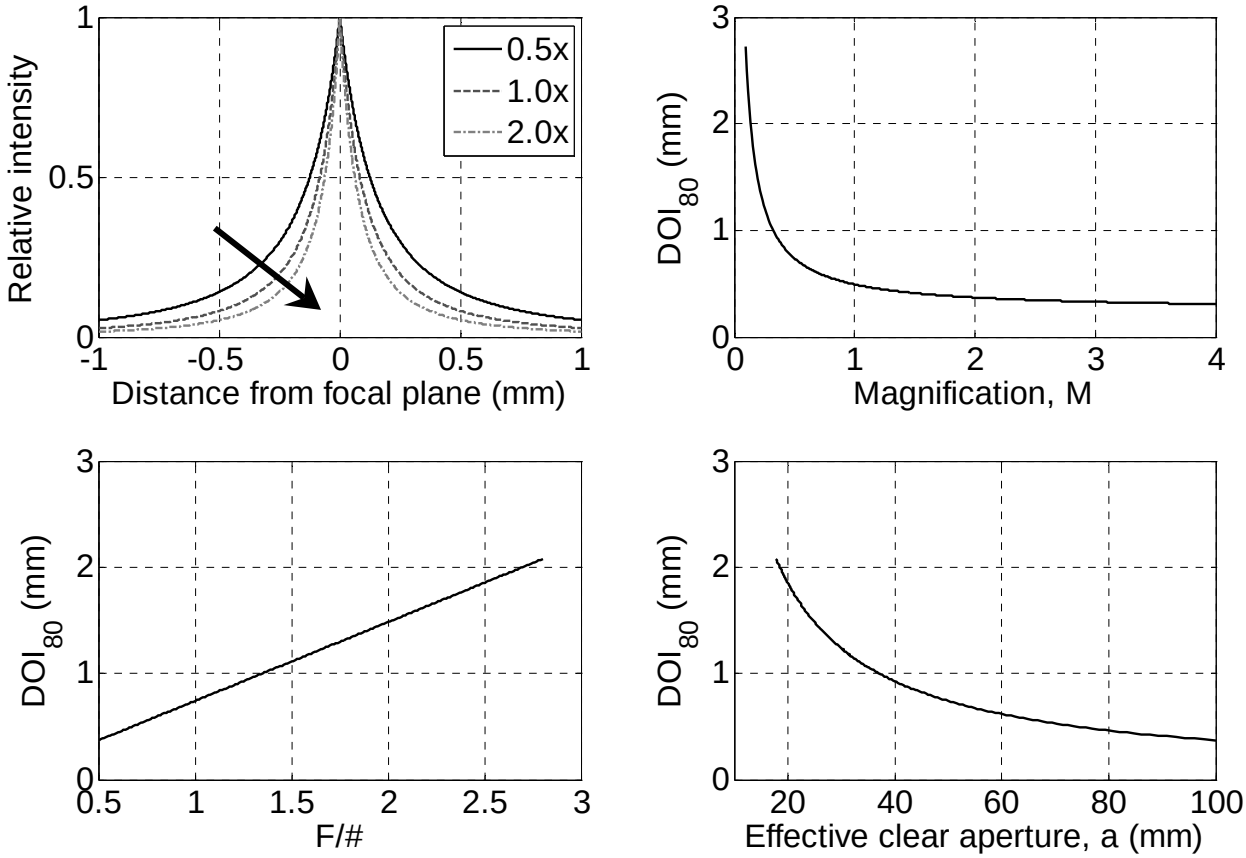

Figure 8-7 Characterization of depth of integration (DOI)
A) Plot of relative intensities as a function of distance from the focal plane for a 50mm f/1 lens operated at three magnifications: 0.5x, 1x and 2x. B) Effects of magnification, *M*, on the depth of field, estimated by DOI_{80}(mm), Eq. (10-11), other lens parameters kept as in (A). C) Effects of the lens F-number on the depth of field, estimated by DOI_{80}(mm). D) Effects of the lens aperture, $a=f/\#F$, on the depth of field, estimated by DOI_{80}(mm).

Factors affecting axial spatial resolution (ASR)

The factors influencing DOI were further examined using the model described in Eq. 8-10 and Eq. 8-11 for a 0.1mm point source imaged at different magnifications and apertures for DOI_{80}. **Figure 8-7A** presents the theoretical curves for a 50mm f/1 lens at three magnifications: 0.5x, 1x and 2x. The DOI_{80} (Eq. 10-11) at 0.5x, 1x, and 2x were 0.742mm, 0.494mm and 0.371mm, respectively. Probing a range of magnifications yields the DOI_{80} curve shown in **Figure 8-7B**. For demagnification (M<1x), DOI_{80} increases rapidly to 2.72mm at 1/10x. Small apertures also increase DOI_{80} as seen in **Figure 8-7D**. The usefulness of the F/# concept is illustrated by the nearly linear relationship when aperture is expressed as F/# in **Figure 8-7C**. Changes in focal length were found to have no effect on DOI_{80} (data not shown). The relative influence of magnification and F-number on DOI_{80} can be deduced from **Figure 8-8** depicting isolines for DOI_{80} over a range of practical magnifications and F/#'s. Isolines more closely approaching horizontal (e.g. at high magnifications) indicate greater

reliance of DOI on F/# than magnification, whereas nearly vertical isolines (e.g. at low magnification) demonstrate magnification's increasing influence.

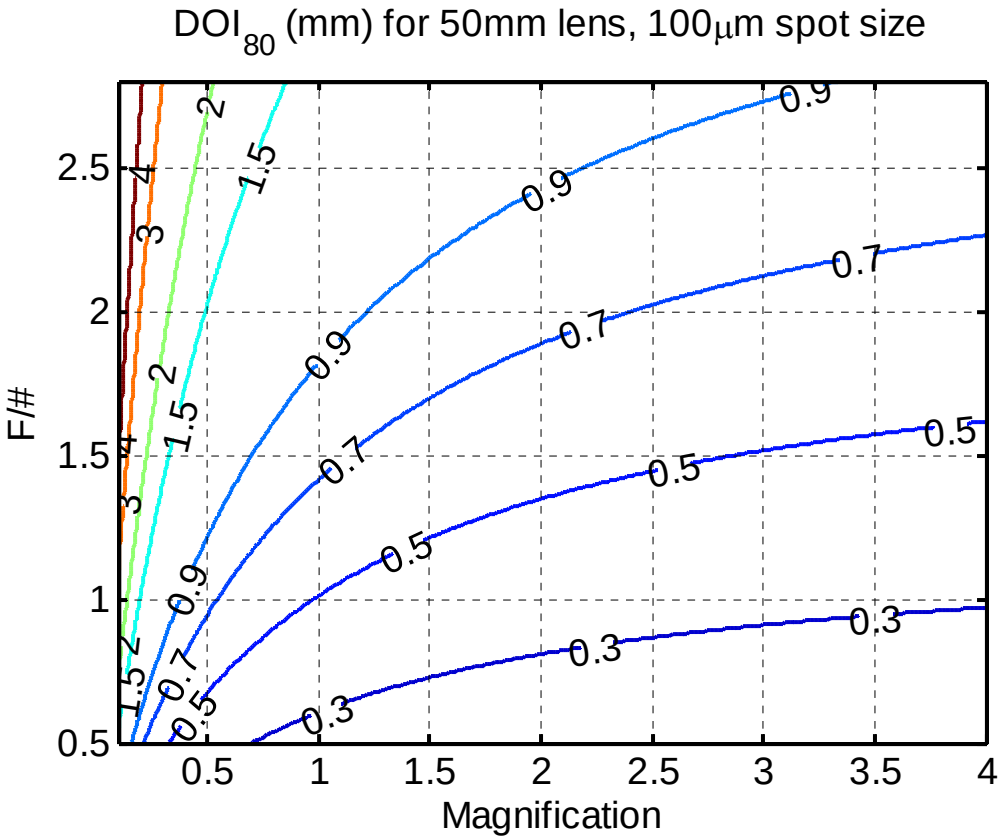

Figure 8-8 Combined effects of magnification and F-number on the depth of integration (DOI).
Contour lines connect points with identical DOI_{80}(mm). A 50mm lens and a 0.1mm spot size are used in the calculations.

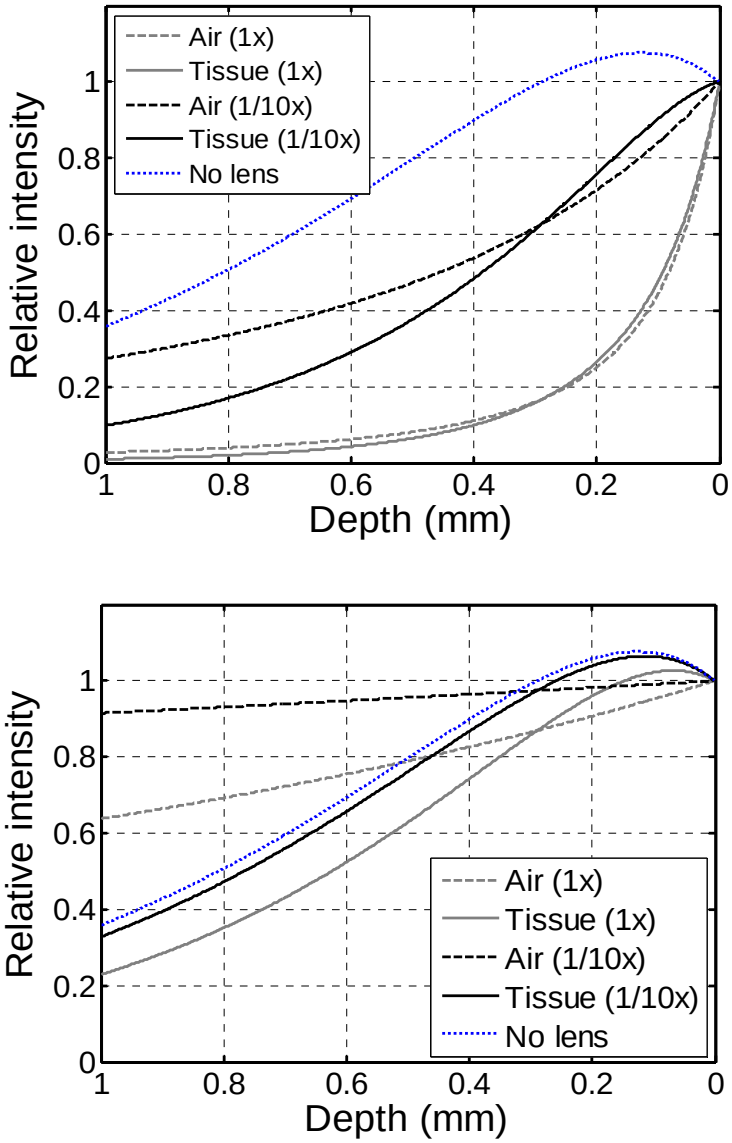

Figure 8-9 Combined effects of tissue scattering and optics on the depth of integration (DOI)

A) A 50mm f/1 lens and a 0.1mm spot were used in the calculations. B) A 50mm f/1 lens and a 2mm spot were used in the calculations. Eq. (14) was used to simulate the effects of tissue scattering and photon absorption ("no lens" curve). The optics-dictated drop in intensity for "air" is shown in dashed lines for two magnifications (M=1/10x and 1x). Finally, the "no lens" tissue curves were convolved with the optics response to obtain how the lens would limit the DOI in tissue (solid curves for the two examined magnifications). Note the depth-limiting effect of the lens at 1x magnification in (A), where a 0.1mm point source was considered. When a 2mm spot size was simulated in (B), the tissue absorption and scattering properties dominated the response regardless of lens characteristics and magnification.

Competing contributions of tissue attenuation and optics in determining ASR

The previous results have assumed uniform illumination throughout depth and no loss of fluorescence intensity as the signal emanates from deep within tissue. To address these issues, we used the simple model (Eq. 8-14) described in Baxter et al (Baxter, Mironov et al. 2001) for constructing a profile of fluorescence intensity for epicardial tissue (C_1=927; C_2=702; C_3=1; k_1=1; k_2=1.8; k_3=1; δ_{ex}=0.71mm; δ_{em}=1.33mm) ignoring the effects of optics ("no lens" curve in **Figure 8-9**). To maintain consistency with our previous calculations of intensity profiles, we normalized the results to the intensity encountered at the surface (z=0) where the focal plane is presumed to lie. Alongside, we plotted the model profile for a 0.1mm point source with a 50mm f/1 lens (**Figure 8-9A**) at 1x and 1/10x magnification. Clearly, when compared to the intensity profile of tissue attenuation alone, the DOI is dominated by the quality of the lens. This assumes a small point-like source surrounded by darkness, but the smallest spacing expected in optical mapping of cardiac tissue is usually 1 to 2mm (Mironov, Vetter et al. 2006). Repeating the same calculations for a 2mm spot size (**Figure 8-9B**) reverses the results such that tissue attenuation, not optics, determines DOI. Thus, the interplay of lenses, tissue properties and the propagation pattern determine how deep layers contribute to the measured signal at the surface. For a 0.1mm spot size, high NA lenses operated at magnifications M>1x have the ability to restrict the DOI to distances smaller than estimated from tissue absorption and scattering (**Figure 8-7**, **Figure 8-8**, and **Figure 8-9**). Even so, optical sectioning with resolutions better than 200μm would be difficult without special confocality-facilitating techniques (Bernus, Wellner et al. 2005; Ramshesh and Knisley 2006), where the acquisition speed becomes a major issue.

V. Discussion and Conclusions

Photographic lenses have been employed in optical mapping systems with broad-field illumination to escape the poor NA of low magnification microscope objectives. However, as F/# is appropriate only for infinite conjugate distances, proper comparison between a microscope objective and photographic lens can only be achieved by converting the effective F/# for the expected operating conditions to numerical aperture used for conditions of finite conjugate distances (**Table 8-1**). Furthermore, the use of NA and wavelength to determine spatial resolution is only accurate when diffraction is the limiting factor. Our results show that photographic and specialty lenses operated close-up often suffer loss of contrast at spatial frequencies outside the diffraction limits. Spatial resolution, therefore, becomes more a function of CTF and object contrast rather than a fixed value.

While the monochromatic diffraction-limited modulation transfer function (MDMTF) predicts better performance for larger aperture lenses, in practice subtle aberrations, e.g. stray light, can result in worse contrast as the aperture is widened. This is most clearly seen with photographic lenses where diffraction limited resolution occurs around f/5 or greater – opening such lenses wider (lower F/#) results in loss of resolution from aberrations (Rosenbruch 1960). Similarly, specialty wide-aperture lenses, while collecting more light than "slower" lenses, might optimize light gathering ability while sacrificing resolution. In this regard, the resolution of a lens does not necessarily follow its rated aperture as demonstrated here with the Navitar f/1.0 having better resolution than the Rodenstock f/0.75. Another possibility for the poor performance of the Rodenstock lens (having both worse transmission properties and resolution in spite of its superior NA) is the age of the lens. Improved manufacturing and engineering processes of modern lenses combined with the inevitable flow of glass might have adversely affected the Rodenstock lens compared to the recently produced (2005) Navitar lens. Nevertheless, our results indicate that relying on the quoted F/# or NA of a lens to judge resolution may be misleading, and short of empirically testing each lens the actual resolution obtained is difficult to judge.

As previously reported, the use of two photographic lenses in a tandem-lens configuration (Ratzlaff and Grinvald 1991) can result in superior performance than either lens alone when focused closer than the hyperfocal distance. This is because there is no degradation of the rated F/# when the lenses are in infinity focus. However, the trade-off is the numerous glass elements that interpose between the object and the sensor, possibly reducing the total amount of light reaching in the sensor. Despite the individual lenses in the tandem lens setup having worse F/# than the Rodenstock and Navitar 50mm fixed-focus lenses, the tandem lens has an effective focal length of just 36mm with a 20mm aperture stop (limited by the 55mm f/2.8 lens) yielding a composite F/# of 1.84. Compared to the f/1.5 of the Navitar lens operated at 0.5x magnification (**Table 8-1**), the tandem lens should result in 59% transmission vs. 89% of Navitar's lens. The tandem lens' measured transmission of 64% indicates that the additional glass elements might not have played a substantial role, but without physically testing such a lens it is difficult to say whether an equivalently sized aperture tandem lens will out-perform a single lens.

Ideally, CTF curves are measured with a detector having infinite resolution and monochromatic diffraction-limited operation. With a 12μm square pixel, the camera used here

for testing would be expected to exhibit decreasing contrast for spatial features less than 12-24μm. This is reflected in the CTF curve for the projected target image where contrast begins to fall sharply around 15-20μm (**Figure 8-1**). The loss of contrast for all tested lenses at approximately 35μm indicates the increasing impact that optics has on spatial resolution for detectors with pixel sizes smaller than 35μm. Note that this finding is independent of magnification since all measurements refer to the image plane (i.e. for 0.5x magnification all values on the x-axis need to be multiplied by two to obtain actual resolution in the object). The background adjusted CTF curves in **Figure 8-5** hint at steadily decreasing contrast even with spatial frequencies as low as 40μm (the largest tested feature size). While some detectors in optical mapping have larger pixel sizes, especially photodiode arrays, some modern CCD and CMOS imagers in use have pixel sizes around 8μm and as small as 2.3μm. Thus, the use of detector pixel size to determine spatial resolution is not always valid.

Even with relatively large pixel sizes, poor object contrast can significantly impair LSR. In optical mapping, poor contrast in the specimen is a reflection of low signal amplitude and/or low signal-to-noise ratios (SNR). One of the key determinants in signal amplitude and SNR is the dye response – the styryl potentiometric dyes are notorious for their weak fractional response, whereas the newer calcium dyes can generate intensity changes more than 100% of baseline fluorescence. For example, while the high contrast Fluo-4 optical data can achieve LSR better than our sensor's 12μm pixels, di-8-ANEPPS becomes optically limited at 14-17μm in the imaging plane (the actual resolution is 28-34μm for 0.5x de-magnification).

The limitations of contrast on LSR come about mainly through the discrete nature of digital imaging systems as the ability to resolve between different intensities is limited by the amount of light needed to change 1GL. For most systems, this is a function of dark noise and the bit-resolution of the sensor; however techniques such as removal of background bias via AC-coupling in photodiode arrays (PDA's) can dramatically extend the effective dynamic range (Obaid, Koyano et al. 1999) and thus intensity resolution. It should be noted, however, that "background" as used in this paper refers mostly to the "resting" fluorescence level of the specimen and not ambient light or other noise sources. Contrast in optical mapping is focused primarily on differences between "resting" and "excited" fluorescence.

The importance of knowing the actual LSR achieved is highlighted in recent reports on the spatiotemporal frequencies found in cardiac tissue (Bien and Entcheva 2006; Mironov, Vetter et al. 2006) where the highest spatial frequency, found at the wavefront where resting cells transition to the excited state, was measured to be in the range of 1-2mm for a broad range of conditions. We must be confident, however, that our imaging system's LSR is capable of much finer detail. Some verification might come about from imaging other-than-normal propagation patterns, e.g. re-entrant spirals, where conduction velocity falls and high spatial frequencies can be found (Bien and Entcheva 2006). When such opportunities are not feasible or practical, as in the on-going debate over pin-wheels in the visual cortex (Polimeni, Granquist-Fraser et al. 2005), empirical testing such as done here for our imaging system can serve to demonstrate the capability of detecting very fine spatial features. Moreover, the discussion and analysis so far have focused on the wavefront where the contrast is greatest. For optical mapping of repolarization, the contrast is significantly worse and the LSR can rapidly degrade.

When the analysis of resolution is extended to three-dimensional preparations, depth-resolved imaging requires thin optical sections. In this sense, the use of the word "resolution" is a misnomer as one measures not the distance between two point sources along the optical axis (depth) where they can no longer be distinguished, but rather the limits of observing a point source away from the focal plane. Using this definition, point sources far away from the focal plane might still be detectable above the image noise, but the lateral localization of such a point will be extremely poor. For instance, an infinitely small point source 1mm away from the focal plane of a 50mm f/1 lens will project a circle of confusion 0.295mm wide at 0.7x magnification, or 4.1mm at 5x magnification. Unfortunately, without additional information, such fluorescence signals may be ambiguously interpreted as broad (low spatial frequency) activity in the focal plane, or deeper fine (high spatial frequency) activation.

Although admittedly simple models of light attenuation due to tissue were used here, the results indicate that depending upon the magnification and aperture of the lens employed as well as the size of the fluorescent region, optical "sectioning" can be limited either by failure to excite/capture emitted fluorescence (tissue effects) or by the numerical aperture (lens effects). More complex models, such as photon diffusion simulations that include the effects of lateral light scatter coupled with detailed ionic models of electrical activity, have recently been published (Hyatt, Mironov et al. 2003; Bishop, Rodriguez et al. 2006), but they ignore the impact of lenses. The adverse impact of lateral scatter on LSR is expected to be greater for thick tissue than thin, monolayer specimens. Moreover, lateral scattering may also affect the intensity profile over depth and ASR in a complex fashion dependent upon the distribution of light sources in depth. Given the simplicity of our lens performance model, it would be relatively straightforward to couple these results with already developed photon-diffusion models of light-tissue interactions in order to obtain more precise assessment of the relative contribution of scattering to image resolution.

In summary, our analysis shows that LSR and ASR achieved by an optical mapping system vary according to the conditions of imaging and the optics employed. This is an important point when interpreting optical signals and considering filtering parameters to improve signal quality. Theoretical predictions for ASR and LSR can only be made for assumed fluorescence intensity distributions in 3-D space and time, depending on spatial frequency/contrast and location of the object (electrical waves) with respect to the focal plane. The constantly changing patterns of propagation in cardiac tissue in 3-D space (Choi and Salama 1998; Efimov and Mazgalev 1998) make estimation of the dynamically variable LSR and ASR a very challenging task. For solving the inverse problem, i.e. predicting depth-resolved patterns from optical mapping on the surface, one may need to also consider optics and detector performance in addition to previously explored factors related to dye-tissue interactions and tissue scattering. For proper interpretation of optical mapping results, one needs to be confident of the lower bound of LSR and ASR.

Appendix: Circle of Confusion

The term "*circle of confusion*" refers to the non-confocal nature of regular lens-mediated image formation. A three-dimensional cone of light exists in the image domain in response to a point-object on the optical axis of the lens. This is seen as a blur spot (the point spread function in the image plane) reflecting contributions by points on the optical axis but outside

the focal plane. For each of these out-of-focus points, the equivalent in the image plane will not be a point but rather a circle with energy spread over an area.

Based on simple geometrical considerations and ray tracing, the size of the circle of confusion can be estimated using the classic lensmaker equation, which relates the lens-object distance *s* to the lens-image distance d in a lens with a focal length *f*. We adopt the convention for strictly positive values of *s* and *d*.

Eq. 8-18)
$$\frac{1}{s}+\frac{1}{d}=\frac{1}{f}$$

As depicted in **Figure 8-1A**, given an ideal lens, one with no aberrations present, a point at the *s*-plane would focus onto an infinitesimally small point at the *d*-plane. A point in front of *s* at a distance s_f, (distance measured from the lens) will focus behind d at a distance d_f. In the *d*-plane of the image, the point would be out of focus and would be seen as a circle (i.e. circle of confusion) with diameter c_f. Similarly, a point behind s at a distance s_r focuses in front of d at a distance d_r. Its circle of confusion at d has a diameter c_r.

For a point at s_f, the diameter of the imaged circle of confusion, c_f, can be calculated using the following expression, in which a represents the aperture diameter of the lens:

Eq. 8-19)
$$c_f = a\left|\frac{d_f - d}{d_f}\right|$$

By combining Eqs (A1) and (A2), the size of the circle of confusion can be expressed as a function of the distance *z* from the s-plane (the focal plane):

Eq. 8-20)
$$c_f = a\left|1 - d\left(\frac{1}{f}-\frac{1}{s-z}\right)\right|$$

Similarly, for a given object at a point s_r, the diameter, c_r, of the imaged circle of confusion, can be calculated using Eq. (A4), which can be further simplified to Eq. (A5):

Eq. 8-21)
$$c_r = a\left|\frac{d - d_r}{d_r}\right|$$

Eq. 8-22)
$$c_r = a\left|d\left(\frac{1}{f}-\frac{1}{s+z}\right)-1\right|$$

As evident from Eqs (A3) and (A5), c_f and c_r are equivalent for any given distance z. Hence, we define the diameter of the circle of confusion, c, as follows:

Eq. 8-23) $$c = c_f = c_r = a\left|1 - d\left(\frac{1}{f} - \frac{1}{s+z}\right)\right|$$

Furthermore, we can combine the lens maker Eq. (A1) with an expression for the lens magnification, M (A7), to obtain new expressions for s and d:

Eq. 8-24) $$M = \frac{f}{f-s} = \frac{-d}{s}$$

Eq. 8-25) $$s = \frac{(M-1)f}{M}$$

Eq. 8-26) $$d = -(M-1)f$$

Substituting (A8) and (A9) into Eq. (A6) yields a new expression for the circle of confusion, which depends on three lens parameters: aperture, a, magnification, M, and focal length, f:

Eq. 8-27) $$c = aM^2\left|\frac{z}{Mf - f + zM}\right|$$

Acknowledgements

This work was supported in part by grants from The National Science Foundation (BES-0503336), The Whitaker Foundation (RG-02-0654) and the American Heart Association (0430307N) to EE, and a National Research Service Award to HB (1F30ES01337101).

9. A HIGH-DEFINITION ULTRA-WIDEBAND MACROSCOPIC RECORDER (HUMR)

Abstract

Using specifications drawn up from previous considerations for spatiotemporal resolution requirements, several imaging systems were tested for optical mapping of EHTs and a high definition ultra-wideband macroscopic recorder (HUMR) was constructed. Based on the previous data regarding performance of several different lens configurations, the new Navitar 50mm f/1.0 lens was chosen for the optics. The final design included a structural element to hold lenses and filters in place (including a provision for tandem lens imaging if desired), an intensified high definition, high speed ultra-wideband CMOS camera with on-board memory and CameraLink interface. Excitation light was provided through a trifurcated light guide set at very shallow angle for oblique illumination. Imaging propagation of a re-entrant (spiral) wave, we demonstrate the importance of high spatial resolution for specific regions/conditions.

Introduction

Based on our previous calculations in Chapter 7, we have decided upon a minimum field of view of 35mm with spatial resolution at least 0.250mm to capture propagation of events at our expected velocities (under 30cm/s). Such a system would need to image at least 200 frames per second and requires a minimum of 140 by 140 pixels. Several systems met these stringent requirements: relatively new "electron multiplying" CCDs (EMCCD) from Andor and Roper Scientific, and many high speed CMOS detectors. Through actual trials conducted with Fluo-4 AM stained HTCs, we learned to our dismay that although the EMCCD devices exhibited great sensitivity, the lacked the speed required for imaging propagation (<200fps, full frame). The EMCCDs that could run at more than 200fps were restricted to 128x128 pixels – insufficient for our resolution requirements.

We thus tested several CMOS and CCD camera systems including the Cooke pco1200hs CMOS camera, SciMedia's Ultima and MiCAM02, as well as an inexpensive high speed CMOS camera from Silicon Imaging. The CMOS imagers we reviewed were all relatively insensitive, but the Cooke pco.1200hs CMOS camera stood out with 12μm^2 pixel sizes (compared to typical 6-8μm^2 size of CMOS cameras) together with the monstrous SciMedia's MiCAM Ultima boasting 100μm^2 pixels (albeit at only 100x100 pixel resolution). The larger pixel sizes are important as they capture more light and offset somewhat the poor sensitivity of CMOS imagers in general. This is borne out by the ability of the MiCAM Ultima to operate somewhat without an additional intensifier – an ability none of the other CMOS cameras can match. However, the pco.1200hs paired with a 3rd generation (GenIII) intensifier produced higher quality signals at much higher spatial resolutions (1280x1024 pixels) than the MiCAM Ultima, and at a price that was about $20,000 cheaper.

SciMedia's CCD camera, the MiCAM 02 (maximum resolution is 384x256 pixels) was also tested. Unfortunately, we were unsuccessful in recording clean signals and imaging propagation with the MiCAM 02. Ultimately, we chose the Cooke's pco.1200hs due to its exceptional spatial resolution (1280x1024 12μm^2 pixels), fast acquisition rates (>600fps, full frame), fast readout rates (base CameraLink configuration), and price. When run at its native resolution, signal quality deteriorated rapidly at frame rates beyond 200fps despite >10,000x gain from the GenIII intensifier. Initially, we resorted to off-line spatial averaging (binning) every 2x2 or 4x4 pixels to improve signal to noise ratios, but later after our requests for hardware-based pseudo-binning, spatial averaging in 2x2 pixel regions was performed in the FPGA of the pco.1200hs camera.

Despite the binning process, the imaging system retained a high degree of spatial resolution. Coupled with the GenIII intensifier having a micro-channel plate architecture (improving the resolution of the intensifier itself) with a 15.6μm diameter matched well with the 12μm pixel size (24μm after 2x2 binning) of the camera. In addition, the intensifier had a 18mm diameter input and fiber-optic coupled output that projected to the pco.1200hs's sensor measuring 15.36 x 12.29mm (19.67mm diagonal) covering most of the imaging sensor's active area.

Methods

Imaging system

As stated earlier, the final imaging system was composed of Cooke's pco1200hs CMOS camera (Cooke Corporation) attached to a GenIII intensifier (model VS4-1845 with extended blue response option, VideoScope International) mounted to a tall (>1m) copy stand (SuperRepro by Firenze) with standard tripod mounting screws. The copy stand was used to accurately position the camera both in the vertical plane as well as in the horizontal plane using a rack-and-pinion design that moved the camera closer or further away from the support stand. At 0.5x optical magnification, the smallest resolvable feature will be 44μm (twice the effective pixel size).

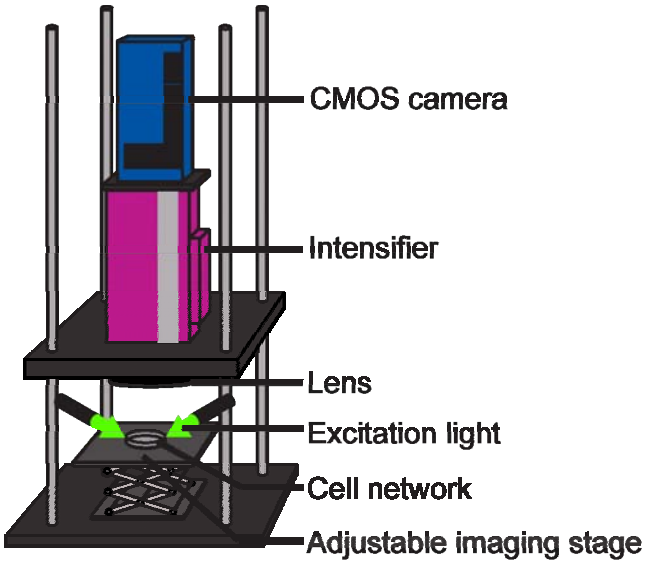

Figure 9-1 Imaging setup.
Schematic depiction of the high definition, ultra-wideband macroscopic recorder used to image fluorescence signals from EHTs. The samples were illuminated by fiber optic light guides positioned above and to the side and imaged through a 50mm f/0.75 lens with a Gen III intensifier and high speed CMOS camera.

Structural support stand

After selecting the imaging system, a structural support had to be designed to hold lenses in place for the imaging system. The support stand was a simple rectangular platform with threaded rods in each corner and plates with holes drilled through them suspended by machine nuts at each corner along the rods (Figure 9-1). Custom, high N.A. lenses were first employed for macroscopic imaging and tandem lens configuration was desired for highest performance. The stand was designed to hold either one or two lenses (for tandem-lens designs) in place against the intensifier while permitting the insertion of a standard 1" emission filter before the intensifier input. A C-mount filter holder was borrowed from the microscopic Ionoptix design and attached to the intensifier input (C-mount). Plates with custom holes drilled and tap to fit a variety of lenses was machined and held in place with nuts along a threaded rod at each corner of the support structure (Figure 9-2). The design was flexible enough to permit new lens mounting plates to be machined and accommodate both a single lens and tandem lens design.

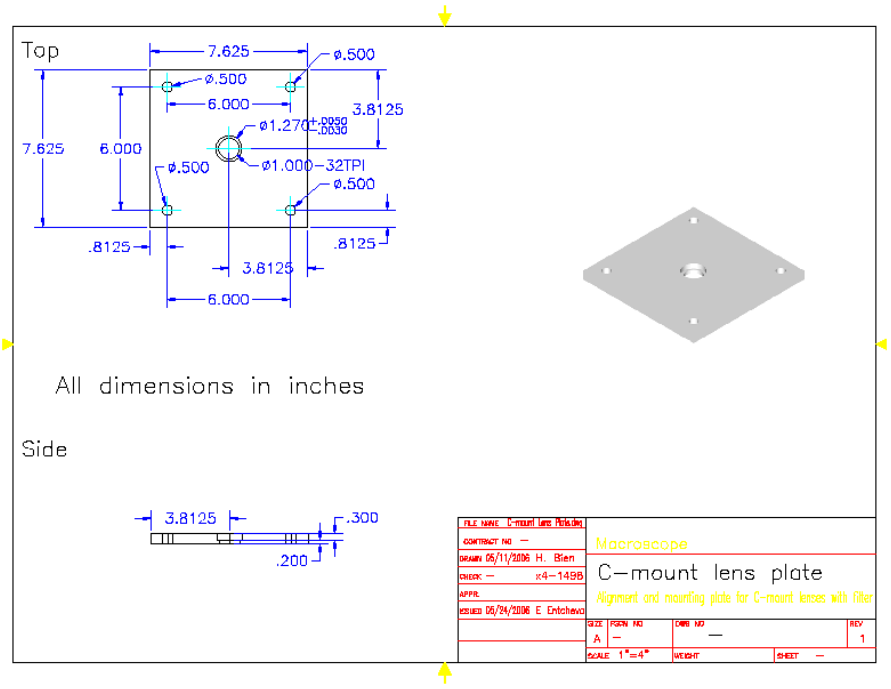

Figure 9-2 Diagram and specifications for custom lens mounting plate.
This particular design is for standard C-mount lenses. Various other lenses, e.g. Rodenstock lenses, required different sized center holes and thread pitch.

Optics

Originally, the HUMR used a Rodenstock 50mm f/0.75 lens, but after contrast and resolution testing in Chapter 8 we opted instead for the Navitar 50mm f/1.0 lens with superior contrast. The focal length of 50mm was chosen to enable a decent working distance for 0.5x magnification. With the Navitar Platinum 50mm lens, the working distance to the front edge of the lens was about 60mm.

Tandem lens setups are possible with two Navitar Platinum 50mm lenses for 1x magnification or a 50mm Navitar lens combined with a 25mm f/0.95 Navitar lens for 2x/0.5x magnifications. For details on how to setup a tandem lens assembly and theoretical performance parameters, see Chapter 8, "Numerical aperture alone does not predict lens resolution."

Unfortunately, attempts to use the Rodenstock lenses in a tandem lens assembly failed due to the unusually short distance between the focal plane of the image when focused at infinity and the back surface of the lens (<10mm). This did not permit the insertion of an emission filter between the lens and the intensifier, and would have required instead a much larger emission filter screwed into the front of the lens at great expense.

Most of the subsequent macroscopic movies were recorded using the single Navitar Platinum 50mm f/1.0 lens as a tandem lens setup would have required prohibitively close working distances (the working distance in a tandem-lens assembly is equal to the distance

between the back edge of the lens and the focal plane of the image for a subject at infinity; for C-mount specifications this is a mere 17.526mm from the back flange).

Illumination

A 250W quartz-tungsten-halogen (QTH) lamp with F/1.0 condenser (model 66184, Newport Optics (formerly Oriel)) was used to excite samples. To reduce the possibility of filter breakage due to excessive heat, a "cold mirror" was placed in front of the excitation filter removing most of the infrared radiation. After the excitation filter, the light was passed into a trifurcated light guide and directed at a 35mm Petri dish (removable) at a very shallow angle.

Empirical testing had revealed that illumination at a very shallow angle improved image contrast compared to angled illumination closer to 45°. To maximize the light, the light guides were placed up against the side walls of the Petri dish and held in place on a thermally controlled perfusion plate with hot glue. Stimulator leads were magnetically attached to the base of the perfusion plate for electrical stimulation of HTCs.

Computer interface and frame grabber

The CameraLink interface of the Cooke pco.1200hs camera required a CameraLink frame grabber. Due to the excessively wide bandwidth of the camera (>1GB/s), we required a fast connection between the frame grabber and the hard disk drive. At the time, the only options for such high bandwidth framegrabbers was a PCI-Express CameraLink frame grabber from National Instruments (NI-1429e). Since then, there are now several other PCI-Express CameraLink frame grabber options (Matrox, etc.). The PCI-Express interface comes in several flavors – the NI-1429e has a 16x PCI-Express bandwidth capable of handling >1GB/s. Unfortunately, the CameraLink connection itself between the camera and the framegrabber is limited to a mere 250MB/s due to the "base" configuration of CameraLink available on the pco.1200hs. There are now newer cameras with "Full" CameraLink interfaces (utilizing dual CameraLink ports per camera) that can stream up to 500MB/s. Thankfully, the on-board memory of the pco.1200hs is capable of storing images at the full rate of 1GB/s, and we then download the saved images through the frame grabber to the computer at less-than-real-time frame rates.

The high definition, high speed imaging of the camera results in an enormous data stream that can occupy 7GB of data in just 14 seconds (full resolution, 200fps). We thus used a dual 3.2Ghz Xeon host computer with 6GB of SDRAM and four 250GB SATA hard disk drives operated in RAID5 configuration and an additional 250GB SATA hard disk drive for the operating system. Through empirical testing, it was discovered that the onboard SATA controller provided faster write thoroughputs and thus images were saved to the operating system hard drive first before being moved to the more secure RAID5 drive array.

Heart tissue constructs

HTCs were engineered as previously described (Bien, Yin et al. 2003) and stained with either calcium sensitive Fluo-4 AM for 20 minutes followed by a 20 minute washout period in Tyrode's solution, or voltage sensitive di-8 ANEPPS for 20 minutes. After staining, HTCs were transferred to a petri dish for examination under the macroscope. HTCs were either

electrically paced at various rates from a point electrode placed at the edge of the Petri dish or exhibited sustained re-entrant (spiral wave) activity.

Results

Data transfer rates are limited by hard drive performance

Despite our best efforts, data transfer between the camera and the PC remained rather slow. A full recording lasting just 14 seconds takes 5 minutes to save to disk due to the slow write speeds of the hard disk drives. Custom multi-threaded applications did not improve the speed by much as the bottleneck resides in the hardware itself. Due to the overhead of the application library used to acquire images from the camera, the delay in saving data to the drive increases as a function of the number of frames transferred. For small regions of interest (ROI) selected where the numbers of frames can easily reach 10,000 frames in 4GB of on-board memory, another technique for optimizing transfers would be multi-frame transfers from the frame-grabber. Instead of transferring a single frame at a time, integral multiples of frames would be packed into a "container frame" and sent out from the camera to reduce the number of function calls required to acquire images. Other potential time-saving techniques include on-camera binning that is now implemented via upgraded firmware. With 2x2 spatial binning, the data rate is reduced by a factor of 4 and the resulting 250MB/s data-rate comes within range of the CameraLink "base configuration" specification.

Despite advertisements claiming write speeds greater than 200MB/s for RAID systems, we have found that in actual practice such speeds are only seen for a short duration and that extended sustained writes are often much slower. Even when quoting sustained write speeds, most tests consider 100MB or at most 1GB to be "sustained". When saving a 7GB file, however, the sustained rate is closer to 20MB/s in our system – far below the acquisition bandwidth.

Spatial frequency content of optical maps of HTCs

An elegant study by Mironov et al. used experimental data from paced activation in pig hearts to formulate practical resolution limits in optical mapping of cardiac excitation(Mironov, Vetter et al. 2006). In the examined conditions, little to no content was found >130Hz in the temporal domain and <3mm in space, thereby justifying the use of aggressive filters to improve signal-to-noise ratio (SNR) with minimal overall distortion of signals (<3%). The remarkably low resolution was attributed to tissue absorption and photon scattering by the authors. They suggested that in purely two-dimensional systems, such as cultured cardiomyocyte monolayers, higher frequencies more reflective of microelectrode measurements might still be obtained.

We tested this hypothesis by imaging cell monolayers with the HUMR where the aforementioned interference factors are not present but instead resolution may be limited by optical parameters and image contrast (via the modulation transfer function of the system), see for example Chapter 8. We provide an example of a spiral captured by HUMR undergoing meander with a sharp inflection point in the tip trajectory (Figure 9-3) containing very high spatial frequencies.

Although, as discussed by Mironov et al., the fastest component of an action potential in the time domain (the upstroke) translates into the highest spatial frequency which is at the wavefront, the spatial frequency spectrum may gain higher frequency components through regions with closely spaced wavefronts, including wave collisions, tight wavefront curvature (wavebreaks or tip of a spiral wave) and steep spatial gradients (fine obstacles or spatially discordant alternans). In addition, such regions tend to exhibit lower conduction velocities as per the eikonal equation, thus further increasing the spatial frequency as the actual spatial frequency is scaled by conduction velocity where lower velocities require higher spatial resolution. These high frequency content areas are found in only a small portion of the field of view but are most affected by low-pass filtering; the abundance of lower-frequency domains can readily mask such distortions from overly aggressive filtering. In our example, the spiral wavetip trajectory in a cell monolayer subjected to increasing spatial filtering in the frequency domain lead to negligible global but substantial local errors (Figure 9-3).

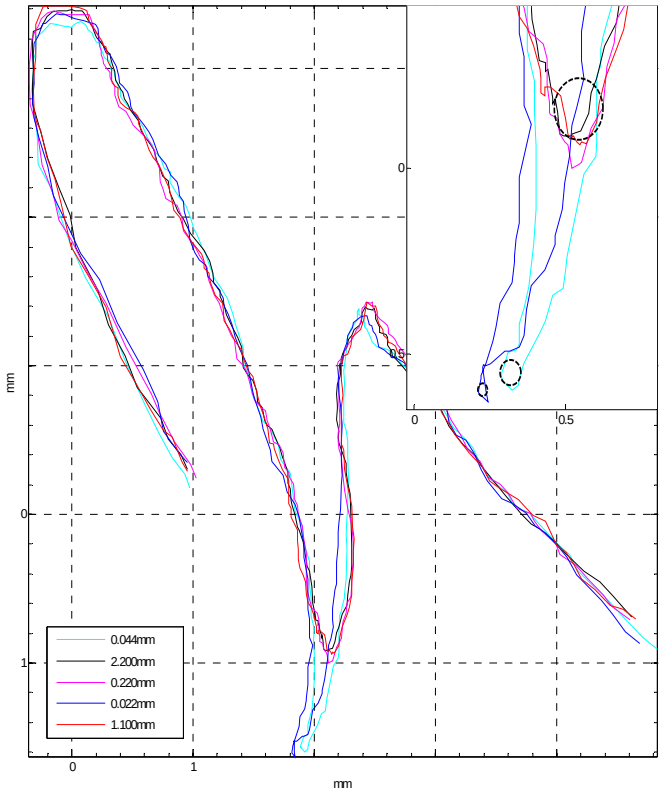

Figure 9-3 Aggressive filtering distorts areas of high spatial frequency.
Shown are tip trajectories for a spiral imaged by HUMR after spatial filtering with a Bartlett window of various radii: 0.022mm, 0.044mm, 0.220mm, 1.1mm, and 2.2mm. The paths mostly super-impose upon each other except at the inflection point. Inset is a zoomed in view of the inflection point. Broken circles describe the estimated radii of curvature at the sharpest inflection point of the spiral tip trajectory. Scales bar is 1mm for the main and 0.5mm for the inset.

Discussion

Because the dynamics of excitable tissue impose a limit on wavefront curvature, an ideal spatial cut-off size might be half the critical radius of curvature. The latter has been estimated to be <200μm, but the exact value in cardiac tissue remains unknown(Fast and Kleber 1997). Computer simulations have demonstrated under-estimation of maximum curvature by 14% even when resolution was chosen at one fourth the simulated critical wavefront curvature(Kay and Gray 2005). Interpolation improved the accuracy of the estimated curvature, but never recovered the peak curvature measured at the highest resolution. In general, it is not possible to take full advantage of aggressive filtering and improved SNR when local dynamics in areas with high wavefront curvature is of particular interest. High-resolution imaging in cell monolayers has the potential to provide more precise experimental estimates of the critical wavefront curvature and the curvature-velocity relationship for cardiac tissue.

Thus, an ideal solution would be even faster hard drives, or for those with unlimited budgets, solid-state storage devices such as offered by Texas Memory Systems (terabytes of RAM, supplier for the National Security Agency's supercomputers).

Real-time processing of the data stream would be one method of reducing the required bandwidth. Machine vision technologies using line-scan cameras have been successful at real-time processing of high-speed images. Their advantage, however, is that they do not need to store the video data. For scientific applications, storage of the raw video stream is a requirement to enable both off-line analysis and third party confirmation of experimental results. What is required is a fast parametric compression of waveform data not unlike that used for motion pictures, e.g. MPEG-2 and MPEG-4. Ideally, such a compression algorithm would focus not on removing high frequency content indistinguishable to the human eye, but rather leverage the typical waveform morphology expected at each pixel and characterize it with an analytical curve.

One possible method is to break the transient into the traditional 4 phases (rest, depolarization, plateau, and recovery) and fit curves to each segment. The system would then need to only save the parameters describing the curves for each segment compressing data in the temporal domain in a highly efficient manner. Further compression can be achieved by examining propagation patterns and encoding wavefronts as geometric curves providing dense spatial compression. Such compression technologies are probably off in the future as they impose significant computational demands on a system that is generating more than 200MB/s of data.

The other, more futuristic, alternative to reduction in bandwidth is not reduction *per se*, but rather more intelligent use of available bandwidth. Specifically, the use of detectors with variable spatial and temporal resolution, mimicking the human vision system, would permit for fine spatial detail at low temporal resolution in the central region ("region of interest") while low resolution, high-speed periphery is still being monitored. Such a design can be easily achieved with uneven pixel sizes or a combination of technologies, e.g. a CCD/CMOS sensor surrounded by a PDA array. The main limitation of this technique is that, like the human eye, a real-time video processing unit will be required to track the object of interest and maintain it within the central, high detail area.

The improved image contrast from highly oblique illumination may be due to reducing the amount of stray light reflected off the surface of the solution and into the intensifier. In fact, at angles greater than the critical angle, the excitation light will remain trapped within the solution bathing the HTCs and not travel back to the imaging system. This is different from total internal reflection fluorescence (TIRF) imaging where only a thin layer is excited due to total internal reflection. Here, the excitation light is deep under the surface of the solution along the sides of the Petri dish containing the HTC and illuminates the entire volume of the Petri dish.

The trifurcated light guide provides rather uneven illumination to the sample due to the configuration of the light guides. Better would be four to six light guides to more evenly distribute the light among the Petri dish. Another option would be to use plastic light pipes to evenly disperse the light in a ring around the sample at very oblique angles (Figure 9-4). Plastic light pipes utilize microscale grooves etched in plastic to guide light along internal reflections similar to fiber optics. Such a system would undoubtedly loose light intensity as it scatters within the medium, but by simply increasing the excitation intensity one can overcome this loss.

A 250W QTH lamp wastes most of the energy in the form of heat (hence the need for the cold mirror). Far more efficient would be a large bundle of high intensity LEDs combined through a condenser to a fiber optic light guide which can then be used to directly illuminate the sample or interfaced with the proposed circumferential lightguide providing a more even illumination solution. An additional benefit of LED illumination is the possibility for high-speed electronic switching for multi-spectral acquisition. This has to be matched with an imaging system capable of handling fast fluctuations in light intensity – a characteristic that most amplifiers, including intensifiers, do poorly.

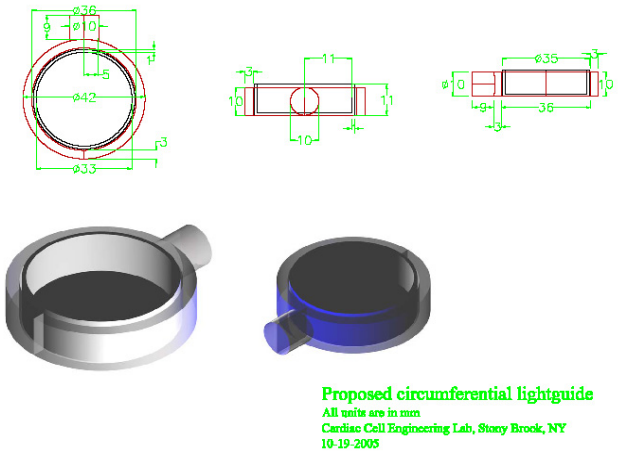

Figure 9-4 Possible plastic light pipe for circumferential lighting.
A schematic of a proposed circumferential plastic light pipe for coupling a fiber optic light guide input to a 35mm petri dish. The device is split into two identical halves. Light would come in on the extended protrusion (blue color) from the circular base and distribute it evenly along the edges of a petri dish.

Conclusion

We have successfully constructed a HUMR capable of imaging propagation at 200fps with a maximum 44μm resolution (actual resolution depends upon the dye used and the resultant image contrast – see Chapter 8 for details). By examining the tip trajectory of a spiral wave that nearly reversed direction leaving a sharp inflection point in the spiral tip path, we were able to demonstrate how localized high spatial frequency regions can become distorted by aggressive spatial filtering without much loss in the overall (global) details.

10. ALGORITHMS FOR AUTOMATED WAVEFORM MORPHOLOGY ANALYSIS

Abstract

Assisted or automated waveform characterization is essential in handling vast quantities of data as collected by high-speed imaging. A simple but effective algorithm is presented that accurately identifies unique transient events and characterizes their morphology with minimum user intervention. The algorithm was implemented in MATLAB for rapid prototyping and independent verification by human operators was performed. The algorithm appears rather robust against noise interference and can be applied to a variety of signals from single-channel PMT recordings to ultra-wide band high definition, high speed imaging. Ultimately, the development of a fully automatic transient characterization algorithm will permit operations akin to data mining in optical recordings.

Introduction

Assisted or automated data analysis is a requirement when recording large amounts of data. At the most basic level, fluorescence intensity movies can be analyzed on a pixel-by-pixel basis – essentially ignoring the spatial dimension and focusing solely on the temporal axis. Such a 0-dimensional space (one dimension if you include time) also occurs when recording from a single-channel device such as a photomultiplier tube. Therefore, an algorithm for analysis of a signal over time can be employed to study both single-channel recordings and optical movies. Analysis of such signals requires, at minimum, delineation of discrete "waveform" events and characterization of such waveform. In fluorescence signals recorded from cardiac myocytes, the waveform events (transients) can be either action potentials in the case of transmembrane voltage, or calcium transients in the case of intra-cellular free calcium concentration.

In experimental data, noise is always present and the algorithm must be relatively immune to the effects of noise. We present here a simple algorithm for detection of transient "events" and characterization of waveforms that has been successfully employed in conditions of noise and verified by independent human operators.

Methods

Pre-processing

The first step in most signal analysis is conditioning the signal to achieve greater consistency and normalize values. While there are many mechanisms available to achieve this effect, the algorithm presented here does not rely on any specific pre-processing techniques. The only requirement is that the transient must be initiated by an upwards (increasing value) monotonic rise. This can be easily accomplished even for those fluorescence signals that decrease upon depolarization via multiplying the entire signal by -1.

For movie recordings where signal-to-noise ratios were low, spatial averaging (two by two pixel kernels) followed by temporal filtering with Savitzky-Golay polynomial approximation of order 2 over 11 to 15 samples were applied to reduce noise. Movie recordings are also often recorded in integral formats (8, 10, 12, or 16-bits) and therefore are first scaled to their full dynamic range before being converted into IEEE floating-point format (double precision) for analysis.

Difference signal

The algorithm consists of two parts: transient detection and waveform characterization. The first part, transient detection, utilizes a difference signal similar in concept to the derivative. Under conditions of noise, the first derivative is often rather noisy and rapidly fluctuates between positive and negative values. Fortunately, in our system, the start of a transient is often marked by a rapid depolarizing event, which is captured as either a sharp increase or decrease in fluorescence depending on the parameter being imaged and the response of the dye. Such a large and rapid increase in signal often overwhelms the inherent noise and results in a monotonic change in fluorescence intensity (the rate of change, clearly, varies rapidly as a result of noise introduced into the system). Taking advantage of this fact, a difference signal is constructed by the subtraction of a time-delayed version of the signal from the original trace, i.e.

Eq. 10-1) $$ds(i) = s(i + \tau) - s(i)$$

where *ds(i)* is the difference signal, *s(i)* is the original signal trace sampled discretely as a function of time (samples) *i*. The delay, τ, is chosen by the user to approximate the duration of depolarization. Typically, for our setups this is in the range of 5 to 11 samples at 250 samples per second (corresponds to 20 to 44ms). To avoid confusion with the similar practice of embedded delay return mapping, we defined this delay τ as the monotonic duration or *mono_len*.

Thresholding

The start of each transient can now be identified through simple thresholding of the signal. However, as the magnitude (amplitude) of each transient varied, a fixed-value threshold was not necessarily appropriate. Therefore, a normalization process was introduced that scaled the difference signal to values between -1 and 1.

The difference signal was divided into blocks of '*env_width*' samples long in duration and all points greater than 90% of the maximum value in each block were identified as "high" values. Since the difference signal must contain both positive and negative values (or else the original signal would be changing monotonically), the lower points can be identified as less than 90% of the minimum value in each block. Adjacent points within each set ("high" and "low") were eliminated by keeping only the larger (smaller for lower) value of the pair. Finally, an upper and lower envelope function was constructed using piece-wise cubic Hermite polynomial estimation between identified points in the "high" (corresponds to the upper envelope) and "low" (corresponds to the lower envelope) sets. The difference signal was then scaled to values between -1 (at the lower envelope) to +1 (at the upper envelope).

After normalization, transient events are delineated by points having a difference signal that exceeds a user-specified threshold. Since the threshold crossing usually occurs over several sampled time points, for all points separated by less than a user-defined minimum duration, *min_width*, the point with the maximum difference is used to identify the start of each transient event, $s(i_{start})$.

Waveform analysis

Each transient event is now defined to begin at the identified starting point (peak difference signal) and ends at the datum point just prior to the start of the next transient event. The maximum (peak) difference signal corresponds more to the peak dF/dt rather than the "true" transient start – defined here loosely as the first departure from baseline. To identify the true transient start, the latest point with a negative first derivative, i.e. the point just prior to the monotonic rise, is marked as $i_{start,adj}$. A line is then fit to several points prior to the $i_{start,adj}$ as an estimate of the baseline (s_{bl})

Eq. 10-2)

$$s_{bl}(i) = m_{bl} \cdot i + c_{bl} \text{ for } i_{start,adj} - bl_{samples} \le i \le i_{start,adj}$$

where m_{bl} and c_{bl} are fitted parameters, $bl_{samples}$ is the number of samples prior to the adjusted starting time used for baseline estimation. A second line is then also fit to a point before and after peak dF/dt to approximate the monotonic depolarization event, s_{dep}.

Eq. 10-3)

$$s_{dep}(i) = m_{dep} \cdot i + c_{dep} \text{ for } i_{start} - 1 \le i \le i_{start} + 1$$

The moment the signal departed from baseline, t_{start}, is estimated to occur at the intersection of the two lines, i.e.

Eq. 10-4)

$$t_{start} = \frac{c_{dep} - c_{bl}}{m_{bl} - m_{dep}}$$

The additional advantage of this technique is that the baseline estimate can then be used to normalizing all values to 0 at the baseline. Normalization can occur either through subtraction of the baseline fit, $s_{bl}(i)$, the average of all points used to determine the baseline, or the value of datum point closest to t_{start}.

The peak (systolic) value can then be computed in several different ways. The simplest method is the maximum value recorded for the entire transient event duration. Other more complex methodologies such as transition through positive/negative in the first derivative or even first sustained overall negative first derivative were tested and found inferior to maximum value under conditions of noise.

The triangular shape of many of our rat cardiac transients precludes a derivative-type approach, e.g. inflection point, in identifying the end of a transient event. Traditionally, the end of a transient can be defined as when the signal falls 80% from its peak value, denoted as

APD_{80} or CTD_{80} for action potential duration or calcium transient duration, respectively. This is easily accomplished by calculating the threshold, e.g. 20% of peak for an 80% decline or 50% of peak for 50% decline, and collecting all data points in the vicinity of the threshold. An automatic ranging algorithm is used where the neighborhood about the threshold is gradually increased until a sufficient number of points, typically eight, are captured. A line is then fit to the captured points and the intersection of this line with the threshold is used as the time of transient end. An identical algorithm is used to determine when the transient first crossed the threshold, but this time is not used in any of our analysis.

Results

An implementation of this algorithm was done in MATLAB (Mathworks) and has been slowly improved over time. Transient event detection with enveloping threshold can be seen in Figure 10-1. For such a short recording, the benefits of enveloping are not obvious, but for longer recordings with wandering baseline or diminishing systolic amplitude, the envelope permits capture of widely varying amplitudes. Such a situation becomes even more important when alternans (beat-to-beat alternation in amplitude or duration) is prominent.

One potential disadvantage of the enveloping technique occurs under conditions of widely varying beat frequency. If over the envelope width no transient occurs, the envelope will shrink to the size of noise and pick up numerous invalid beats. The use of a minimum signal value helps avoid such situations, but in general for signals with relatively constant frequency the best solution is to pick envelope widths that encompass at least one transient.

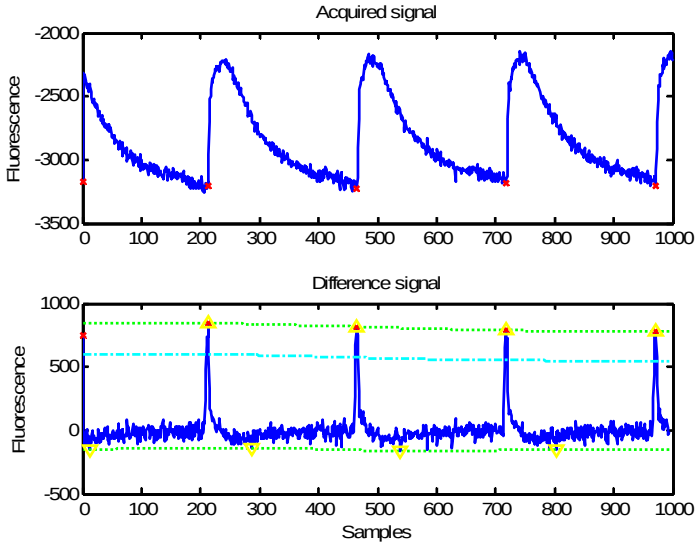

Figure 10-1 Example transient event detection.
The original signal is shown above the computed difference signal (delayed by 7 samples). Envelopes are drawn in broken green lines, and the broken cyan line represents the threshold. Yellow triangles depict the points used to construct the envelopes while red 'x' marks the peak difference signal. In this example (neonatal rat cardiomyocytes paced at 1Hz sampled at 250Hz), the peak difference signal comes very close to the initial departure point from baseline.

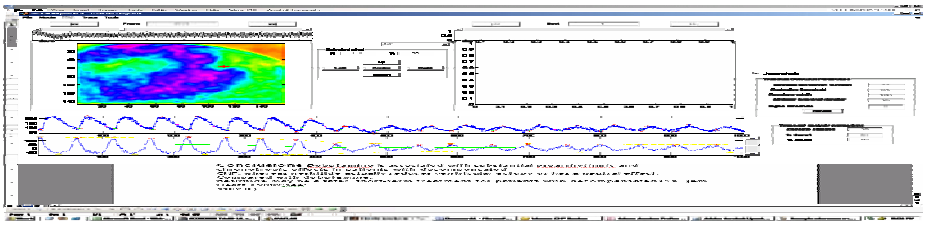

Figure 10-2 Transient detection in long recording of slowly decaying amplitude.
The benefits of enveloping for transient detection is clear in this example signal taken from a macroscopic recording of intra-cellular calcium during re-entry. The top panel is a plot of fluorescence intensity over samples, the difference signal is plotted below. Detected transients at the peak difference signal is circled in red on both plots, and the broken line represents the envelope signal used for threshold normalization. The threshold itself is shown as a thin green line midway between the two broken lines.

An annotated transient is shown in Figure 10-4 for a relatively clean signal (from Figure 10-1 and not pre-processed in any fashion, i.e. no filtering applied). Many of the alternative measurement methods for peak systolic values are within 1 sample time from each other with <5% difference in fluorescence values, and therefore the least complex method was often chosen in the interests of time.

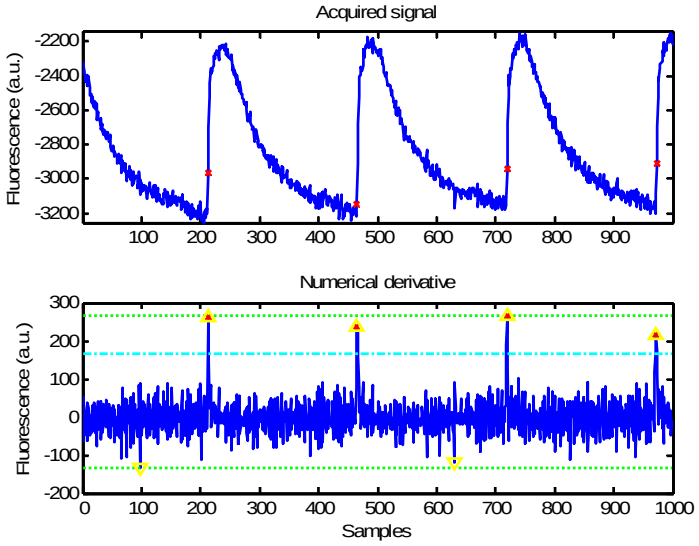

Figure 10-3 Numerical derivative of sample signal.
The same signal from Figure 10-1 is shown above with numerical derivative instead of difference signal. For clean signals, the derivative is still useable, but the signal to noise ratio is clearly worse. Note also the different locations of the starting point in the original signal (identified with red 'x') compared to the difference signal method.

Independent verification by human operators was performed on more than a thousand individual transients – disagreements occurred only in conditions of exaggerated noise. Variation in human operator identified waveform datum points, e.g. peaks, and durations, were

similar to those between human and computer algorithm (unpublished data). The MATLAB implementation has thus far been employed in the analysis of over several million transients with reasonable success, although its performance in MATLAB leaves much to be desired when analyzing large movies (1,000 by 1,000 channels for 3,000-6,000 frames).

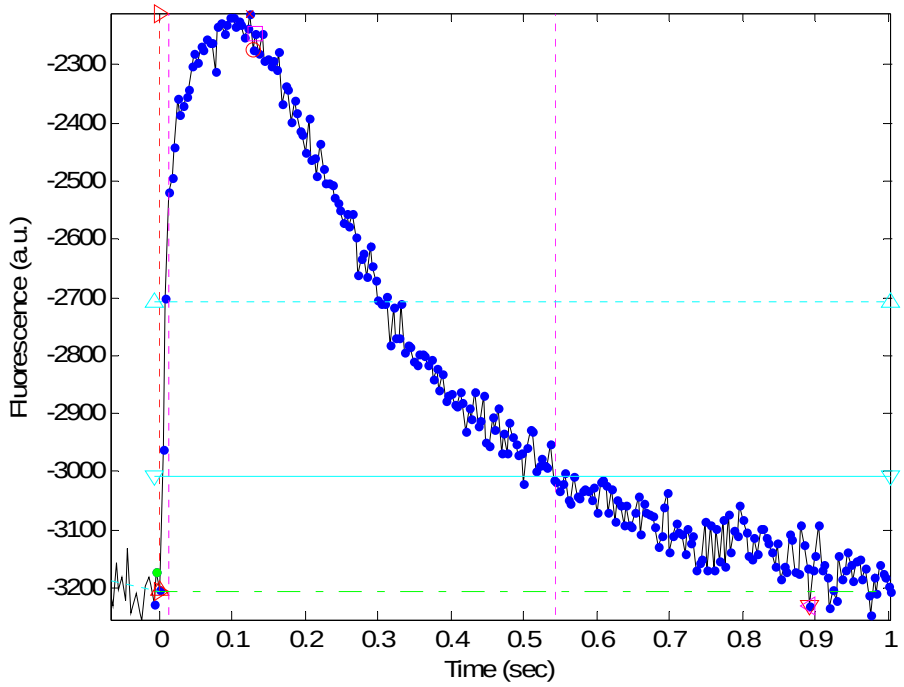

Figure 10-4 Waveform analysis: annotated example transient.
The first transient from Figure 10-1 in detail. Shown are recorded data points in blue dots and the closest datum point to the starting time as green dot. The maximum positive dF/dt is plotted as an upwards pointing red triangle (coinciding with the start time indicated by right pointing red triangle); the most negative dF/dt is plotted with red downwards pointing triangle (superimposed on the estimated end of signal as determined by average dF/dt falling below threshold value, denoted here as purple leftward pointing triangle). Additional annotations include the departure threshold (cyan broken line with upwards pointing cyan triangles) and return threshold (cyan broken line with triangles pointing down) as well as the baseline (broken green line) and start time, $i_{start,adj}$ shown here as red vertical dashed line with red rightwards pointing triangles. The times when the signal was estimated to cross the departure and return thresholds are marked in purple dashed lines. Maximum value attained is marked with red 'x', red circle is last value before sustained negative dF/dt, and the first sustained falling negative value is encircled in red.

Discussion

Future improvements to the algorithm include automatic threshold selection and dynamic envelope width. Currently, the user has to fine-tune five to six different parameters to get accurate transient event data. For analysis of movies where there are many channels all with potentially different characteristics requiring different parameters, the user cannot be expected to supply tens of thousands of 6-parameter sets for each pixel/channel. Thus, a more robust and intelligent selection method is called for.

Preliminary analysis, however, with recorded movies, has demonstrated that within reasonable bounds, the algorithm does appear to work. Perhaps the most difficult events to distinguish arise in the case of alternans. We have noted a gradual, continuous transition from clear 2:2 alternans, i.e. beat-to-beat variation in systolic intra-cellular calcium levels, towards 2:1 block, i.e. the second stimulus fails to elicit a response. As the system transitions (typically over space, but this can also be observed over time with continued high frequency pacing), the second alternating beat typically declines in amplitude until it becomes lost in the noise. For such conditions, it becomes impossible to distinguish extremely small amplitude "alternans" from noise alone, and thus the algorithm "fails".

The ability for the calcium transients to gradually diminish until they become buried in noise forces one to reconsider the "all-or-nothing" approach typically taken towards action potentials and borrowed for calcium transient analysis. Classifications of 2:2 alternans versus 2:1 blocks become subjective so long as a continuum exists. Such a paradox threatens the very definition of a transient as the second "alternans" transient can be examined by itself. In such a case, one can clearly see a gradual decline in systolic levels underscoring the idea that for calcium transients at least, a continuum exists rather than "all-or-none" response. Such behavior has also been observed when examining fluorescence data from cells stained with potentiometric dyes, but the poor signal to noise ratios and lackluster response of such dyes preclude a convincing argument of a continuum of graded action potentials.

The possibility of graded action potentials has great implications on propagation and expected spatiotemporal patterns. Instead of a Turing-like model where cells must occupy discrete, well-defined states, e.g. the typical four phases of an action potential, each cell instead exists in a continuum of activation "states". Propagation then would depend on a critical activation state which is not guaranteed to be constant across space or time. Much more complex spatiotemporal patterns would be expected from such a system which mimics a fuzzy-logic system.

Conclusion

We have developed a robust algorithm for detecting and characterizing transient events from fluorescence recordings of cardiac myocytes. We have implemented the algorithm in MATLAB and demonstrated its ability to discern transients even in conditions of poor signal to noise ratios, and verified its accuracy with independent human operators. Key limitations to the algorithm remain the requirement for the operator to fine-tune several parameters for transient detection, and thus the application of the algorithm to widely varying data such as encountered in spatial recordings of fibrillation or other less coherent/organized spatiotemporal patterns remains a significant challenge.

11. MULTI-PARAMETER STATE SPACE AND PHASE MAPS

Abstract

Visualization of massive quantities of data as collected from a HUMR requires appropriate methods. A common approach has been the use of return or phase maps. We compared the performance of several return mapping techniques in handling experimentally recorded fluorescence data with low signal to noise ratios. We demonstrate how frequency domain analysis via windowed Fourier transforms can result in superior noise rejection, and provide a rationale for seeking a linear phase transform.

Background

Cardiac cells and excitable cells in general, undergo periodic (stationary or non-stationary) changes in their state – distinct all-or-nothing excitatory events known as action potentials take place periodically. Identifying the *state of an excitable cell* (or the *phase in the cell cycle)* experimentally at any moment in time is complicated by the fact that the state is controlled by multiple state variables, undergoing non-linear changes in time, and that unavoidable noise contamination is present in the measurements. For example, in a mathematical model of a ventricular myocyte (the Luo Rudy model (Luo and Rudy 1994)) more than 10 such state variables are defined, including the transmembrane potential, ion channel gates and ion concentrations. Experimentalists normally monitor 1 or 2 of these state variables – typically, the transmembrane potential, V_m, and/or intracellular calcium, $[Ca^{2+}]_i$, in cardiomyocytes. From the measured state variable(s) the state of the cells or tissue is inferred. In that, the inferred information is our *best guess* at the actual state of the system. This guess can provide useful information about availability for a new excitatory event, important in electrical stimulation and cardioversion or defibrillation.

The values of the measured state variables, V_m and $[Ca^{2+}]_i$ – are not well suited as excitation history indicators – they are ambiguous due to their cycling nature within a single period. To avoid the ambiguity cardiac research has resorted exclusively to the use of a standard nonlinear dynamics approach – phase plane analysis. In this approach, given the signal for the experimentally measured state variable, a return map (RM) is created by the use of a time-shifted version of the original signal. A loop is formed in the phase plane for a truly cycling signal as the excitable cell is going through its discrete states within a period. Then, the trajectory along this loop is used as a *state tracking tool*. The utility of phase mapping for better outlining critical phase singularity spots (spatial locations encircled by the full range of phase values and having undefined phase angle themselves) and for improving visualization, has been recognized by Gray et al. (Gray, Pertsov et al. 1998) with the application of a *reduced version of the phase plane analysis* specifically for the image processing of spatial optical maps of cardiac arrhythmias. The method is reduced in that it uses the phase angle as a sole indicator of state and discards other determinants of the trajectory, such as the magnitude of the radius vector. This reduced RM implies cycling behavior, so that a phase angle can be extracted and related

to a state. Subsequent efforts in this regard have improved on the way RM are constructed to provide better phase angle estimates (i. e. better state tracking) from experimental data (Iyer and Gray 2001; Bray and Wikswo 2002; Rogers 2004).

The interest in the application of phase mapping for detection of *phase singularities (PS)* stems from our current understanding of lethal cardiac arrhythmias, such as polymorphic ventricular tachycardia (VT) ventricular fibrillation (VF) or atrial fibrillation (AF), which revolves around *reentrant mechanisms* (Moe 1962; Jalife, Gray et al. 1998; Chen, Wu et al. 2003). Thus PS, naturally occurring at the core of such reentrant activity, can yield condensed information about the existence and dynamics of a persisting arrhythmia (Gray, Pertsov et al. 1998; Valderrabano, Chen et al. 2003) or a pro-arrhythmic polarization, induced during a defibrillation attempt (Efimov, Cheng et al. 1998; Trayanova and Eason 2002). A strong correlation has been established between PS and wavebreaks (a major factor in the transition from VT to VF), thus confirming the utility of phase mapping for arrhythmia monitoring, characterization and prediction (Liu, Peter et al. 2003). Since theoretical studies have revealed that the extinction of spiral (reentrant) waves is extremely sensitive to the location and timing of the delivered electrical stimuli (Biktashev and Holden 1994; Biktashev and Holden 1998; Eason and Trayanova 2002), phase mapping can be potentially utilized for real-time electrical intervention (Pak, Liu et al. 2003)or for guiding ablation procedures in the heart (Pak, Oh et al. 2003).

In this paper, we approach the problem of state tracking from experimental time-varying signals by means not involving RM. Our analysis is based on two premises in the context of spatiotemporal analysis of cardiac arrhythmias:

1. In the conditions of insufficient information – i.e. inferred state of the system from measurements of 1 or 2 state variables, it might be beneficial to enforce uniqueness and linearity of state (phase) during a cycling period.
2. The classical (embedded delay) RM approach is sub-optimal for low SNR experimental signals (such as encountered during arrhythmias);

Our reasoning for the first premise is as follows. The purpose of introducing phase mapping was to avoid ambiguity from the original measurements. During periods of little change in the measured state variable, V_m or $[Ca^{2+}]_I$, the phase is ambiguous. For example, RM-based phase values remain constant or almost constant during the plateau or during the diastolic interval, yet the state of the system is probably changing, especially in high frequency pacing conditions. Instead of trying to mimic the morphology of the recorded state variable (as in the RM approach), we propose to assign unique phase/state to each time moment of the cell cycle. In the simplest case, this can be achieved through linear interpolation between consecutive moments of excitation. This assumes that the cell never exactly "comes to rest", which is reasonable for driven cardiac cells or re-entrant activity at rapid activation rates. We demonstrate this idea by presenting ATIP (activation time interpolated phase), which is a good state tracker in conditions of insufficient information about a (complex) oscillating system and tolerable levels of noise.

The function of the secondary periodic function in phase plane analysis is to resolve ambiguities, i.e. separate the pathways of excitation and recovery, thus creating a loop for each cycle. Using a version of the original signal as a secondary function (embedded delay(Gray, Pertsov et al. 1998), Hilbert transform(Bray and Wikswo 2002) or integral(Rogers 2004)) preserves or even may enhance the noise in the measurement, thus hindering its applicability for low SNR conditions. Such recordings are normally encountered in mapping clinically-relevant cardiac arrhythmias, esp. ventricular fibrillation, and particularly in regions of interest – i.e. PS regions. As the imaging of these phenomena is brought to the cellular level, as demonstrated in this paper, SNR problems are even more pertinent (Entcheva, Lu et al. 2000). **What is needed to handle the low SNR is a noise-free secondary function matching the local frequency of the original signal.**

This paper combines the two ideas into a conceptually simple noise-immune version of the ATIP state tracker by using STFT-phase (a Short-Time Fourier Transform based phase extraction). This non-traditional application of Fourier analysis focuses on the phase associated with the local (in time) dominant frequency in the signal. Unlike traditional RM approaches, the STFT-phase outputs not only phase and frequency information, but also power, which can be used as a confidence measure for the state determination. We demonstrate that this approach for inferring state possesses superior noise immunity. For signals with certain level of local stationarity, an apparent increase in temporal resolution can be achieved via interpolation due to the linear nature of the obtained phase readings. We validate the technique using model-simulated data and demonstrate its applicability in the spatiotemporal analysis of optically recorded cardiac arrhythmias in engineered cardiac cell networks (Bien, Yin et al. 2003), where the SNR issues are particularly relevant.

Experimental and Computational Methods

A. Experimental optical recordings of transmembrane potential and intracellular calcium in engineered heart tissue constructs (EHTs)

Experimental data on intracellular calcium and transmembrane potentials were collected from engineered heart tissue constructs (EHT) using optical methods as described previously (Bien, Yin et al. 2003). Briefly, neonatal ventriculocytes were seeded onto an elastic polymeric scaffold and cultured for several days until a well-networked cardiac syncytium is formed. Samples were then stained with Fura-2 AM ester (Molecular Probes, OR) for intracellular calcium or di-8-ANEPPS (Molecular Probes) for transmembrane potentials imaging. Microscopic (single-cell) measurements were performed using a single channel photomultiplier tube (PMT) at 1kHz, while macroscopic recordings covering an area approximately 8x8mm were made using an intensified CCD system (MTI-Dage) at 60 frames per second (Bien, Yin et al. 2003; Entcheva, Bien et al. 2004).

B. Algorithmic and Computational Issues

Short-time Fourier analysis of acquired spatial video sequences was performed by speed-optimized custom-written software in C/C++ and Matlab. Model computations of action potentials were also implemented and executed in C/C++. Experimental recordings were imported into the analysis software as ASCII single channel fluorescence traces in time or as multi-page tiff images in time for spatial optical maps. The raw fluorescence signals were used

for all calculations presented here after baseline subtraction and stretching to maximize the dynamic range.

B1. Synthetic model signals

Synthetic model action potentials for testing the various methods of estimating phase were generated using the Luo-Rudy (LRd) model (Luo and Rudy 1994; Faber and Rudy 2000; Hund, Otani et al. 2000) computed using time integration with a variable step size, and interpolated at some sampling frequency, F_s.

B2. Return map (RM) – based phase calculations

Return maps were constructed by parametric plots of the presumed periodic cardiac signal, *x(t)*, and a secondary periodic function formed by some transformation of the original signal, *T[x(t)]*, to resolve ambiguities in repeated signal values over time. The angle obtained from the return maps as the four-quadrant arctangent about the center of rotation (assumed to be at the origin) was then used to estimate phase:

Eq. 11-1)
$$\phi(t) = \tan^{-1}\left(\frac{x(t)}{T[x(t)]}\right)$$

Traditional Embedded Delay Return Maps (**EDRM**) simply use a time-shifted (delayed) version of the original signal as the secondary function, *T[x(t)]*. In this study, the delay τ is chosen to be roughly ¼ the duration of the action potential / transient duration as per Gray et al. (Gray, Pertsov et al. 1998; Iyer and Gray 2001).

An alternative approach, implemented here, involves a constant phase shift as opposed to a constant time-shift (Keener 2000; Bray and Wikswo 2002). Using the inherent $\frac{-\pi}{2}$ phase shift in the imaginary component of a Hilbert-transformed signal, *H(x(t))*, as the secondary function, *T[x(t)]*, avoids the need to specify *ad hoc* a time delay and permits analysis of signals with time-varying frequencies. The Hilbert Transform Return Map (**HTRM**) involves the calculation of the Cauchy principal value *P* of *x(t)*. Note that the HTRM method is known as a way to obtain *instantaneous frequency* using the derivative of the phase with respect to time. Yet another recently proposed technique (not implemented here) uses the integral of the original signal as a secondary function to produce an Integral Return Map (**IRM**) (Rogers 2004).

Eq. 11-2)
$$T[x(t)] = \begin{cases} x(t-\tau) \rightarrow EDRM \\ \mathrm{Im}[H(x(t))] = \mathrm{Im}\left[\frac{1}{\pi} P\left[\int_{-\infty}^{\infty} \frac{x(T)}{t-T}\, dT\right]\right] \rightarrow HTRM \\ \int_{-\infty}^{t} x(T)\, dT \rightarrow IRM \end{cases}$$

For all RM-based methods, it is particularly important to ensure zero mean value of the signal over time in order to locate the centroid about the origin for phase extraction. We

accomplished this by a method similar to previous approaches (Bray and Wikswo 2002; Rogers 2004). More specifically, a piecewise cubic Hermite interpolating polynomial was fitted using the data point just prior to the start of every excitation event, where the value of the signal is assumed to be at rest, and then subtracted from the original data. This method ensured true correction of oscillations in the diastolic levels of the signals. Then, to eliminate the DC bias component, the mean value of the signal over the entire recording epoch was subtracted.

B3. Activation-time interpolated phase (ATIP)

In contrast to return map – based approaches, we introduce as a control an intuitive *linear phase* calculation based on activation time. The basis for this approach is provided by the defining characteristic of activation – the rapid change during depolarization or calcium entry where the signal should change monotonically over a certain period of time. This is the ideal technique for tracking state (phase in the cycle) in noise-free signals.

The practical implementation of finding the maximum upstroke velocity point (activation time) here involves the calculation of a difference signal $\Delta x(t)$ by subtracting a time-shifted signal from the original signal, which enhances the apparent rate of change of the upstroke while suppressing zero-mean noise:

Eq. 11-3)
$$\Delta x(t) = \frac{x(t) - x(t - j)}{j}$$

The number of samples shifted, ***j***, is set to be the minimum duration of the upstroke. Points in time where $\Delta x(t)$ exceeds a predefined threshold set as some factor, ***s***, of the standard deviation, σ, are then considered candidate transient activation times:

Eq. 11-4)
$$\Delta x(t) > s \cdot \sigma$$
$$\sigma^2 = \frac{1}{N-1}\sum_{k=1}^{N}(\Delta x(k) - \Delta\bar{x})^2$$

To eliminate duplicate activation times as might arise by especially prolonged upstrokes, two additional criteria must be met. Between every two successive transients there must be a minimum number of samples ($w_{\min}$) reflecting the shortest possible transient, and a signal value that exceeds the starting level of the next transient, i.e. requiring a local extremum to occur between the two transients.

The phase is then simply computed as a linear interpolation from $-\pi$ at the start of the transient to $+\pi$ right before the start of the next transient. For the kth excitation event, the phase would be:

Eq. 11-5)
$$\phi(t)_k = 2\pi \frac{t - t_{act}(k)}{[t_{act}(k+1) - 1/Fs] - t_{act}(k)} - \pi \Bigg| \quad t_{act}(k) \le t < t_{act}(k+1)$$

where $t_{act}(k)$ is the time of activation for the k^{th} transient and F_s is the frequency of sampling.

B4. Short-time Fourier Transform (STFT) for phase determination

In this study, we adopt a new dynamic in time Fourier-based calculation of phase. While a standard Fourier transform lacks temporal information as to when a particular frequency was encountered, the Short-time Fourier Transform (STFT) or windowed Fourier transform yields a frequency spectrum for every instant in time (Gabor 1949; Nawab, Quatieri et al. 1988). STFT is performed by multiplying the signal *x(t)* with a sliding window of a specified width *h(t)* before applying the Fourier transform $\Im(\omega,t)$.

Eq. 11-6)
$$\Im(\omega,T)=\int_{-\infty}^{\infty}x(t+T).h(-t)e^{-i\omega t}dt$$

The discrete version of the STFT was performed with a Hamming window; and typically zero-padding was used at the end as needed to improve the apparent frequency resolution:

Eq. 11-7)
$$F(q,t)=\sum_{k=1}^{N}h(d,k+t)x(k)\omega_N^{(k-1)(q-1)}$$
$$\omega_N=e^{(-2\pi i)/N}$$
$$h(d,m+1)=0.54-0.46\cos(2\pi\tfrac{m}{d-1})$$

In Eq. 7, *F(q, t)* is the Fourier transform for the q^{th} frequency bin at time *t*, and *h(d, m)* is the m^{th} coefficient of the symmetric Hamming windowing function of width *d*. *N* is the number of frequency bins for the fast Fourier-transform (FFT), and ω_N is the normalized frequency.

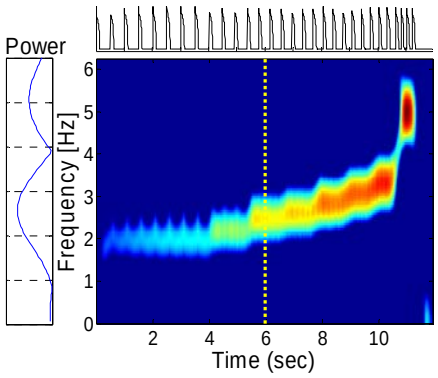

Figure 11-1 Example STFT analysis of non-stationary signal.
The spectrum over time is shown in color with the color representing the amplitude, the y-axis the frequency, and the x-axis the time instant. Also ploted are the original signal (above) and the average spectrum (left).

STFT analysis of a non-stationary signal is illustrated in **Figure 11-1**. The temporal signal consisted of an LRd model action potentials paced at progressively increasing frequencies between 2 and 5Hz. The applied Hamming window (with tapering ends) was about 1sec in duration, and 2^{11} frequency bins were used. The power-frequency spectrum for a selected moment in time (dotted line at 6 sec after the start) is shown in the left panel. The two visible peaks represent the dominant frequency (2.5Hz at this time instant) and the first harmonic.

In traditional applications of STFT, the time-specific frequency spectrum is the useful output, as for example used previously in a cardiac application (Choi, Nho et al. 2002). Here, for the purposes of state tracking we focus on the *phase of the detected dominant frequency (DF)* at each spatial location. The selection of DF was not ambiguous because of the highly localized nature of the measurements in this study – PMT recordings were at the single cell level, while spatial measurements were also with much higher resolution (even after binning <80x80μm per pixel) than used in most optical mapping studies before.

For each moment in time, the dominant frequency (DF) was determined as the frequency bin q^* with the highest magnitude excluding the 0 frequency bin (DC component) and the negative frequencies. The phase angle was then calculated as the argument of the STFT, i.e. the angle formed by the imaginary and real parts of the Fourier transform at the DF:

Eq. 11-8)
$$\phi(t) = \arg\left(F(q^*, t)\right) \tag{8}$$

Unlike the Hilbert transform, the DF in STFT is not instantaneous, but a *local frequency*, i.e. it has a more intuitive meaning for local signal characterization. Since the excitation events are not perfect sinusoidal signals and are not symmetric, the phase returned by the STFT

should be corrected to align the start of a transient to the -π phase. Factors affecting the absolute phase offset in STFT and a strategy for optimization is outlined in Appendix 1.

B5. Phase estimation accuracy and noise susceptibility analysis

The accuracy of phase as determined by a particular method was assessed by plotting the detected phase against the fraction of basic cycle length (BCL), determined using ATIP to detect the start of an excitation event. A linear regression line was constructed relating estimated phase versus phase in BCL, determined as linear clock from beginning to end. The error in phase estimation was defined as a deviation from this regression line.

A noise vector of the same length (N) as a model signal was generated using zero-mean Gaussian-distributed numbers with a standard deviation of 1. To obtain various noise levels, this vector was then scaled by a factor $\boldsymbol{u}$ and added to the original (clean) model signal. The peak-to-peak signal-to-noise ratio ($\boldsymbol{SNR}_{p\text{-}p}$) was calculated as the signal amplitude determined to be maximum value attained since the model data's baseline was set to 0, divided by the root mean square (RMS) value of the scaled noise vector, *noise*:

Eq. 11-9)
$$SNR_{p-p} = \frac{\max(x(t)) - \min(x(t))}{\sum_{k=1}^{N} \sqrt{\frac{noise(k)^2}{N}}}$$

Results

Time-varying signals and STFT phase determination

Time-varying (non-stationary) signals are characteristic for cardiac arrhythmias. While ventricular fibrillation (VF) has often been described as "chaotic", previous studies have demonstrated a restricted range of frequencies encountered. For example, the range of frequencies observed in VF of Langendorff perfused rabbit heart was 14±2~3Hz (Choi, Nho et al. 2002). In this study, we generated a test time-varying signal (LRd), where activation occurred in a random fashion at 3.6±1.8Hz with maximum instantaneous change 42%. The fully random beat-to-beat behavior is unlikely in actual arrhythmias, but was chosen to challenge the STFT-phase algorithm. The maximum instantaneous frequency jump allowed was also larger than typical for experimental VF – 30% between 14 to 17Hz was reported in (Choi, Nho et al. 2002). The lower absolute value for the model frequencies better matched our cooled EHT constructs, where maximum sustained activations were at lower rates.

Phase was determined in these noise-free signals using all four modalities: EDRM with τ=10 samples (40ms), HTRM, STFT using 2^{15} frequency bin and a sliding Hamming window of 255 samples (approximately 1s) wide, and ATIP (j=4ms, s=2.0, and w_{min}=100ms). **Figure 11-2** presents a comparison between all phase evaluation methods, with a trace on the bottom showing the random BCL during the time course of the signal.

The lack of noise in the model system made ATIP phase determinations ideal in that upstrokes were precisely identified and the baseline remained fixed throughout. EDRM and HTRM appeared as inverted images of ATIP phase, reflecting merely the arbitrary sign

convention corresponding to the direction for rotation in the return map. Note however that while STFT is almost identical to ATIP, traditional return map approaches - EDRM and to a lesser degree HTRM - demonstrate regions of non-linearity and even phase ambiguity (phase during diastole and portions of the plateau remains the same). STFT phase has a minimal drift with regard to ATIP especially at dramatic frequency shifts due to the Fourier-based nature of STFT.

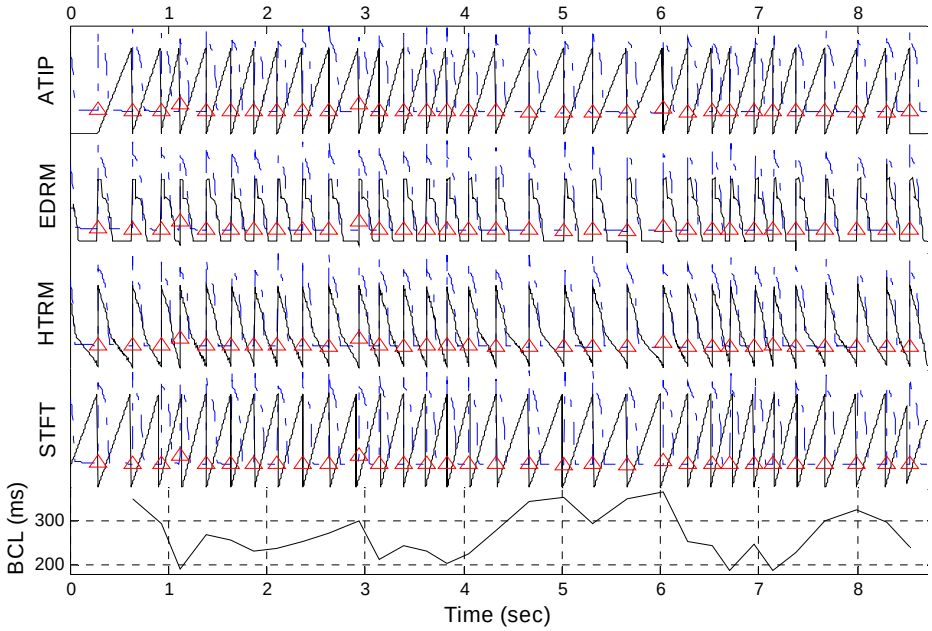

Figure 11-2 LRd signal paced at random intervals at 3.6±1.8Hz with maximum instantaneous jump of 42%.
The phase estimated using the various methods labeled on the left is plotted in solid black lines, while the dot-dashed line in the background represent the original transmembrane potential signal used for analysis. Red triangles mark the start of the action potential as determined by ATIP. The bottom panel is a trace of the interval between stimuli, or the basic cycle length (BCL).

Improved noise rejection when using STFT-phase

The experimental utility of any state tracking method depends on its noise rejection properties. When fluorescence measurements are performed at the scale of a single cell or a layer of cells, the signal-to-noise ratio in the obtained recordings is often very low due to the combination of low quantum efficiency of the fluorescent dyes for voltage and calcium and no integration over tissue mass. Up to 2 orders of magnitude weaker signals can be observed (Entcheva, Bien et al. 2004) compared to whole heart measurements(Baxter, Mironov et al. 2001). To explore this aspect, the clean LRd signal was corrupted with zero-mean additive Gaussian noise with scale factors u ranging from 10 to 50 yielding SNR_{p-p} of 12 down to

almost 1. An example of the test signal at SNR_{p-p} of 6 and 2 are shown next to the original signal in **Figure 11-3**.

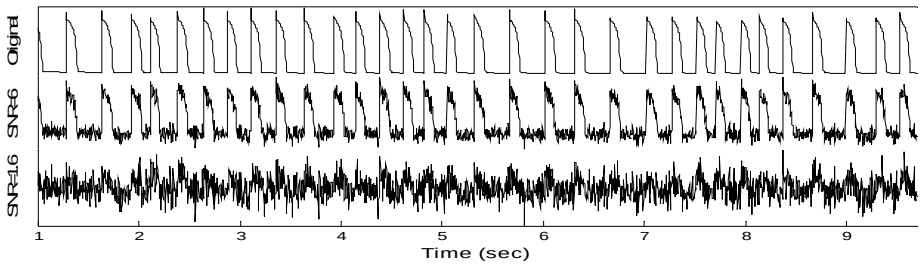

Figure 11-3 Example LRd signals corrupted with zero-mean additive Gaussian noise.
Two different SNR levels are shown with the original, uncorrupted signal on top.

The ideal linear phase of a noise-free LRd signal was obtained through ATIP. Therefore, the results of phase estimation of the various methods at different SNR_{p-p} levels were compared against ATIP-derived phase of the clean signal. The error analysis is shown in **Figure 11-4**. For comparison, a random sequence of numbers ranging from $-\pi$ to $+\pi$ was used as an uncorrelated control against which ATIP phase was fitted yielding RMSE around 2.0. As expected, ATIP performance suffered dramatically as SNR_{p-p} decreased due to its confusion of true upstroke events with noise spikes. EDRM and HTRM were relatively immune to noise until SNR_{p-p} decreased to about 6 whereas STFT was able to properly detect phase down to SNR_{p-p} of <1.6. Even at SNR_{p-p}=1.03 where the amplitude of the noise is roughly the same as that of the signal itself, the RMSE of STFT-phase was only about 0.4 (**Figure 11-5**). The absolute vertical offset (error) of EDRM, HTRM and STFT at high SNR_{p-p} (>12) reflect the particular choice of phase $-\pi$ (with respect to the activation time) and possible non-linearities in the phase during the cycle (this particularly holds for EDRM). More informative in assessing noise susceptibility is the relative change in error when SNR_{p-p} drops. For the range of SNR_{p-p} (12 to 1) shown in **Figure 11-4**, this relative increase in error was 1.9, 1.4, 1.2 and 0.3 radians for ATIP, HTRM, EDRM and STFT, respectively. The inherent filtering property of the STFT-phase method was clearly demonstrated in this analysis. While most experimentalists routinely apply heavy filtering to the raw signals prior to any phase analysis, it is virtually impossible to design a conventional filter without phase distortion for non-stationary cardiac action potentials with a morphology including a sharp upstroke and slow recovery.

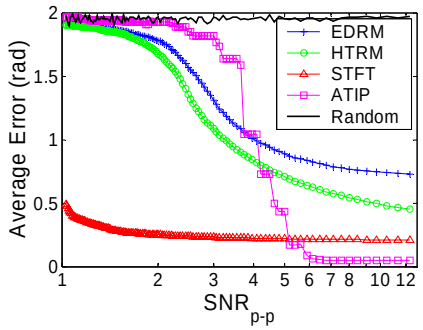

Figure 11-4 Impact of zero-mean Gaussian additive noise on various phase estimation methods.
Shown are the average phase errors (in radians) at different noise levels quantified by the peak-to-peak signal to noise ratio (SNRpp). Increases in error from SNR of about 12 to SNR of 1 were 1.2, 1.4, 0.3 and 1.9 radians for EDRM, HTRM, STFT, and ATIP, respectively. A purely random phase would result in average phase errors of about 2 radians.

Subframe temporal resolution using STFT-phase (software strobing)

Acquisition rate in optical mapping with high spatial resolution is limited by the data flow capacity of the computer interface and by the levels of the measured fluorescence (how long of an integration period is needed to obtain useful SNR). For signals exhibiting some repeatable pattern and local stationarity in time, strobing can be considered. Because of the Fourier roots of the STFT approach and its pattern searching ability, it is possible to obtain an apparent higher temporal resolution (or *subframe resolution*) than the acquisition rate used. This idea is the software analog of hardware-implemented strobing, which has been used in cardiac mapping before(Lin, Abbas et al. 1997). To demonstrate the subframe resolution property of STFT, we used time-varying model (LRd) action potentials sampled at 1kHz (**Figure 11-6**). The resultant signal was then further down-sampled every 20^{th} point to achieve a 50Hz effective resolution signal which was used for STFT phase analysis using 2^{15} frequency bins and a Hamming window width of 51 samples (roughly 1s). A sub-resolution 1 sample (1ms) shift was then introduced in the 1kHz data and the resultant shifted signal down-sampled again to 50Hz. Activation time, i.e. when phase was equal to $-\pi$, was estimated by interpolating between STFT computed phases using Eq. 11-10 where t_{act} is the activation time, (t_1, ϕ_1) and (t_2, ϕ_2) are the time/phase pairs of two successive data points that have a difference close to 2π. To achieve robustness in the selection of the start of an excitation event, adjacent points with differences greater than π, i.e. $(\phi_2-\phi_1)<-\pi$, were used.

Eq. 11-10)

$$t_{act} = t_1 + \frac{\pi - \phi_1}{r}$$

$$r = \frac{(\phi_2 + 2\pi) - \phi_1}{t_2 - t_1}$$

For comparison, ATIP was performed to determine the true activation time using the 1kHz data with a threshold setting of twice the standard deviation and a minimum transient duration of 25ms, and the same settings were applied for the reduced sampling rate signal ATIP. None of the other state trackers considered here have similar ability – to offer subframe temporal resolution in the acquired signals.

While STFT-phase demonstrated remarkable noise immunity and accuracy in determining phase with superior temporal resolution in the idealized LRd model, several significant differences exist between the LRd action potential (modeled after a guinea pig cardiomyocyte) and experimental signals recorded using optical techniques from our EHTs constructed from neonatal rat ventriculocytes. The most striking difference is in the action potential (or calcium transient) duration and subtle beat-to-beat variations inherent in a biological system not otherwise accounted for in a perfect idealized model. Therefore, STFT-phase analysis was further extended to experimental 1D and 2D signals.

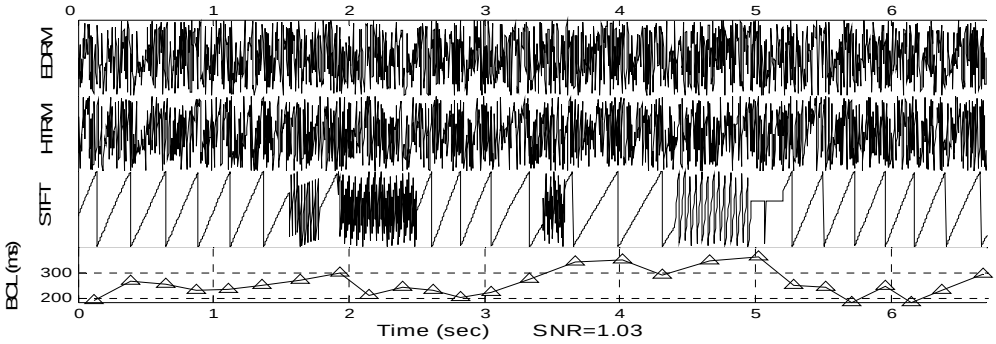

Figure 11-5 Phase estimation at minimum SNR (1.03) demonstrates failure of EDRM and HTRM.
STFT contains errors only in regions of large frequency changes as expected from its Fourier roots which expect a stationary signal.

Phase by STFT in experimental VF-like recordings

Intracellular calcium concentrations in EHTs undergoing self-sustained, irregular, spontaneous activation (VF-like activity) was recorded with a PMT at 250Hz. After baseline subtraction, experimental data were analyzed using all four phase estimation methods. STFT was performed with 2^{15} frequency bins and 251-sample wide Hamming window. EDRM using τ=10 samples and HTRM phase estimates were compared against ATIP (j=1 sample, s=1.2SD threshold, w_{min}=100ms minimum duration). For these experimental data the $SNR_{p\text{-}p}$=7.8 using Eq. (9), considering the amplitude of the variations during baseline (isopotential) periods as the RMSE of noise. At this noise level, ATIP was still able to reliably detect upstrokes and hence

yielded perfect linear phase regardless of frequency changes. As shown in **Figure 11-6**, noise in the data caused sharp spikes in detected phase using EDRM and HTRM (they appear as thick, vertical bands). The same signal analyzed using STFT showed no such defects, and even abrupt frequency changes were handled well. In this experimental recording frequencies were around 7.2±0.7Hz with maximum instantaneous changes of 35%, similar to previous reports of VF in whole heart preparations (Gray, Pertsov et al. 1998).

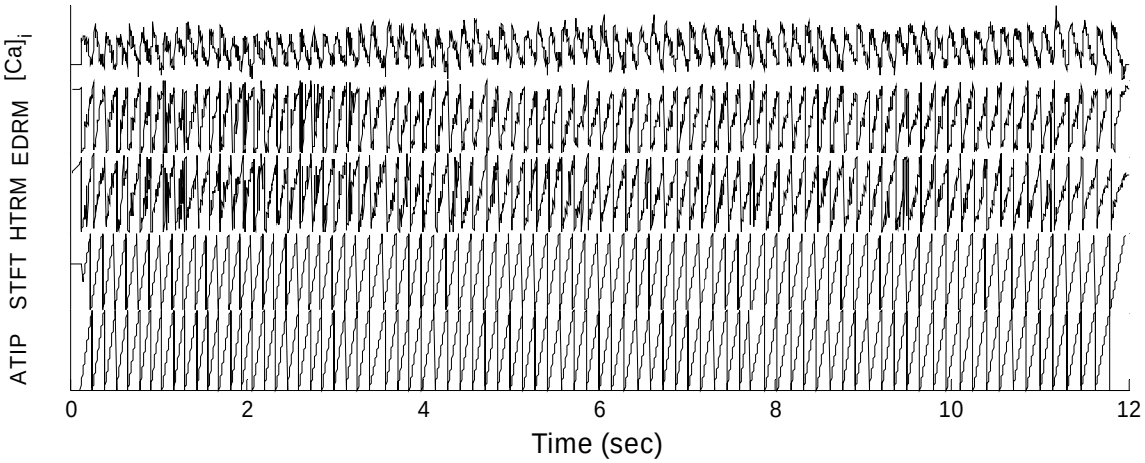

Figure 11-6 Phase estimation of spontaneously active EHTs demonstrates the robust nature of STFT in adverse noisy environments.
Shown above are phase over time of experimentally acquired intra-cellular calcium signals from fluorescently stained, spontaneously active EHTs. While HTRM and EDRM tracks the phase, the STFT and ATIP have much less noise.

Discussion

Analysis of dynamic time-varying signals, such as encountered during cardiac arrhythmias, brings into focus an important duality: instantaneous vs. global frequency or tracking. Return map – based methods for phase calculation are on the one side of the spectrum, while traditional Fourier analysis is on the other side of the spectrum. Even within the EDRM approach, the choice of the embedded delay reflects the duality mentioned above – how close should the secondary periodic signal follow the original and what consequences does this choice have on noise susceptibility or interpretation? Interestingly, the recent heated debate about the nature of fibrillation (Berenfeld, Pertsov et al. 2001; Choi, Liu et al. 2001) was based on perceived weaknesses in the analysis methods, illustrating exactly the duality discussed here. Methods dealing with instantaneous tracking and instantaneous frequency (EDRM, HTRM) are perfect in following sudden changes in time, but are naturally more susceptible to noise, while Fourier-based techniques act as effective low-pass signal smoothing filters. Additionally, instantaneous frequency does not carry intuitive, meaningful information when analyzing the dynamics of the system; it obscures the sequence of important excitation events by zooming in on a particular time point. In arrhythmia analysis, there is a fragile balance between instantaneous tracking and total loss of local information in time, and this balance can be provided, in our opinion, by the STFT-phase approach.

Although implementation of RM techniques is simpler, conceptually STFT-phase seems the natural choice for phase mapping, particularly in the context of PS detection, as argued below. While performing calculations for PS localization, each point is represented only by an angle value (the phase angle value). Thus, the RM technique, which also carries information about distance from the point of origin (magnitude of oscillations), useful in non-linear dynamics analysis, has been stripped to a mere angle calculation when applied to *spatial phase mapping* (Gray, Pertsov et al. 1998; Bray and Wikswo 2002; Rogers 2004). Ironically, the information richness of the RM approach (encoding also variations in the radius vector) becomes a noise-introducing feature, since it complicates the choice of origin while calculating the phase angle. An ideal secondary periodic signal used to wrap around the original signal in the phase plane, should only be concerned with the frequency of the original signal and not with the magnitude of the oscillations. **Thus the problem of constructing a phase map for angle extraction becomes one of detecting frequency in a time-varying signal, in order to apply a simple secondary signal, *y(t)***. STFT phase calculations ignore phase map features and provide noise-resistant angle information. The result is a linear phase, very much like in the ATIP approach. However, unlike the ATIP method, the STFT ultimately turns out to be superior in localizing PS, where SNR dramatically drops and RM-based techniques (or ATIP) become inadequate.

STFT-phase mapping, as proposed here, is more than a tool for phase singularity detection. It provides additional benefits as summarized below:

1. Inherent filtering properties and superior noise immunity allow applicability in low SNR conditions and help reveal subtle, otherwise invisible, propagation events (compare quality of 2D phase maps). This property also facilitates better PS localization. Even though, researchers using traditional RM-phase approaches apply substantial filtering prior to phase calculations (to avoid low SNR interference), the filtering provided naturally by the STFT-phase calculation is superior, as it is executed in the frequency domain.
2. As a corollary of the linearity of STFT phase, interpolation of phase is possible and an apparent increase of temporal resolution (subframe resolution) can be achieved by software means. This feature can be exploited in low-light level conditions where further increase in the acquisition rate is not possible. Note that even though ATIP also offers linear phase, interpolation is not possible because ATIP's determination of transient/action potential start times uses acquired data points and cannot distinguish between sub-frame depolarization changes. Additionally, linearity of phase (in STFT and ATIP) avoids ambiguity during diastolic intervals providing a clock, as it were, during diastole. Note that in RM (especially in EDRM with low delays), track of time

in diastole (diastolic interval) is not possible and implies the cell remains at a constant state throughout diastole. A good analogy would be the pressure-volume loop in a cardiac cycle – during diastole if one were to monitor merely the pressure, one would see very little changes during diastolic filling, yet the heart's volume is rapidly changing over time.

3. STFT-phase calculations yield as a byproduct a full time-specific frequency spectrum and confidence measure (power) for the calculations. This can be extended into a powerful tool for quantitative characterization of complexity of the spatiotemporal phenomena. The spectral information can reveal deeper levels of dynamic behavior – alternans etc. Because of the non-instantaneous nature of the frequency information provided by STFT, it can also be used for analysis of spatial frequency domains and their dynamics in time, as proposed previously (Zaitsev, Berenfeld et al. 2000).

While the number of frequency bins may not seem excessive given the large memory capacities of modern computers, two-dimensional STFT analysis of high resolution images will require an inordinate amount of signals to be analyzed (each pixel results in a signal trace), and combined with the dramatic increase in computational demand due to the slowly sliding time window of STFT makes any additional size increases impractical. Nevertheless, dedicated hardware FFT implementations may easily remove this barrier and digital signal processing (DSP) chips can be programmed to make real-time high resolution STFT a reality.

Given today's limitations in processing power, we have found the Hilbert transform technique to be vastly faster than STFT. Despite its sensitivity to noise, the Hilbert transform is an extremely rapid and versatile technique that can be applied to experimental signals after spatial and/or temporal filtering to improve SNR. In many ways, the comparison between Hilbert transforms and STFT is not really valid, as they can be shown to be mathematically equivalent(Bruns 2004). Therefore, for efficiency we have often choose to use instead the Hilbert transform.

There are situations, however, where the Hilbert transform is lacking compared to STFT. While both the Hilbert and STFT use Fourier-type decomposition, the Hilbert transform relies on an inverse Fourier transform to yield an imaginary result. Therefore, although the Hilbert "traverses" the frequency domain, one cannot perform frequency-domain analyses. One of the spectral (frequency domain) properties that might prove useful is the phase of a signal. As indicated earlier, the Hilbert transform only provides instantaneous phase and cannot provide an estimate of lower-frequency signals. For instance, the cardiac action potential at 1Hz is composed of many different instantaneous frequencies, but a strong peak can be detected at 1Hz due to the repetitive signal. The Hilbert transform can never recover this lower frequency, and therefore the phase information from these "local" (as opposed to instantaneous) frequencies is lost.

When phase analysis is carried over to analyze 2-D images over time, one would like to correlate signals from one location with respect to its neighbor. Auto-correlation techniques have been used previously to examine correlation length during ventricular fibrillation(Bayly, KenKnight et al. 1998). Comparison of phase differences between two adjacent regions has not been performed directly. Such an analysis would permit one to estimate conduction delays, i.e. blocks, and identify out-of-phase regions for higher-order patterns such as occurring in alternans (beat-to-beat variations). STFT provides the opportunity for exactly such comparisons and a phase difference map to be generated that can highlight regions of phase shifts at selected frequencies.

The method should be applicable for many areas outside cardiac mapping. It is particularly well suited for problems involving: (1) periodic changes in highly complex systems, with limited number of observable variables and very high levels of noise; (2) need for high temporal resolution of identifying a state in a system's cycle (or phase). Experimental tracking of phase differences in a coupled oscillator type of system might be a potential application. The method can be generalized to utilizing measurements form more than one state variable by combining their STFT-phase estimates through a multi-entry state predictor, such as a Kalman filter of Bayesian estimator.

Limitations

Co-existing frequencies at a given location, such as in alternans, present a problem for phase mapping, in general. STFT is no exception, since it only deals with the dominant frequency and its associated phase. STFT does provide full spectrum information, thus the other frequencies are recoverable, as long as a visualization approach is found to represent them. Another typical problem in traditional STFT analysis, not phase-related, is the choice of time vs. frequency resolution (the uncertainty principle). Most methods developed for improving the frequency resolution (Choi, Nho et al. 2002) are not compatible with phase mapping, since they do not return phase. Extensive zero-padding, found here to have a positive effect on the determination of absolute phase, is also known for increasing the apparent frequency resolution.

Limitations of the method proposed here include its more restrictive nature compared to classical phase plane analysis. Just like the reduced RM, it assumes periodicity in the observed signals. Additionally, even though it successfully handles time-varying signals, very high degree of non-stationarity will cause less than optimal performance – for example, the subframe resolution will be hard to achieve, and absolute phase estimates might become less reliable.

In conclusion, the STFT-phase approach has direct utility for the experimentalist, mapping complex arrhythmias in low SNR conditions. This is especially important when dealing with optical mapping in engineered cardiac tissue constructs, a new emerging area of arrhythmia research.

Mapping of arrhythmias in EHTs can resolve important debates in cardiac arrhythmia research, due to simplicity and lack of complicating structural details introducing ambiguity in whole heart optical mapping. The spectral phase mapping approach, presented in this study,

together with the experimental demonstration of complex spatio-temporal patterns in this model system, might become powerful tools for improved understanding and prevention of lethal arrhythmias.

Appendix 1

Parameter optimization and phase alignment for STFT

The major factor affecting STFT performance is the size of the windowing function. Large (long duration) windows enable high frequency resolution at the expense of poor temporal tracking whereas short durations enable tracking of relatively non-stationary events but poor frequency resolution, according to the uncertainty principle. We have found that a window size of approximately 1.5 to 2 times the duration of the lowest frequency signal to be optimal in detecting the dominant frequency while tracking rapidly changing signals. However, even purely stationary sinusoidal signals will yield phase offsets if the window does not contain an exact multiple of the wavelength. Therefore, a fixed window size will yield varying phase offsets for signals of different frequencies.

Zero padding

The degree of phase offset due to incomplete windowing was assessed by performing standard FFT analysis on pure sinusoidal signals of frequencies ranging from 1Hz to 5Hz and sampled at 1kHz, windowed at lengths varying from an exact multiple of the signal period (thrice the period) to one sample short of the next multiple.

We tested whether zero-padding, a commonly employed technique to improve the frequency estimates from FFT analysis is zero-padding, where the signal is extended in time by appending a series of zeros, would impact phase errors by gradually adding zeros of increasing length to the sinusoidal signal described above and analyzing the maximal phase offset error encountered. Zero-padding is useful when the window duration is short in terms of samples, limiting the frequency resolution as noted earlier. Since the windowing function tapers off to zero at either end, zero-extension merely reduces the granularity of the FFT frequency result without necessarily increasing the true frequency resolution or resolving ability. An unexpected benefit of zero-padding the signal in addition to the improved ability to specify the dominant frequency was observed in that the maximum phase error due to window lengths not exactly equal to a multiple of the signal period decreased as the zero-padding increased. Therefore, for STFT calculations of phase, we have employed extensive zero-padding near the memory limits of the workstation, namely 2^{15} (32,767) frequency bins.

Signal morphology

Despite extensive zero-padding, due to the asymmetry of the signals (fast upstroke with slow repolarization), the STFT phase tended to align more towards the middle of the interval between two events rather than at the start of the first transient. To correct for the asymmetry, the LRd model paced at selected frequencies ranging from 0.5 to 6Hz was used and the STFT phase at depolarization (as determined using ATIP analysis) was plotted against frequency. A strictly linear relationship emerged, confirmed also by further testing with experimental intracellular calcium restitution data. Combined with zero padding, this linear correction of frequency dependence is easy to implement.

For STFT analysis of new signals, we suggest first examining the STFT detected phase at the time of depolarization when the phase should have been $-\pi$. Then, by plotting the STFT dominant frequency against the phase offset from $-\pi$ one may construct a linear correction curve for asymmetric signals to be analyzed. Remarkably, the linear correction curve does not vary much despite great differences in morphology, e.g. the correction curve for very rapid and short LRd action potentials differed only slightly from the curve for slower rising experimental $[Ca^{2+}]_i$ transients. Thus, for scenarios where multiple-frequency (restitution) data cannot be analyzed, the application of the correction curve as derived for the LRd model may be substituted with little loss in phase accuracy.

Phase alignment is only necessary for correlation of the reported phase with the original signal. If no comparison of phase will be directly made, i.e. if only phase differences between different channels will be used, then phase correction is not necessary as the correction factor will automatically cancel out. However, in our experiments where we needed to compare several different phase calculation methods, it became imperative for us to align the phase to a common point in order to permit valid comparisons.

Appendix 2

Noise immunity of phase methods in tracking the state of a complex system

Consider the state of a complex system, including multiple state variables, $p_i(t)$, in noise-free conditions:

Eq. 11-11) $$S(t) = \{p_1(t), p_2(t),..., p_i(t),..., p_n(t)\}$$

In the presence of additive Gaussian noise, N(t), the state of the system becomes:

Eq. 11-12) $$S_N(t) = \{p_1(t), p_2(t),..., p_i(t),..., p_n(t), N(t)\}$$

The estimated state of the system, based on observation of a selected noise-contaminated state variable, $p_i(t)$:

Eq. 11-13) $$\langle S(t)\rangle \rightarrow \langle P_i(t)\rangle = \{p_i(t) + N(t)\}$$

For all RM-based approaches the excitability state (phase), φ_1, is calculated from observations of the transmembrane potential or the intracellular calcium concentration as a state variable, $p_i(t)$:

Eq. 11-14) $$\varphi_1 = \tan^{-1}\left(\frac{\langle P_i(t)\rangle}{T[\langle P_i(t)\rangle]}\right) = \tan^{-1}\left(\frac{\{p_i(t) + N(t)\}}{T[\{p_i(t) + N(t)\}]}\right)$$

The transformation function, $T[(p_i(t)]$, is the secondary periodic variable in any RM formulation, as shown previously in Eq. 11-2. In the presence of noise, the estimated value of this secondary function becomes:

Eq.11-15)

$$T\left[\left\langle P_i(t)\right\rangle\right]=\begin{cases}\left\langle P_i(t+\tau)\right\rangle=\left\{P_i(t+\tau)+N(t+\tau)\right\}\rightarrow EDRM\\ \mathrm{Im}(H(\left\langle P_i(t)\right\rangle))=\mathrm{Im}(H(\left\{P_i(t)+N(t)\right\}))=\mathrm{Im}(H(P_i(t)))+\mathrm{Im}(H(N(t)))\rightarrow HTRM\\ \int_{-\infty}^{t}\left\langle P_i(t)\right\rangle dt=\int_{-\infty}^{t}\left\{P_i(t)+N(t)\right\}dt=\int_{-\infty}^{t}P_i(t)dt+\int_{-\infty}^{t}N(t)dt\rightarrow IRM\end{cases}$$

When using a Fourier-based technique to calculate phase, φ_2, after considering the properties of the Fourier transform, the estimated state can be determined using a dominant frequency, ω, as follows:

Eq. 11-16)

$$\begin{aligned}&\varphi_2=\arg\left(\Im\left[\left\langle P_i(t)\right\rangle\right]_\omega\right)=\arg\left(\Im\left[\left\{p_i(t)+N(t)\right\}\right]_\omega\right)=\\&=\arg\left(\Im\left[p_i(t)\right]_\omega+\Im\left[N(t)\right]_\omega\right)=\arg\left(\Im\left[p_i(t)\right]_\omega+a\right)\\&\Im\left[N(t)\right]_\omega=\Im\left[N(t)\right]_{\varpi\neq\omega}=a\end{aligned}$$

Under the *assumption for* additive *white noise*, ***a*** in Eq. 11-16 is a frequency-independent, noise-related constant (noise will influence all frequencies in the same way). This makes noise separable from the actual signal, i.e. the corrected version of the Fourier transform (dealing only with the true signal) is recoverable to some degree by choosing a DF:

Eq. 11-17)

$$\varphi_2\approx\arg\left(\Im\left[p_i(t)\right]_{corr}\right)_\omega$$

In contrast, from Equations (A2.4 and A2.5), it is obvious that the noise distorts the estimates of phase in a complex (uncorrectable) way for all RM-based approaches, since it factors in the numerator and denominator. Regardless of the choice of a secondary variable, the numerator is always using the noise-contaminated original signal directly.

This can explain the superior noise immunity of STFT-phase, as long as the noise is equally distributed across all frequencies. In contrast, all RM-based approaches contain a time-dependent noise component embedded in the calculation of state.

12. CALCIUM INSTABILITIES IN MAMMALIAN CARDIOMYOCYTE NETWORKS

Abstract

Before we can address the concept of an "arrhythmogenic index," we must first outline the boundaries of permissible behavior for cardiac dynamics. Specifically, by learning the constraints of the cardiomyocyte electrophysiology, we can better predict and understand how arrhythmias might develop. The degeneration of a regular heart rhythm into fibrillation (a chaotic or chaos-like sequence) can proceed via several classical routes described by nonlinear dynamics: period-doubling, quasiperiodicity or intermittency. In this study we experimentally examine one aspect of cardiac excitation dynamics - the long-term evolution of intracellular calcium signals in cultured cardiomyocyte networks subjected to increasingly faster pacing rates via field stimulation. In this spatially-extended system, we observed alternans and higher order periodicities, extra beats, and skipped beats or blocks. Calcium instabilities evolved non-monotonically with prevalence of phase locking or Wenckebach rhythm, low-frequency magnitude modulations (signature of quasiperiodicity), and switches between patterns with occasional bursts (signature of intermittency), but period-doubling bifurcations were rare. Six ventricular fibrillation (VF)-resembling episodes were pace-induced, for which significantly higher complexity was confirmed by approximate entropy (ApEn) calculations. The progressive destabilization of the heart rhythm by co-existent frequencies, seen in this study, can be related to theoretically predicted competition of control variables (voltage and calcium) at the single cell level, or to competition of excitation and recovery at the cell network level. Optical maps of the response revealed multiple local spatiotemporal patterns, and the emergence of longer-period global rhythms as a result of wavebreak-induced reentries.

Introduction

Instabilities in cardiac repolarization, known as T-wave alternans (TWA) in the ECG, are observed in a variety of pathological conditions, and can be used as predictors of arrhythmic events (Nearing, Huang et al. 1991; Rosenbaum, Jackson et al. 1994). Previous findings that action potential duration (APD) can alternate in single cardiac cells confirmed TWA's cellular level origin (Pastore, Girouard et al. 1999). Recently, compelling experimental and modeling evidence demonstrated that APD and T-wave alternans may reflect not only abnormalities in repolarizing ionic currents, but may directly stem from alternations in intracellular calcium cycling, or be closely linked to calcium-related processes. Supporting evidence includes: inhibition of APD alternans by decreasing L-type calcium current magnitude or calcium-induced inactivation in a computer model (Fox, McHarg et al. 2002) and elevation of the threshold for APD alternans by calcium chelation (Walker, Wan et al. 2003). Additionally, small scale oscillations in the sarcoplasmic reticulum (SR) load were proposed as a possible mechanism in the generation of cell-level alternans (Diaz, O'Neill et al. 2004); and moreover, calcium alternans were shown to persist in action potential clamp conditions both in computer models and experiments (Chudin, Goldhaber et al. 1999; Shiferaw, Watanabe et

al. 2003). Overall, the important role of intracellular calcium ($[Ca^{2+}]_i$) dynamics in the onset and evolution of cardiac instabilities, makes calcium signals a natural choice for mechanistic studies of cardiac rhythm destabilization.

Experimentally, instabilities in calcium handling, known as alternans, usually refer to beat-to-beat alternations (large-small) in the magnitude of the calcium transients. They have been examined at the tissue level (Lab and Lee 1990; Wu and Clusin 1997; Choi and Salama 2000; Pruvot, Katra et al. 2004) and at the sub-cellular level (Blatter, Kockskamper et al. 2003; Diaz, O'Neill et al. 2004) using fluorescent indicators. Constant-magnitude alternans by themselves can persist for a long time without necessarily deteriorating into highly complex arrhythmias; thereby presenting an indirect indicator of possible arrhythmogenesis. An interesting question is how exactly further destabilization of the alternans occurs, and which route toward chaotic or chaos-like signals, such as observed in ventricular fibrillation, is followed? At least three classical routes to chaos have been outlined previously in nonlinear dynamics theory: period-doubling, intermittency and quasiperiodicity (Hilborn 1994). Each of these local bifurcation paths can reveal information about the system and the mechanisms leading to its destabilization.

There is dearth of experimental evidence for the evolution of calcium dynamics into higher-order rhythms (beside constant magnitude alternans) despite predictions of theoretical models for such rich dynamic behavior. Due to technical difficulties with fluorescent measurements using calcium-sensitive probes, e.g. photobleaching and mechanical movement, long-term calcium dynamics is an under-studied and not well understood process. This study explores the temporal evolution of instabilities in intracellular calcium at the cellular level, while cells are in their natural (cell network) environment. In contrast to previous reports, the measurements are done in 1) an externally stimulated (non-oscillating) and 2) spatially extended (non-clamped) system with measurement sites at least several space constants away from the electrodes. The experimental model - anisotropic cultured cardiomyocyte networks on elastic microgrooved surfaces (Bien, Yin et al. 2003) was previously reported to operate in a wider dynamic range of calcium handling (Yin, Bien et al. 2004), i.e. exhibiting larger systolic calcium levels, faster rise in diastolic calcium with rapid pacing etc. This wider dynamic range is expected to facilitate the observation of richer calcium dynamics. In the present study, we use long-term calcium recordings and nonlinear dynamics analysis to address the following questions: 1) what routes does temporal evolution of calcium instabilities follow; 2) can a multicellular monolayer model system exhibit complex fibrillation-like behavior with no discernable temporal patterns; and 3) how does the evolution of local dynamics relate to the global response and the propagation patterns in spatially extended tissue?

Materials and Methods

Experimental Model and Stimulation Conditions

The protocol of primary cardiomyocyte culture has been documented previously (Bien, Yin et al. 2003). Briefly, the ventricles of the hearts of 3-day-old Sprague-Dawley rats were digested enzymatically using trypsin and collagenase, cardiomyocytes were collected after centrifugation and preplating, and then seeded on fibronectin-coated microgrooved polydimethylsiloxane scaffolds (0.8x1cm in size) at a high density of 0.4×10^6 cells/cm^2. Cell constructs were kept in Medium 199 at 37°C. Polydimethylsiloxane or PDMS was molded out

of metal templates, designed using acoustic micromachining (Entcheva and Bien 2005a) to enforce anisotropy. Spatial optical mapping confirmed connectedness and wave propagation across the samples (Bien, Yin et al. 2003).

Calcium measurements were performed at day 4-6 after culturing. Rectangular samples (1.2x0.8cm) were perfused with Tyrode's solution at 30±2°C. Electrical field stimulation was applied with 5ms bipolar pulses delivered through embedded Platinum electrodes in the sides of the chamber, parallel to the longer scaffold sides and to the direction of anisotropy. The strength of the field was 5-10V/cm, guaranteeing field strengths at least 2 times the threshold for stimulation, which was 2-3V/cm at 1Hz pacing. The frequency of pacing was varied in the range 0.5 to 9Hz.

Local Intracellular Calcium Measurements in Cardiomyocyte Networks

Intracellular calcium levels were determined locally using a Fura-2 ratiometric fluorescence measurement technique, as described previously (Bien, Yin et al. 2003; Yin, Bien et al. 2004). The imaged area was restricted by a mechanical aperture to approximately 200x100μm area in the central portion of the scaffold. Reduced excitation light and high-sensitivity detector (photomultiplier tube, PMT, Electron Tubes, Ltd, UK) allowed for continuous exposure and recordings without apparent signs of photobleaching and toxicity. In a subset of samples, cells were co-labeled with di-8-ANEPPS and Fura-2. Co-localized, sequential in time measurements of voltage and calcium were then performed only for patterns stable over time. Temporal markers (stimulus timing) were used to relate voltage and calcium response.

Spatial Optical Maps of Propagation

In a subset of samples (n=4), spatial optical mapping was performed to uncover: 1) the patterns of direct polarization during electrical field stimulation at various field strengths; and 2) the spatiotemporal patterns at the induction and evolution of instabilities. We applied ultra-high resolution imaging with an intensified camera system (CMOS 1280x1024 pixels, Cooke, Romulus, MI), using temporal resolution of 200 frames per second and spatial resolution of 20μm per pixel. Data processing of the raw un-binned data included subtraction of baseline fluorescence, temporal Savitzky-Golay filter (width 7, order 2) and a spatial Gaussian filter with 5 pixel kernel. Color maps of propagation were generated from the original images by converting intensity into phase values using the Hilbert transform (Bray and Wikswo 2002); wavefront was tracked by a black line. Activation maps were generated by calculating times of activation (maximum slope) for each pixel and displaying contour maps of isochrones. Sequences of frames were combined in movies with playback at four-times slower speed. Movies are made available as supplemental on-line information.

Figure 12-1 Calcium instability patterns.
A. Alternans and higher order periodicity (N=M>1) - 2:2 and 3:3 rhythms are shown; **B.** Skipped beats and blocks (N>M) - 2:1, 3:1, 4:1, 4:2, 3:2, 4:3 rhythms shown; **C.** Extra beats (N<M) – 1:2 and 1:3 response shown. External stimuli marks are plotted below the calcium transients.

Data Processing and Analysis of Temporal Patterns

All data processing and analysis was automated using a custom-developed program written in Matlab 7 (MathWorks, Natick, MA). The raw experimental data from the PMT recordings were filtered using Savitzky-Golay filter (width 31, order 2). Calcium systolic levels were determined using peak height of calcium transients with respect to the preceding diastolic levels (at the foot of the transient). The latter was automatically detected by analyzing time-shifted versions of the original signal. In the case of fibrillation-like data, peak detection was manually confirmed due to the high irregularity in the signals. In this study, more than 20,000 PMT recordings of calcium transients were analyzed.

Classification of Instability Patterns

The patterns of intracellular calcium dynamics were defined as N:M rhythms, where M calcium transients are recorded in response to N external stimuli. The data were classified into three categories (**Figure 12-1**):

4. N=M>1 alternans or higher order periodicities, e.g. 2:2, 3:3 rhythms**;**
5. N>M skipped beats or blocks, e.g. 2:1, 3:1, 3:2, 4:1, 4:2, 4:3 rhythms (including Wenckebach (N+1):N patterns)**;**
6. N<M extra beats, e.g. 1:2, 1:3 rhythms.

Only patterns which appeared at least twice contiguously were classified as a pattern. In the text, we treat longer-period rhythms (higher N and M) or rhythms with higher difference between N and M as more *complex*. Furthermore, we use the terms *monotonic* or *non-monotonic* switch of patterns to define progressively increasing (or decreasing) complexity in time (monotonic) or combination of decrease and increase in complexity with time (non-monotonic).

Poincaré and Frequency Maps

Poincaré maps are a classical tool in non-linear dynamics for determining whether a system is deterministic or random by plotting current value of a state variable against its previous value (Hilborn 1994). A discernable pattern in the Poincaré plot is formed for a deterministic system in contrast to a formless space-filling structure in a random system. One-to-one response and purely periodic signals appear as tight clusters. Poincaré maps were constructed by plotting peak height value of a calcium transient, p(n), against the peak value of the previous transient, p(n-1).

Frequency maps are an alternative representation, displaying how well cells respond to external pacing, by relating stimulation frequency (x-axis) and response rate (y-axis). In general, points on the diagonal of the frequency map refer to normal 1:1 response or alternans (N=M), whereas points falling in the region to the left of the diagonal are associated with extra beats (N<M), and points to the right represent skipped beats/block (N>M) (**Figure 12-2**)**.** Higher distance from the diagonal reflects higher instabilities or failure to externally control the system. In some cases different frequencies were color-coded for better tracking of the calcium response in the phase and frequency plane.

Figure 12-2 Wenckebach calcium rhythms.
A. Contiguous episode of mixed 3:2, 4:3, and 2:1 rhythms; B. Calcium peak height variations from beat to beat; C. Poincare map; D. Frequency map, all points fell in the region to the right of the diagonal, indicating the existence of skipped beats/blocks.

Short-Time Fourier Transform (STFT)

Short-time Fourier Transform (STFT) is a signal processing technique for time-variant spectral analysis (Mainardi, Bianchi et al. 2002). In contrast to traditional Fast Fourier Transform (FFT), STFT takes into consideration the time variations in the signal and partitions it into a series of time segments by applying a window function for the application of FFT. A Hamming window was chosen here. STFT can be mathematically expressed as follows:

Eq. 12-1) $$s(t,\omega) = \frac{1}{\sqrt{2\pi}} \int e^{-j\omega\tau} s(\tau) h(t-\tau) d\tau$$

where, $s(\tau)$ is signal in the time domain, $s(t,\omega)$ is the FFT time-dependent spectrum, and $h(t-\tau)$ is the window function.

In this study, STFT was performed on both original calcium transients and on extracted calcium systolic levels data (one value per period) for pattern detection. In the former case, the dynamics of the instability patterns was examined in the frequency domain. For example, two frequency bands in the STFT plot usually imply the occurrence of 2:2 alternans in the original signal. The second application of STFT was targeting the detection of patterns and slow modulation embedded in VF-like calcium signals. Systolic calcium levels (one point per transient) were used in this case instead of the original signals. Since calcium peak height values are not equally sampled in the time domain due to changing oscillation rate, the output of the STFT was expressed as normalized periodicity ($beats^{-1}$) with beat number instead of frequency with time. This analysis approach was found to be superior in pattern detection.

Approximate Entropy (ApEn) as a Complexity Measure

The ApEn has been used as a measure of system complexity (Pincus 1991). A low value of ApEn usually reflects predictability and regularity in a system, whereas a high value indicates disorder and randomness in a system. We found this complexity measure to be more practically applicable (than traditionally used Lyapunov exponents, for example) considering the typical length of the recorded calcium signals. The parameters in the ApEn calculations were adopted from previous heart rate variability studies - filter factor r was set to 20% of the standard deviation (SD) of the original data, an embedded dimension m of 2, and a time lag τ of 1 was applied. Paired t-test was used for statistical analysis.

Results and Discussion

Temporal Dynamics of Calcium Instabilities in Response to External Pacing

To investigate the time evolution of calcium instability patterns in anisotropic samples, a total of 42 long episodes (>1min) under external pacing were examined. No artifacts from photobleaching in the signals of interest (transient magnitude) were registered for the durations used here. Two modes of external stimulation were employed. First, to examine whether the induced patterns are stable over time or undergo further changes, the pacing frequency was increased to the point, at which instabilities were registered and maintained for the duration of recording. Second, the frequency was increased progressively to examine the dynamics beyond the threshold for induction of alternans. For a subset of samples, fast pacing was found to induce non-driven activity. We used stimulation at higher voltages to attempt effective cardioversion (recovery of controlled regular rhythm) in these cases. Spontaneously beating cultures were generally not included, unless overdrive pacing was successful at relatively low frequencies. This resulted in N:M patterns with N<M at an average frequency less than or around 1Hz, with one exception (**Table 12-1**).

N\ M	1	2	3	4	5	6	7	8
1		**27** 0.8±0.1Hz	**7** 0.9±0.1Hz	**1** 0.5Hz				
2	**47** 3.4±0.2Hz	**35** 3.9±0.3Hz	**7** 1.1±0.2Hz		**3** 0.8±0.2Hz			
3	**8** 6±1Hz	**18** 2.8±0.2Hz	**6** 2.3±0.4Hz	**1** 3Hz				
4	**4** 6±1.7Hz	**1** 8Hz	**7** 3±0.4Hz					
5				**6** 3.5±0.2Hz				
6		**1** 3Hz			**2** 3Hz	**1** 4Hz		
7						**3** 5±2Hz	**1** 4Hz	
8							**1** 9Hz	

9				**1** 3Hz				**1** 9Hz

Table 12-1 Diversity and incidence of calcium instability patterns
Diagonal terms (white) show N=M>1 patterns of alternans and higher order periodicities; gray shows extra beats (N<M); black shows skipped beats and blocks (N>M). Numbers in the corresponding cells indicate number of observations and average stimulation frequency at which the patterns were observed.

It was expected that higher rhythm complexity in calcium dynamics would follow one or more of the following classical paths of local bifurcation: period-doubling, intermittency and quasiperiodicity. They can be distinguished by "local" (Poincaré map) analysis of the structure of state space. In contrast, global bifurcations (such as crises) require tracking the behavior of the system over a considerable portion of the state space, analyzing the evolution and interaction between local structures. In crises, an attractor suddenly disappears or changes size, and this is thought to result from collision between the attractor and an unstable fixed point or unstable limit cycle (Hilborn 1994). In experimental systems, crises can be precipitated by the presence of noise (Sommerer, Ditto et al. 1991; Sommerer, Ott et al. 1991), and in our system they are likely to occur due to coarse frequency stepping. Our analysis did not include tracking the size of attractors over long periods of time, thus crises-based route to chaos remains beyond the scope of this study.

Typical *period-doubling*, where the pattern changes from 1:1 to 2:2, 4:4, 8:8 etc., has been the focus of multiple studies dealing with repolarization APD alternans (Guevara, Glass et al. 1981; Hastings, Fenton et al. 2000; Fox, Bodenschatz et al. 2002). *Intermittency* transition to chaos is seen when the system's behavior switches between two qualitatively different states at constant control parameters of the system, as for example shown in simulations with the Lorenz model (Hilborn 1994). This route has been demonstrated in a computer model of calcium oscillations previously (Haberichter, Marhl et al. 2001). In contrast, skipped beats and blocks including Wenckebach-like rhythms (**Figure 12-1 and Figure 12-2**) are believed to be the outcomes of *phase-locking* (Glass 1991), where two independent frequencies lock into a rational ratio, e.g. 1/2, 3/2, 3/4 etc (Hilborn 1994). When the ratio between the two underlying frequencies becomes irrational, *quasiperiodicity* emerges (Hilborn 1994). In an experimental setting, with a finite precision in the computer-acquired signals, it is impossible to differentiate between rational and irrational ratios; therefore we used a surrogate measure for quasiperiodicity, such as the presence of distinct structures in the Poincaré maps (Garfinkel, Chen et al. 1997). The interaction between extrinsic and intrinsic pacing, or the competition between two control processes at incommensurate frequencies can induce oscillation at one frequency that is amplitude-modulated at another frequency, as demonstrated below in examples of quasiperiodicity.

To examine the stability of alternans over time, we *maintained the same pacing frequency* at the threshold at which alternans were observed in 29 cultures. In 21 episodes (72%) dynamically changing N:M instability patterns were registered, while in 8 episodes (28%) the N:M patterns persisted, but the magnitude varied (effective low frequency modulation). From the eight persisting stable N:M patterns under constant pacing frequency, a majority - six cases showed non-monotonic low frequency oscillations in magnitude, while two cases had a monotonic decrease ("damping") in instability magnitude and transition to blocks. As shown

in **Figure 12-3A-C**, the amplitude of 2:2 alternans decreased monotonically with time at 4Hz pacing, confirmed also in the frequency domain (3D STFT plot), where the energy of the 2Hz component increased while the energy of the dominant 4Hz component was decreasing, indicating gradual disappearance of 2:2 alternans and the emergence of a 2:1 block. In contrast, in **Figure 12-3D-F** a more readily observed case of quasiperiodicity is shown, where non-monotonic variation in peak height of 2:2 alternans at 3Hz pacing resulted in shift of energy peaks between 3 and 1.5Hz components in the STFT plot. It was also noticed that a burst of 3:3 alternans (intermittency episode) occurred in the interval dominated by 2:2 alternans. Low frequency modulations and bursts of patterns were often observed in our experiments. Episodes having non-monotonic change in patterns at constant pacing rate also support the possible existence of intermittency (**Figure 12-4**) in calcium dynamics.

Of the dynamically changing N:M patterns, 13 cases (62%) exhibited non-monotonic switch between patterns of different complexity, 7 cases (33%) transitioned from alternans or skipped beats to blocks, and only one case transitioned from blocks to skipped beats or alternans. For example, as shown in **Figure 12-4A-D**, when paced at 4Hz, 4:3 rhythms alternated 3:2 rhythms but eventually switched completely to 2:1 blocks, whereas in **Figure 12-4E-H**, instability patterns varied spontaneously between 1:1 response, 2:2, 3:3, and 4:4 alternans while pacing was maintained at 3Hz.

In a second set of experiments, we examined the effect of further increase in external pacing rate beyond the threshold for alternans. When *progressively increasing the pacing frequency* in 13 samples, 9 episodes (70%) exhibited transitions from alternans or Wenckebach-like rhythms to blocks, and 4 episodes (30%) had a monotonic increase in the order of complexity. This latter case is illustrated in **Figure 12-5**, where increasing pacing frequency from 7 to 8Hz, maintained 2:2 alternans with a transient 4:4 rhythm; when further increasing pacing rate to 9Hz, complex Wenckebach patterns (9:8, 7:6, 8:7 rhythms) completely replaced the 2:2 alternans. Accordingly, the frequency map shows a funnel-like pattern of the increasing complexity as frequency of stimulation increases. Overall, non-monotonic behavior or divergence of the instabilities was prevalent.

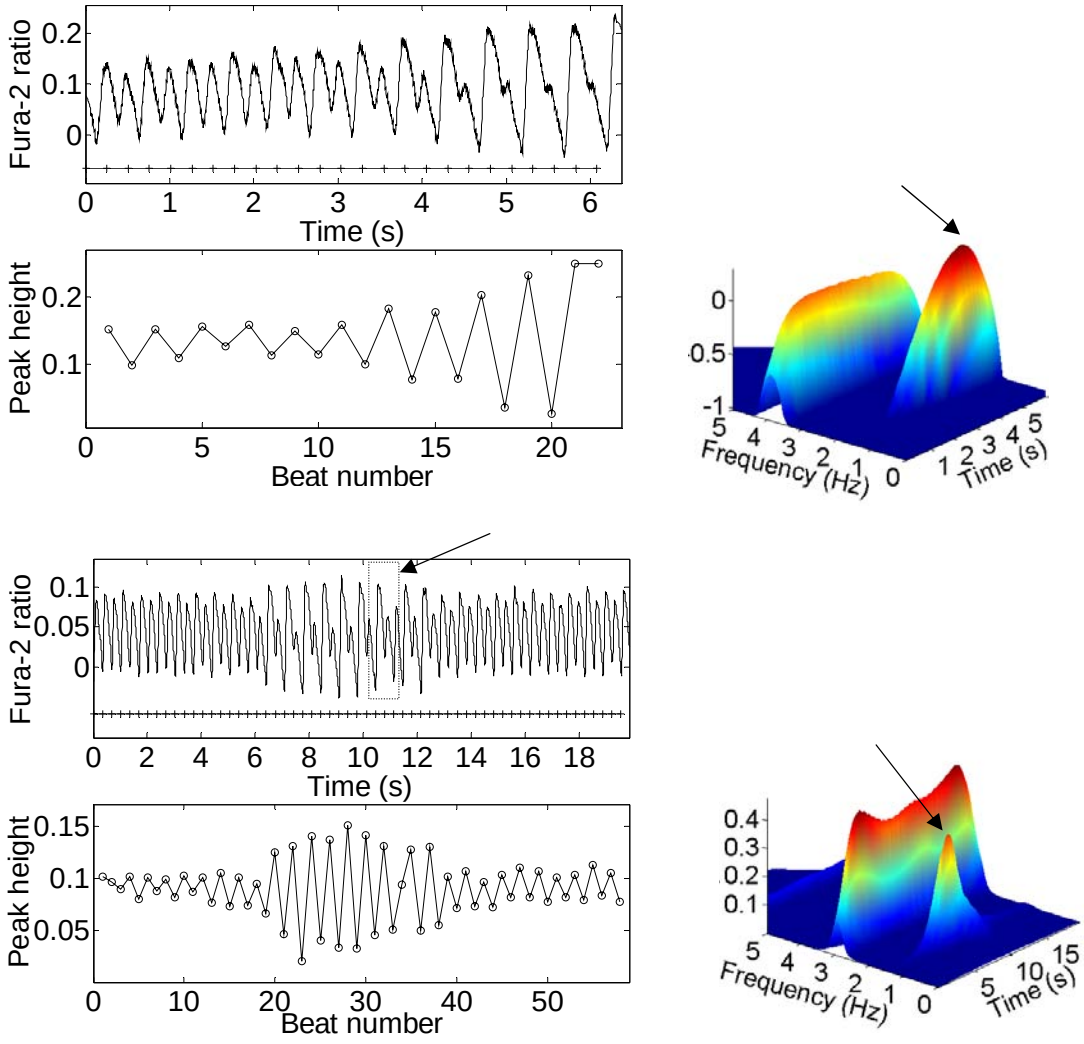

Figure 12-3 Modulation of alternans magnitude under constant pacing frequency.
A. During 4 Hz pacing, 2:2 alternans gradually disappeared with the emergence of a 2:1 block; B. A plot of peak height values against beat number (dashed red line follows alternans magnitude); C. STFT plot showing the energy of the 2Hz component increasing as the energy of the 4Hz component is decreasing; D. During 3Hz pacing in another sample, the magnitude of 2:2 alternans changed non-monotonically, a burst of 3:3 alternans was also observed; E. A plot of peak height values against beat number, indicating the existence of a slow modulation; F. STFT plot - the energy magnitudes of 3 and 1.5Hz alternated.

Classical period-doubling cascade in our experimental recordings was missing. This might indicate a subtle difference in the dynamics of calcium vs. voltage and a certain degree of uncoupling between the two, or could be a result of our approach to analyzing the traces. More specifically, our summary of calcium patterns was a relatively conservative estimate, where only those rhythms, present at least twice in a row, were taken into account as a pattern. For example, as shown in **Figure 12-4,** a 4:4 pattern did exist as a transient event, but was not included in the summary **Table 12-1**. Therefore, the incidence and category of calcium patterns could be underestimated due to the stringent criterion. In addition, the increments in

external stimulation rate were rather coarse, which might obscure possible bifurcations. Further reasons for not seeing period-doubling cascades are discussed below in conjunction with the stimulation conditions. Quasiperiodicity and intermittency periods in calcium dynamics were much more prevalent, both while maintaining external frequency at the alternans threshold level and when the system was further perturbed into more complex patterns.

Calcium Instabilities and VF-like Episodes

We asked the question whether pacing-triggered instabilities in calcium dynamics in our cardiomyocyte networks ever reach the level of fibrillation-like sequence without a discernable pattern. A total of 6 sustained (>20sec) VF-like episodes were registered, typically triggered by rapid external pacing. In two of these episodes a very slow frequency modulation was observed, one episode demonstrated bursts of irregular behavior in between 1:1 response, two episodes exhibited abrupt acceleration of rate and decrease in peak height, and the remaining one case exhibited no distinct pattern.

As shown in **Figure 12-6**, after a short period of 3Hz pacing, cells exhibited very irregular rhythm around 2.5Hz (see STFT performed on the original calcium transients over a 70sec interval, **Figure 12-6B**) in the absence of external stimulation as well as during attempted low-magnitude (5V/cm) 1Hz pacing (magnified in zone I, **Figure 12-6C**). Stem plot of zero baseline peak height signals from zone I revealed the existence of slow modulations (**Figure 12-6E**), which were confirmed by STFT performed on peak height signals (one value per period), **Figure 12-6F**. The low frequency modulation switched from $0.07 beats^{-1}$ to $0.09 beats^{-1}$ during the recording period, while the Poincaré map exhibited space-filling properties with a possible central hole, enhanced with a dotted line circle in **Figure 12-6D**. We tested whether these low frequency modulations might be due to inherent noise in the measurements, rather than being the result of competing processes with incommensurate frequencies. A 1:1 response signal at a comparable pacing rate (3Hz) and level of noise was recorded and analyzed. An order of magnitude lower root-mean-square (RMS) error was found to be due to the noise (0.0059 in this case vs. 0.05 peak deviations in **Figure 12-6D**). The negligible contribution of noise to low frequency modulations seen in the 1:1 signal corroborated the existence of true frequency modulations in this VF-like episode. Additionally, high frequency pacing sometimes triggered spontaneous VF-like activity (**Figure 12-7A**). This episode was represented with a hollow core Poincaré map revealing again quasiperiodicity-consistent behavior for non-paced activity (**Figure 12-7F**). In this recording a successful termination of the disorganized activity (effective cardioversion) was achieved by 13V/cm electric field stimulation (zone II).

An interesting question is whether the complexity of these VF-like calcium recordings is quantifiably higher than the complexity in our other results with complex yet distinctive patterns. To address this question, *approximate entropy values* were computed to quantify the system's complexity. As shown in **Figure 12-8**, the VF-like recordings had higher complexity ($p<0.001$) than a simulated periodic signal with noise (simulated 2:2, 3:3 alternans with 20% additive Gaussian noise), but were also different from a purely random system ($p<0.02$). Comparison of ApEn values in experimental signals confirmed difference between pattern-exhibiting and VF-like recordings in the presence of similar levels of noise ($p<0.02$). We

attempted calculation of Lyapunov exponents (positive value of maximum exponents would have confirmed chaotic behavior), but failed due to lack of sufficient data length. Qualitative Poincaré maps demonstrating distinct structures (central holes) and quantitatively lower ApEn value compared to a random system (**Figure 12-8**) supported the idea that the VF-like calcium traces most likely exhibit higher dimension deterministic chaos, in agreement with previous theoretical and experimental studies of electrical cardiac signals (Glass, Zipes et al. 1995; Garfinkel, Chen et al. 1997; Jalife, Gray et al. 1998; Weiss, Garfinkel et al. 1999). The data presented here constitute one of the first examples of quantifiable VF-like behavior in a thin (<100μm) "healthy" (non-ischemic or treated) and non-oscillating mammalian cardiac preparation, but ultimately a spatially resolved mapping is needed to further ponder about the underlying mechanisms. Previous experimental studies in a similar cultured cell model system have demonstrated wavebreaks and highly irregular rhythms (Bub, Glass et al. 1998; Bub, Tateno et al. 2003; Hwang, Yea et al. 2004; Bub, Shrier et al. 2005; Hwang, Kim et al. 2005). This behavior was not externally stimulated but evolved spontaneously in self-oscillatory cell networks. It was quantified and linked to cell density and cell coupling (Bub, Shrier et al. 2005) or attributed to local structural heterogeneities (Hwang, Kim et al. 2005).

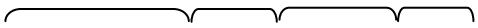

Figure 12-4 Pattern transitions under constant pacing frequency.
A. During 4Hz pacing, Wenckebach 4:3 and 3:2 rhythms alternated and eventually switched completely to 2:1 block; B. A plot of calcium peak height values against beat number; C. Poincaré map; D. Frequency map; E. During 3Hz pacing in another sample, a switch between 2:2, 1:1, 3:3, and 4:4 rhythms occurred; F. A plot of calcium peak height values against beat number; G. Poincaré map; H. Frequency map.

While several lines of evidence confirmed the existence of different routes to chaos in our system, most of the instability patterns did not directly result in fibrillation. 70% of the episodes had a general transition from other patterns to blocks when changing pacing frequency. Previously, it was found that APD alternans evolved into 2:1 blocks instead of turning into more complex rhythms when structural obstacles were present (Pastore and Rosenbaum 2000). The particular topography (microgrooves) used to grow highly anisotropic cell networks might have presented periodic change of connectivity (across the grooves), thus providing the equivalent of structural obstacles to stabilize the propagating waves.

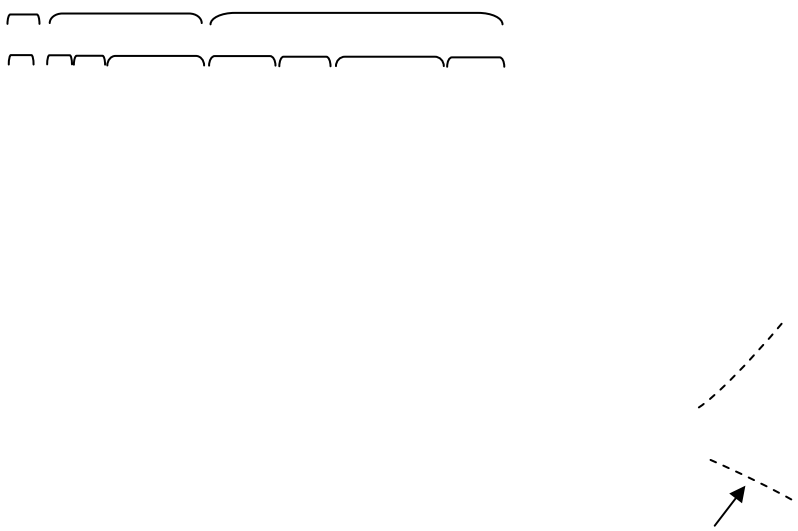

Figure 12-5 Monotonic increase in complexity when gradually increasing external pacing frequency.
A. A transient 4:4 alternans appeared in between the 2:2 alternans when increasing pacing rate from 7Hz to 8Hz. More complex patterns including 9:8, 7:6, and 8:7 rhythms completely replaced 2:2 alternans at 9Hz pacing; B. A plot of calcium peak height values against beat number; C. Poincare map demonstrating wide scatter; D. Frequency responses forming a funnel-like pattern as pacing rate increases.

Links of Quasiperiodicity to Internal V_m - $[Ca^{2+}]_i$ Coupling

Can the observed calcium dynamics be instructive of the properties of the system? Recent theoretical models have examined the interaction between transmembrane voltage (V_m) and $[Ca^{2+}]_i$ as competing control variables within a single cell. Shiferaw et al. (Shiferaw, Sato et al. 2005) predict that the mode of V_m - $[Ca^{2+}]_i$ interaction/coupling can dictate the instability dynamics of the system. The regime of coupling, outlined in this model, depends on inherent ionic mechanisms, linking calcium processes to voltage changes, including the calcium-induced inactivation of the L-type calcium current, and the degree of contribution of the sodium-calcium exchanger. For example, if V_m and $[Ca^{2+}]_i$ are linked by negative coupling, a single cell is capable of exhibiting four different dynamics modes, namely: 1:1 response, concordant (in phase) V_m - $[Ca^{2+}]_i$ alternans, discordant (out of phase) V_m - $[Ca^{2+}]_i$ alternans, and even quasiperiodicity as a single cell phenomenon (Shiferaw, Sato et al. 2005). In conditions of positive V_m - $[Ca^{2+}]_i$ coupling, the expected cardiac excitation dynamics is simpler – only 1:1 response and concordant V_m - $[Ca^{2+}]_i$ alternans are predicted by the theoretical model.

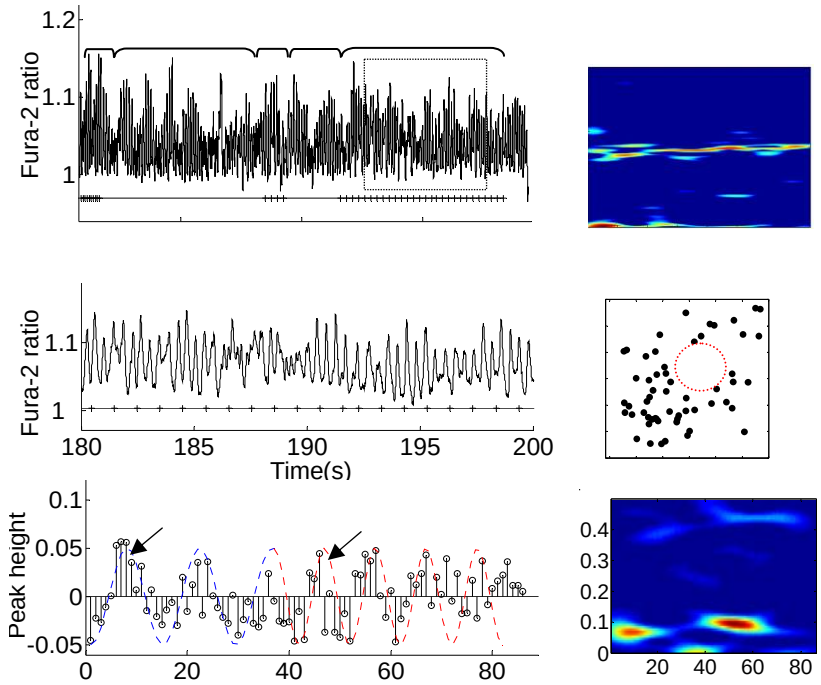

Figure 12-6 VF-like signals with low frequency modulation.
Cells exhibited irregular oscillation (magnified in A. Zone 1) at around 2.5Hz as shown in B. STFT on original recording; C. Stem plot of calcium peak height values from Zone I, with superimposed two simulated envelope curves at 0.07 $beat^{-1}$ and 0.09 $beat^{-1}$, indicating the existence of low frequency modulations; D. A central hole was seen in the Poincare map; C. STFT on peak height values confirms the time low frequency modulations.

Our experimental results showed low frequency modulations in alternans magnitude in six episodes of paced activity, such as in **Figure 12-3**, as well as in two episodes of high complexity (VF-like episodes) (**Figure 12-6** and **Figure 12-7**) with hollow cores in the Poincaré maps. This behavior is indicative of the presence of incommensurate frequencies in the system, or *quasiperiodicity*. In order to directly test whether negative V_m - $[Ca^{2+}]_i$ coupling might be the driving force behind prevalent quasiperiodic dynamics in our experimental model, we double-labeled a subset of samples (n=9) to record transmembrane voltage and calcium in the same cells during pacing-driven stable alternans patterns. Depending on applied frequency, this experiment yielded regions of stable 1:1 response, concordant (in phase) V_m - $[Ca^{2+}]_i$ alternans and quasiperiodicity; the fourth predicted case of discordant V_m - $[Ca^{2+}]_i$ alternans was observed only once (the same sample exhibited both concordant and discordant alternans within a different pacing context). Hence, we concluded that our data are highly suggestive of, but not proving cellular origin of quasiperiodicity via negative V_m - $[Ca^{2+}]_i$ coupling.

Alternative explanations for the quasiperiodicity include at least four multicellular mechanisms. One example is modulated parasystole (Glass, Goldberger et al. 1986) – the co-existence of ectopic ventricular rhythm with the sinus rhythm, or in the context of our experiments – existent ectopic site(s) along with the external pacing. Another multicellular

mechanism includes meandering spiral waves (Zykov 1986; Barkley, Kness et al. 1990; Garfinkel, Chen et al. 1997; Kim, Garfinkel et al. 1997), which can also appear as magnitude-modulated signals. Both of these (ectopic sites or meandering waves) had to be induced by fast pacing and had to persist through further external pacing. Additional possibilities for quasiperiodic behavior include processes driven by conduction velocity restitution – when a circular path (ring of tissue) is provided for wavefront-wavetail interactions of a self-sustained wave (Frame and Simson 1988; Courtemanche, Glass et al. 1993) or when regions of spatially discordant alternans form and their borders drift with respect to the pacing site(Watanabe, Fenton et al. 2001).

Our data were obtained from a single location within a well coupled cell network (lacking macroscopic obstacles), externally paced via electric field stimulation, where modulated parasystole and quasiperiodicity in a ring are less likely. An unperturbed meandering spiral and CV-restitution caused discordant alternans will be hard to sustain due to a spatially restricted region between the directly polarized borders by the electrodes. However, to definitively confirm the mechanism leading to co-existence of incommensurate frequencies in our cardiac model, spatial mapping is needed. Preliminary spatial data provided below illustrate the development of long-period patterns and suggest likely quasiperiodicity scenarios in our model.

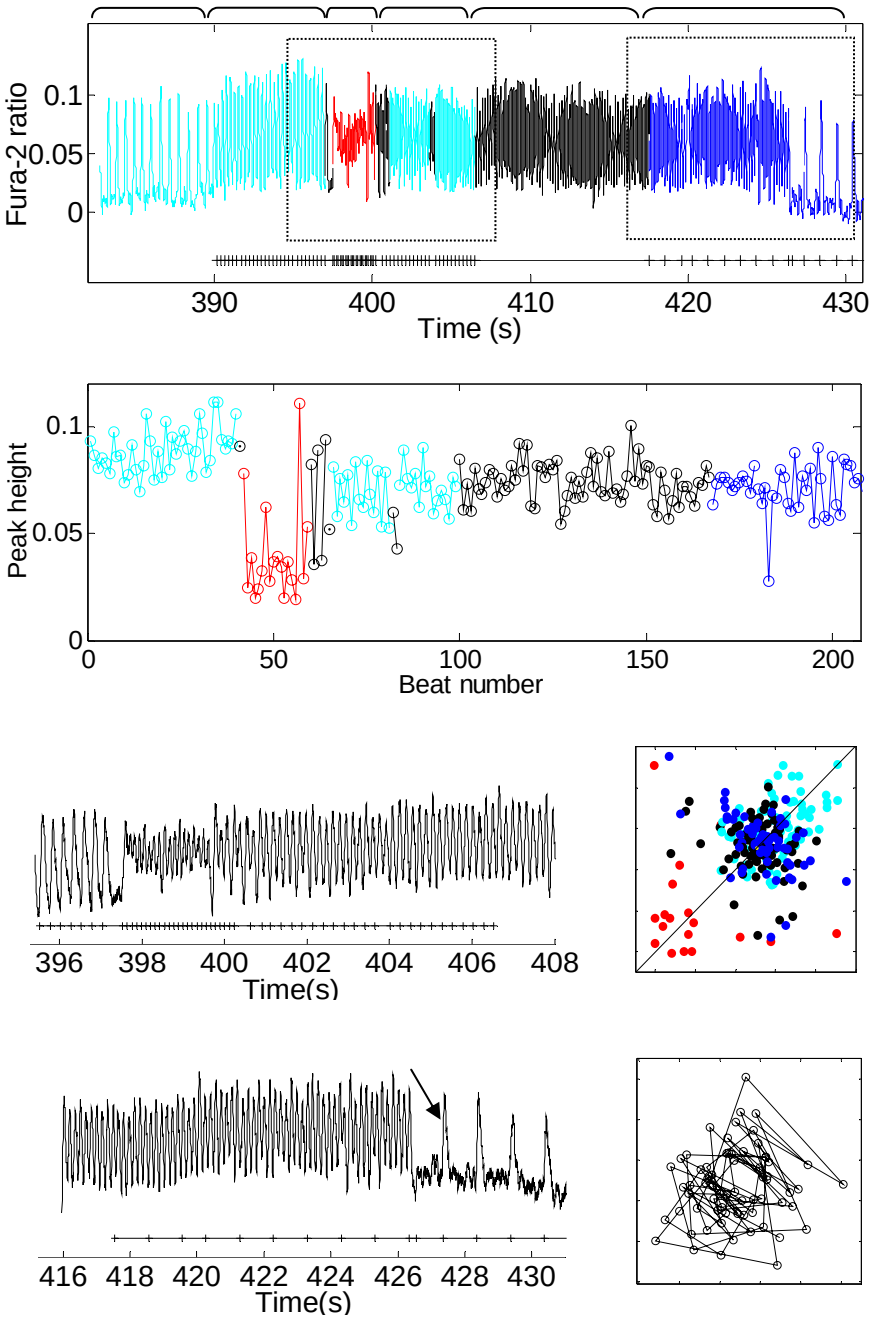

Figure 12-7 VF-like signals showing quasiperiodicity, followed by defibrillation.
A. Entire recording shown with two zones magnified for better illustration. Acceleration of the signal is shown in zone I, which persists during stop of external stimulation. In zone II a defibrillation is shown using 13V/cm electric field pulses at 1Hz. B. A plot of peak height values against beat number for the entire period in A; C. Poincare map of peak height values from the entire episode; D. Poincare map of peak height values from the non-stimulated (encircled) region, demonstrating the presence of a central hole, typical for quasiperiodic signals.

This Experimental Model Contrasted to Previous Studies of Instability Patterns

Most of the previous systematic studies on instability patterns in cardiac preparations have dealt with zero-dimensional or space-clamped systems, where the overall size of the tissue (cell cluster) was small and/or the observation point was in close proximity to the pacing site; electrical stimulation was applied in the form of direct current injection (Guevara, Glass et al. 1981; Guevara, Shrier et al. 1988; Chialvo, Michaels et al. 1990; Guevara and Shrier 1990; Gilmour, Otani et al. 1997; Hall and Glass 1999). In such conditions, the spatial extent of the stimulated tissue plays minimal role in determining the observed response. Regardless of the type of the stimulated tissue - oscillatory (Guevara, Shrier et al. 1988) or non-oscillatory (Purkinje (Chialvo, Michaels et al. 1990; Gilmour, Otani et al. 1997) or ventricular (Hall and Glass 1999)), in the above conditions the instability patterns are believed to arise from inherent nonlinear recovery processes. For simple cases of monotonic recovery of excitability, a framework of pattern formation and evolution was proposed by Guevara et al. in the form of a Farey tree (Guevara, Shrier et al. 1988) – a frequency-independent representation of common N:M response paths. Analysis (Guevara and Shrier 1990) showed that in zero-dimensional systems low stimulation strengths are likely to produce Wenckebach patterns, such as seen in this study. At medium and high strengths, Wenckebach patterns practically disappear and simple 2:1 blocks and alternans (2:2) are seen, along with hysteresis and bistability (multiple patterns at the same pacing frequency depending on the approaching path).

The experiments reported here were done in a spatially extended system (>1cm^2) at supra-threshold values: stimulus strengths were 2.5-5 times the threshold for stimulation. Instead of current injection, electric field stimulation was used (**Figure 12-9**). In these conditions, a gradient of stimulus strengths will be seen over space with the largest polarization expected at the tissue borders facing the electrodes and decreasing fast towards the center. The polarization (transmembrane potentials, V_m) induced by this extracellular field stimulation can be expressed in simplified form for a one-dimensional case (Roth 1994) along the width of the scaffolds, L, under assumptions for 1) constant electric field (constant E); and 2) uniform tissue properties (constant conductivity):

Eq. 12-2)
$$V_m = E\lambda \frac{\sinh\left(\frac{x}{\lambda}\right)}{\cosh\left(\frac{L}{2\lambda}\right)}, \; -L/2 < x < L/2$$

The strength of the applied field is E [V/cm], and the space constant for the tissue is λ [cm]. For our experimental preparation the estimated space constant is 0.036-0.05cm (Jongsma and van Rijn 1972). Using the above values, and considering threshold for activation of 30mV (deviation from resting potential), one can show that the tissue within 0.5 to 1.8mm at each border will get *directly depolarized/hyperpolarized* by the applied stimulation (5-10V/cm). For homogeneous tissue, this leaves a central non-excited region of three or more millimeters width. Thus, *limited propagation* is theoretically possible in the transverse direction from the borders towards the center. The anisotropic structure of our samples features periodic high resistance regions, spaced about 120μm apart across the width of the scaffolds. Gradient in

tissue conductivity is known to serve as effective "activation function" and to bring about polarization away from the borders (Sobie, Susil et al. 1997). Experimental test of these considerations was done by multisite imaging of the response to 2, 5, 10, 15 and 20V/cm. Spatial optical mapping of polarization and propagation patterns at low pacing rates (1Hz) revealed that for E =10V/cm (typical stimulating conditions) or higher, almost instantaneous excitation occurred across the scaffold, while at 5V/cm there was some propagation of border-initiated waves colliding in the middle of the scaffold (**Figure 12-9**). However, at higher pacing rates, the pattern of propagation changed, and space-allowed propagation started playing a more prominent role, as shown below in conjunction with **Figure 12-10** and **Figure 12-11**.

All local measurements were done in the larger central region of the scaffold, away from the directly stimulated borders. In contrast to previous studies in zero-dimensional systems, a range of stimulus strengths over space led to propagated waves rather than direct polarization in some regions (e.g. the center of the scaffolds). This might be viewed as a more "natural" rhythm perturbation. Consistent with this view, we observed a combination of patterns, previously predicted for a wide range of stimulation strengths (Guevara and Shrier 1990) – Wenckebach, alternans and hysteresis. This may also explain the lack of period-doubling cascades, which are expected at higher stimulus strengths. The spatial extent of our samples might have contributed to the complexity of responses, especially at higher frequencies, where conduction velocity restitution can result in slower propagation and larger effective space.

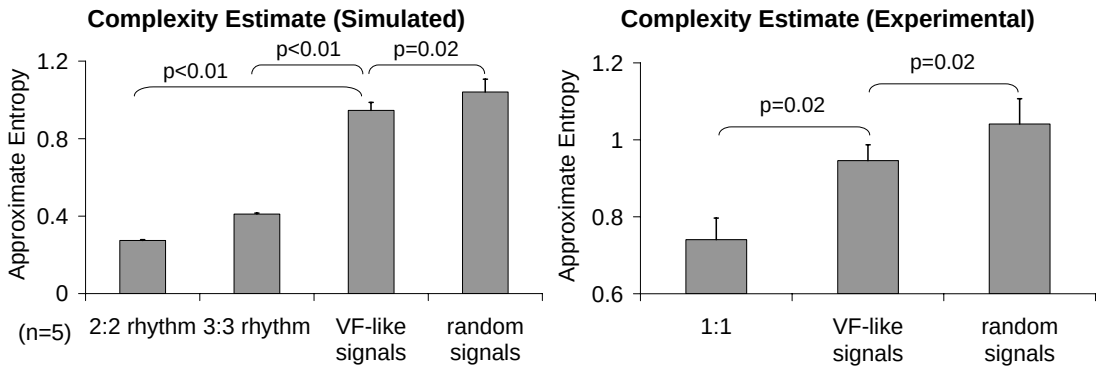

Figure 12-8 Approximate Entropy of VF-like signals.
A. Approximate entropy (ApEn) computed on the six episodes of VF-like signals was significantly higher than the ApEn values of simulated 2:2 and 3:3 alternans with 20% Gaussian noise ($p<0.01$), but differed from purely random signals ($p<0.02$); B. The ApEn value of experimental signals at similar noise level and 1:1 response was significantly lower than the value of VF-like signals ($p<0.02$), confirming the obvious difference between signals with discernable pattern and our VF-like signals.

Spatiotemporal View of Dynamic Instabilities

To track the genesis and evolution of instability patterns in time and space under electric field stimulation, we optically mapped calcium signals in response to pacing in a small subset of samples. At low frequencies, the polarization patterns (1:1) were weakly dependent on field strength and were consistent with theoretical predictions (**Figure 12-9**). As frequency

increased, the polarization spread slower from the borders towards the center leaving a larger effective space for propagation-influenced response.

Alternans and higher order rhythms were seen not only over time, but also in space. **Figure 12-10** is a representative example of the evolution of instabilities in response to 10V/cm pacing at the breakpoint frequency (frequency at which the 1:1 response failed), which was 5Hz in this case. The temporal *global* signal over the entire scaffold is shown in **Figure 12-10A,** while **Figure 12-10B** presents a *local* (PMT-equivalent) signal (200μm square). The same sample shown in **Figure 9** is used, previously demonstrated to have minimal propagation at 10V/cm (almost instantaneous polarization). Colored boxes indicate periods of time from which the phase portraits are computed (**Figure 12-10C and D**). Gray boxes are used only to illustrate the period of the arrhythmia – here a period-8 signal (8:8 rhythm) is observed on the macroscopic level. A different pattern emerges in the later portion of the recording – specifically skipped or blocked beats are present in the local recording but not in the global (macroscopic) view.

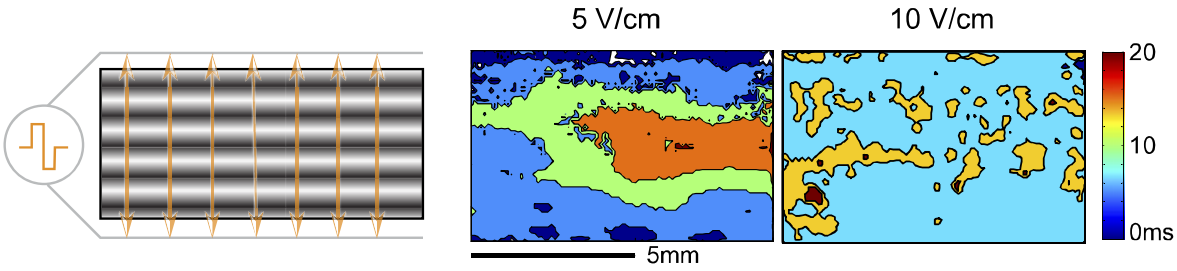

Figure 12-9 Polarization patterns in response to low frequency electric field stimulation.
Activation maps (isochronal contours of excitation times) are shown for 2.5 times the threshold (5V/cm) and five times threshold (10V/cm) stimulation at 1Hz, invoking 1:1 response. Minimal propagation is noted at 5V/cm, while whole-sample activation occurs at 10V/cm.

Figure 12-10C and D represent higher-order rhythms in space-time as phase portraits. The phase encodes the relative temporal position along a transient as illustrated in the inset with the color scale bar underneath a schematic transient. Phase portraits during the time highlighted in red above demonstrate a period-3 spatiotemporal pattern (**Figure 12-10C**). Each column represents an individual successive beat while each row shows the evolution during a beat (selected frames are 40ms apart). The first beat occurs normally but delayed repolarization in the region near the simulated PMT recording permits the formation of a short-lived wavebreak (arrow) in the very next beat (beat 2 of 3). This delayed activation (wavebreak leading to a reentrant wave) then presents a conduction block on the last beat. By the time the next stimulus occurs, enough time has elapsed for normal propagation to recur (first beat of next period). Thus, the co-presence of a wavebreak with the regular stimulus-induced pattern leads to the development of a period-3 rhythm. Movies of longer recordings, including these patterns are available as Supplemental information.

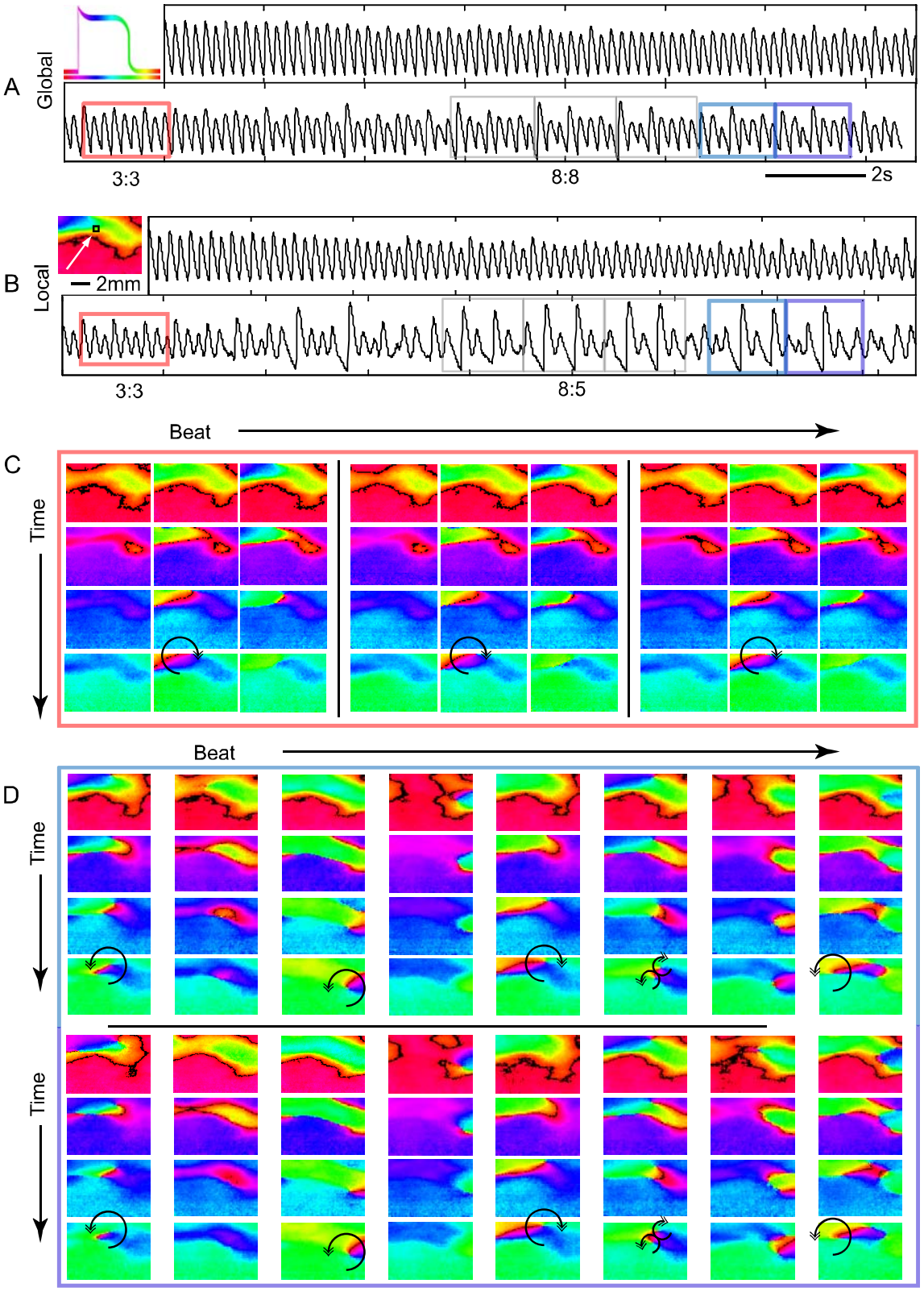
A
Global
3:3
8:8
2s
B
Local
2mm
3:3
8:5
Beat
C
Time
Beat
D
Time
Time

Figure 12-10 (preceding page) Spatiotemporal instability patterns at breakpoint frequency.
A. Shown is the global (space-integrated) signal over an entire scaffold at 10V/cm stimulation at breakpoint frequency. The image to the left explains how phase-related color encodes the relative temporal position along a transient with the color scale bar underneath a schematic transient. B. Pseudo-PMT signal (mean intensity over PMT-equivalent area) taken from the region indicated with a white square. Gray boxes are used to illustrate the period of the arrhythmia – here a period 8 (8:8 rhythm) is observed on the macroscopic level. C. Phase portraits during the time highlighted in red above demonstrate a period 3 spatiotemporal pattern. Each column represents an individual successive beat while each row shows the evolution during a beat (selected frames are 40ms apart). D. Selected beats and spatiotemporal patterns which have spontaneously evolved while maintaining the 5Hz pacing. After around 6 seconds a period-8 pattern emerges (8:8 alternans in the global, and 8:5 block in the local signal), and after another 3 cycles the period-8 pattern shifts abruptly into a different period-8 pattern shown here in light and dark blue rectangles. Again, each column represents a successive beat and each row shows a frame 40ms later than the previous row. The last 4 rows represent the next 8 beats of the pattern in the same format as above. Sites of wavebreak-induced transient reentries are indicated by an arrow. See text for further details; movies are available as Supplemental information.

The evolution of longer-period rhythms was caused by multiple wavebreak-triggered transient reentrant waves, occurring at different spatial locations. **Figure 12-10D** shows selected beats and spatiotemporal patterns which have spontaneously evolved while maintaining the 5Hz pacing. After around 6 seconds a period-8 pattern emerges (8:8 rhythm in the global, and 8:5 block in the local signal), and after another 3 cycles the period-8 pattern shifts abruptly into a different period-8 pattern shown here in light and dark blue rectangles. Again, each column represents a successive beat and each row shows a frame 40ms later than the previous row. The last 4 rows represent the next 8 cycles of the pattern in the same format as above. A second phase singularity is now observed in the lower right corner, and the interaction of the two wavebreaks and the electrode-triggered polarization results in a higher order, longer-period arrhythmia. From the movie of this pattern development, it is seen that the wavebreaks at the different locations in the still images are not stationary but drift or meander over space and this can potentially lead to longer period rhythms and quasiperiodicity, observed in the local records. The particular wavebreak location seems to coincide with curved regions of the wavefronts revealed at lower field strengths even during 1:1 low frequency response. Local wavebreak-induced reentries interacting with the paced wavefronts were confirmed to give rise to longer-period rhythms and complex patterns in three more spatially mapped samples.

Electric field stimulation allowed for spatial distribution and interactions of different instability patterns. **Figure 12-11** illustrates a multitude of local patterns of calcium instabilities that can co-exist in a spatially extended system (same sample used in **Figure 12-9).** Several locations are shown. The lower half of the scaffold, regions 4 and 5, exhibits simple 1:1 response (close to the electrode) or 2:2 alternans. As one approaches the natural wave collision border, far from the electrodes, (see **Figure 12-9**) - regions 1, 3, and 6 - more complex patterns are seen without any skipped beats. Region 6, in particular, has a combination of 3:3 and 2:2 alternans with varying multiples of each pattern. Beyond the collision border, in region 2 and other points in the green area ahead of regions 6 and 1 (data not shown), skipped beats are seen, including Wenckebach (4:3). To aid in visualization of the patterns, alternate periods are shaded in light gray in the traces. Consistent with spatially varying polarization brought about by electric field stimulation, a wide range of patterns can be seen in the spatial domains adjacent to the electrodes and the central regions where propagated waves collide. Interactions between these connected spatial domains and movement of their borders over time may partially explain the variety of local (PMT) responses in the central region and their complex temporal evolution. Overall, these observations underscore the important role of space in shaping the response of the tissue to high-frequency pacing and the higher likelihood of Wenckebach patterns and blocks to be seen in local but not necessarily global signals. Seemingly analogous dynamic changes in Wenckebach type of patterns have been experimentally reported for AV node conduction blocks and mathematically modeled by considering repolarization, "facilitation" (APD restitution), and "fatigue" (conduction velocity restitution) as essential tissue properties (Talajic, Papadatos et al. 1991). However, the observed here variations in the local patterns, only possible in spatially distributed systems (in contrast to the spatially restricted AV node) draw attention to the potential importance of *heterogeneous* response, and can provide a starting point for future theoretical work incorporating space.

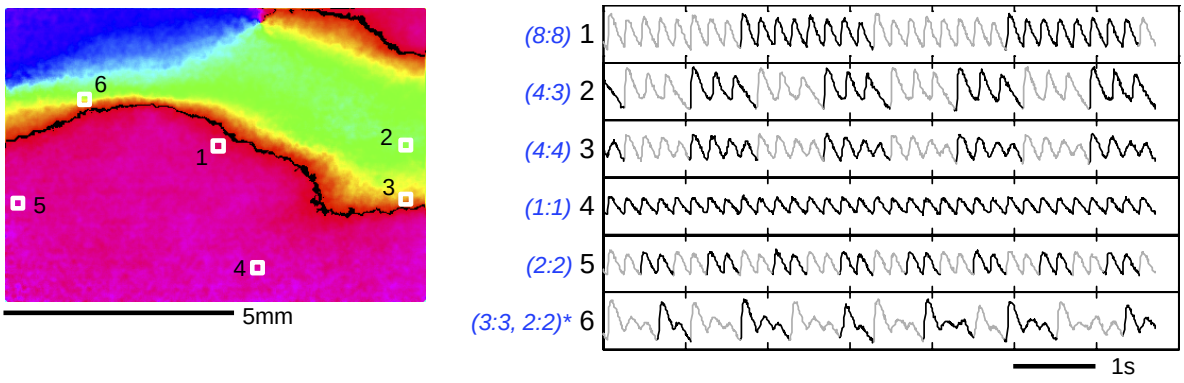

Figure 12-11 Multitude of local instability patterns over space.
On the left is a shown a phase portrait corresponding to the beginning of the traces on the right with white boxes indicating simulated PMT regions (200μm by 200μm) for the respective traces. The lower half of the scaffold, regions 4 and 5, exhibits simple 1:1 response or 2:2 alternans. As one approaches the wave collision border (regions 1, 3, and 6) more complex patterns are seen without any skipped beats. Region 6, in particular, has a combination of 3:3 and 2:2 alternans with varying multiples of each pattern. Beyond the collision border, in region 2 and at other points in the green area ahead of regions 6 and 1 (data not shown), skipped beats are seen. To aid in visualization of the patterns, alternate periods are shaded in light gray in the traces.

Conclusions

In this study, instabilities in intracellular calcium, including classical 2:2 alternans, were induced by rapid pacing via field stimulation in a spatially-extended cardiac system. They were found to dynamically evolve over time, changing magnitude and/or pattern. Quasiperiodic and intermittent behaviors were prevalent in calcium dynamics, while period-doubling was rare. Spatial optical maps revealed longer-period patterns in both time and space during electric field stimulation at high frequency; multiple spatial domains (local patterns) coexisted and interacted within the context of a simpler global rhythm. This highlights the importance of space in shaping the progression of cardiac dynamic instabilities. Pacing-induced VF-like episodes (with significantly higher approximate entropy values) were observed in our experimental 2D cell networks, making this cultured system a potential model for development of new control strategies. This study demonstrates the wider boundaries of calcium dynamics in a spatially-extended cardiac system compared to previous space-clamped results, paving the way towards better understanding and potential control of arrhythmias.

Acknowledgements

We acknowledge support from the Whitaker Foundation (RG-02-0654), the American Heart Association (0430307N), and the Institute for Molecular Cardiology at Stony Brook to EE. We are particularly grateful to Dr. Ki Chon for suggesting some of the techniques used in this study and for helpful discussions.

13. HYSTERESIS IN RHYTHM PATTERNS DURING ELECTRIC FIELD STIMULATION OF CARDIAC TISSUE

Abstract

The study of cardiac dynamics is often complicated by the presence of hysteresis or alternatively a dependence on the initial state. While variously ascribed to cardiac memory or true hysteresis, two distinct paths of frequency-dependent parameters such as calcium transient durations are often observed depending upon the direction of change in pacing rate. We report here that cardiac tissue subjected to fast pacing via electric field stimulation revealed hysteresis in calcium instability patterns (stimulus:response) beyond departure and return to 1:1 (stable response). As expected from existing literature, the pacing frequency at which the first appearance of instabilities occurred (Fa) was higher than that of its ultimate disappearance (Fd). In addition, we observed hysteresis in transitions from one instability pattern to another. In the spatially extended system studied here, 2:2 alternans were the preferred starting point (Fa) in calcium instability development, while 2:1 blocks were more common in the return to Fa from higher pacing rates. Recovery of 1:1 patterns was preceded mostly by 2:2 alternans at Fd. The prevalence of patterns observed in entry into the instability region upon rate acceleration was repeated at exit from the region upon deceleration, and was different from the distribution of patterns within the instability region. In addition to previously reported hysteresis in action potential duration during 1:1 rhythm and alternans magnitude hysteresis (in 2:2 rhythm), our data reveal hysteresis in rhythm pattern transitions not just away from and return to 1:1, but also between different instability patterns, and thus provide insight into the rules of such transitions in electrically stimulated cardiac tissue.

Introduction

Different stimulation history can prompt multivalued responses at a given pacing frequency during electric stimulation of cardiac tissue. This leads to increased complexity in cardiac frequency response and makes the estimation of restitution properties for arrhythmia risk assessment and stratification (Narayan and Smith 2000) and any potential control attempts more difficult.

Hysteresis in the response of cardiac tissue to electric stimulation is defined here as the appearance of alternans or irregular rhythms (**Alt/IR**) at a frequency $\mathbf{F_a}$ during rate acceleration, and the disappearance of **Alt/IR** at a lower frequency ($\mathbf{F_d} < \mathbf{F_a}$) during rate deceleration. The difference between these two points (or any two differing frequencies after the loss of 1:1 rhythm) is linked to short-term memory in the system (Hall and Glass 1999; Walker, Wan et al. 2003; Wu and Patwardhan 2004). Hysteresis in response to pacing has been previously reported for action potential duration (APD) in 1:1 rhythm (Wu and Patwardhan 2004), for alternans magnitude in 2:2 rhythm (Hall and Glass 1999; Walker, Wan et al. 2003), or for isolated patterns of destabilization, such as 1:1 to 2:1 transition (Yehia, Jeandupeux et al. 1999). It has been attributed to slow time constants of recovery in the ion channel

characteristics or to accumulation of calcium or other calcium-related events (Zemlin, Storch et al. 2002; Walker, Wan et al. 2003). The presence of hysteresis in patterns implies *bistability* or *multistability* - depending on the approaching stimulation history path, either 1:1 rhythm or a complex pattern will be observed in the $\mathbf{F_d}$-$\mathbf{F_a}$ region (Hall and Glass 1999; Yehia, Jeandupeux et al. 1999).

In this report, we set out to examine the entirety of patterns and paths taken to and from the **Alt/IR** region, and to uncover the rules of behavior in the border zone with 1:1 rhythm. Previously we have extensively characterized the instability patterns (in intracellular calcium) observed in cardiac tissue subjected to electric field stimulation within the **Alt/IR** region (Bien, Yin et al. 2006). Several classical pathways of destabilization, described in non-linear dynamics, were observed within that region. It was found that electric field stimulation of spatially-extended cardiac tissue is more likely to increase the complexity of the temporal dynamics during pacing compared to space-clamped systems.

As an extension of our previous study (Bien, Yin et al. 2006), here we focus on the system behavior upon entry into the **Alt/IR** region (frequency $\mathbf{F_{a(up)}}$) and exit from the **Alt/IR** region ($\mathbf{F_{a(dn)}}$) till recovery of the 1:1 rhythm ($\mathbf{F_d}$). Thus, the goal was to characterize the observed patterns in the hysteresis region for cardiac tissue, in hopes for better understanding of its frequency response.

Methods

Cultured cardiomyocyte monolayers (n=15) were subjected to electric field stimulation (10V/cm) with increasing pacing frequency (in <50ms steps) beyond the occurrence of alternans or irregular rhythms at frequency $\mathbf{F_{a(up)}}$. This was followed by rate deceleration through $\mathbf{F_{a(dn)}}$ till return to 1:1 rhythm ($\mathbf{F_d}$). Constant-BCL (basic cycle length) protocol was used for pacing, but only about 10-20 beats were used after the initial transient period (first 30 beats) of frequency change and establishment of a pattern. Calcium transients were measured with Fura-2 away from the electrodes (>3mm), and classified as stimulus:response patterns as in (Bien, Yin et al. 2006).

Results and Discussion

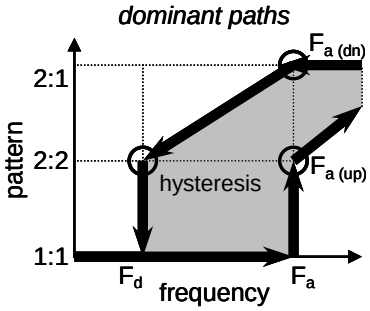

Freq plane / Pattern	F_a (up)	F_a (down)	F_d
2:1	31%	67%	33%
2:2	44%	20%	53%
other	25%	13%	14%

Figure 13-1 Most prevalent path (33%) and resultant hysteresis in the frequency response.
The table indicates the prevalence of each pattern at the corresponding characteristic frequencies; the highest percentage is highlighted**. In the "other" category, most common were Wenckebach patterns.**

The most prevalent pattern at $\mathbf{F_{a(up)}}$ during the transition from 1:1 to **Alt/IR** was 2:2 rhythm (44%), while upon reentry through $\mathbf{F_{a(dn)}}$ the pattern typically has switched to 2:1 blocks (67%), **Figure 13-1**. The return path from **Alt/IR** to 1:1 at $\mathbf{F_d}$ usually was preceded by re-occurrence of 2:2 rhythm (53%). The majority of the other rhythms were Wenckebach N:(N-1) patterns. Clearly, in the $\mathbf{F_d}$-$\mathbf{F_a}$ region multiple patterns were observed along with the 1:1 response, confirming multistability. These data differ from previous studies with current injection in bullfrog tissue with measurements close to the stimulation site, where 76% of the patterns at $\mathbf{F_{a(up)}}$ and 100% of the patterns at $\mathbf{F_d}$ were 2:1 blocks (Hall and Glass 1999). **Figure 2** illustrates all possible patterns and paths observed as the tissue was guided through the pacing frequencies well into the **Alt/IR** region (gray cloud) and back. The behavior of a typical sample is traced by thick arrows. Several observations are of interest here. First, upon rate deceleration in the hysteresis zone, there was a trend for preservation of 2:2 alternans starting at $\mathbf{F_{a(dn)}}$ till recovery of 1:1 rhythm at $\mathbf{F_d}$, while 2:1 blocks at $\mathbf{F_{a(dn)}}$ tended to branch into multiple paths to 2:2, N:N-1 rhythms or stayed 2:1 till $\mathbf{F_d}$. Second, there was high similarity (mirroring) in the variety and prevalence of the exit (from 1:1) and the entry (into 1:1) patterns at $\mathbf{F_{a(up)}}$ and $\mathbf{F_d}$, respectively (**Figure 2**). In contrast, the distribution of the intermediate patterns at $\mathbf{F_{a(dn)}}$ (in pink) was substantially different. The mirroring of patterns at $\mathbf{F_{a(up)}}$ and $\mathbf{F_d}$, reinforced by the different configuration at $\mathbf{F_{a(dn)}}$, supports our claim for *hysteresis in rhythm patterns*. The extent of ($\mathbf{F_d}$-$\mathbf{F_a}$) hysteresis in the examined samples was 99±42ms (mean±S.E.). These new findings extend previously discussed hysteresis in APD during 1:1 response, hysteresis in alternans (2:2) or in isolated patterns (1:1 to 2:1) to a generalized view of hysteresis in the types and prevalence of patterns seen on the way towards higher instabilities and back to 1:1 rhythm (**Figure 2**). This includes hysteresis in rhythm transitions that are not directly linked to the 1:1 pattern (e.g. 2:2 - 2:1 transitions).

In the $\mathbf{F_d}$-$\mathbf{F_a}$ frequency range, we observed co-existence of alternans, hysteresis and phase locking (Wenckebach rhythms). This is in contrast to theoretical predictions for a space-clamped system, where strength of the stimulus delineates regions of Wenckebach rhythms (at low strength), hysteresis (at medium) and alternans (at high strength) (Guevara and Shrier

1990). We believe that the variety of responses observed here reflects the spatial gradients created by a typical electric field stimulation and the ensuing interactions in a spatially-extended system (Bien, Yin et al. 2006). In summary, our data reveal a higher-order hysteresis in cardiac rhythm patterns during electric field stimulation, and may guide the definition of transition rules between such patterns.

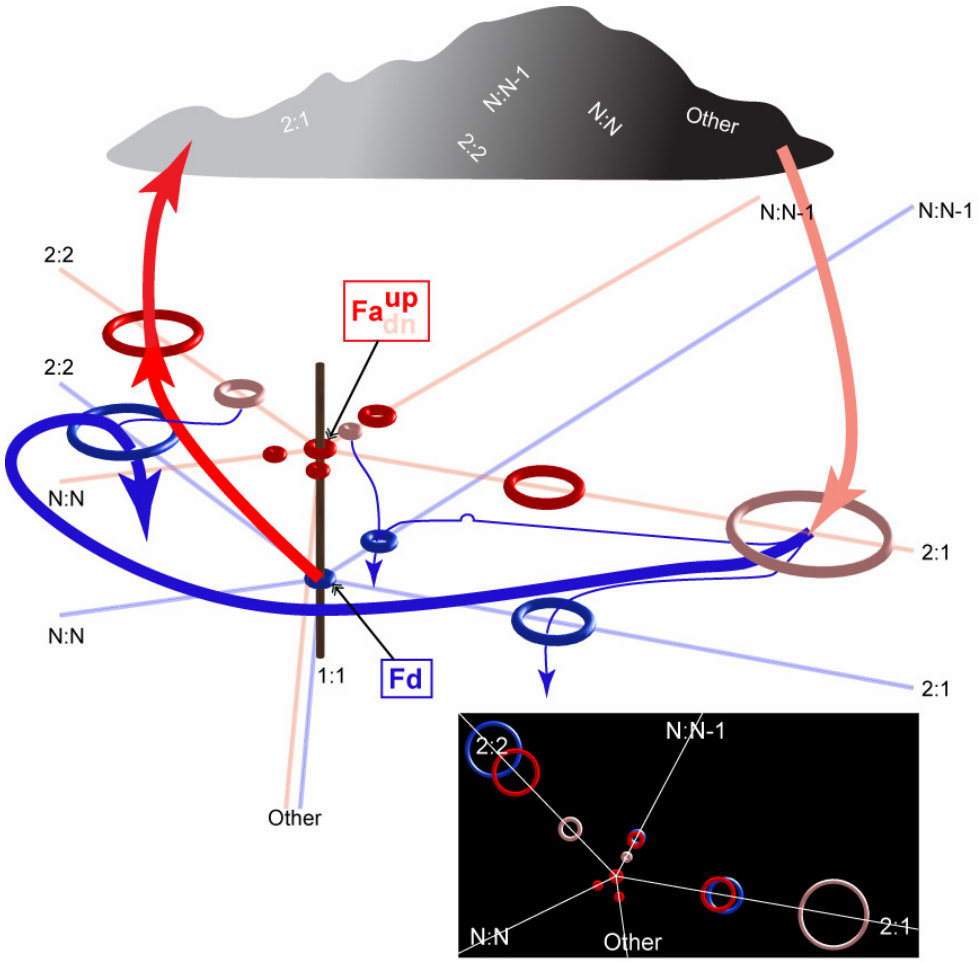

Figure 13-2 Multitude of patterns and paths traversed from 1:1 rhythm to the region of instability and back.
Different patterns (2:2, 2:1, N:N, N:N-1 and "others") at characteristic frequency planes are represented by rings, whose diameter and spacing from the "frequency pole" are proportional to the prevalence of the respective pattern (larger rings far from the pole indicate higher prevalence). Same patterns are positioned on the same radial line. Rings in the different planes are colored differently – blue for the F_d plane (return to 1:1 rhythm upon rate deceleration); red for the F_a-plane during rate acceleration ($F_{a\text{-}up}$) and pink during rate deceleration ($F_{a\text{-}dn}$), respectively. Rings on the frequency pole represent 1:1 rhythm. The gray cloud indicates the instability region Alt/IR after frequency F_a (for characterization of this region see (7)). Thick arrows follow the behavior of a representative sample; thin blue arrows show all observed paths in the tested samples when decreasing pacing frequency from F_a to F_d. Inset is a top view of all patterns and their respective positioning; small arrows point to the high similarity between the distribution of blue (F_d) and red ($F_{a\text{-}up}$) patterns and the dissimilar distribution of the pink patterns ($F_{a\text{-}dn}$).

Acknowledgements

We thank graduate student Adiba Ali for help with some of the experiments. This work was partially supported by grants to EE from Whitaker Foundation (RG-02-0654) and the American Heart Association (0430307N).

14. SPATIALLY DISCORDANT ALTERNANS AND MEANDERING SPIRALS

Abstract

Spatially discordant alternans (SDA) can lead to asynchrony in the heart function. They are known precursors to wavebreaks and reentrant activity, which can further deteriorate into lethal arrhythmias, including ventricular fibrillation (VF). In this study, we examine the temporal evolution of calcium SDAs, the interactions between co-existing SDA regions and spiral waves (SW), and the effects of such interactions on SW stability.

Ultra-high resolution optical imaging of calcium waves was applied to capture the evolution of emerging SDAs over time as pacing-induced SW developed in cardiomyocyte networks. The following new phenomena are reported here: 1) spatial association of the SW reentrant path with radial arrangement of the SDA domains; 2) temporal evolution of the SDA domains (dynamic expansion, contractions and shift along the SW path); 3) SW tip hypermeandering regions covering up to 1cm^2 area as a result of SDA-caused heterogeneous propagation – the SW tip remained primarily confined to the border zones between the SDA domains, where 2:1 block is seen (100% of the samples). These results suggest a potential mechanism of destabilization of SW via hypermeandering due to the presence of SDAs which may be important in the transition from ventricular tachycardia to VF.

Introduction

Beat-to-beat alternations in duration or amplitude, known as *alternans*, have been proposed to represent instabilities that may lead to arrhythmias(Karma 1994). When two different regions, both exhibiting alternans become out of phase, i.e. one region has long action potential duration while the other region is short, spatially discordant alternans (SDA) exists. SDA is distinguished from discordance between two different alternating parameters, typically action potential duration and intra-cellular calcium peak systolic levels. Experimentally, SDAs have been demonstrated to result in re-entrant activity, typically manifested as spiral waves(Pastore, Girouard et al.; Pham, Quan et al.; Pruvot, Katra et al.). It has been further proposed that SDAs are required for the transition from ventricular tachycardia (VT) – fast, synchronized activity – to ventricular fibrillation (VF) – ineffective (and hence fatal), rapid and irregular beating of the heart. The existence of SDAs has been thought to arise from gradients in ion currents between the base and apex of the heart(Pastore, Girouard et al. 1999), but computational models have demonstrated the possibility of SDAs in homogenous systems via conduction velocity restitution(Qu, Garfinkel et al.; Watanabe, Fenton et al.; Qu, Karagueuzian et al.) or disparate scales of propagation velocity between voltage and calcium alternans(Shiferaw, Sato et al.).

Using an established cultured neonatal rat cardiomyocyte model, we set out to answer the following questions: 1) Can SDAs exist in isotropic tissue as predicted by computer

simulations? 2) Can SDAs co-exist with re-entrant activity such as spiral waves? 3) How do SDAs and spiral waves interact when they are both present at the same time?

Methods

Neonatal rat cardiomyocyte culture

The protocol of primary cardiomyocyte culture has been documented previously (Bien, Yin et al. 2003). Briefly, the ventricles of the hearts of 3-day-old Sprague-Dawley rats were digested enzymatically using trypsin and collagenase, cardiomyocytes were collected after centrifugation and preplating, and then seeded on fibronectin-coated polydimethylsiloxane scaffolds (0.8x1cm in size) at a high density of 0.4×10^6 cells/cm^2. Cell constructs were kept in Medium 199 at 37°C and changed every 2-3 days.

Intra-cellular calcium imaging

Cardiomyocytes were stained with Fluo-4AM (Molecular Probes, Oregon) for 20 minutes and washed out for another 20 minutes in room temperature Tyrode's solution. The imaging setup is shown in Figure 9-1 where a 250W quartz-tungsten-halogen light source was filtered through a 480nm excitation interference filter to provide illumination through a bifurcated light guide. Images were captured through a Gen III intensifier connected to a high-definition (1024x1280 pixels), high speed (200fps) CMOS camera digitized at 10 bits per sample. Optical magnification achieved was 0.5x with a Rodenstock f/0.75 lens resulting in maximum spatial resolution of 0.022mm per pixel. Re-entrant activity was induced via rapid pacing (>4Hz) with point electrodes and the stimulator stopped when spiral waves were visible.

Image processing

Images were converted from 16-bit to 8-bit format (having a dynamic range of 0-255). Baseline subtraction and scaling to full dynamic range was performed for every movie. Spatial averaging (binning) of 2 by 2 pixels was performed to reduce the total size of the dataset. A 10 by 10 pixel Bartlett spatial filter was applied to increase the signal-to-noise ratio as suggested by Mironov et al. (Mironov, Vetter et al.). Re-scaling to full dynamic range was done again after filtering to avoid the blunting effect of low-pass filters.

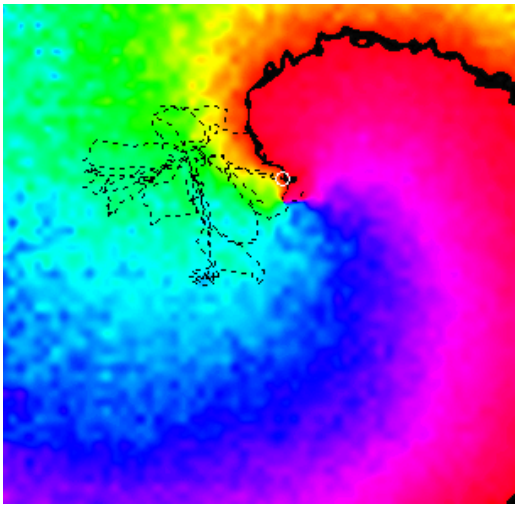

Figure 14-1 Example phase map of spiral wave with tip trajectory outlined.
Hilbert-transform phase map with red denoting the end and start of a transient and the black line approximates the wavefront. The spiral wave is turning counter-clockwise and the tip of the spiral wave at this instant is identified with the white circle. The previous history of the tip trajectory is also shown in broken black lines.

Phase maps were generated using the Hilbert transform (Bray and Wikswo) and the spiral tip identified over every frame by manual input. Spiral tip trajectory was recorded for all episodes of spiral wave activity. Peak calcium levels for each transient was detected using a custom adaptive algorithm, and beat matching across space was accomplished through collection of beats closest to a selected reference clock (typically provided by the activation times of a pixel far away from the tip of the spiral).

Alternans maps

SDAs were initially identified as regions with different phase in the Hilbert transform phase maps. Confirmation was accomplished by analyzing each transient and characterizing its peak amplitude. Alternans maps were then constructed by displaying the difference between the current beat's amplitude and the next – this is positive for small to big transitions and negative for big to small transitions. The alternans maps were then animated over time with transparency linearly falling to completely transparent for the next beat while the next beat's alternans maps becomes more visible, reaching a maximum at the start of the next beat. SDA regions were outlined by areas having differences greater than a specified threshold.

Tip trajectory analysis

The area enclosed by the tip trajectory was estimated by fitting a convex hull to all trajectory points using MATLAB and its area calculated. Stray or errant points, however, had the potential to profoundly impact the convex hull, and thus an alternative method was used to confirm our findings. Due to the repetitive (cyclical) nature of spiral waves, the tip trajectory often re-traces its previous path. Thus, the number of unique locations traversed by the tip trajectory is a rough estimate of the area "covered" by the core of the spiral wave. Normalization for the duration of recording is accomplished by expressing the number of

unique points as the percentage of all data points. Two-sample Student's t-test were performed with significance determined at $p<0.05$.

Results

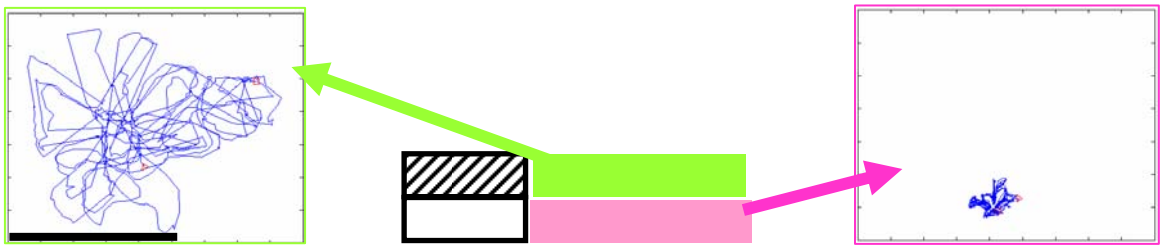

Figure 14-2 Spiral waves with co-existing SDAs meander more than those without. The trajectory of typical spiral waves with (left) and without (right) SDAs are shown above at the same spatial scale. The recording duration for all samples were similar (approximately 10-14 seconds).

Spiral waves with SDAs were observed in 7 out of the 14 cases recorded. The SDAs remained present throughout the entire recording but often changed locations and shape over time(**Figure 14-3**). The most striking difference between the behaviors of spiral waves with SDAs and those without was the exaggerated meandering seen of the spiral wave tip (**Figure 14-2**). Spiral waves in the presence of SDAs covered a much larger area than those without, and this was quantified by examining the convex hull area of the spiral tip trajectory (**Figure 14-4, left**). The percentage of unique locations traversed by the spiral tip trajectory was also found to be significantly larger for those with SDAs (**Figure 14-4, right**).

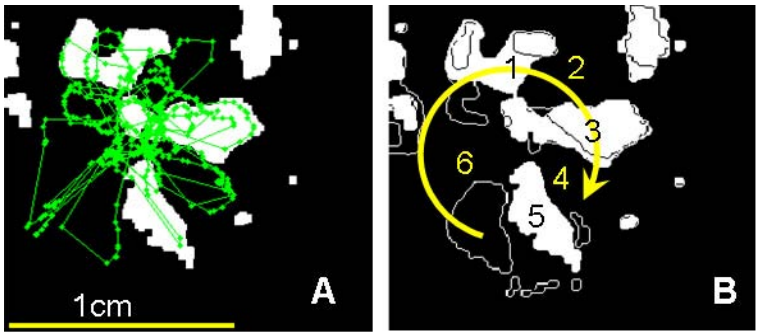

Figure 14-3 Spiral wave tip trajectory avoids SDA regions and evolution of SDAs. (binary thresholded difference between consecutive beats), highlighting in white the transition from high-to-low calcium transients, show the radial arrangement of 6 SDA regions along the reentrant path. The tip of the spiral tracked over 13 beats is superimposed to show the preference of the meandering path for the border regions (A). The SDA evolution is illustrated by superimposing alternans maps for 2 sequential odd beats (border outlines shown for one of them); arrow indicates the reentrant path (B).

Closer examination of the spiral tip trajectory indicates a tendency to travel along the nodal lines separating two discordant regions. Comparing the magnitude of alternans for the

locations traversed by the tip did not appear significantly different from a randomly selected path through the imaged area. However, the size of the transition area, i.e. the space around a nodal line, was found to vary considerably from 2.58mm to 0.658mm depending upon the size of the SDA regions (Figure 14-5). When one considers the errors inherent in subjective localization of the spiral tip combined with the narrow width of the nodal line, the lack of significance may not be indicative of a true lack of difference.

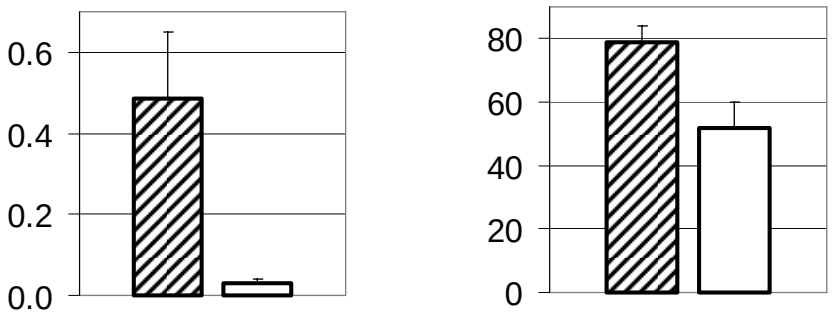

Figure 14-4 Area traversed by spiral wave's core is greater in those with SDA.
The area of the convex hull of spiral waves in the presence of SDAs is significantly larger than those without. Similarly, the percent of unique locations traversed by the spiral wave tip is greater for re-entry with SDAs.

The wavefront also appears to be retarded as it crosses nodal lines (**Figure 14-6**). The slower wavefront propagation across nodal lines is also in agreement with tip velocity. Preliminary analysis so far indicates that the tip trajectory is much faster inside an SDA region compared to in the transition zone. The changes in conduction velocity actually affects wavefront curvature similar to how light is bent passing through regions of varying indices of refraction. We have observed alternating conduction velocities together with alternating curvatures to the point of sign reversal, i.e. concave to convex transitions, when the wavefront passes through regions of alternans.

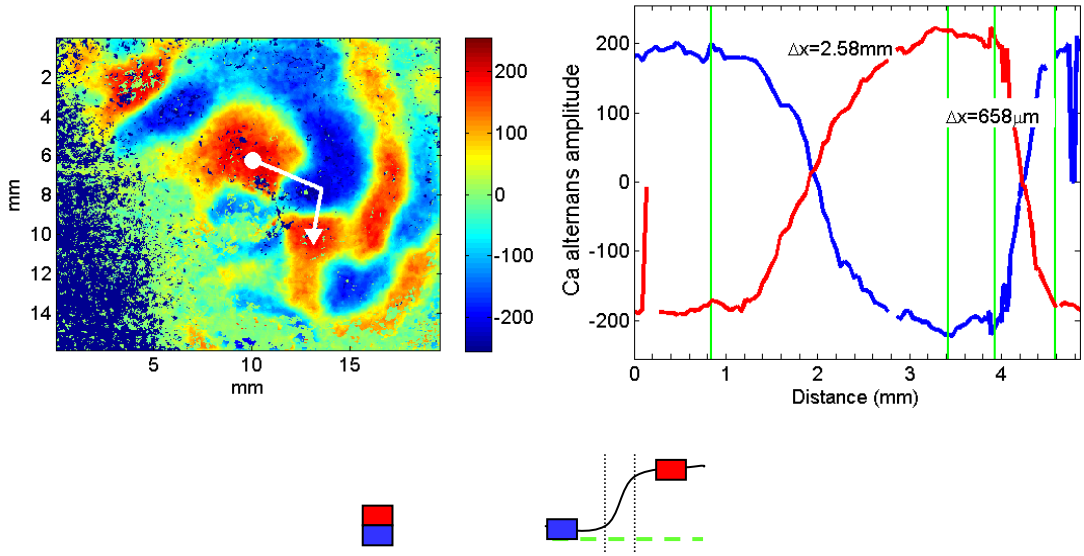

Figure 14-5 SDA transition zones vary as a function of SDA region size.
On the left is a difference map showing several SDA regions of variable size. Starting from the white dot, a profile of alternans magnitude is taken along the white line towards the white arrowhead. The calcium alternans amplitude is shown on the right as a function of distance from the white dot demonstrating the variable sizes (from 2.58mm to 0.658mm) seen in the transition zone between two discordant regions. The transition zone is loosely defined as the area in-between two regions, depicted schematically above.

The interaction of spiral waves and SDAs is also suggested by the radial arrangements of SDA regions around the spiral tip (**Figure 14-7**), seen in many of the recorded episodes with SDA. A quantitative measure of radial position will be developed to ascertain whether there exists an organizational association between spiral waves and SDA regions. A simple explanation of apparent radial positioning without a true association with spiral wavefront could be the bias of centering the region of interest over the spiral when noted. Such a central position of the spiral wave tip would tend to make any organization of SDA regions appear to be arranged in a concentric manner about the tip. A quantitative measure taking this bias into account would be better able to determine whether spiral waves might organize SDA regions.

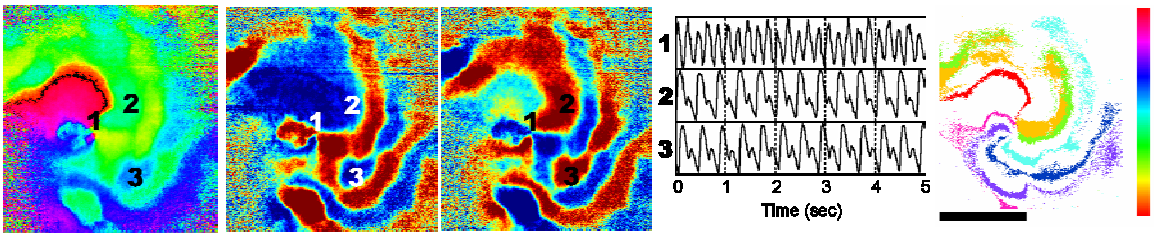

Figure 14-6 Spiral waves with SDAs in phase, alternans difference, and isochrone maps
From left to right, shown are a single snapshot of a Hilbert phase map of a clockwise rotating spiral wave with spatially discordant alternans (visible as distinct regions with different phase). SDA difference maps are then shown with red indicating regions of increasing (small to big) calcium transients and blue decreasing transients. Signal traces from identified locations in the SDA difference map is presented to the right. Far right is an isochrone map demonstrating a retardation of propagation at the borders of discordant alternans regions.

Discussion

This is the first report of SDAs in the setting of re-entrant, non-paced, activity. Such a condition permits complex interactions between the excitation patterns, i.e. the spiral wave, and the SDA regions. Our data suggest that such an interaction does occur, and moreover there may even be spatial organization of SDAs about spiral wave tips. Further analysis will reveal whether such organizing behavior occurs and whether the spiral tip trajectory is influenced by SDA regions.

The variation of conduction velocity and tip velocity about SDA regions and nodal lines brings about distinct possibilities for mechanisms of spatial organization. The tendency for the spiral tips to stay away from SDA regions may in fact be an illusion arising from faster tip velocities within SDA regions and thus reducing the amount of time spent inside a region.

Conduction velocity can be computed first as spatial maps of conduction *slowness* or the inverse of velocity. Mapping data is more amendable to spatial gradients then temporal derivatives. Thus, times of activation (or any other reference point) can be noted for each pixel and the spatial gradient estimated to determine the local conduction slowness vector. Due to the high spatial resolution of HUMR, simple numerical differencing algorithms will fail due to the noise present in locating activation times. Thus, a biquadratic surface can be fit over the point of interest to the times of activation around it. Using multiple linear regression, we can then obtain the analytical equation for the activation time (T) surface of the form

Eq. 14-1) $$T(x,y) = c_1 y^2 + c_2 y + c_3 x \cdot y + c_4 x + c_5 x^2$$

where c_1, c_2, c_3, c_4, and c_5 are constants to be fit and T(x,y) is the activation time at location (x,y). Note that the surface is forced to pass through (0,0,0) because the pixel of interest is centered at (0,0) and the activation time there is defined to be zero. Armed with such a description, the velocity vector is easily calculated at (0,0) to be

Eq. 14-2)

$$v_x(x,y) = \frac{\partial \Gamma(x,y)}{\partial x} = \frac{c_4}{c_2^2 + c_4^2}$$

$$v_y(x,y) = \frac{\partial \Gamma(x,y)}{\partial y} = \frac{c_2}{c_2^2 + c_4^2}$$

where $v_x(x,y)$ and $v_y(x,y)$ are the x- and y- velocity components, respectively.

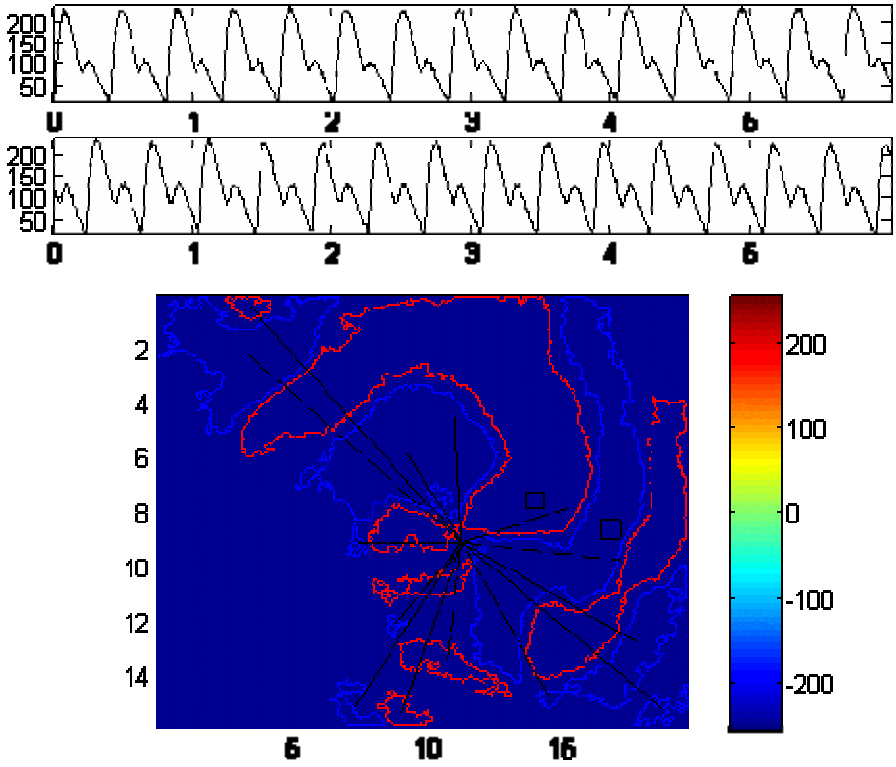

Figure 14-7 Radial arrangements of SDA regions.
SDA regions are outlined in blue (negative difference) and red (positive difference). Thin black lines connect the spiral tip (the intersection of all black lines) and the centroids of all the SDA regions. Signal traces from the two black rectangles are shown above the difference map.

In addition to estimating the conduction velocity, the biquadratic surface also permits one to estimate the rate of change of velocity, or acceleration, at the point (0,0). Normally, one would simply take the derivative of velocity with respect to time. However, due to the nature of optical mapping, it is far easier to take the derivative with respect to space. Reconciling the two is possible once one knows the velocity v(x,y) because

Eq. 14-3)

$$x^2 + y^2 = (v(x,y) \cdot dT(x,y))^2$$

where dT(x,y) represents the time difference from the origin (0,0) to the point (x,y) and v(x,y) is the speed at location (x,y). Multiplying each component of the acceleration vector by the appropriate component in the velocity vector yields a spatially transformed version of acceleration:

Eq. 14-4)

$$a_x = \frac{\partial v_x(x,y)}{\partial x} \times \frac{\partial x}{\partial t} = \frac{\partial v_x(x,y)}{\partial x} \times v_x = \frac{dv_x(x,y)}{dt}$$
$$a_y = \frac{\partial v_y(x,y)}{\partial y} \times \frac{\partial y}{\partial t} = \frac{\partial v_y(x,y)}{\partial y} \times v_y = \frac{dv_y(x,y)}{dt}$$

where a_x and a_y are the components of acceleration in the x- and y- axis, respectively. Combining Eq. 14-2 with Eq. 14-4 and solving for x=0 and y=0 yields

Eq. 14-5)

$$a_x = \frac{2c_5}{c_2^2 + c_4^2} - \frac{c_4(2c_2c_3 + 4c_4c_5)}{(c_2^2 + c_4^2)^2}$$
$$a_y = \frac{2c_1}{c_2^2 + c_4^2} - \frac{c_2(2c_3c_4 + 4c_1c_2)}{(c_2^2 + c_4^2)^2}$$

Curvature can then be computed by resolving v_x and v_y into a direction field using $\arctan(v_x/v_y)$ and repeating the previous analysis except replacing the times of activation with the scalar direction. The resultant vector will be the rate of change of velocity with respect to time ($d\theta/dt$) in terms of pure directional change. Generating the curvature is now trivial since there exists only one unique circle of radius *r* such that a point on that circle travels with velocity v(x,y) and moves with angular velocity $d\theta/dt$.

The evolution of SDA regions over time makes for a difficult analysis as the patterns constantly change and shift. However, the patterns of evolution and the SDA region remodeling themselves provide fertile ground for further analysis into interactions between spiral waves and SDA, revealing mechanisms of progression towards ventricular fibrillation.

Conclusion

There is a wealth of data already collected from the 14 samples imaged. Although the samples were re-entrant and not paced, limited restitution type data can be gleaned from the SDA samples since they undergo a continuous change in conduction velocity and hence diastolic interval. By plotting the distribution of conduction velocity or calcium transient duration against the measured DI, one can see the restitution relationship over a limit range of DIs. Furthermore, armed now with the ability to compute curvature at any given point, one can also determine the eikonal relationship. So far, the critical radius of curvature in cardiac tissue remains to be experimentally verified. A single snapshot of a rotating spiral wave will reveal the eikonal relationship instantly in that the spiral wavefront will curve with greater curvature until it hits the critical curvature at the tip of the spiral. To date, such data have not been collected and the actual value remains unknown.

15. EFFECT OF PM-EXPOSED AM CONDITIONED MEDIA ON HTC'S

Abstract

We tested the hypothesis that particulate matter air pollution results in increased cardiovascular morbidity via inflammatory mediators secreted from lung tissue exposed to particulate matter dust. Neonatal rat ventriculocytes (NRVM) were cultured in media conditioned by NR8383 rat alveolar macrophage (AM) cells challenged with particulate matter (PM) or lipopolysaccharide (LPS). High levels of TNF-α were detected in media conditioned by AM and activated with PM or LPS, but little to no IL-1β was measured. NRVMs cultured for 24 hours in PM activated AM conditioned media (P+ group) displayed faster calcium kinetics and larger calcium transients. LPS activated AM conditioned media (L+ group) also exhibited faster dynamics but significantly less than P+ despite having higher levels of secreted TNF-α. Finally, quiescent AM conditioned media (S+ group) was observed to have shorter calcium transient durations compared to control (S- group). Taken together, these results suggest a "stress"-type response to soluble factors released from PM or LPS activated AM and that PM induces a different cytokine profile from LPS in AM.

Introduction

Ambient particulate matter is known to induce pulmonary inflammation(Nel, Diaz-Sanchez et al. 2001; Kodavanti, Schladweiler et al. 2002; Becker, Soukup et al. 2003; Gilmour, O'Connor et al. 2004; Ishii, Fujii et al. 2004), and inflammatory cytokines are also known to perturb cardiac rhythms(Peters, Liu et al. 2000; Rich, Schwartz et al. 2005). Studies of the more well-studied inflammatory cytokines, e.g. tumor necrosis factor alpha (TNF-α) and interleukin-1beta (IL-1β), have been performed on cardiac myocytes(Bick, Wood et al. 1999) and over-expressed in transgenic mice(Dibbs, Diwan et al. 2003). As discussed in Chapter 6, particulate matter exposure is expected to induce release of a cocktail of cytokines from alveolar macrophages. While it is tempting to extrapolate these findings to implicate cytokines as a mechanism of cardiac arrhythmias, no study to date has examined the direct effect of such cytokine cocktails on the function of cardiac myocytes. Without such studies, the postulated mechanism can only remain a hypothesis. Using the imaging and analysis techniques outlined in the previous chapters, we characterized the effects of secreted factors from alveolar macrophages exposed to particulate matter on cardiomyocyte networks.

Methods

Cell culture

Neonatal rat cardiomyocytes were isolated and cultured as described previously(Bien, Yin et al.). Briefly, after enzymatic digestion and fibroblast isolation, cardiomyocytes were plated onto 18x7mm polydimethylsiloxane (PDMS) scaffolds for one week prior to experiments. Cardiomyocyte culture medium consists of Medium 199 with 2% fetal culture serum (M199/2%FCS) and changed every 2-3 days.

Rat alveolar macrophage cell line NR8383 (ATCC) were sub-cultured and maintained as per the manufacturer's instructions. Briefly, the fraction of cells in suspension were removed and replaced with fresh F12K medium supplemented with 15% fetal calf serum (F12k/15%FCS). Expansion to more flasks is accomplished by pooling the suspended fraction of several culture flasks to achieve the recommended cell density of 1-4x10^5 cells/mL and seeded into T75 flasks.

In-vitro PM exposure

One day prior to the *in-vitro* PM, LPS, or sham exposure, small 50mL conical tubes for tissue culture were seeded with 3x10^5 cells/mL in 10mL volumes. Two days prior to the experiment, the 50mL conical tubes had their culture medium replaced with F-12k/15% FCS culture medium inoculated with distilled H_2O (S+), 10ng/mL LPS (L+), or 0.1mg/mL NIST SRM 1649a (P+). Additional tubes were filled with 10mL of each of the culturing solutions but without any NR8383 cells as controls (L-, P-, and S-). All tubes were incubated at 37°C and 5% CO_2 for 24 hours (Figure 15-1).

At the end of the 24 hour period, all tubes were spun down at 1,200rpm to remove AM cells and debris including particulate matter. LPS, being a rather small molecule, as well as any aqueous leechables from PM, remain in the supernatant. HTCs were then cultured for another 24 hours in each of the conditioned media and their respective controls. At the end of the final 24 hour period, HTCs were removed from the incubator and assessed for their functional response. Samples were also collected and frozen at -80°C for later measurements of TNF-α and IL-1β levels in the culture medium.

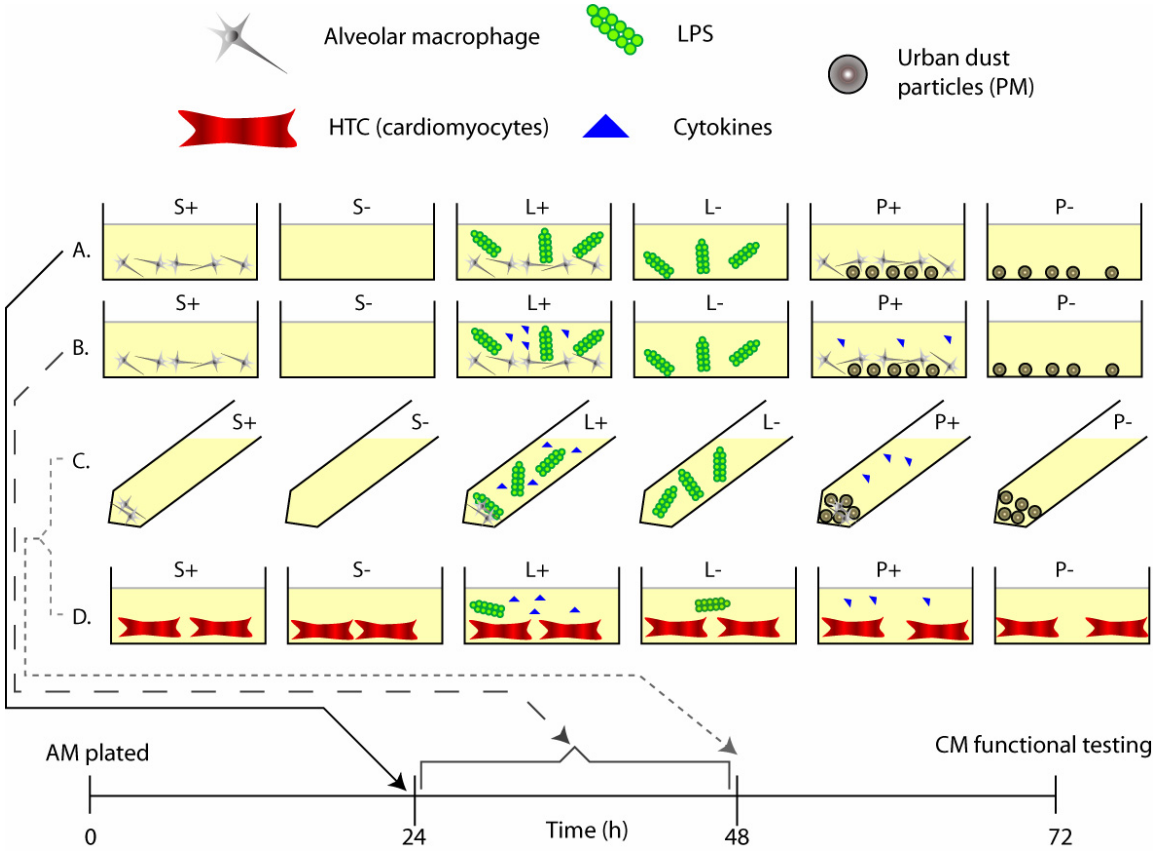

Figure 15-1 Schematic diagram and timeline of *in-vitro* PM exposure model.
A. Empty vehicle (sham), LPS, or SRM 1649a (PM) are used to inoculate conical tubes either pre-plated 1 day prior with alveolar macrophages (AM) or fresh, empty tubes. B. After 24 hours, activated AM secrete a mixture of cytokines. C. The conditioned media is then collected, centrifuged to remove AM and PM, and a sample frozen at -80°C. D. The remaining media is then used to treat HTCs with conditioned media from each group for an additional 24 hours before undergoing functional testing. Samples in group "S" received media treated with sham, group "L" were treated with LPS, and group "P" were treated with PM. Groups with "+" suffix denote conditioned media (AM present) whereas those with "-" suffix were culture media alone (without AM).

Measurements of secreted TNF-a and IL-1β

Samples of the dosing media (sham, LPS, and PM) were collected to ensure no exogenous sources of IL-1β and TNF-α exist. Confirmation of activation was provided by sampling the supernatants of AM exposed to various agents after the 24 hour period. The culture medium for each HTC was sampled once more just prior to functional testing indicating the final levels of TNF-α and IL-1β seen by the cardiomyocytes.

All samples were stored at -80°C until ready for analysis. Quantitation was done by rat TNF-α and rat IL-1β ELISA kits (Biosource) as per the manufacturer's instructions. A four-parameter sigmoid curve was fit to the calibration samples run on every ELISA plate and used to determine the concentration of secreted TNF-α and IL-1β.

Microscopic measurements of transmembrane voltage and intra-cellular calcium

On the day of functional testing, HTC samples from the 6 experimental groups (S+, S-, L+, L-, P+, and P-, $n \geq 5$ per dosing group) will be stained with both a voltage indicator dye (di-8 ANEPPS, Molecular Probes) and a calcium indicator dye (Fura-2 AM, Molecular Probes). The scaffolds were placed into a temperature controlled perfusion chamber at 30°C with a line electrode placed at one end and the microscope objective observing the other end at a known, measured, distance. HTCs were microscopically examined for holes or defects between the stimulator and point of observation. HTCs with defects were not used or the observation point was relocated to ensure a clear, continuous line of tissue to the stimulator. Fluorescence will be collected by a PMT mounted on the microscope through appropriate optical elements to isolate the specific wavelength for each dye.

Samples were paced from the line stimulator at 1.5 times the threshold voltage (determined at 1Hz pacing rate) starting at 1Hz and gradually increasing in frequency until clear 2:1 conduction block was noted at two successive frequencies. At each pacing rate, HTCs were permitted to equilibrate for 60 beats and then 20 beats were recorded for calcium fluorescence followed by another 20 beats for voltage fluorescence. The pacing rate was then increased and the sample entrained for another 60 beats.

The first experiment used step sizes of 0.5Hz until 2Hz and then 0.2Hz thereafter. The second experiment used 0.5Hz steps until 3Hz and then 0.2Hz thereafter. Stepping size was varied to ensure no sample was probed for more than 20 minutes. The highest frequency attained before loss of 1:1 capture is recorded as the maximum capture rate (MCR).

Data analysis and statistics

Automated waveform characterization was performed using the software described in Chapter 10 and 2-way ANOVAs across group and pacing rate conducted with the Tukey post-hoc adjustment in MATLAB on all measurable parameters. Significance will be set at $p<0.05$. MCR, threshold for stimulation, and distances from stimulator were also examined for differences using 2-way ANOVA with Tukey post-hoc comparisons.

For transient analysis, ANOVA was performed within experiments, i.e. harvest and culture, to avoid the large variability between cultures often noted in primary cells. Frequencies greater than 3.0Hz, while recorded and analyzed, were also removed to ensure all groups had representation at each probed frequency (otherwise ANOVA would fail).

Results

PM and LPS-activated AM conditioned media resulted in robust and sustained TNF-a levels

After 24 hours of exposure to LPS or PM, activated AM released large quantities of TNF-α (Figure 15-2, left "Initial") compared to both sham with AM and all groups without AM. Surprisingly, these levels became even higher after an additional 24 hours with HTCs. When compared per experiment (the first experiment did not have the "initial" group), the increase became significant in the L+ group. The slight amount of TNF-α measured for the L- group (LPS without macrophages) was not significantly different from sham or control (no AM) groups.

IL-1β levels were extremely low – none were significantly different from shams (S-). The measured values were near the extreme limits of the assay and thus variability was high. Initial levels of IL-1β were below detection limits (3pg/mL per manufacturer's instructions), and all measured values were well within the noise floor.

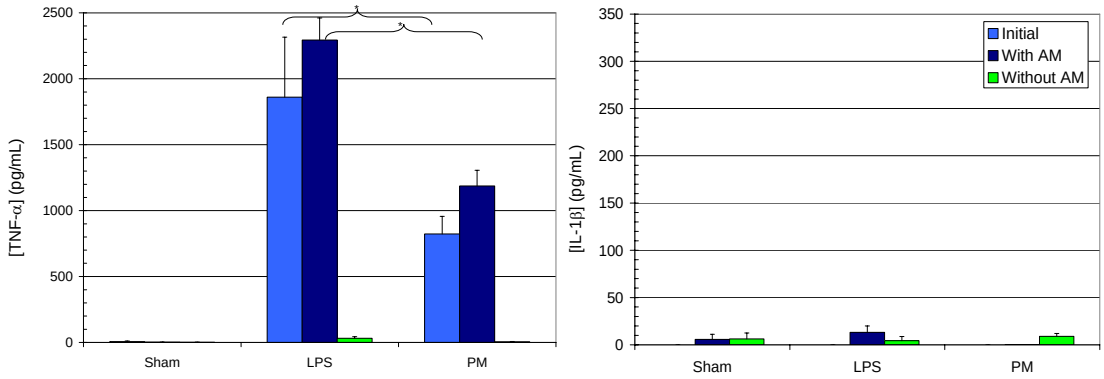

Figure 15-2 Both PM and LPS induced high levels of TNF-α
Culture media were assayed for [TNF-α] and [IL-1β] both at the initial time point (24 hours after activating AM) and at the end of a 24 hour incubation (treatment) period with HTCs. Culture media were conditioned either in the presence ("With AM") or absence ("Without AM") of AM. TNF-α and IL-1β levels were undetectable at the initial time point for groups without AM (data not shown). Displayed are means±SE for each group representing 3 different experiments ($n \geq 6$ per group). Groups with brackets indicate differences are significant to $p<0.05$. Not indicated are LPS and PM groups, both initial and with AM, are significantly different from all other groups.

Maximum capture rate (MCR) differed significantly only for S+ in the second experiment

The highest pacing rate that still resulted in 1::1 capture of stimulus::response was recorded as the maximum capture rate (MCR) for each sample (Figure 15-3A). There were no significant differences noted between groups in the first experiment ("Culture 1") while the second experiment ("Culture 2") had the sham controls (S+) failing 1::1 pacing relatively early on. To avoid bias in transient analysis, only data collected from pacing rates between 1.0 and 3.0Hz were considered. Furthermore, the experiments were analyzed separately to avoid culture-to-culture variations and permit extraction of data during both conditions where MCR did not differ as well as those where it did.

Distance from stimulator differed only in Culture 1 for P+ versus S+

While in general the observation point was selected to be ≥1.0cm away from the line electrode to avoid stimulus artifacts, P+ and P- samples were significantly closer than S+ in the first culture (Figure 15-3B). However, P- and S- were later found to have nearly identical transient morphologies indicating that the difference in distance did not have a significant effect on HTC function. Furthermore, in the second culture the distances were no longer significantly different and if anything, the S+ sample tended to be slightly closer.

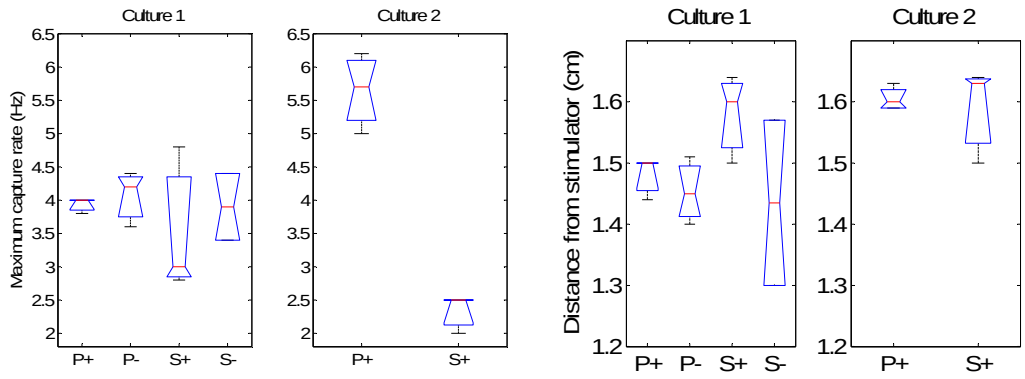

Figure 15-3 Maximum capture rate (MCR) and distance from stimulator.
Shown are box and whisker plots indicating the median (red centerline), upper and lower quartiles (whiskers), and a robust estimate of uncertainty about the median (notched edges) for A. the highest pacing rate achieved that maintained 1::1 capture, and B. distance from stimulator to observation point. Non-overlapping notches indicate significant difference at $p<0.05$.

Quiescent (sham activated) AM conditioned media (S+) shortened CTD at 1Hz

Examining the effect of the presence of AM by itself, i.e. quiescent (sham activated) AM or group S+, on HTCs via conditioned media versus true controls (HTCs cultured in fresh F-12k media) or group S-, reveals significantly shortened CTDs at 1Hz but not at higher frequencies (Figure 15-4A). Nevertheless, the trend for CTDs to be shorter persisted until about 2.6Hz where they converged. Although the time to peak was not significantly different (Figure 15-4C), due to the prolonged CTD at 1Hz, the time to fall 80% of peak amplitude from peak (time to baseline) was significantly shorter at 1Hz and merged at higher frequencies (Figure 15-4D). Peak calcium amplitude and rates of rise and fall were not significantly different (Figure 15-4B, Figure 15-4E, and Figure 15-4F).

PM treated media in the absence of AM (P-) did not differ from sham controls without AM

To control for the presence of possible contaminants and aqueous phase leachables from PM, a group having only PM but not AM (P-) was also tested. P- and S- groups were nearly identical across all variables studied (Figure 15-4A through Figure 15-4F). Importantly, the L- group (LPS without AM) differed from both P- and S-. First, L- transients were significantly larger in normalized amplitude ($\Delta F/F_0$) and shorter throughout the 1.0Hz through 2.6Hz frequency range (Figure 15-4A and Figure 15-4B). Consistent with the greater amplitude but similar times to peak, L- had faster rates of rise (rate of change of fluorescence during activation) than P- or S- (Figure 15-4E). Times to peak and return to baseline as well as fall rates were not significantly different (Figure 15-4C, Figure 15-4D, and Figure 15-4F).

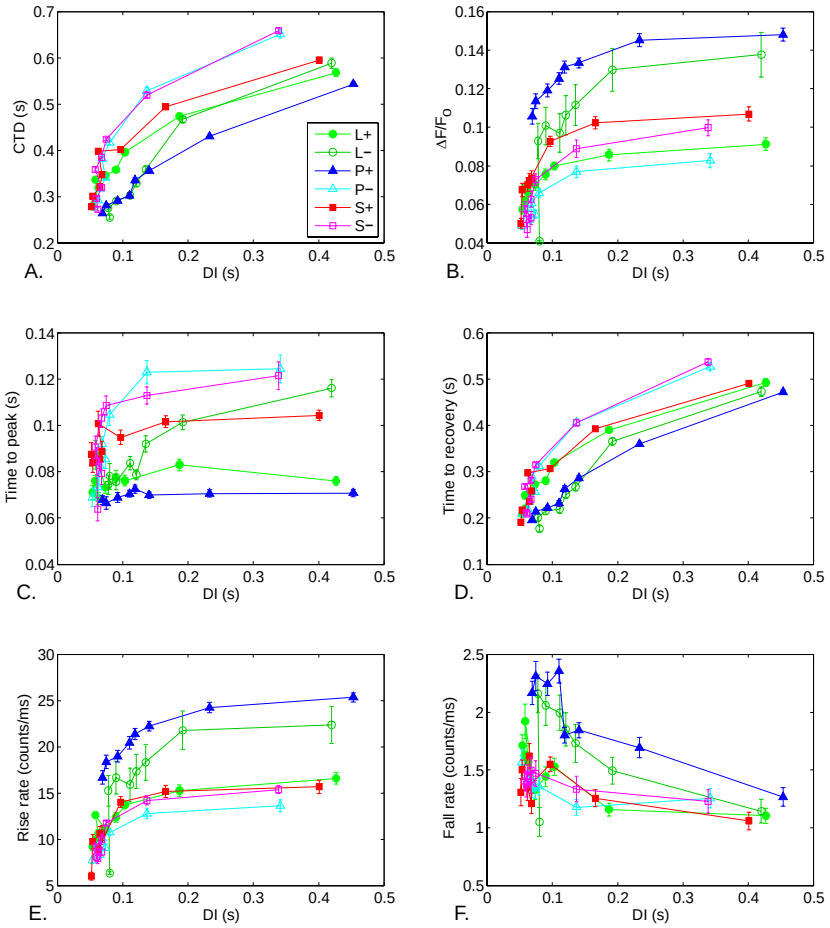

Figure 15-4 Effect of exposure to AM-conditioned media or control media without AM. A. CTD_{80} for each group are plotted against the corresponding DI. B. The systolic calcium amplitude, reflected here as the normalized fluorescence intensity, is plotted against DI. C. The time from initial deflection to peak fluorescence is displayed against DI. D. The time from peak fluorescence to 80% of the peak amplitude (CTD_{80}) is plotted against DI. E. The rate of increase in fluorescence during activation (measured as electron counts from the PMT) is shown for each group against the corresponding DI. F. The rate of decline in fluorescence during recovery is plotted against DI. Shown are means+/-SE of transients recorded per group (N>=20 transients per group, per frequency).

PM activated AM conditioned media (P+) shortened time to peak and increased rise rates

Since the presence of AM, even quiescent, appears to shorten CTD, we compared PM activated AM conditioned media (P+) against quiescent sham activated AM conditioned media (S+). Up until 2.8Hz, P+ samples had significantly decreased CTD_{80} times compared to S+ (Figure 15-4A). This difference, however, was not repeated in a second experiment (Figure 15-5A). The time to peak and rise rate were significantly different for both experiments up to 2.0Hz beyond which the differences merged (Figure 15-4C, Figure 15-5C, Figure 15-4E, and

Figure 15-5E). The normalized peak amplitude remained significantly higher for P+ compared to S+ across both experiments (Figure 15-4B and Figure 15-5B). Time to baseline and fall rates were not significantly different (Figure 15-4D and Figure 15-4F).

PM activated AM conditioned media (P+) induced changes distinct from LPS activated AM (L+)

To determine whether the changes observed for PM-activated AM conditioned media might be due to the presence of LPS in PM, we also tested LPS activated AM conditioned media (L+). Compared to P+, L+ samples had significantly longer CTD_{80} throughout the frequency range from 1.0Hz to 2.6Hz (Figure 15-4A). Once again, however, this CTD_{80} effect was not observed in a repeated experiment (Figure 15-5A) where P+ samples had longer CTD_{80} than L+. The normalized peak fluorescence change ($\Delta F/F_0$) remained significantly larger for P+ compared to L+ transients across both cultures (Figure 15-4B and Figure 15-5B), but time to peak was not significantly different between P+ and L+ samples for both cultures (Figure 15-4C and Figure 15-5C). This, combined with the amplitude changes, results in significant differences for rise rates (Figure 15-4E). No significant differences, however, were observed for time to baseline and fall rates (Figure 15-4D and Figure 15-4F).

LPS alone (L-) resembled changes from PM activated AM conditioned media (P+) but distinct from L+

To rule out direct effects of LPS on HTCs, we also studied samples with 10ng/mL of LPS but without any AM (L-). To our surprise, the L- group tracked the P+ group fairly closely in all variables except for CTD_{80} and time to peak at 1.0Hz and 1.5Hz (Figure 15-4A through Figure 15-4F). CTD_{80} for L- was significantly different from S- and even P+ transients. The peak amplitudes were significantly different from all other groups except P+ where they also shared significant differences in times to peak and rise rate.

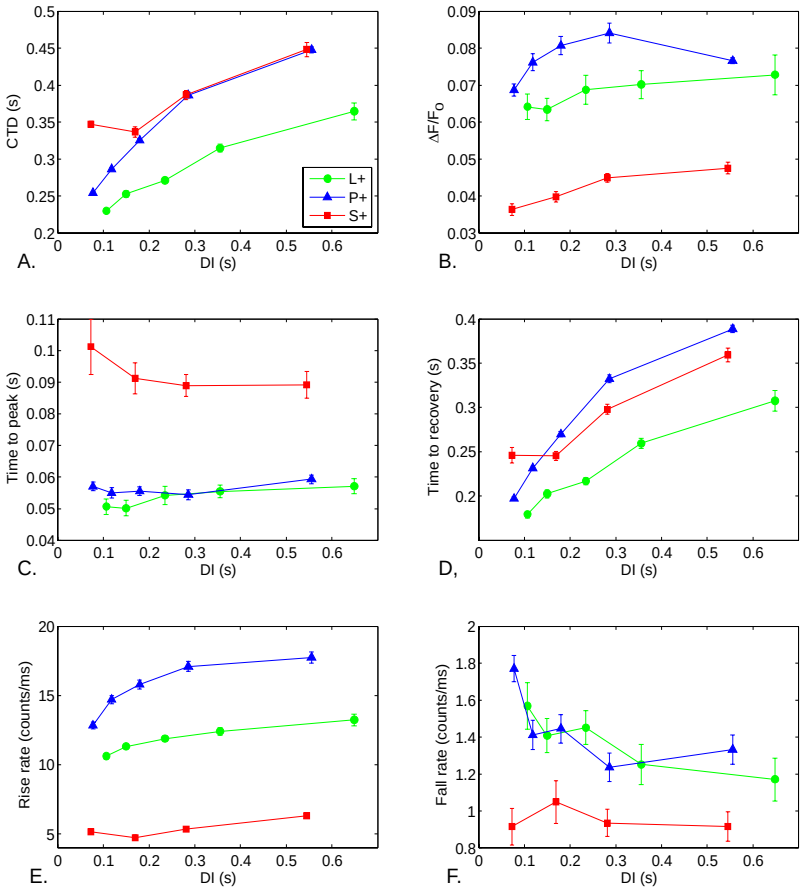

Figure 15-5 Effect of LPS or PM activated AM conditioned media on HTCs.
A second experiment was performed similar to the first and the results are presented here as in Figure 15-4. A. A plot of CTD_{80} versus DI. Note the unusual shape for S+ at the shortest DI – this is due to loss of samples due to pacing beyond MCR. B. Normalized fluorescence intensity. C. Time from initial change in fluorescence to peak fluorescence. D. Time from peak fluorescence to return to 80% peak fluorescence. Note again unusual shape at shortest DI for S+ due to inability of samples to follow pacing rate. E. Rate of change of fluorescence during activation. F. Rate of change of fluorescence during relaxation (recovery). Shown are means+/-SE for transients from each group (N>=10 transients per group, per frequency).

Schematic models of calcium transients at 1Hz and 2Hz

Schematic model calcium transients can be drawn using spline curves with nodes fixed at specified locations: start of transient and baseline, time to peak and amplitude, and finally 20% of peak amplitude at CTD_{80} along with enforcing the local tangent to the nodes at the start and end of the transient to have slopes equal to the rates of rise and fall (Figure 15-6A). By drawing such transients for all groups at both 1Hz and 2Hz (Figure 15-6B), the six plots of Figure 15-4 and Figure 15-5 are more readily digested. The great differences in peak

amplitudes can mask subtle changes in timing, so we scaled all transients to the same peak amplitude in Figure 15-6C.

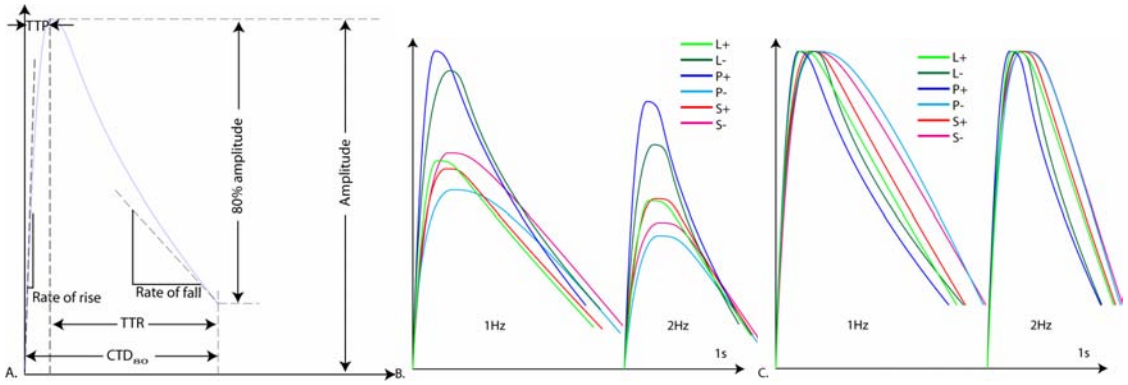

Figure 15-6 Schematic transients for each group at 1 and 2Hz.
A. Schematic of key points used in describing the morphology of a calcium transient. The same points and lines are used to construct exemplar transients from splines with nodes located at the peak and CTD_{80}. Tangents to the splines at each node were also fixed to match the rates of rise and fall. TTP = time to peak; TTR = time to recovery. B. Exemplar transients were constructed to scale matching amplitude (peak height), duration (CTD_{80}), time to peak, and rates of rise and fall for means of each group as shown in Figure 15-4. C. The same schematic transients as (B) but normalized to peak amplitude to better reveal timing differences. Shown are examples for both 1Hz and 2Hz. The limits of the horizontal and vertical axes represent 1 second and 1000 counts, respectively, for both 1Hz and 2Hz transients.

Discussion

TNF-a levels persisted throughout 24 hours in culture with HTCs

The activation of AM by LPS or PM induced a potent response of large amounts of TNF-α secretion with undetectable levels of IL-1β. This is in contrast to earlier work (Chapter 6) where we demonstrated that LPS stimulation, in particular, results in more IL-1β secretion than PM stimulation. As this result was repeated over three different experiments, one possibility is that IL-1β is rather unstable and storage at -80°C is insufficient to preserve it. Previously, due to timing issues, IL-1β was assayed immediately after the end of the exposure. However, for functional testing, IL-1β culture media samples were routinely stored frozen at -80°C for weeks at a time until several experiment runs were combined into a single ELISA run.

Nevertheless, there was a hint that LPS alone may have incited HTCs to secrete TNF-α as reported earlier for murine cultured cardiomyocytes at doses as low as 10ng/mL(Wright, Singh et al. 2002). The levels of TNF-α measured for L- group (LPS alone without AM) were in the range described by Wright et al., approximately 50pg/mL, but failed to show a significant difference from S-. This might be due to the high variability of TNF-α measurements at the low end of the scale where the assay was purposely curtailed early to enhance the precision of higher concentrations such as that found in L+ and P+ groups.

Even if LPS by itself was capable of inducing HTCs to secrete TNF-α, it is interesting to note that only HTCs treated with activated AM conditioned media (from either LPS or PM exposure) exhibited sustained TNF-α levels after an additional 24 hours incubation. This suggests that LPS, by itself, may be insufficient to induce a full TNF-α response or that TNF-α remained relatively stable over the 24 hour period. That the latter is probably not the case is hinted by reports of the *instability* of TNF-α in culture medium (as well as blood, serum, etc.) by Corti et al. (Corti, Fassina et al. 1992). In point of fact, their results suggest that at concentrations below 10ng/mL TNF-α may dissociate into biologically inactive monomers. It is unclear whether the ELISA kits we used from BioSource capture the biologically active homotrimeric form of TNF-α or is sensitive to TNF-α monomers as well. Unfortunately, it leaves the possibility open that the detected TNF-α concentrations may not have biological activity.

Quiescent AM conditioned media alters HTC function independent from TNF-a and IL-1β

The observed differences in CTD_{80} between S+ and S- hints at a factor (cytokine) that is neither TNF-α nor IL-1β secreted from AM constitutively that results in shortening of CTD. The ELISA results indicate no TNF-α nor IL-1β were detectable in the sham activated AM conditioned media. While normally alveolar macrophages (resident macrophages in the lung) do not come into contact with cardiac tissue, their secreted factors may very well flow downstream from the pulmonary vasculature and into the heart. Many studies have focused on the role both infiltrating and resident macrophages play in various cardiac pathologies (for reviews see (Meldrum 1998; Frangogiannis, Smith et al. 2002; Frangogiannis and Entman 2005)), but none have examined the normal physiological role of macrophages in cardiac tissue. For example, Morimoto et al. have demonstrated that over-expression of monocytes chemoattractant protein-1 (MCP-1) in cardiac tissue recruited macrophage infiltration but improved remodeling after myocardial infarction (MI)(Morimoto, Takahashi et al. 2006). The notion, therefore, that macrophages are "active" only after MI or other cardiac pathology remains rather firmly embedded in published literature. Unfortunately, the role resident cardiac macrophages may play in normal cardiac physiology remains unstudied. It remains a tantalizing possibility that alveolar macrophages, through some unknown secreted factor(s), modulate cardiac function and underscores the potential complexity of biology where two components separated by great distances but connected through blood might interact in previously unheard of ways.

No effect of leachables or other aqueous phase contaminants from PM were found in HTCs

Surprisingly, simply mixing PMs in culture media and then culture HTCs in the presence of possibly contaminated culture media did not result in any changes in HTC function. This may be explained by two distinct possibilities: either no aqueous phase leachables were present in SRM 1649a, or whatever leachables that dissolved into the culture media were either biologically inert or remained at concentrations below which their activity can be observed.

This is in contrast to previous studies examining the role LPS and other aqueous phase material, particularly metals, adsorbed onto PM has on cardiac function(Graff, Cascio et al. 2004; Wold, Simkhovich et al. 2006; Wallenborn, McGee et al. 2007). However, a key difference between those experiments and these sets of experiments is that HTCs were not directly exposed to PM. The bulk particulates were removed via centrifugation and only the

conditioned medium permitted to contact HTCs. It is possible that the effects of PM on cardiac tissue may require a pathway involving direct contact with particulates.

Furthermore, the difference in HTC function between L- group and P- argues against LPS as the mediator of changes. If LPS were present in PM, one would expect P- samples to appear similar to L- samples. That the P- group tracked instead the S- group implies both that LPS was either not present or below 10ng/mL, and that the aqueous fraction absorbed onto PM did not have an effect on HTC function. One cannot rule out, however, the unlikely possibility that leachables from PM canceled the effects of LPS in such a manner as to mimic untreated (S-) samples.

Increased calcium kinetics were observed for HTCs cultured in PM-activated AM conditioned media

While the shortening of CTD_{80} was rather weak in that it failed to repeat on a second experiment, the faster time to peak and rates of calcium increase were consistent across both cultures. The faster kinetics indicate a possible "stress" reaction of the cardiomyocytes to the secreted cytokines, but is at odds with published literature reports on the effects of exogenous TNF-α on cardiomyocytes(Janczewski, Kadokami et al. 2003) where they found decreased calcium amplitudes, longer time to peak, and overall depressed calcium kinetics primarily for male transgenic mice over-expressing TNF-α but also in female transgenics as well. The differences noted between these transgenic experiments and our results might be explained by the use of neonatal rat ventriculomyocytes (NRVM) in the HTCs as opposed to postnatal cardiomyocytes. Several studies have suggested that NRVM either lack one of the two sub-types of TNF receptors(Comstock, Krown et al. 1998) or have built-in innate protection against apoptosis from TNF-α(Comstock, Krown et al. 1998; Hickson-Bick, Jones et al. 2006). The precise signal transduction pathway of TNF-α in cardiomyocytes has not been delineated completely, yet, but it is thought that type I TNF receptors (TNF-RI) results in apoptosis whereas type II TNF receptors (TNF-RII) have a cardioprotective effect(Higuchi, McTiernan et al. 2004). There is some evidence to suggest that NRVM lack TNF-RI(Comstock, Krown et al. 1998) and thus possibly converting TNF-α from a pro-apoptotic signal to an anti-apoptotic signal. In fact, the response of cardiomyocytes in general to TNF-α stimulation differs from that of other cells, e.g. non-myocyte cardiac cells, in that both pro-apoptotic and anti-apototic mechamisms are engaged(Kubota, Miyagishima et al. 2001) for postnatal rat myocytes.

Although fluorescence data collected was not normalized to account for differences in staining intensity or excitation variability, e.g. ratiometric imaging, we have noted increased fluorescence amplitudes in calcium transients across two different experiments for HTCs treated with PM-activated AM conditioned media (P+). It is tempting to conclude that TNF-α secreted by the P+ group induced a form of "hypertrophy" which would account for the increased fluorescence consistent with previous reports of TNF-α inducing hypertrophy in neonatal cardiomyocytes(Condorelli, Morisco et al. 2002). This, however, is at odds with the lack of increased amplitude for the LPS-activated AM conditioned media group (L+) despite both having measurable TNF-α levels. In fact, L+ samples had higher TNF-α levels than P+, but the dose-response of HTCs to TNF-α is not necessarily monotonic. For example, LPS-stimulated TNF-α secretion from cardiomyocytes displayed a biphasic distribution(Wright, Singh et al. 2002) suggesting that different TNF-α levels and/or combinations of other cytokines released by activated AM may result in alternate phenotypes.

HTC changes from PM activated AM conditioned media may not be due to TNF-a or IL-1β

Despite ELISA testing showing that both PM (P+) and LPS (L+) activated AM secreted rather large amounts of TNF-α and slight amounts of IL-1β, the HTCs treated by conditioned media from the two different stimuli differed in their functional assessment. Although the actual concentrations of TNF-α differed significantly between P+ and L+, there is also the possibility that the combination of TNF-α and some other as-yet-unidentified factor may be responsible for the changes in HTC behavior. In fact, it is also possible that TNF-α may not be the mediating cytokine. The levels of TNF-α and IL-1β should not be interpreted as causal for HTC effects and instead are merely indicators of AM activation. They serve best as proxies for indicating that AM cells were different from sham inoculated AM, and have little to no significance beyond that.

Actual identification of the cytokine or cytokines responsible for the HTC changes – if it even is a cytokine – requires additional experiments with blocking antibodies and adding exogenous sources of suspected mediating factors. In Chapter 16, we will present some evidence for how IL-1β might affect HTC function but only at doses much greater than that detected here for activated AM.

Limitations

The most attractive aspect of the reduced *in-vitro* model is also its greatest limitation. While such a model can provide deeper understanding for how cytokines fundamentally influence cardiac myocytes, the combined (potentially synergistic or antagonistic) effect of other cell types are ignored. For example, it is rather well established now that endothelial cells can profoundly influence cardiac behavior(Mohacsi, Magyar et al. 2004), and the role particulate matter air pollution plays in modifying endothelium remains under active investigation(Brook, Brook et al. 2003). By co-culturing different cell types in our *in-vitro* model system – an ongoing lab effort – we can elucidate the individual contributions of each cell type in the response, and better understand the combined effects in a living organism. Furthermore, the additional knowledge gained from exploring mechanisms of arrhythmogenesis could help engineer future anti-arrhythmic therapies.

Conclusion

Particulate matter (PM) induces alveolar macrophages (AM) to release a cocktail of cytokines including TNF-α and IL-1β. When HTCs were treated with culture media conditioned by PM activated AM, faster calcium dynamics ensued in contrast to previous literature reports of the effects of TNF-α. Several possibilities exist that can explain this discrepancy. First, the cocktail of cytokines including TNF-α may not replicate the effect of TNF-α alone. Second, neonatal rat cardiomyocytes are reported to have different TNF-α responses than non-myocytes and even postnatal myocytes, used in many of the previous reports. Lastly, HTCs may have undergone a "hypertrophic" response consistent with previous reports and gave the false impression of faster kinetics due to optical measurements.

Interestingly, LPS activated AM released greater levels of TNF-α, but had a less pronounced effect on calcium dynamics than PM activated AM suggesting that factors other than TNF-α played a role or that TNF-α had a bimodal response. Furthermore, the presence

of quiescent (sham activated) AM affected calcium transient durations in a manner that is independent of TNF-α or IL-1β (none were detectable by ELISA) hinting at a possible, constitutive or regulatory role for macrophages (resident, infiltrating, or remotely connected via vasculature) during normal cardiac electrophysiology.

16. DIRECT ARRHYTHMOGENIC ACTION OF IL-1B IN CARDIOMYOCYTE NETWORKS

Abstract

The respiratory system reacts to variety of environmental stressors by triggering the release of vast amounts of inflammatory cytokines with far-reaching potential to affect the functionality of critical organ systems. We hypothesized that interleukin-1β (IL-1β), a major inflammatory signaling molecule, can directly alter the propensity of cardiac tissue to arrhythmia occurrence. We employed an in vitro experimental model and fast optical mapping of excitation. Engineered cardiomyocyte networks were treated with different concentrations of IL-1β (0.2 to 10ng/ml), and their response to electrical stimulation was imaged using fluorescent dual-labeling for voltage and calcium. Prolongation of action potential duration was found after 48-hour exposure to IL-1β. The latter clearly lowered the threshold for occurrence of instabilities (alternans) in the treated group vs. control (5.7±0.4 Hz vs. 7.8±0.9 Hz). The underlying mechanisms of IL-1β arrhythmogenicity were studied by applying a two-factor (treatment and pacing frequency) ANOVA analysis to compare multiple parameters shaping the voltage and calcium response. Our results suggest that the arrhythmogenic potential of IL-1β is brought about by significant decrease in conduction velocity of propagation, combined with prolongation of the action potential repolarization phase, both of which are known to promote instabilities (alternans) in the high-frequency range. These findings can explain cardiac functional abnormalities in a range of inflammation-precipitated conditions, including exposure to particulate matter.

I. Introduction

Alveolar macrophages (AM) release a host of inflammatory mediator molecules (cytokines) in response to activation by particulate matter (PM) in the lungs or when subjected to other environmental stressors. Often, a multitude of cytokines is released at once, leading to an inflammatory cocktail entering the bloodstream. The classical (well studied) inflammatory cytokine IL-1β is known to be a part of this immunological cocktail secreted by PM-activated AMs (Ishii, Fujii et al. 2004). Upon entering the bloodstream, there is a great likelihood that cardiac tissue will be exposed to the inflammatory cocktail. The direct effects of IL-1β on cardiac electrophysiology during an inflammatory condition, either particulate matter induced or otherwise, are not well understood.

A series of previous studies have found a link between exposure to IL-1β and altered calcium handling in treated cardiomyocytes (Thaik, Calderone et al. 1995; Bick, Liao et al. 1997; McTiernan, Lemster et al. 1997; Bick, Wood et al. 1999). More specifically, IL-1β (2-5ng/ml over 24h) was shown to suppress the gene expression of the Na/Ca exchanger (Carrillo, Cafferata et al. 1998), the SERCa pump, Ryanodine receptors, and L-type Ca2+ channels (Thaik, Calderone et al. 1995), or to completely abolish calcium transients (Combes, Frye et al. 2002) in neonatal rat cardiomyocyte preparations. An increase in diastolic and systolic calcium levels was found in other studies upon treatment with IL-1β and TNF-α both at 10ng/ml (Bick, Liao et al. 1997; Bick, Wood et al. 1999). The various effects of IL-1β on calcium handling are further reflected in contractility measurements. Chronotropic effect, i.e. increase in spontaneous beating rate was reported for cardiomyocytes subjected to pharmacological treatment with both IL-1β and TNF-α (Oddis, Simmons et al. 1994). In contrast, (Combes, Frye et al. 2002) demonstrated complete elimination of contractions after long-term (4 days) exposure to IL-1β (2ng/ml) combined with UV exposure. Similarly, general depression of contractility was seen in cardiomyocytes treated with high doses of IL-1β and TNF-α (Weisensee, Bereiter-Hahn et al. 1993). Furthermore, alterations in action potential morphology and duration were reported for excised guinea pig ventricular tissue superfused with IL-1β (Li and Rozanski 1993). More specifically, the cytokine prolonged action potential duration (APD90) in isolated cells, and at least partially, the effects were attributed to IL-1β – induced changes in the L-type Ca2+ channels.

The studies discussed above, dealing with IL-1β impact on cardiac electrophysiology have omitted several important aspects. First, previous research has not considered the cytokine effects in a spatially-extended system, i.e. as they relate to electrical wave propagation. Second, effects on transmembrane voltage or intracellular calcium have been quantified for a fixed frequency only. Thus restitution (frequency dependent) effects of IL-1β in treated cardiomyocytes have not been previously reported. Both spatial and restitution related aspects of cardiac function are generally important determinants of propensity to arrhythmias. Hence, for assessing potential arrhythmogenic effects of inflammatory cytokines on the heart, it is imperative to consider both of these characteristics.

We set out to obtain measurements of these properties with an imaging system that can record electrical wave propagation speeds (conduction velocity, CV) in addition to more

traditional parameters (action potential duration, calcium transient duration (CTD), etc.) in monolayer cardiomyocyte networks. These measurements were done while dynamically changing the stimulation frequency to mimic heart rate changes and probe the restitution response. We hypothesized that IL-1β is capable of directly increasing the arrhythmogenicity of cardiac tissue in a dose-dependent and frequency-dependent manner through changes in APD, CTD, and CV.

II. Materials and Methods

Neonatal rat cardiomyocytes were cultured on flat elastic scaffolds as previously described (Bien, Yin et al. 2003). Briefly, cardiac myocytes from three day old Sprague-Dawley rats were isolated with trypsin and collagenase and fibroblasts were removed through a preplating process. Myocytes were plated at a density of $4x10^5$ cells/cm^2 onto fibronectin-coated PDMS scaffolds. Cells were maintained at 37°C with 5% CO_2 in culture medium with 10% fetal bovine serum on the first two days after culture, and switched to 2% fetal bovine serum thereafter. On the fifth day after culture, the scaffolds were treated with lyophilized recombinant Rat IL-1β (Biosource) in culture medium at serially diluted doses of 0, 0.2, 1, 5, or 10 ng/mL (n = 13-22 per dose) – within range of prior IL-1β studies using neonatal rats (Thaik, Calderone et al. 1995; Bick, Liao et al. 1997; Tatsumi, Matoba et al. 2000; Combes, Frye et al. 2002). After dosing, cells were returned to their previous environment and incubated for a period of 48 hours.

At the end of the treatment period and prior to imaging, the samples were sequentially stained for intracellular calcium and transmembrane voltage using 10μM FURA-2 (Molecular Probes) and 75μM di8-ANEPPS (Molecular Probes) fluorescent dyes in Tyrode's solution for 20 and 10 minutes, respectively. The samples were then washed with excess Tyrode's solution for an additional 10 minutes. The cells were transferred to a microscopic perfusion chamber on an inverted microscope, where they were perfused with Tyrode's solution at 30°C for the duration of the experiment. To examine the dynamic changes in function, the cells were paced at increasing frequencies via a line platinum electrode until loss of 1:1 response and occurrence of alternans. The frequency was increased progressively and the last 20 beats were recorded for each step. Alternating wavelengths specific to the voltage and the calcium dye were used to obtain both signals sequentially. The emitted fluorescent signals from the cells were captured using a photomultiplier tube focused on a region at a known distance from the line electrode along the length of the scaffold.

Data analysis was conducted using MATLAB (Mathworks). Custom written transient analysis software was used to measure various parameters of the obtained waveforms for calcium and voltage, such as the action potential duration measured at 80% of repolarization, (APD80), calcium transient duration measured at 80% of repolarization (CTD80), the time delay between the stimulation and response. Conduction velocity was calculated based on the aforementioned time delay and the distance between the electrode and the imaging site. Averaging for each parameter was done at each dose per frequency. The frequency response of these parameters was studied for the pacing range 2Hz to 5Hz. Restitution curves were constructed by power curve fits of the form ax^b for APD and CTD or linear fits for CV, determined empirically based on the average values of the data type across this frequency

range. If normalization was necessary, data at each dose and frequency was normalized against the control average value at 2Hz. Statistical comparisons based on 95% confidence intervals were performed at each dose and frequency. ANOVA with Tukey-Kramer post-hoc test was used to check for significance at $p<0.05$.

Confirmatory macroscopic imaging was performed using an intensified 1024x1280 CMOS camera (pco, Germany) imaging the entire scaffold. For these measurements, cells were stained with Fluo-4 calcium dye for 20 minutes and washed with Tyrode's solution for 20 minutes. The imaging was conducted at room temperature. Cells were paced at increasing frequencies using a line electrode until alternans occurred. The recorded movies were analyzed in MATLAB using Hilbert-transform based phase mapping (Bray and Wikswo 2002) to determine the depolarization state of cells at any given time.

III. Results

Treatment with IL-1β led to earlier occurrence of alternans and other instabilities upon external pacing. This phenomenon was clearly dose-dependent (**Figure 16-1**). The higher treatment doses (1, 5, and 10ng/ml) were found to be statistically different from control ($p<0.05$), with the largest difference registered at the 10ng/ml: an average break frequency of 5.7Hz compared to 7.8Hz in control samples. To clarify the mechanisms leading to earlier loss of 1:1 response, various action potential and calcium transients were analyzed.

Action potential duration was affected by the cytokine treatment. Using normalized power curve fits of APD responses over the 2-5Hz frequency range, a dose-dependent prolongation of APD80 was revealed (**Figure 16-2**). Furthermore, this effect was frequency modulated, i.e. the difference in APD80 between groups was most pronounced at 2Hz, while APDs converged to the same value at higher frequencies. A comparison of the APD dose response curve at 2 and 5Hz emphasizes this point (**Figure 16-2**): the 2Hz dose response curve slopes upwards from 0.2-10 ng/mL IL-1β, with the 1 and 10ng/mL doses being significantly different from control ($p<0.05$), while the 5Hz dose-response curve remains virtually flat.

Calcium transient duration (CTD) was examined for treatment-induced changes based on the previous literature on calcium handling alterations by IL-1β. Although CTD80 mimicked prolongation trend observed in APD80, our analyses revealed no statistically significant differences across the frequency and dose ranges (data not shown). The CTD restitution slopes were not significantly different, nor were systolic calcium levels.

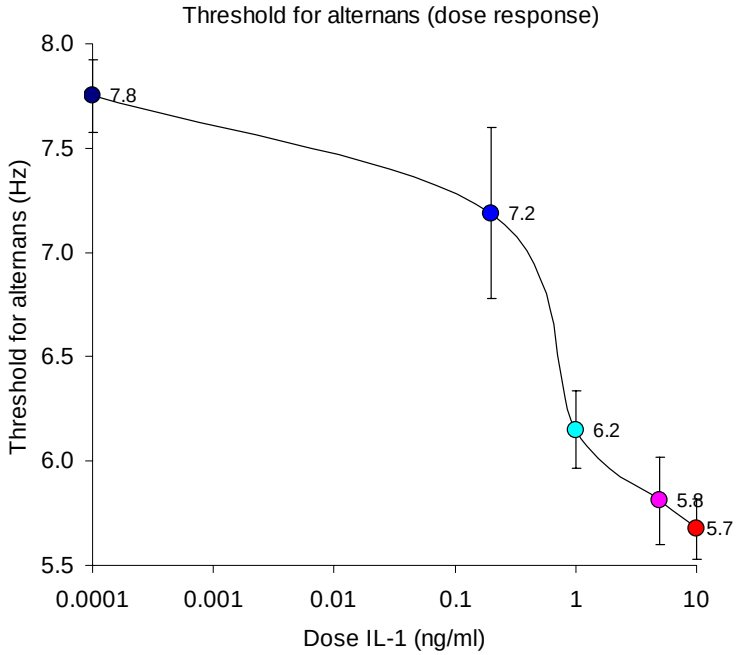

Figure 16-1. IL-1β lowers the threshold for alternans in a dose-dependent manner. Upon external pacing at increasing frequencies (dynamic restitution protocol), a clear dose-dependent change was observed in the highest frequency at which samples were able to follow 1:1 before exhibiting instabilities (alternans). Shown are mean±SE, significance (*) at $p<0.05$.

Further analysis of wave propagation revealed suppression in conduction velocity induced by IL-1β treatment (**Figure 16-3**). When the conduction velocities of each dose were plotted against frequency, it became evident that treatment with IL-1β had depressed the conduction velocity in a dose-dependent manner. This effect was also frequency dependent, but unlike APD and CTD, larger differences were seen at higher pacing frequencies (**Figure 16-3**). At 5Hz, the differences between control and the higher doses (1, 5, 10ng/mL IL-1β) were all significantly different ($p<0.05$), while at 2Hz only 10ng/mL IL-1β was significantly different from control.

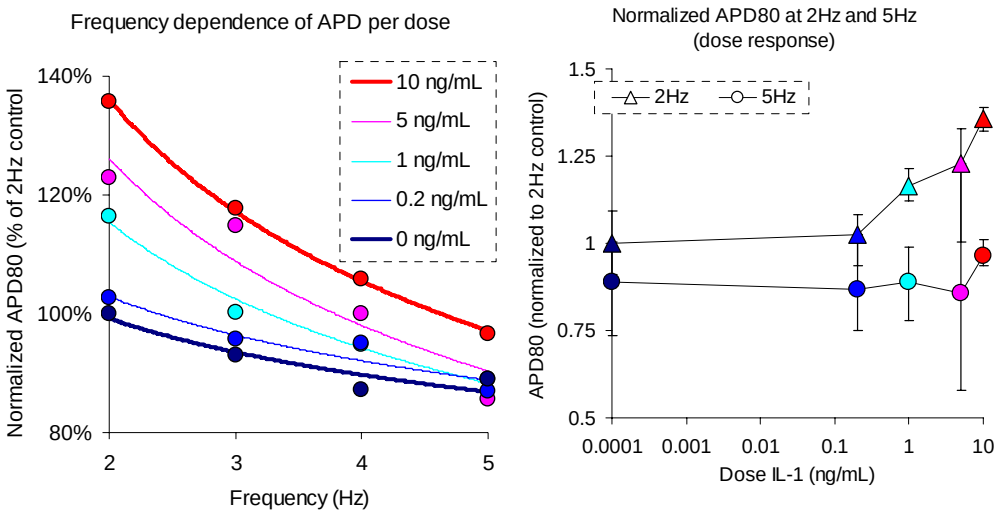

Figure 16-2 IL-1β prolongs action potential duration (APD) as a function of dose.
For the frequency range 2-5Hz, APD shortened with frequency and prolonged with dose – average values shown normalized to 2Hz control APD. The effects of IL-1β on APD were found to be frequency-dependent, i.e. stronger effects were seen at lower frequencies (2Hz vs. 5Hz). Treated samples had a trend towards a steeper APD-frequency relationship.

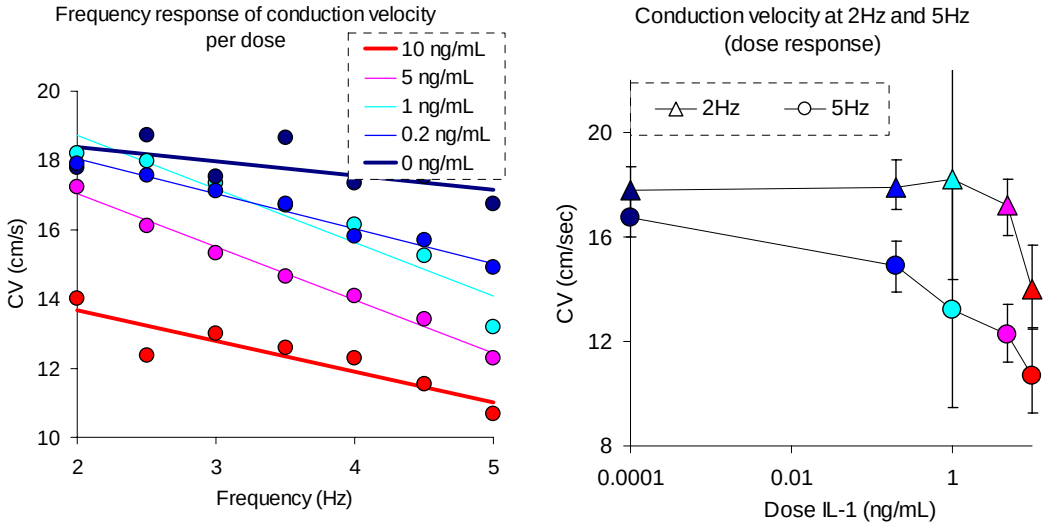

Figure 16-3 IL-1β lowers conduction velocity (CV) as a function of dose.
CV exhibited a substantial dose-dependent and frequency-dependent slowing. The effects of IL-1β were more pronounced at higher frequencies (5Hz vs. 2Hz). Treatment slightly steepened the CV-frequency relationship. Shown are mean values with 95% confidence intervals; significance (*) is at $p<0.05$.

Macroscopic imaging of IL-1β treated samples (10ng/ml) stained with Fluo-4 was also performed to examine alterations to wave propagation in response to treatment. When compared to control samples imaged in the same manner, the IL-1β treated scaffolds upheld the trend in alternans threshold in the microscopic trials. Analysis at frequencies around the break frequency revealed that spatially discordant alternans eventually preceded wavebreaks (**Figure 16-4** and **Figure 16-5**). Regions of alternans created the heterogeneity substrate, causing a subsequent wave breakup, initiation of a reentrant wave and degeneration of the system into a fibrillation-like state (**Figure 16-5**).

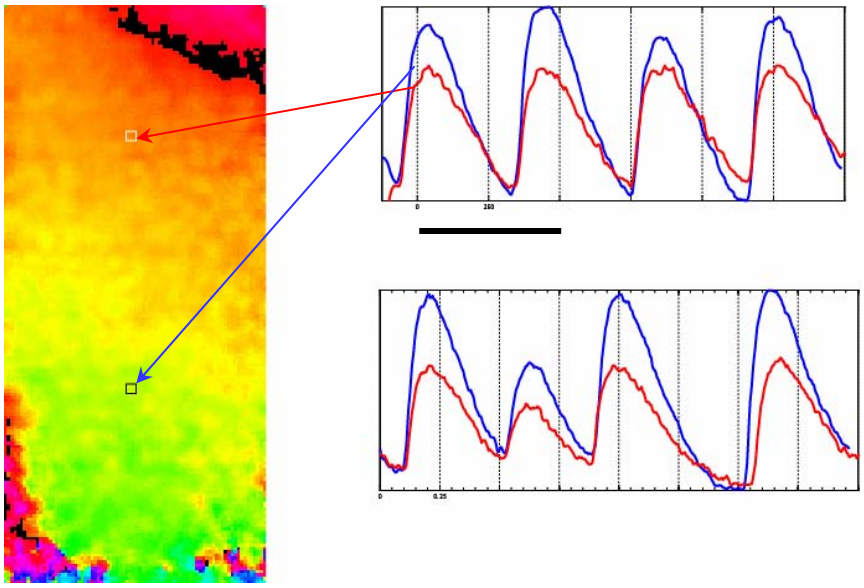

Figure 16-4 Local alternans heralds the onset of arrhythmias.
A phase map of normal propagation with traces of calcium from two locations is shown. On top, at 2.2Hz pacing, only local alternans are seen (blue region). At 2.4Hz pacing, alternans and blocks develop in both regions. Shown sample is 1.2x0.7cm in size.

IV. Discussion and Conclusions

Our goal was to characterize dose-dependent changes in cardiac electrophysiology upon direct exposure to an inflammatory cytokine IL-1β. This analysis was designed to address spatial and frequency-related aspects, omitted in previous studies of direct cytokine effects on the heart. We found dose-dependent decrease in the threshold for alternans, i.e. the treated samples exhibited alternans and other instabilities at lower frequencies than controls (**Figure 16-1**). This is a new finding that might help explain inflammation-linked arrhythmias in stressed hearts (exercise or other exertion activities). We sought to reveal the mechanism of this enhanced propensity to instabilities.

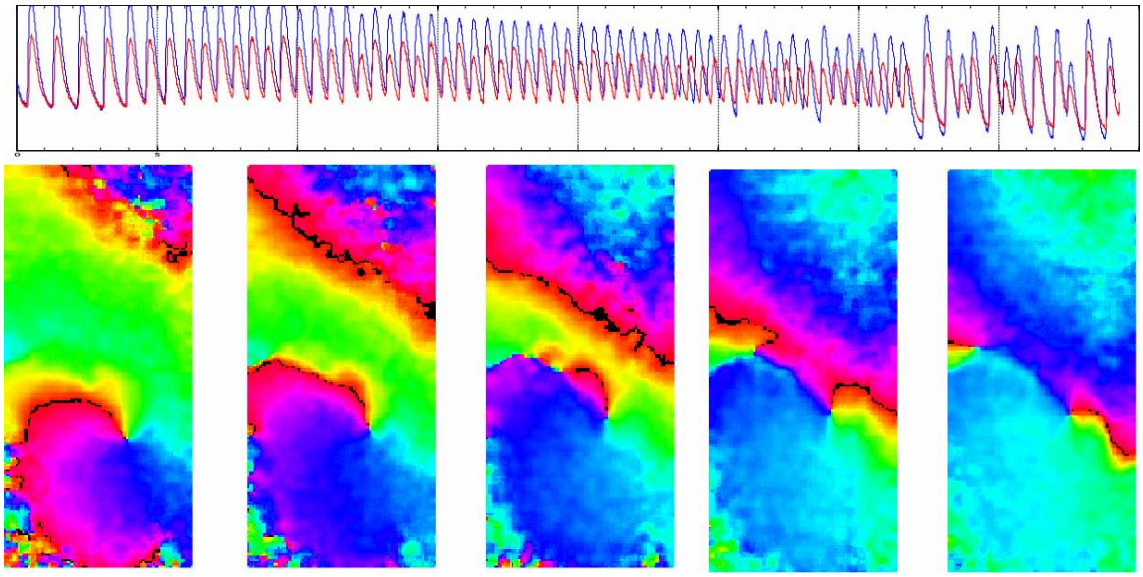

Figure 16-5 Amplitude alternans predict the induction of a spiral in a IL-1β treated sample (10ng/ml).
Time traces from the two areas indicated in Figure 4 show the evolution of amplitude alternans in intracellular calcium, followed by a conduction block. Series of phase maps, 250ms apart demonstrate how the spiral interacted with the paced wavefronts, creating an obstacle (*) for the next beat. Pacing line electrode is on top.

Probing various waveform and propagation characteristics yielded somewhat surprising results that calcium dynamics was not significantly altered – only a trend for CTD prolongation at higher IL-1β doses was observed. However, statistically significant APD80 prolongation was measured at a range of IL-1 β doses, confirming previous reports in single guinea pig cells (Li and Rozanski 1993). Interestingly, this APD prolongation was modulated by frequency and was most pronounced at lower frequencies. This led to effective steeper APD restitution slopes for IL-1β - treated samples (**Figure 16-2**). Similarly, CV restitution was also steepened in treated cells (**Figure 16-3**) with overall suppression in CV across the frequency range. Unlike APD (and CTD), the largest dispersion of CV upon treatment was seen at the higher frequencies.

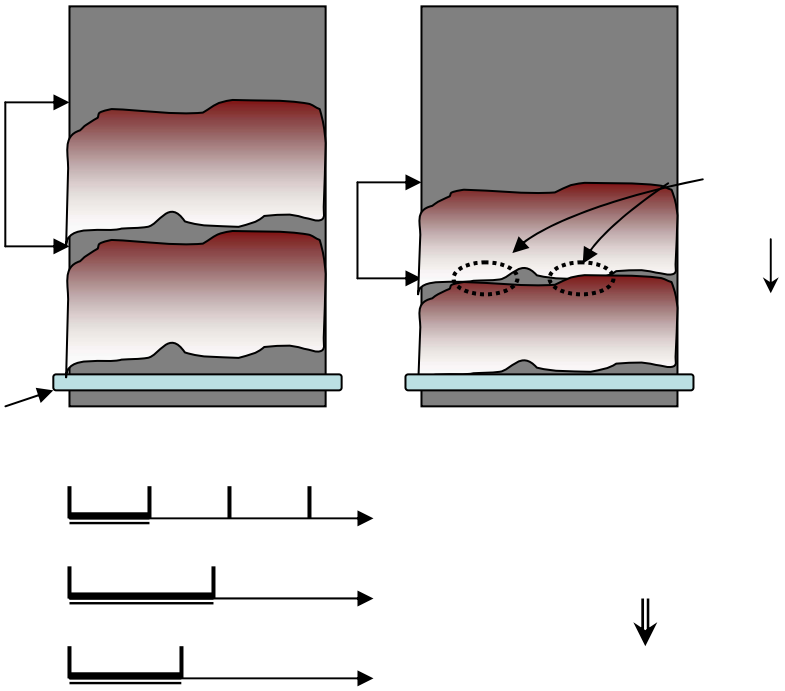

Figure 16-6 Mechanism of instability induction.
An abstract model illustrates how observed changes in properties (CV and APD) due to cytokine treatment may increase the level of wavefront-waveback interactions and thus result in earlier alternans and blocks, as demonstrated experimentally.

Based on these data, we present a simple model of wavebreaks and early occurrence of alternans in IL-1β -treated cardiac tissue (**Figure 16-6**). Normal wave propagation occurs as long as one propagation wave does not collide with the tail end of the previous propagation wave (i.e. by not encountering an area that is depolarizing or in its refractory period). The spacing between waves or "diastolic wavelength" is a function of wave's conduction velocity and action potential duration, both of which are known to decrease as pacing frequency increases. At some frequency, the system will reach a critical point where the combined action of the shorter action potential duration and the lower conduction velocity will be such that the system is unable to fully recover from the first depolarization wave before another wave comes. IL-1β -treated cardiac tissue has lower conduction velocity and longer action potential duration than control at any given frequency. At high frequencies, the "diastolic wavelength" (space between successive waves) becomes almost exclusively a function of CV because of negligible APD prolongation at higher rates. Since IL-1β -treated samples have lower conduction velocity at a given frequency and higher CV restitution, the collision of successive waves will inevitably occur at a lower pacing frequencies compared to control. Confirmation of this theory is obtained from macroscopic imaging of IL-1β -treated samples, where

wavefront-waveback collisions were observed that led to spatially discordant alternans and subsequent reentry induction (**Figure 16-4** and **Figure 16-5**).

The observation that significant APD changes were only mirrored by a trend but not significant CTD changes induced by the cytokine treatment was somewhat surprising in view of multiple previous reports. Generally, calcium signals mimic voltage signals. The lack of significance in the calcium parameters may hint at some degree of voltage-calcium uncoupling in the system – longer APDs are not matched with proportionally long CTDs. This could lead to adverse effects on contraction and force generation in the system and could also contribute to the systemic instabilities that ultimately cause the breakdown of wave propagation.

Future studies should look at the molecular mechanisms behind the reported here functional changes in IL-1β - treated samples. For example, the suppression of CV reported here can be due to gap junctional uncoupling or to sodium current suppression. We tend to believe the former mechanism because of no significant differences between APD rise time (data not shown) and because of previous reports indicating possible effects of inflammatory cytokines on gap junctions. IL-1β treatment clearly suppressed Connexin-43 expression in astrocytes (John, Kondo et al. 1999) and differentially inhibited heterologous (myoendothelial) gap junctions (Hu and Cotgreave 1997). Treatment with bacterial lipopolysaccharide (LPS) had similar negative effects on cardiac Connexin-43 in vivo (Fernandez-Cobo, Gingalewski et al. 1999). Another limitation of the current study is the single cytokine exploration. It is understood that the combined action of IL-1β with other inflammatory cytokines may lead to positive feedback responses and stronger functional changes.

In summary, we have demonstrated that IL-1β directly alters the function of cardiac tissue through dose-dependent and frequency-dependent changes in action potential duration and conduction velocity, which ultimately lead to a more arrhythmogenic substrate and easier occurrence of instabilities.

Acknowledgements

This work was supported in part by grants from the National Science Foundation (BES-0503336), the Whitaker Foundation (RG-02-0654) and the American Heart Association (0430307N) to EE, and a National Research Service Award to HB (1F30ES01337101).

17. FUTURE OUTLOOK

The evidence linking particulate matter air pollution and cardiovascular disease is growing. Earlier epidemiological studies have only demonstrated weak associations with particulate matter exposure and cardiac morbidity(Pope 2004) leaving the question open as to whether particulate matter induces cardiac arrhythmias. A recent follow-up to a large, multi-center study has demonstrated that reduction in particulate matter levels was associated with decreased cardiac mortality(Laden, Schwartz et al. 2006). Taken together, these results provide compelling evidence that particulate matter air pollution is indeed linked to cardiovascular disease, and that understanding the mechanisms driving particulate-matter induced cardiovascular morbidity and mortality would be an important step forward in this public health matter. There are few other disease models where the exposed population is so vast and so varied and where sub-populations more vulnerable to exposure exist but have yet to be identified.

This project attempted to answer just one aspect of particulate matter's association with cardiac arrhythmias. In doing so, it sets the stage for future studies and advancement in the knowledge of not just pollution's effects on human health, but also better understanding of inflammation's effects on cardiac tissue and fundamental behaviors of re-entrant, spiral wave activity. From the simple extension of identifying the composition of cytokines released from the pulmonary vascular bed after exposure to particulate matter to future studies on the role of neurohormonal systems in pollution-induced cardiac arrhythmias, the field remains invitingly open to future discoveries. It is hoped that such an endeavor will bring together disparate fields and culminate in greater understanding much as cross-pollination results in more robust plants.

LIST OF REFERENCES

Akins, R. E. (2002). "Can tissue engineering mend broken hearts?" *Circ Res* **90**(2): 120-2.

Alexis, N. E., J. C. Lay, et al. (2006). "Biological material on inhaled coarse fraction particulate matter activates airway phagocytes in vivo in healthy volunteers." *J Allergy Clin Immunol* **117**(6): 1396-403.

Alfaro-Moreno, E., L. Martinez, et al. (2002). "Biologic effects induced in vitro by PM10 from three different zones of Mexico City." *Environ Health Perspect* **110**(7): 715-720.

Andor, T. (2003). "Making sense of sensitivity: Signal-to-noise, dynamic range and background photons." from www.andor.com

Arnoczky, S. P., M. Lavagnino, et al. (2002). "In situ cell nucleus deformation in tendons under tensile load; a morphological analysis using confocal laser microscopy." *J.Orthop.Res* **20**(1): 29-35.

Arutunyan, A., L. M. Swift, et al. (2002). "Initiation and propagation of ectopic waves: insights from an in vitro model of ischemia-reperfusion injury." *Am.J Physiol Heart Circ.Physiol* **283**(2): H741-H749.

Arutunyan, A., D. R. Webster, et al. (2001). "Localized injury in cardiomyocyte network: a new experimental model of ischemia-reperfusion arrhythmias." *Am J Physiol Heart Circ Physiol* **280**(4): 1905-15.

Bagate, K., J. J. Meiring, et al. (2004). "Vascular effects of ambient particulate matter instillation in spontaneous hypertensive rats." *Toxicol Appl Pharmacol* **197**(1): 29-39.

Barkley, D., M. Kness, et al. (1990). "Spiral-wave dynamics in a simple model of excitable media: The transition from simple to compound rotation." *Physical Review. A* **42**(4): 2489-2492.

Bateson, T. F. and J. Schwartz (2004). "Who is sensitive to the effects of particulate air pollution on mortality? A case-crossover analysis of effect modifiers." *Epidemiology* **15**(2): 143-149.

Baxter, W. T., J. M. Davidenko, et al. (1997). "Technical features of a CCD video camera system to record cardiac fluorescence data." *Ann Biomed Eng* **25**(4): 713-25.

Baxter, W. T., S. F. Mironov, et al. (2001). "Visualizing excitation waves inside cardiac muscle using transillumination." *Biophys.J.* **80**(1): 516-530.

Bayly, P. V., B. H. KenKnight, et al. (1998). "Spatial organization, predictability, and determinism in ventricular fibrillation." *Chaos* **8**(1): 103-115.

Becker, S., J. M. Soukup, et al. (2003). "Response of human alveolar macrophages to ultrafine, fine, and coarse urban air pollution particles." *Exp Lung Res* **29**(1): 29-44.

Berenfeld, O., R. Mandapati, et al. (2000). "Spatially distributed dominant excitation frequencies reveal hidden organization in atrial fibrillation in the Langendorff-perfused sheep heart." *J.Cardiovasc.Electrophysiol.* **11**(8): 869-879.

Berenfeld, O., A. M. Pertsov, et al. (2001). "What is the organization of waves in ventricular fibrillation?" *Circ.Res.* **89**(3): E22.

Bernus, O., M. Wellner, et al. (2005). "Simulation of voltage-sensitive optical signals in three-dimensional slabs of cardiac tissue: application to transillumination and coaxial imaging methods." *Phys.Med Biol* **50**(2): 215-229.

Bick, R. J., J. P. Liao, et al. (1997). "Temporal effects of cytokines on neonatal cardiac myocyte Ca2+ transients and adenylate cyclase activity." *Am J Physiol* **272**(4 Pt 2): H1937-44.

Bick, R. J., D. E. Wood, et al. (1999). "Cytokines increase neonatal cardiac myocyte calcium concentrations: the involvement of nitric oxide and cyclic nucleotides." *J Interferon Cytokine Res* **19**(6): 645-53.

Bien, H. and E. Entcheva (2006). "Spatial frequency content in optical mapping of cardiac cell monolayers." *Am J Physiol Heart Circ Physiol* **291**(3): H1484; author reply H1484-5.

Bien, H., L. Yin, et al. (2002). *Cardiac cell networks on elastic microgrooved scaffolds*, Houston, TX.

Bien, H., L. Yin, et al. (2003). "Cardiac cell networks on elastic microgrooved scaffolds." *IEEE Eng Med Biol Mag* **22**(5): 108-112.

Bien, H., L. Yin, et al. (2006). "Calcium instabilities in mammalian cardiomyocyte networks." *Biophys J* **90**(7): 2628-40.

Biktashev, V. N. and A. V. Holden (1994). "Design Principles of A Low-Voltage Cardiac Defibrillator Based on the Effect of Feedback Resonant Drift." *Journal of Theoretical Biology* **169**(2): 101-112.

Biktashev, V. N. and A. V. Holden (1998). "Reentrant waves and their elimination in a model of mammalian ventricular tissue." *Chaos* **8**(1): 48-56.

Bishop, M. J., B. Rodriguez, et al. (2006). "Synthesis of voltage-sensitive optical signals: application to panoramic optical mapping." *Biophys.J.* **90**(8): 2938-2945.

Blatter, L. A., J. Kockskamper, et al. (2003). "Local calcium gradients during excitation-contraction coupling and alternans in atrial myocytes." *J Physiol* **546**(Pt 1): 19-31.

Bouthillier, L., R. Vincent, et al. (1998). "Acute effects of inhaled urban particles and ozone: lung morphology, macrophage activity, and plasma endothelin-1." *Am J Pathol* **153**(6): 1873-84.

Bray, M. A. and J. P. Wikswo (2002). "Considerations in phase plane analysis for nonstationary reentrant cardiac behavior." *Phys.Rev.E.Stat.Nonlin.Soft.Matter Phys.* **65**(5 Pt 1): 051902.

Bray, M. A. and J. P. Wikswo (2003). "Examination of optical depth effects on fluorescence imaging of cardiac propagation." *Biophys.J.* **85**(6): 4134-4145.

Briggs Dd, J. (2004). "Chronic obstructive pulmonary disease overview: prevalence, pathogenesis, and treatment." *J Manag Care Pharm* **10**(4 Suppl): S3-10.

Brook, R. D., J. R. Brook, et al. (2003). "Air pollution: the "Heart" of the problem." *Curr Hypertens Rep* **5**(1): 32-9.

Brook, R. D., B. Franklin, et al. (2004). "Air pollution and cardiovascular disease: a statement for healthcare professionals from the Expert Panel on Population and Prevention Science of the American Heart Association." *Circulation* **109**(21): 2655-2671.

Bruns, A. (2004). "Fourier-, Hilbert- and wavelet-based signal analysis: are they really different approaches?" *J Neurosci Methods* **137**(2): 321-32.

Bub, G., L. Glass, et al. (1998). "Bursting calcium rotors in cultured cardiac myocyte monolayers." *Proc Nat Acad Sci USA* **95**: 10283-10287.

Bub, G., A. Shrier, et al. (2002). "Spiral wave generation in heterogeneous excitable media." *Phys.Rev.Lett.* **88**(5): 058101.

Bub, G., A. Shrier, et al. (2005). "Global organization of dynamics in oscillatory heterogeneous excitable media." *Phys Rev Lett* **94**(2): 028105.

Bub, G., K. Tateno, et al. (2003). "Spontaneous initiation and termination of complex rhythms in cardiac cell culture." *J.Cardiovasc.Electrophysiol.* **14**(10 Suppl): S229-S236.

Bullen, A. and P. Saggau (1998). "Indicators and optical configuration for simultaneous high-resolution recording of membrane potential and intracellular calcium using laser scanning microscopy." *Pflugers Arch.* **436**(5): 788-796.

Bullen, A. and P. Saggau (1999). "High-speed, random-access fluorescence microscopy: II. Fast quantitative measurements with voltage-sensitive dyes." *Biophys J* **76**(4): 2272-87.

Bullen, A., P. Saggau, et al. (1997). "High-speed, random-access fluorescence microscopy: I. High-resolution optical recording with voltage-sensitive dyes and ion indicators." *Biophys J* **73**(1): 477-91.

Bursac, N., K. K. Parker, et al. (2002). "Cardiomyocyte cultures with controlled macroscopic anisotropy: a model for functional electrophysiological studies of cardiac muscle." *Circ.Res.* **91**(12): e45-e54.

Cabo, C., A. M. Pertsov, et al. (1994). "Wave-front curvature as a cause of slow conduction and block in isolated cardiac muscle." *Circ Res.* **75**(6): 1014-1028.

Carrillo, C., E. G. Cafferata, et al. (1998). "TGF-beta1 up-regulates the mRNA for the Na+/Ca2+ exchanger in neonatal rat cardiac myocytes." *Cell Mol Biol (Noisy-le-grand)* **44**(3): 543-51.

Cesari, M., B. W. Penninx, et al. (2003). "Inflammatory markers and onset of cardiovascular events: results from the Health ABC study." *Circulation* **108**(19): 2317-22.

Cesari, M., B. W. Penninx, et al. (2003). "Inflammatory markers and cardiovascular disease (The Health, Aging and Body Composition [Health ABC] Study)." *Am J Cardiol* **92**(5): 522-8.

Chauhan, V., D. Breznan, et al. (2004). "Effects of ambient air particles on nitric oxide production in macrophage cell lines." *Cell Biol Toxicol* **20**(4): 221-239.

Chen, C., D. Hirdes, et al. (2003). "Gray-scale photolithography using microfluidic photomasks." *Proc Natl.Acad.Sci.U.S.A* **100**(4): 1499-1504.

Chen, C. S., M. Mrksich, et al. (1997). "Geometric control of cell life and death." *Science* **276**(5317): 1425-1428.

Chen, L. C. and J. S. Hwang (2005). "Effects of subchronic exposures to concentrated ambient particles (CAPs) in mice. IV. Characterization of acute and chronic effects of ambient air fine particulate matter exposures on heart-rate variability." *Inhal Toxicol* **17**(4-5): 209-216.

Chen, P. S., T. J. Wu, et al. (2003). "A tale of two fibrillations." *Circulation* **108**(19): 2298-2303.

Cheng, H., M. R. Lederer, et al. (1996). "Calcium sparks and [Ca2+]i waves in cardiac myocytes." *Am J Physiol* **270**(1 Pt 1): C148-C159.

Cheung, J. Y., D. L. Tillotson, et al. (1989). "Cytosolic free calcium concentration in individual cardiac myocytes in primary culture." *Am.J.Physiol* **256**(6 Pt 1): C1120-C1130.

Chialvo, D. R., D. C. Michaels, et al. (1990). "Supernormal excitability as a mechanism of chaotic dynamics of activation in cardiac Purkinje fibers." *Circ Res* **66**(2): 525-45.

Choi, B. R., T. Liu, et al. (2001). "Ventricular fibrillation: Mother rotor or multiple wavelets?" *Circ.Res.* **89**(4): E30.

Choi, B. R., W. Nho, et al. (2002). "Life span of ventricular fibrillation frequencies." *Circ.Res.* **91**(4): 339-345.

Choi, B. R. and G. Salama (1998). "Optical mapping of atrioventricular node reveals a conduction barrier between atrial and nodal cells." *Am J Physiol* **274**: H829-H845.

Choi, B. R. and G. Salama (2000). "Simultaneous maps of optical action potentials and calcium transients in guinea-pig hearts: mechanisms underlying concordant alternans." *J Physiol* **529 Pt 1**: 171-88.

Chudin, E., J. Goldhaber, et al. (1999). "Intracellular Ca2+ dynamics and the stability of ventricular tachycardia." *Biophys J* **77**: 2930-2941.

Clark, P., P. Connolly, et al. (1990). "Topographical control of cell behaviour: II. Multiple grooved substrata." *Development* **108**(4): 635-44.

Cohen, L. B., B. M. Salzberg, et al. (1978). "Optical methods for monitoring neuron activity." *Annu.Rev.Neurosci.* **1**: 171-182.

Coltman, J. W. (1954). "The Specification of Imaging Properties by Response to A Sine Wave Input." *Journal of the Optical Society of America* **44**(6): 468-471.

Combes, A., C. S. Frye, et al. (2002). "Chronic exposure to interleukin 1beta induces a delayed and reversible alteration in excitation-contraction coupling of cultured cardiomyocytes." *Pflugers Arch* **445**(2): 246-56.

Comstock, K. L., K. A. Krown, et al. (1998). "LPS-induced TNF-alpha release from and apoptosis in rat cardiomyocytes: obligatory role for CD14 in mediating the LPS response." *J Mol Cell Cardiol* **30**(12): 2761-75.

Condorelli, G., C. Morisco, et al. (2002). "TNF-alpha signal transduction in rat neonatal cardiac myocytes: definition of pathways generating from the TNF-alpha receptor." *Faseb J* **16**(13): 1732-7.

Corporation, L. S. I. L. (2005). "Storage Solutions and Adapters."

Corti, A., G. Fassina, et al. (1992). "Oligomeric tumour necrosis factor alpha slowly converts into inactive forms at bioactive levels." *Biochem J* **284 (Pt 3)**: 905-10.

Courtemanche, M., L. Glass, et al. (1993). "Instabilities of a propagating pulse in a ring of excitable media." *Physical Review Letters* **70**(14): 2182-2185.

Curtis, A. S. G. and C. D. Wilkinson (1998). "Reactions of cells to topography." *Journal of Biomaterials Science-Polymer Edition* **9**(12): 1313-1329.

Denvir, D. J. and E. Conroy. (2003). "Electron multiplying CCD technology: the new ICCD."

Detrait, E., J. B. Lhoest, et al. (1999). "Fibronectin-pluronic coadsorption on a polystyrene surface with increasing hydrophobicity: relationship to cell adhesion." *J Biomed Mater Res* **45**(4): 404-13.

Deutsch, J., D. Motlagh, et al. (2000). "Fabrication of microtextured membranes for cardiac myocyte attachment and orientation." *J Biomed Mater Res* **53**(3): 267-75.

Devalia, J. L., H. Bayram, et al. (1997). "Mechanisms of pollution-induced airway disease: in vitro studies in the upper and lower airways." *Allergy* **52**(38 Suppl): 45-51; discussion 57-8.

Devaraj, S., T. W. Du Clos, et al. (2005). "Binding and Internalization of C-Reactive Protein by Fcgamma Receptors on Human Aortic Endothelial Cells Mediates Biological Effects." *Arterioscler Thromb Vasc Biol.*

Diabate, S., S. Mulhopt, et al. (2002). "In vitro effects of incinerator fly ash on pulmonary macrophages and epithelial cells." *Int J Hyg Environ Health* **204**(5-6): 323-6.

Diaz, M. E., S. C. O'Neill, et al. (2004). "Sarcoplasmic reticulum calcium content fluctuation is the key to cardiac alternans." *Circ Res.* **94**(5): 650-656.

Dibbs, Z. I., A. Diwan, et al. (2003). "Targeted overexpression of transmembrane tumor necrosis factor provokes a concentric cardiac hypertrophic phenotype." *Circulation* **108**(8): 1002-1008.

Ding, L., R. Splinter, et al. (2001). "Quantifying spatial localization of optical mapping using Monte Carlo simulations." *IEEE Trans.Biomed.Eng* **48**(10): 1098-1107.

Dockery, D. W., C. A. Pope, et al. (1993). "An association between air pollution and mortality in six U.S. cities." *N Engl J Med* **329**(24): 1753-1759.

Domke, J., W. J. Parak, et al. (1999). "Mapping the mechanical pulse of single cardiomyocytes with the atomic force microscope." *Eur.Biophys.J* **28**(3): 179-186.

Donaldson, K., V. Stone, et al. (2001). "Ambient particle inhalation and the cardiovascular system: potential mechanisms." *Environ Health Perspect* **109 Suppl 4**: 523-527.

E.P.A., U. S. (2003). Air Quality Index: A Guide to Air Quality and Your Health. Washington, D.C., US Environmental Protection Agency.

E.P.A., U. S. (2004a). Air Quality Criteria for Particulate Matter (October 2004), Volume I. E. P. Agency. Washington, D.C., US Environmental Protection Agency. **1**.

E.P.A., U. S. (2004b). Air Quality Criteria for Particulate Matter (October 2004), Volume II. E. P. Agency. Washington, D.C., US Environmental Protection Agency. **2**.

E.P.A., U. S. (2004c). The Particle Pollution Report: Current Understanding of Air Quality and Emissions through 2003. Research Triangle Park, NC, US Environmental Protection Agency.

E.P.A., U. S. (2005a). Map of Nonattainment Areas, US Environmental Protection Agency

E.P.A., U. S. (2005b). The Plain English Guide to the Clean Air Act. Washington, D.C., US Enivronmental Protection Agency.

Eason, J. and N. Trayanova (2002). "Phase singularities and termination of spiral wave reentry." *J.Cardiovasc.Electrophysiol.* **13**(7): 672-679.

Efimov, I. and T. Mazgalev (1998). "High-resolution, three-dimensional fluorescent imaging reveals multilayer conduction pattern in the atrioventricular node." *Circulation* **98**: 54-57.

Efimov, I. R., Y. Cheng, et al. (1998). "Virtual electrode-induced phase singularity: a basic mechanism of defibrillation failure." *Circ Res* **82**: 918-925.

Efimov, I. R., V. P. Nikolski, et al. (2004). "Optical imaging of the heart." *Circ.Res.* **95**(1): 21-33.

Ehrenberg, B., D. L. Farkas, et al. (1987). "Membrane potential induced by external electric field pulses can be followed with a potentiometric dye [published erratum appears in Biophys J 1987 Jul;52(1):following 141]." *Biophys J* **51**(5): 833-7.

Eisner, D. A., H. S. Choi, et al. (2000). "Integrative analysis of calcium cycling in cardiac muscle." *Circ Res.* **87**(12): 1087-1094.

Entcheva, E. and H. Bien (2003). "Tension development and nuclear eccentricity in topographically controlled cardiac syncytium." *J Biomed Microdev* **5**(2): 163-168.

Entcheva, E. and H. Bien (2005a). "Acoustic micromachining of three-dimensional surfaces for biological applications." *Lab Chip* **5**(2): 179-83.

Entcheva, E. and H. Bien (2005b). "Macroscopic optical mapping of excitation in cardiac cell networks with ultra-high spatiotemporal resolution." *Prog.Biophys Mol.Biol.*

Entcheva, E., H. Bien, et al. (2004). "Functional cardiac cell constructs on cellulose-based scaffolding." *Biomaterials* **25**(26): 5753-5762.

Entcheva, E., Y. Kostov, et al. (2004). "Fluorescence imaging of electrical activity in cardiac cells using an all-solid-state system." *IEEE Trans.Biomed.Eng* **51**(2): 333-341.

Entcheva, E., S. N. Lu, et al. (2000). "Contact fluorescence imaging of reentry in monolayers of cultured neonatal rat ventricular myocytes." *J Cardiovasc Electrophysiol* **11**(6): 665-76.

Faber, G. M. and Y. Rudy (2000). "Action potential and contractility changes in [Na(+)](i) overloaded cardiac myocytes: a simulation study." *Biophys J* **78**(5): 2392-404.

Fast, V., B. Darrow, et al. (1996). "Anisotropic activation spread in heart cell monolayers assessed by high-resolution optical mapping. Role of tissue discontinuities." *Circ Res* **79**: 115-127.

Fast, V. and A. Kleber (1993). "Microscopic conduction in cultured strands of neonatal rat heart cells measured with voltage-sensitive dyes." *Circ Res* **73**: 914-925.

Fast, V., S. Rohr, et al. (1998). "Activation of cardiac tissue by extracellular electrical shocks. Formation of secondary sources at intercellular clefts in monolayers of cultured myocytes." *Circ Res* **82**: 375-385.

Fast, V. G., E. R. Cheek, et al. (2004). "Effects of electrical shocks on Cai2+ and Vm in myocyte cultures." *Circ Res.* **94**(12): 1589-1597.

Fast, V. G. and R. E. Ideker (2000). "Simultaneous optical mapping of transmembrane potential and intracellular calcium in myocyte cultures." *J Cardiovasc Electrophysiol* **11**(5): 547-56.

Fast, V. G. and A. G. Kleber (1995a). "Block of impulse propagation at an abrupt tissue expansion: evaluation of the critical strand diameter in 2- and 3-dimensional computer models." *Cardiovasc Res* **30**: 449-459.

Fast, V. G. and A. G. Kleber (1995b). "Cardiac tissue geometry as a determinant of unidirectional conduction block: assessment of microscopic excitation spread by optical mapping in patterned cell cultures and in a computer model." *Cardiovasc Res* **29**: 697-707.

Fast, V. G. and A. G. Kleber (1997). "Role of wavefront curvature in propagation of cardiac impulse." *Cardiovasc Res* **33**: 258-271.

Fernandez-Cobo, M., C. Gingalewski, et al. (1999). "Downregulation of connexin 43 gene expression in rat heart during inflammation. The role of tumour necrosis factor." *Cytokine* **11**(3): 216-24.

Fink, C., S. Ergun, et al. (2000). "Chronic stretch of engineered heart tissue induces hypertrophy and functional improvement." *Faseb J* **14**(5): 669-79.

Folch, A. and M. Toner (2000). "Microengineering of cellular interactions." *Annu.Rev.Biomed.Eng* **2**: 227-256.

Fox, J. J., E. Bodenschatz, et al. (2002). "Period-doubling instability and memory in cardiac tissue." *Phys.Rev.Lett.* **89**(13): 138101.

Fox, J. J., J. L. McHarg, et al. (2002). "Ionic mechanism of electrical alternans." *Am J Physiol Heart Circ Physiol* **282**(2): H516-H530.

Frame, L. H. and M. B. Simson (1988). "Oscillations of conduction, action potential duration, and refractoriness. A mechanism for spontaneous termination of reentrant tachycardias." *Circulation* **78**(5 Pt 1): 1277-87.

Frampton, J. E., C. H. Orchard, et al. (1991). "Diastolic, systolic and sarcoplasmic reticulum [Ca2+] during inotropic interventions in isolated rat myocytes." *J Physiol (Lond)* **437**: 351-75.

Frangogiannis, N. G. and M. L. Entman (2005). "Chemokines in myocardial ischemia." *Trends Cardiovasc Med* **15**(5): 163-9.

Frangogiannis, N. G., C. W. Smith, et al. (2002). "The inflammatory response in myocardial infarction." *Cardiovasc Res* **53**(1): 31-47.

Gabor, D. (1949). "Theory of communication." *Proc IEEE* **93**(26): 429-457.

Garfinkel, A., P. S. Chen, et al. (1997). "Quasiperiodicity and chaos in cardiac fibrillation." *J Clin.Invest* **99**(2): 305-314.

Gavett, S. H., S. L. Madison, et al. (1997). "Metal and sulfate composition of residual oil fly ash determines airway hyperreactivity and lung injury in rats." *Environ Res* **72**(2): 162-172.

Gillis, A. M., V. G. Fast, et al. (1996). "Spatial changes in transmembrane potential during extracellular electric shocks in cultured monolayers of neonatal rat ventricular myocytes." *Circ Res* **79**: 676-690.

Gillis, A. M., V. G. Fast, et al. (2000). "Mechanism of ventricular defibrillation : the role of tissue geometry in the changes in transmembrane potential in patterned myocyte cultures." *Circulation* **101**(20): 2438-45.

Gilmour, M. I., S. O'Connor, et al. (2004). "Differential pulmonary inflammation and in vitro cytotoxicity of size-fractionated fly ash particles from pulverized coal combustion." *J Air Waste Manag Assoc* **54**(3): 286-95.

Gilmour, R. F., Jr., N. F. Otani, et al. (1997). "Memory and complex dynamics in cardiac Purkinje fibers." *Am J Physiol* **272**(4 Pt 2): H1826-32.

Girouard, S. D., K. Laurita, et al. (1996). "Unique properties of cardiac action potentials recorded with voltage-sensitive dyes." *J Cardiovasc Electrophysiol* **7**: 1024-1038.

Glass, L. (1991). "Cardiac arrhythmias and circle maps-A classical problem." *Chaos.* **1**(1): 13-19.

Glass, L., A. L. Goldberger, et al. (1986). "Dynamics of pure parasystole." *Am J Physiol* **251**(4 Pt 2): H841-7.

Glass, L., D. Zipes, et al. (1995). Nonlinear dynamics and chaos in cardiac oscillatory systems. *Cardiac electrophysiology. From cell to bedside.* Philadelphia, PA, W.B.Saunders Co**:** 363-370.

Goldmark, P. C., R. Snepvangers, et al. (1949). "The Columbia Long-Playing Microgroove Recording System." *Proceedings of the Institute of Radio Engineers* **37**(8): 923-927.

Gong, H., Jr., C. Sioutas, et al. (2003). "Controlled exposures of healthy and asthmatic volunteers to concentrated ambient particles in metropolitan Los Angeles." *Res Rep Health Eff Inst*(118): 1-36; discussion 37-47.

Graff, D. W., W. E. Cascio, et al. (2004). "Metal particulate matter components affect gene expression and beat frequency of neonatal rat ventricular myocytes." *Environ Health Perspect* **112**(7): 792-798.

Gravereaux, D. W. (1985). "Engineering Highlights of the Lp Record." *Journal of the Acoustical Society of America* **77**(4): 1327-1331.

Gray, R. A., A. M. Pertsov, et al. (1998). "Spatial and temporal organization during cardiac fibrillation." *Nature* **392**(6671): 75-78.

Grinvald, A. and R. Hildesheim (2004). "VSDI: a new era in functional imaging of cortical dynamics." *Nat.Rev.Neurosci.* **5**(11): 874-885.

Grinvald, A., B. M. Salzberg, et al. (1977). "Simultaneous recording from several neurones in an invertebrate central nervous system." *Nature* **268**(5616): 140-142.

Grinvald, A., A. Shoham, et al. (2001). In-vivo optical imaging of cortical architercture and dynamics. U. Windhorst and H. Johansson, Springer Verlag.

Gross, D., L. M. Loew, et al. (1986). "Optical imaging of cell membrane potential changes induced by applied electric fields." *Biophys J* **50**(2): 339-48.

Group, P.-S. (2005). "PCI bus specifications."

Grynkiewicz, G., M. Poenie, et al. (1985). "A new generation of Ca2+ indicators with greatly improved fluorescence properties." *J Biol Chem.* **260**(6): 3440-3450.

Guatimosim, S., K. Dilly, et al. (2002). "Local Ca(2+) signaling and EC coupling in heart: Ca(2+) sparks and the regulation of the [Ca(2+)](i) transient." *J Mol.Cell Cardiol.* **34**(8): 941-950.

Guevara, M. R., L. Glass, et al. (1981). "Phase locking, period-doubling bifurcations, and irregular dynamics in periodically stimulated cardiac cells." *Science* **214**(4527): 1350-3.

Guevara, M. R. and A. Shrier (1990). "Rhythms produced by high-amplitude periodic stimulation of spontaneously beating aggregates of embryonic chick ventricular myocytes." *Ann N Y Acad Sci* **591**: 11-22.

Guevara, M. R., A. Shrier, et al. (1988). "Phase-locked rhythms in periodically stimulated heart cell aggregates." *Am J Physiol* **254**(1 Pt 2): H1-10.

Gurantz, D., R. T. Cowling, et al. (2005). "IL-1beta and TNF-alpha upregulate angiotensin II type 1 (AT1) receptors on cardiac fibroblasts and are associated with increased AT1 density in the post-MI heart." *J Mol Cell Cardiol* **38**(3): 505-15.

Haberichter, T., M. Marhl, et al. (2001). "Birhythmicity, trirhythmicity and chaos in bursting calcium oscillations." *Biophys.Chem.* **90**(1): 17-30.

Hall, K. and L. Glass (1999). "Locating ectopic foci." *J Cardiovasc Electrophysiol* **10**(3): 387-98.

Hansson, G. K. (2005). "Inflammation, atherosclerosis, and coronary artery disease." *N Engl J Med* **352**(16): 1685-1695.

Harkema, J. R., G. Keeler, et al. (2004). "Effects of concentrated ambient particles on normal and hypersecretory airways in rats." *Res Rep Health Eff Inst*(120): 1-68.

Hastings, H. M., F. H. Fenton, et al. (2000). "Alternans and the onset of ventricular fibrillation." *Phys.Rev.E.Stat.Phys.Plasmas.Fluids Relat Interdiscip.Topics.* **62**(3 Pt B): 4043-4048.

Helmke, R. J., V. F. German, et al. (1989). "A continuous alveolar macrophage cell line: comparisons with freshly derived alveolar macrophages." *In Vitro Cell Dev Biol* **25**(1): 44-8.

Henriksen, P. A. and D. E. Newby (2003). "Therapeutic inhibition of tumour necrosis factor alpha in patients with heart failure: cooling an inflamed heart." *Heart* **89**(1): 14-8.

Hetland, R. B., F. R. Cassee, et al. (2005). "Cytokine release from alveolar macrophages exposed to ambient particulate matter: heterogeneity in relation to size, city and season." *Part Fibre Toxicol* **2**: 4.

Hickson-Bick, D. L., C. Jones, et al. (2006). "The response of neonatal rat ventricular myocytes to lipopolysaccharide-induced stress." *Shock* **25**(5): 546-52.

Higuchi, Y., C. F. McTiernan, et al. (2004). "Tumor necrosis factor receptors 1 and 2 differentially regulate survival, cardiac dysfunction, and remodeling in transgenic mice with tumor necrosis factor-alpha-induced cardiomyopathy." *Circulation* **109**(15): 1892-7.

Hilborn, R. C. (1994). *Chaos and nonlinear dynamics: an introduction for scientists and engineers*. New York, Oxford University Press.

Hu, J. and I. A. Cotgreave (1997). "Differential regulation of gap junctions by proinflammatory mediators in vitro." *J Clin Invest* **99**(10): 2312-6.

Hund, T. J., N. F. Otani, et al. (2000). "Dynamics of action potential head-tail interaction during reentry in cardiac tissue: ionic mechanisms." *Am J Physiol Heart Circ Physiol* **279**(4): 1869-79.

Hunt, A., J. L. Abraham, et al. (2003). "Toxicologic and epidemiologic clues from the characterization of the 1952 London smog fine particulate matter in archival autopsy lung tissues." *Environ Health Perspect* **111**(9): 1209-1214.

Hwang, S. M., T. Y. Kim, et al. (2005). "Complex-periodic spiral waves in confluent cardiac cell cultures induced by localized inhomogeneities." *Proc.Natl.Acad.Sci.U.S.A.*

Hwang, S. M., K. H. Yea, et al. (2004). "Regular and alternant spiral waves of contractile motion on rat ventricle cell cultures." *Phys Rev Lett* **92**(19): 198103.

Hyatt, C. J., S. F. Mironov, et al. (2003). "Synthesis of voltage-sensitive fluorescence signals from three-dimensional myocardial activation patterns." *Biophys.J.* **85**(4): 2673-2683.

Hynecek, J. (2001). "Impactron - A new solid state image intensifier." *Ieee Transactions on Electron Devices* **48**(10): 2238-2241.

Hynecek, J. and T. Nishiwaki (2003). "Excess noise and other important characteristics of low light level imaging using charge multiplying CCDs." *Ieee Transactions on Electron Devices* **50**(1): 239-245.

Inoue, S. and K. R. Spring (1997). *Video microscopy. The fundamentals*. New York, Plenum Publishing Corp.

Intel, C. (2005). "Disk Interface Technology: Quick Reference Guide."

Iravanian, S., Y. Nabutovsky, et al. (2003). "Functional Reentry in Cultured Monolayers of Neonatal Rat Cardiac Cells." *Am.J Physiol Heart Circ.Physiol.*

Ishida, H., C. Genka, et al. (1999). "Formation of planar and spiral Ca2+ waves in isolated cardiac myocytes." *Biophys.J* **77**(4): 2114-2122.

Ishihara, Y. and J. Kagawa (2003). "Chronic diesel exhaust exposures of rats demonstrate concentration and time-dependent effects on pulmonary inflammation." *Inhal Toxicol* **15**(5): 473-92.

Ishii, H., T. Fujii, et al. (2004). "Contribution of IL-1 beta and TNF-alpha to the initiation of the peripheral lung response to atmospheric particulates (PM10)." *Am J Physiol Lung Cell Mol Physiol* **287**(1): L176-83.

Iyer, A. N. and R. A. Gray (2001). "An experimentalist's approach to accurate localization of phase singularities during reentry." *Ann.Biomed.Eng* **29**(1): 47-59.

Iyriboz, Y. (2004). "A recent exposure to mustard gas in the United States: clinical findings of a cohort (n = 247) 6 years after exposure." *MedGenMed* **6**(4): 4.

Jalife, J., R. Gray, et al. (1998). "Self-organization and the dynamical nature of ventricular fibrillation." *Chaos* **8**(1): 79-93.

Janczewski, A. M., T. Kadokami, et al. (2003). "Morphological and functional changes in cardiac myocytes isolated from mice overexpressing TNF-alpha." *Am J Physiol Heart Circ Physiol* **284**(3): H960-9.

John, S. A., R. Kondo, et al. (1999). "Connexin-43 hemichannels opened by metabolic inhibition." *J Biol Chem* **274**(1): 236-40.

Johnson, P. L., W. Smith, et al. (1999). "Errors caused by combination of Di-4 ANEPPS and Fluo3/4 for simultaneous measurements of transmembrane potentials and intracellular calcium." *Ann.Biomed.Eng* **27**(4): 563-571.

Jongsma, H. J. and H. E. van Rijn (1972). "Electronic spread of current in monolayer cultures of neonatal rat heart cells." *J Membr Biol* **9**(4): 341-60.

Jongsma, H. J. and R. Wilders (2000). "Gap junctions in cardiovascular disease." *Circ Res* **86**(12): 1193-7.

Kakugo, A., S. Sugimoto, et al. (2002). "Gel machines constructed from chemically cross-linked actins and myosins." *Adv Mater* **14**(16): 1124-1126.

Karma, A. (1994). "Electrical alternans and spiral wave breakup in cardiac tissue." *Chaos* **4**(3): 461-472.

Katz, R. H., G. A. Gibson, et al. (1989). "Disk System Architectures for High-Performance Computing." *Proceedings of the Ieee* **77**(12): 1842-1858.

Kay, M. W. and R. A. Gray (2005). "Measuring curvature and velocity vector fields for waves of cardiac excitation in 2-D media." *IEEE Trans.Biomed.Eng* **52**(1): 50-63.

Keener, J. P. (2000). *Principles of Applied Mathematics: Transformation and Approximation*. Cambridge, MA, Perseus Books.

Kido, S., N. Hasebe, et al. (2005). "Tachycardia-induced myocardial ischemia and diastolic dysfunction potentiate secretion of ANP, not BNP in hypertrophic cardiomyopathy." *Am J Physiol Heart Circ Physiol.*

Killingsworth, C. R., S. A. Shore, et al. (1997). "Rat alveolar macrophages express preprotachykinin gene-I mRNA-encoding tachykinins." *Am J Physiol* **273**(5 Pt 1): L1073-81.

Kim, Y. H., A. Garfinkel, et al. (1997). "Spatiotemporal complexity of ventricular fibrillation revealed by tissue mass reduction in isolated swine right ventricle. Further evidence for the quasiperiodic route to chaos hypothesis." *J Clin.Invest* **100**(10): 2486-2500.

Knisley, S. and B. Hill (1995). "Effects of bipolar point and line stimulation in anisotropic rabbit epicardium: Assessment of the critical radius of curvature for longitudinal block." *IEEE Trans Biomed Eng* **42**(10): 957-966.

Knisley, S. B. (1995). "Transmembrane voltage changes during unipolar stimulation of rabbit ventricle." *Circ Res* **77**: 1229-1239.

Kodavanti, U. P., M. C. Schladweiler, et al. (2002). "Pulmonary and systemic effects of zinc-containing emission particles in three rat strains: multiple exposure scenarios." *Toxicol Sci* **70**(1): 73-85.

Koike, E., S. Hirano, et al. (2004). "cDNA microarray analysis of rat alveolar epithelial cells following exposure to organic extract of diesel exhaust particles." *Toxicol Appl Pharmacol* **201**(2): 178-185.

Kong, W., G. P. Walcott, et al. (2003). "Emission ratiometry for simultaneous calcium and action potential measurements with coloaded dyes in rabbit hearts: reduction of motion and drift." *J Cardiovasc.Electrophysiol.* **14**(1): 76-82.

Kubota, T., M. Miyagishima, et al. (2001). "Overexpression of tumor necrosis factor- alpha activates both anti- and pro-apoptotic pathways in the myocardium." *J Mol Cell Cardiol* **33**(7): 1331-44.

Kucera, J. P., A. G. Kleber, et al. (1998). "Slow conduction in cardiac tissue, II. Effects of branching tissue geometry." *Circ Res* **83**: 795-805.

Kumagai, Y. (2004). "Strategies against high blood pressure in the early morning." *Clin Exp Hypertens* **26**(2): 107-118.

Kurebayashi, N., H. Yamashita, et al. (2004). "Behavior of Ca(2+) waves in multicellular preparations from guinea pig ventricle." *Am.J.Physiol Cell Physiol* **287**(6): C1646-C1656.

Lab, M. J. and J. A. Lee (1990). "Changes in intracellular calcium during mechanical alternans in isolated ferret ventricular muscle." *Circ Res* **66**(3): 585-95.

Lackowicz, J. R. (1999). *Principles of Fluorescence Spectroscopy*. New York, NY, Kluwer Academic/Plenum Publishers.

Laden, F., J. Schwartz, et al. (2006). "Reduction in fine particulate air pollution and mortality: Extended follow-up of the Harvard Six Cities study." *Am J Respir Crit Care Med* **173**(6): 667-72.

Laskin, D. L., L. Morio, et al. (2003). "Peroxides and macrophages in the toxicity of fine particulate matter in rats." *Res Rep Health Eff Inst*(117): 1-51.

Laurita, K. R. and A. Singal (2001). "Mapping action potentials and calcium transients simultaneously from the intact heart." *Am J Physiol Heart Circ Physiol* **280**(5): 2053-60.

Levy, J. I., S. L. Greco, et al. (2002). "The importance of population susceptibility for air pollution risk assessment: a case study of power plants near Washington, DC." *Environ Health Perspect* **110**(12): 1253-1260.

Li, Y. H. and G. J. Rozanski (1993). "Effects of human recombinant interleukin-1 on electrical properties of guinea pig ventricular cells." *Cardiovasc Res* **27**(3): 525-30.

Lin, S. F., R. A. Abbas, et al. (1997). "High-resolution high-speed synchronous epifluorescence imaging of cardiac activation." *Review of Scientific Instruments* **68**(1): 213-217.

Linos Photonics Gmb, H. (2006). Linos Pre-designer, Linos Photonics.

Lipp, P. and E. Niggli (1993). "Microscopic spiral waves reveal positive feedback in subcellular calcium signaling." *Biophys.J* **65**(6): 2272-2276.

Liu, L. J., M. Box, et al. (2003). "Exposure assessment of particulate matter for susceptible populations in Seattle." *Environ Health Perspect* **111**(7): 909-918.

Liu, Y. B., A. Peter, et al. (2003). "Spatiotemporal correlation between phase singularities and wavebreaks during ventricular fibrillation." *J.Cardiovasc.Electrophysiol.* **14**(10): 1103-1109.

Loew, L. M., L. B. Cohen, et al. (1992). "A naphthyl analog of the aminostyryl pyridinium class of potentiometric membrane dyes shows consistent sensitivity in a variety of tissue, cell, and model membrane preparations." *J Membr.Biol* **130**(1): 1-10.

London, B., L. C. Baker, et al. (2003). "Calcium-dependent arrhythmias in transgenic mice with heart failure." *Am J Physiol Heart Circ Physiol* **284**(2): H431-41.

Lundblad, L. K., J. Thompson-Figueroa, et al. (2005). "TNF-{alpha} Over-expression in Lung Disease: a Single Cause Behind a Complex Phenotype." *Am J Respir Crit Care Med.*

Luo, C. H. and Y. Rudy (1994). "A dymanic model of the cardiac ventricular action potential: I. Simulations of ionic currents and concentration changes." *Circ Res* **74**: 1071-1096.

Magari, S. R., J. Schwartz, et al. (2002). "The association between personal measurements of environmental exposure to particulates and heart rate variability." *Epidemiology* **13**(3): 305-310.

Mainardi, L. T., A. M. Bianchi, et al. (2002). "Time-frequency and time-varying analysis for assessing the dynamic responses of cardiovascular control." *Crit Rev.Biomed.Eng* **30**(1-3): 175-217.

Maniotis, A. J., C. S. Chen, et al. (1997). "Demonstration of mechanical connections between integrins, cytoskeletal filaments, and nucleoplasm that stabilize nuclear structure." *Proc.Natl.Acad.Sci.U.S.A* **94**(3): 849-854.

McTiernan, C. F., B. H. Lemster, et al. (1997). "Interleukin-1 beta inhibits phospholamban gene expression in cultured cardiomyocytes." *Circ Res* **81**(4): 493-503.

Meldrum, D. R. (1998). "Tumor necrosis factor in the heart." *Am J Physiol* **274**(3 Pt 2): R577-95.

Mironov, S. F., F. J. Vetter, et al. (2006). "Fluorescence imaging of cardiac propagation: spectral properties and filtering of optical action potentials." *Am J Physiol Heart Circ Physiol* **291**(1): H327-35.

Moe, G. K. (1962). "On Multiple Wavelet Hypothesis of Atrial Fibrillation." *Archives Internationales de Pharmacodynamie et de Therapie* **140**(1-2): 183-&.

Mohacsi, A., J. Magyar, et al. (2004). "Effects of endothelins on cardiac and vascular cells: new therapeutic target for the future?" *Curr Vasc Pharmacol* **2**(1): 53-63.

Molecular, E. (2005). "Optical Microscopy Primer: Proximity-focused image intensifiers."

Morad, M. and G. Salama (1979). "Optical probes of membrane potential in heart muscle." *J Physiol* **292**: 267-295.

Morimoto, H., M. Takahashi, et al. (2006). "Cardiac overexpression of monocyte chemoattractant protein-1 in transgenic mice prevents cardiac dysfunction and remodeling after myocardial infarction." *Circ Res* **99**(8): 891-9.

Murphy, D. B. (2001). *Fundamentals of Light Microscopy and Electronic Imaging*. New York, Wiley-Liss.

Nadziejko, C., K. Fang, et al. (2002). "Effect of concentrated ambient particulate matter on blood coagulation parameters in rats." *Res Rep Health Eff Inst*(111): 7-29.

Narayan, S. M. and J. M. Smith (2000). "Exploiting rate-related hysteresis in repolarization alternans to improve risk stratification for ventricular tachycardia." *J Am Coll Cardiol* **35**(6): 1485-92.

National Center for Health, S. (2004). Health, United States, 2004. With Chartbook on Trends in the Health of Americans. Hyattsville, Maryland.

National, S. (2005). "Interface Products Selection Guide."

Nave, B. T., M. Becker, et al. (2002). "Validation of targets and drug candidates in an engineered three-dimensional cardiac tissue model." *Drug Discov.Today* **7**(7): 419-425.

Nawab, S. H., T. F. Quatieri, et al. (1988). Short-time Fourier transform. *Advanced Topics in Signal Processing*. Englewood Cliffs, NJ, Prentice-Hall.

Nearing, B. D., A. H. Huang, et al. (1991). "Dynamic tracking of cardiac vulnerability by complex demodulation of the T wave." *Science* **252**(5004): 437-40.

Nel, A. E., D. Diaz-Sanchez, et al. (2001). "The role of particulate pollutants in pulmonary inflammation and asthma: evidence for the involvement of organic chemicals and oxidative stress." *Curr Opin Pulm Med* **7**(1): 20-6.

Noujaim, S. F., E. Lucca, et al. (2004). "From mouse to whale: a universal scaling relation for the PR Interval of the electrocardiogram of mammals." *Circulation* **110**(18): 2802-2808.

Nurkiewicz, T. R., D. W. Porter, et al. (2004). "Particulate matter exposure impairs systemic microvascular endothelium-dependent dilation." *Environ Health Perspect* **112**(13): 1299-1306.

Obaid, A. L., T. Koyano, et al. (1999). "Spatiotemporal patterns of activity in an intact mammalian network with single-cell resolution: optical studies of nicotinic activity in an enteric plexus." *J Neurosci* **19**(8): 3073-93.

Oberdorster, G., Z. Sharp, et al. (2004). "Translocation of inhaled ultrafine particles to the brain." *Inhal Toxicol* **16**(6-7): 437-445.

Oddis, C. V., R. L. Simmons, et al. (1994). "Chronotropic effects of cytokines and the nitric oxide synthase inhibitor, L-NMMA, on cardiac myocytes." *Biochem Biophys Res Commun* **205**(2): 992-7.

Otsu, N. (1979). "Threshold Selection Method from Gray-Level Histograms." *Ieee Transactions on Systems Man and Cybernetics* **9**(1): 62-66.

Pak, H. N., Y. B. Liu, et al. (2003). "Synchronization of ventricular fibrillation with real-time feedback pacing: implication to low-energy defibrillation." *Am.J.Physiol Heart Circ.Physiol* **285**(6): H2704-H2711.

Pak, H. N., Y. S. Oh, et al. (2003). "Catheter ablation of ventricular fibrillation in rabbit ventricles treated with beta-blockers." *Circulation* **108**(25): 3149-3156.

Pastore, J. M., S. D. Girouard, et al. (1999). "Mechanism linking T-wave alternans to the genesis of cardiac fibrillation." *Circulation* **99**(10): 1385-94.

Pastore, J. M. and D. S. Rosenbaum (2000). "Role of structural barriers in the mechanism of alternans-induced reentry." *Circ.Res.* **87**(12): 1157-1163.

Patel, N. S., D. Paris, et al. (2005). "Inflammatory cytokine levels correlate with amyloid load in transgenic mouse models of Alzheimer's disease." *J Neuroinflammation* **2**(1): 9.

Patterson, R. H., G. A. Gibson, et al. (1988). *A case for redundant arrays of inexpensive disks (RAID)*, Chicago, ACM Press.

Payne, J. P., S. J. Kemp, et al. (2004). "Effects of airborne World Trade Center dust on cytokine release by primary human lung cells in vitro." *J Occup Environ Med* **46**(5): 420-7.

Peters, A. (2005). "Particulate matter and heart disease: Evidence from epidemiological studies." *Toxicol Appl Pharmacol* **207**(2 Suppl): 477-82.

Peters, A., E. Liu, et al. (2000). "Air pollution and incidence of cardiac arrhythmia." *Epidemiology* **11**(1): 11-7.

Peters, A. and C. A. Pope (2002). "Cardiopulmonary mortality and air pollution." *Lancet* **360**(9341): 1184-1185.

Peters, A., S. von Klot, et al. (2004). "Exposure to traffic and the onset of myocardial infarction." *N Engl J Med* **351**(17): 1721-1730.

Peters, A., S. von Klot, et al. (2005). Air Pollution, Personal Activities, and Onset of Myocardial Infarction in a Case-Crossover Study. Boston, MA.

Pham, Q., K. J. Quan, et al. (2003). "T-wave alternans: marker, mechanism, and methodology for predicting sudden cardiac death." *J Electrocardiol* **36 Suppl**: 75-81.

Pincus, S. M. (1991). "Approximate entropy as a measure of system complexity." *Proc.Natl.Acad.Sci.U.S.A* **88**(6): 2297-2301.

Pino, P., T. Walter, et al. (2004). "Fine particulate matter and wheezing illnesses in the first year of life." *Epidemiology* **15**(6): 702-708.

Polimeni, J. R., D. Granquist-Fraser, et al. (2005). "Physical limits to spatial resolution of optical recording: clarifying the spatial structure of cortical hypercolumns." *Proc Natl Acad Sci U S A* **102**(11): 4158-63.

Pope, C. A. (2000). "Epidemiology of fine particulate air pollution and human health: biologic mechanisms and who's at risk?" *Environ Health Perspect* **108 Suppl 4**: 713-723.

Pope, C. A. (2004). "Air pollution and health - good news and bad." *N Engl J Med* **351**(11): 1132-1134.

Pope, C. A., R. T. Burnett, et al. (2002). "Lung cancer, cardiopulmonary mortality, and long-term exposure to fine particulate air pollution." *JAMA* **287**(9): 1132-1141.

Pope, C. A., M. L. Hansen, et al. (2004). "Ambient particulate air pollution, heart rate variability, and blood markers of inflammation in a panel of elderly subjects." *Environ Health Perspect* **112**(3): 339-345.

Pruvot, E. J., R. P. Katra, et al. (2004). "Role of calcium cycling versus restitution in the mechanism of repolarization alternans." *Circ Res* **94**(8): 1083-90.

PULNix America, e. a. (2005) "Specifications of the Camera Link Interface Standard for Digital Cameras and Frame Grabbers." DOI:

Qu, Z., A. Garfinkel, et al. (2000). "Mechanisms of discordant alternans and induction of reentry in simulated cardiac tissue." *Circulation* **102**(14): 1664-70.

Qu, Z., H. S. Karagueuzian, et al. (2004). "Effects of Na(+) channel and cell coupling abnormalities on vulnerability to reentry: a simulation study." *Am J Physiol Heart Circ Physiol* **286**(4): H1310-21.

Ramshesh, V. K. and S. B. Knisley (2003). "Spatial localization of cardiac optical mapping with multiphoton excitation." *J.Biomed.Opt.* **8**(2): 253-259.

Ramshesh, V. K. and S. B. Knisley (2006). "Use of light absorbers to alter optical interrogation with epi-illumination and transillumination in three-dimensional cardiac models." *J.Biomed.Opt.* **11**(2): 24019.

Ratzlaff, E. H. and A. Grinvald (1991). "A tandem-lens epifluorescence macroscope: hundred-fold brightness advantage for wide-field imaging." *J Neurosci Meth* **36**(2-3): 127-37.

Reff, A., B. J. Turpin, et al. (2005). "Functional group characterization of indoor, outdoor, and personal PM: results from RIOPA." *Indoor Air* **15**(1): 53-61.

Reilly, C. A., J. L. Taylor, et al. (2003). "Capsaicinoids cause inflammation and epithelial cell death through activation of vanilloid receptors." *Toxicol Sci* **73**(1): 170-181.

Rich, D. Q., J. Schwartz, et al. (2005). "Association of short-term ambient air pollution concentrations and ventricular arrhythmias." *Am J Epidemiol* **161**(12): 1123-32.

Riley, M. R., D. E. Boesewetter, et al. (2005). "Comparison of the sensitivity of three lung derived cell lines to metals from combustion derived particulate matter." *Toxicol In Vitro* **19**(3): 411-9.

Ringbaek, T., N. Seersholm, et al. (2005). "Standardised mortality rates in females and males with COPD and asthma." *Eur Respir J* **25**(5): 891-895.

Robbins, M. S. and B. J. Hadwen (2003). "The noise performance of electron multiplying charge-coupled devices." *Ieee Transactions on Electron Devices* **50**(5): 1227-1232.

Roberts, E. S., J. H. Richards, et al. (2003). "Oxidative stress mediates air pollution particle-induced acute lung injury and molecular pathology." *Inhal Toxicol* **15**(13): 1327-46.

Rogers, J. M. (2004). "Combined phase singularity and wavefront analysis for optical maps of ventricular fibrillation." *IEEE Trans.Biomed.Eng* **51**(1): 56-65.

Rohr, S. and J. P. Kucera (1997). "Involvement of the calcium inward current in cardiac impulse propagation: induction of unidirectional conduction block by nifedipine and reversal by Bay K 8644." *Biophys J* **72**: 754-766.

Rohr, S. and J. P. Kucera (1998). "Optical recording system based on a fiber optic image conduit: Assessment of microscopic activation patterns in cardiac tissue." *Biophys J* **75**: 1062-1075.

Rohr, S., J. P. Kucera, et al. (1997). "Paradoxical improvement of impulse conduction in cardiac tissue by cellular uncoupling." *Science* **275**: 841-844.

Rohr, S., J. P. Kucera, et al. (1998). "Slow conduction in cardiac tissue, I. Effects of a reduction of excitability versus a reduction of electrical coupling on microconduction." *Circ Res* **83**: 781-794.

Rohr, S. and B. M. Salzberg (1994). "Multiple site optical recording of transmembrane voltage (MSORTV) in patterned growth heart cell cultures: assessing electrical behavior, with microsecond resolution, on a cellular and subcellular scale." *Biophys.J* **67**(3): 1301-1315.

Rohr, S., D. Shoelly, et al. (1991). "Patterned growth of neonatal rat heart cells in culture. Morphological and electrophysiological characteristics." *Circ Res* **68**: 114-130.

Rosenbaum, D. S., L. E. Jackson, et al. (1994). "Electrical alternans and vulnerability to ventricular arrhythmias." *N Engl J Med* **330**(4): 235-41.

Rosenbruch, K. J. (1960). "Die optischen Bildfehler und die Uebertragungsfunktion." *Optik* **17**: 249-77.

Ross, W. N., B. M. Salzberg, et al. (1977). "Changes in absorption, fluorescence, dichroism, and Birefringence in stained giant axons: : optical measurement of membrane potential." *J Membr.Biol* **33**(1-2): 141-183.

Roth, B. J. (1994). "Mechanisms for electrical stimulation of excitable tissue." *Crit Rev Biomed Eng* **22**(3-4): 253-305.

Ruwhof, C., A. E. van Wamel, et al. (2000). "Cyclic stretch induces the release of growth promoting factors from cultured neonatal cardiomyocytes and cardiac fibroblasts." *Mol.Cell Biochem.* **208**(1-2): 89-98.

Sakai, T. and K. Kamino (2001). "Optical mapping approaches to cardiac electrophysiological functions." *Jpn.J Physiol* **51**(1): 1-18.

Salama, G. and L. M. Loew (1988). Optical measurements of transmembrane potential in heart. *Spectroscopic membrane probes*. Boca Raton, Florida, CRC Press**:** 137-199.

Salama, G. and M. Morad (1976). "Merocyanine 540 as an optical probe of transmembrane electrical activity in the heart." *Science* **48**: 485-487.

Salzberg, B. M. (1989). "Optical recording of voltage changes in nerve terminals and in fine neuronal processes." *Annu.Rev.Physiol* **51**: 507-526.

Schwartz, J. (2001). "Is there harvesting in the association of airborne particles with daily deaths and hospital admissions?" *Epidemiology* **12**(1): 55-61.

Sharifov, O. F., R. E. Ideker, et al. (2004). "High-resolution optical mapping of intramural virtual electrodes in porcine left ventricular wall." *Cardiovasc.Res.* **64**(3): 448-456.

Sharma, R. and S. Pervez (2004). "A case study of spatial variation and enrichment of selected elements in ambient particulate matter around a large coal-fired power station in central India." *Environ Geochem Health* **26**(4): 373-381.

Sheesley, R. J., J. J. Schauer, et al. (2005). "Seasonal and spatial relationship of chemistry and toxicity in atmospheric particulate matter using aquatic bioassays." *Environ Sci Technol* **39**(4): 999-1010.

Shiferaw, Y., D. Sato, et al. (2005). "Coupled dynamics of voltage and calcium in paced cardiac cells." *Phys Rev E Stat Nonlin Soft Matter Phys* **71**(2 Pt 1): 021903.

Shiferaw, Y., M. A. Watanabe, et al. (2003). "Model of intracellular calcium cycling in ventricular myocytes." *Biophys.J* **85**(6): 3666-3686.

Simpson, D. G., L. Terracio, et al. (1994). "Modulation of cardiac myocyte phenotype in vitro by the composition and orientation of the extracellular matrix." *J Cell Physiol* **161**(1): 89-105.

Smith, W. J. (1990). *Modern Optical Engineering*. Boston, MA, McGraw -Hill.

Sobie, E. A., R. C. Susil, et al. (1997). "A generalized activating function for predicting virtual electrodes in cardiac tissue." *Biophys J* **73**(3): 1410-23.

Sommerer, J. C., W. L. Ditto, et al. (1991). "Experimental confirmation of the scaling theory for noise-induced crises." *Physical Review Letters* **66**(15): 1947-1950.

Sommerer, J. C., E. Ott, et al. (1991). "Scaling law for characteristic times of noise-induced crises." *Physical Review. A* **43**(4): 1754-1769.

Soukup, J. M. and S. Becker (2001). "Human alveolar macrophage responses to air pollution particulates are associated with insoluble components of coarse material, including particulate endotoxin." *Toxicol Appl Pharmacol* **171**(1): 20-26.

Spach, M. and J. F. Heidlage (1995). "The stochastic nature of cardiac propagation at a microscopic level. Electrical description of myocardial architecture and its application to conduction." *Circ Res* **76**: 366-380.

Spach, M. S., J. F. Heidlage, et al. (1998). "Extracellular discontinuities in cardiac muscle. Evidence for capillary effects on the action potential foot." *Circ Res* **83**: 1144-1164.

Spach, M. S., J. F. Heidlage, et al. (2000). "Electrophysiological effects of remodeling cardiac gap junctions and cell size: experimental and model studies of normal cardiac growth." *Circ Res* **86**(3): 302-11.

Spengler, J. D., P. Koutrakis, et al. (1996). "Health effects of acid aerosols on North American children: air pollution exposures." *Environ Health Perspect* **104**(5): 492-9.

Streeter, D. D., R. M. Berne, et al. (1979). Gross morphology and fiber geometry of the heart. *Handbook of Physiology, section 2: The Cardiovascular System*. Bethesda, MD, American Physiological Society**:** 61-107.

Sullivan, J., L. Sheppard, et al. (2005). "Relation between short-term fine-particulate matter exposure and onset of myocardial infarction." *Epidemiology* **16**(1): 41-48.

Takahashi, A., P. Camacho, et al. (1999). "Measurement of Intracellular Calcium." *Physiol Rev* **79**(4): 1089-1125.

Talajic, M., D. Papadatos, et al. (1991). "A unified model of atrioventricular nodal conduction predicts dynamic changes in Wenckebach periodicity." *Circ Res* **68**(5): 1280-93.

Tang, Z., B. S. McGowan, et al. (2004). "Gene expression profiling during the transition to failure in TNF-alpha over-expressing mice demonstrates the development of autoimmune myocarditis." *J Mol Cell Cardiol* **36**(4): 515-530.

Tatsumi, T., S. Matoba, et al. (2000). "Cytokine-induced nitric oxide production inhibits mitochondrial energy production and impairs contractile function in rat cardiac myocytes." *J Am Coll Cardiol* **35**(5): 1338-46.

Thaik, C. M., A. Calderone, et al. (1995). "Interleukin-1 beta modulates the growth and phenotype of neonatal rat cardiac myocytes." *J Clin Invest* **96**(2): 1093-9.

Thomas, C. H., J. H. Collier, et al. (2002). "Engineering gene expression and protein synthesis by modulation of nuclear shape." *Proc.Natl.Acad.Sci.U.S.A* **99**(4): 1972-1977.

Tien, J., C. M. Nelson, et al. (2002). "Fabrication of aligned microstructures with a single elastomeric stamp." *Proc Natl.Acad.Sci.U.S.A* **99**(4): 1758-1762.

Tominaga, T., Y. Tominaga, et al. (2001). "Simultaneous multi-site recordings of neural activity with an inline multi-electrode array and optical measurement in rat hippocampal slices." *Pflugers Arch* **443**(2): 317-22.

Tominaga, T., Y. Tominaga, et al. (2000). "Quantification of optical signals with electrophysiological signals in neural activities of Di-4-ANEPPS stained rat hippocampal slices." *J Neurosci Methods* **102**(1): 11-23.

Trayanova, N. and J. Eason (2002). "Shock-induced arrhythmogenesis in the myocardium." *Chaos.* **12**(3): 962-972.

Tsien, R. Y. (1983). "Intracellular measurements of ion activities." *Annu.Rev.Biophys.Bioeng.* **12**: 91-116.

Tung, L. and A. G. Kleber (2000). "Virtual sources associated with linear and curved strands of cardiac cells." *Am J Physiol Heart Circ Physiol* **279**(4): 1579-90.

Uemura, K., S. Adachi-Akahane, et al. (2005). "Carbon monoxide protects cardiomyogenic cells against ischemic death through L-type Ca2+ channel inhibition." *Biochem Biophys Res Commun* **334**(2): 661-8.

Valderrabano, M., P. S. Chen, et al. (2003). "Spatial distribution of phase singularities in ventricular fibrillation." *Circulation* **108**(3): 354-359.

van Eeden, S. F., W. C. Tan, et al. (2001). "Cytokines involved in the systemic inflammatory response induced by exposure to particulate matter air pollutants (PM(10))." *Am J Respir Crit Care Med* **164**(5): 826-830.

van Wamel, A. J., C. Ruwhof, et al. (2001). "The role of angiotensin II, endothelin-1 and transforming growth factor-beta as autocrine/paracrine mediators of stretch-induced cardiomyocyte hypertrophy." *Mol.Cell Biochem.* **218**(1-2): 113-124.

Veness, M. J., G. Delaney, et al. (1999). "Lung cancer in patients aged 50 years and younger: clinical characteristics, treatment details and outcome." *Australas Radiol* **43**(3): 328-333.

Voelkel, K., H. F. Krug, et al. (2003). "Formation of reactive oxygen species in rat epithelial cells upon stimulation with fly ash." *J Biosci* **28**(1): 51-55.

Walker, G. M., H. C. Zeringue, et al. (2004). "Microenvironment design considerations for cellular scale studies." *Lab Chip.* **4**(2): 91-97.

Walker, M. L., X. Wan, et al. (2003). "Hysteresis Effect Implicates Calcium Cycling as a Mechanism of Repolarization Alternans." *Circulation.*

Wallenborn, J. G., J. K. McGee, et al. (2007). "Systemic Translocation of Particulate Matter-Associated Metals Following a Single Intratracheal Instillation in Rats." *Toxicol Sci.*

Watanabe, M. A., F. H. Fenton, et al. (2001). "Mechanisms for discordant alternans." *J Cardiovasc Electrophysiol* **12**(2): 196-206.

Weisensee, D., J. Bereiter-Hahn, et al. (1993). "Effects of cytokines on the contractility of cultured cardiac myocytes." *Int J Immunopharmacol* **15**(5): 581-7.

Weiss, J. N., A. Garfinkel, et al. (1999). "Chaos and the transition to ventricular fibrillation: a new approach to antiarrhythmic drug evaluation." *Circulation* **99**(21): 2819-26.

Whitesides, G. M., E. Ostuni, et al. (2001). "Soft lithography in biology and biochemistry." *Annu.Rev.Biomed.Eng* **3**: 335-373.

Wilen, A., J. P. Schade, et al. (2002). *Introduction to PCI Express: A Hardware and Software Developer's Guide*, Intel Press.

Windisch, H., W. Muller, et al. (1985). "Fluorescence monitoring of rapid changes in membrane potential in heart muscle." *Biophys.J* **48**(6): 877-884.

Winfree, A. (1997). "Heart muscle as a reaction-diffusion medium: the roles of electric potential diffusion, activation front curvature, and anisotropy." *Int J Bifurc Chaos* **7**(3): 487-526.

Winfree, A. T. (1998). "A spatial scale factor for electrophysiological models of myocardium." *Prog Biophys Mol Biol* **69**(2-3): 185-203.

Witkowski, F., L. J. Leon, et al. (1998). "A method for visualization of ventricular fibrillation: Design of a cooled fiberoptically coupled image intensified CCD data acquisition system incorporating wavelet shrinkage based adaptive filtering." *Chaos* **8**(1): 94-102.

Witkowski, F., L. J. Leon, et al. (1998). "Spatiotemporal evolution of ventricular fibrillation." *Nature* **392**: 78-82.

Wold, L. E., B. Z. Simkhovich, et al. (2006). "In vivo and in vitro models to test the hypothesis of particle-induced effects on cardiac function and arrhythmias." *Cardiovasc Toxicol* **6**(1): 69-78.

Wottrich, R., S. Diabate, et al. (2004). "Biological effects of ultrafine model particles in human macrophages and epithelial cells in mono- and co-culture." *Int J Hyg Environ Health* **207**(4): 353-61.

Wright, G., I. S. Singh, et al. (2002). "Endotoxin stress-response in cardiomyocytes: NF-kappaB activation and tumor necrosis factor-alpha expression." *Am J Physiol Heart Circ Physiol* **282**(3): H872-9.

Wu, J. Y., L. B. Cohen, et al. (1999). Optical measurement of membrane potential. *Fluorescent and luminescent probes for biological activity: A practical guide to technology for quantitative real-time analysis*. San Diego, CA, Academic Press**:** 389-404.

Wu, J. Y., Y. W. Lam, et al. (1998). "Voltage-sensitive dyes for monitoring multineuronal activity in the intact central nervous system." *Histochem.J* **30**(3): 169-187.

Wu, R. and A. Patwardhan (2004). "Restitution of action potential duration during sequential changes in diastolic intervals shows multimodal behavior." *Circ Res* **94**(5): 634-41.

Wu, T. J., S. F. Lin, et al. (2002). "Two types of ventricular fibrillation in isolated rabbit hearts: importance of excitability and action potential duration restitution." *Circulation* **106**(14): 1859-1866.

Wu, Y. and W. T. Clusin (1997). "Calcium transient alternans in blood-perfused ischemic hearts: observations with fluorescent indicator fura red." *Am.J.Physiol* **273**(5 Pt 2): H2161-H2169.

Xia, Y. N., J. Tien, et al. (1996). "Non-photolithographic methods for fabrication of elastomeric stamps for use in microcontact printing." *Langmuir* **12**(16): 4033-4038.

Yehia, A. R., D. Jeandupeux, et al. (1999). "Hysteresis and bistability in the direct transition from 1:1 to 2:1 rhythm in periodically driven single ventricular cells." *Chaos* **9**(4): 916-931.

Yin, L., H. Bien, et al. (2004). "Scaffold Topography Alters Intracellular Calcium Dynamics in Cultured Cardiomyocyte Networks." *Am J Physiol Heart Circ Physiol.*

Zaitsev, A. V., O. Berenfeld, et al. (2000). "Distribution of excitation frequencies on the epicardial and endocardial surfaces of fibrillating ventricular wall of the sheep heart [see comments]." *Circ Res* **86**(4): 408-17.

Zemlin, C., E. Storch, et al. (2002). "Alternans and 2:1 rhythms in an ionic model of heart cells." *Biosystems* **66**(1-2): 1-10.

Zimmermann, W. H., K. Schneiderbanger, et al. (2002). "Tissue Engineering of a Differentiated Cardiac Muscle Construct." *Circ Res* **90**(2): 223-230.

Zwillinger, D. (1996). *CRC: Standard Mathematical Tables and Formulae*. Boca Raton, FL, CRC Press.

Zykov, V. S. (1986). "Cycloidal Circulation of Spiral Waves in Excitable Medium." *Biofizika* **31**(5): 862-865.